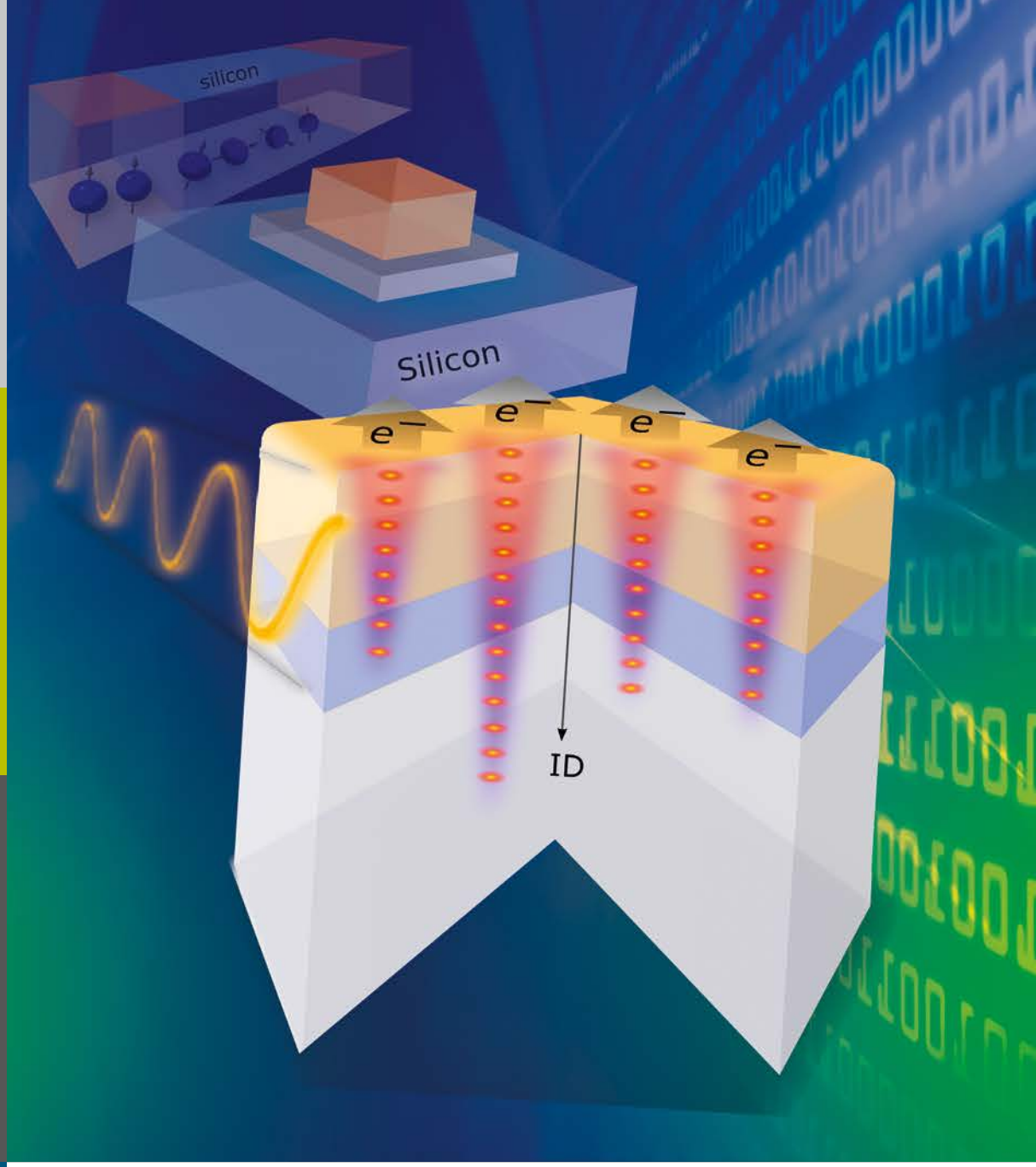

Magnetic Oxide Heterostructures: EuO on Cubic Oxides and on Silicon

Christian Caspers

JÜLICH
FORSCHUNGSZENTRUM

Member of the Helmholtz Association

Schriften des Forschungszentrums Jülich
Reihe Schlüsseltechnologien / Key Technologies Band / Volume 69

Forschungszentrum Jülich GmbH
Peter Grünberg Institute (PGI)
Electronic Properties (PGI-6)

Magnetic Oxide Heterostructures: EuO on Cubic Oxides and on Silicon

Christian Caspers

Schriften des Forschungszentrums Jülich
Reihe Schlüsseltechnologien / Key Technologies Band / Volume 69

ISSN 1866-1807 ISBN 978-3-89336-891-4

Bibliographic information published by the Deutsche Nationalbibliothek.
The Deutsche Nationalbibliothek lists this publication in the Deutsche Nationalbibliografie; detailed bibliographic data are available in the Internet at http://dnb.d-nb.de.

Publisher and Distributor: Forschungszentrum Jülich GmbH
Zentralbibliothek
52425 Jülich
Tel: +49 2461 61-5368
Fax: +49 2461 61-6103
Email: zb-publikation@fz-juelich.de
www.fz-juelich.de/zb

Cover Design: Grafische Medien, Forschungszentrum Jülich GmbH

Printer: Grafische Medien, Forschungszentrum Jülich GmbH

Schriften des Forschungszentrums Jülich
Reihe Schlüsseltechnologien / Key Technologies, Band / Volume 69

D 464 (Diss., Duisburg, Univ., 2013)

ISSN 1866-1807
ISBN 978-3-89336-891-4

The complete volume is freely available on the Internet on the Jülicher Open Access Server (JUWEL) at www.fz-juelich.de/zb/juwel

Zusammenfassung

In dieser Doktorarbeit untersuchen wir fundamentale Eigenschaften von ultradünnen Europiumoxidfilmen (EuO). EuO ist ein Modellsystem eines lokalisierten $4f$ Heisenberg-Ferromagneten, in dem die ferromagnetische Kopplung – eine hohe Kristallqualität vorausgesetzt – durch biaxiale Gitterspannung verändert werden kann. Außerden ist das magnetische Oxid EuO perfekt als Tunnelkontakt mit Spinfunktionalität für die Siliziumspintronik geeignet. Jedoch verhindern die reaktiven chemischen Eigenschaften von EuO und Si bis heute eine erfolgreiche Implementierung in die siliziumbasierte Halbleitertechnologie.

Mit dem Ziel, fundamentale Eigenschaften der magnetischen und elektronischen Struktur ultradünner EuO Filme zu untersuchen, wachsen wir im ersten Teil dieser Arbeit dünne EuO Filme auf leitfähigen YSZ-Substraten mit Volumenschichtdicken bis hinunter zu einem Nanometer mittels Molekularstrahlepitaxie für Oxide (MBE). Diese EuO Filme besitzen einkristalline Qualität und magnetische Eigenschaften von Volumenkristallen. Wir überprüfen die Stöchiometrie der abgedeckten dünnen Filme mittels Photoemissionsspektroskopie im harten Röntgenstrahlenbereich (HAXPES). In Photoemissionsspektroskopie führen wir zudem eine spezielle magnetische Charakterisierung durch unter Ausnutzung des magnetischen Zirkulardichroismuseffekts (MCD) von Eu Kernschalenspektren. Dieser erlaubt Einblicke in die inneratomare Austauschkopplung von dünnen EuO Filmen. Wir erhalten signifikante MCD-Asymmetrien bis zu 49% in der Photoemission des Eu $4d$-Multipletts. Dies ermöglicht uns, die komplexen magnetischen und elektronischen Eigenschaften von ultradünnen EuO Filmen, kohärent auf leitfähigem YSZ gewachsen, zu erforschen.
Eine biaxiale Gitterspannung, welche auf einkristallines EuO wirkt, ist auf fundamentaler Ebene interessant, da sie die magnetischen und elektronischen Eigenschaften kontrolliert verändert. Dafür untersuchen wir epitaktische EuO/$LaAlO_3$ (100)-Schichtsysteme, welche eine Gitterstreckung von 4.2% auf EuO ausüben. EuO übernimmt übergangslos die laterale Gitterkonstante von $LaAlO_3$, wobei die senkrechte Gitterkonstante konstant den Literaturwert von EuO zeigt und daher ein Poissonverhältnis von $\nu_{\mathrm{EuO}} \approx 0$ besitzt. Die streckende Gitterspannung verringert die Curietemperatur signifikant um 12.3 K. Der MCD-Effekt bietet eine elementspezifische magnetische Charakterisierung: Die MCD-Asymmetrie der Eu-Kernschalenphotoemission zeigt eine geringere Reduzierung aufgrund der Gitterspannung als volumenintegrierende magnetische SQUID-Messungen. Daher ist der Einfluss der Gitterspannung auf den inneratomaren Austausch (MCD-Effekt) signifikant anders als auf die Spinordnung der $4f^7$ Schale (SQUID-Messung). Hierdurch zeigt sich, dass der MCD von EuO bedeutende Einblicke in die fundamentalen magnetischen Eigenschaften bietet.

Im zweiten Teil dieser Doktorarbeit beantworten wir die Frage, wie EuO direkt auf Silizium integriert werden kann. Wir legen den Schwerpunkt auf die Optimierung der EuO/Si-Grenzschicht. Aufgrund der extrem hohen chemischen Reaktivität und oberflächenkinetischen Eigenschaften von Eu, EuO und Si während der EuO-Synthese führen wir zunächst eine thermodynamische Analyse durch. Dadurch gewinnen wir drei *in situ* Methoden zur Passivierung von Si (001)-Oberflächen. Mit diesen führen wir eine ausführliche Optimierungsstudie durch, und werten die Oberflächenpassivierung und die resultierenden Grenzschichtreaktionsprodukte mittels einer HAXPES-Analyse aus. Das Minimum der Siliziumoxide an der Grenzschicht ist $d_{\mathrm{opt}}(SiO_x) = 0.69$ nm, während die Silizide zu $d_{\mathrm{opt}}(EuSi_2) = 0.20$ nm optimiert wurden – beides deutlich im Subnanometerbereich.
Zusammenfassend können wir ultradünne EuO/Si (001)-Schichtsysteme mit hoher struktureller und chemischer Qualität sowie mit magnetischen Eigenschaften ähnlich eines Volumenkristalls präparieren. Die Grenzschichtkontamination ist deutlich kleiner als eine geschlossene Bedeckungsschicht. Dadurch erreichen wir eine heteroepitaktische Integration von EuO direkt auf Si (001), welche die experimentelle Basis für kohärentes Tunneln darstellt. Dies ist die erste Studie, welche die direkte Integration von hochqualitativem EuO auf Si (001) umsetzt – ohne zusätzlich aufgebrachte Pufferschichten. Diese optimierten EuO/Si Schichtstrukturen ebnen den Weg für zukünftige Spintronikelemente mit EuO-Tunnelkontakten.

Abstract

In the thesis at hand, we explore fundamental properties of ultrathin europium oxide (EuO) films. EuO is a model system of a localized $4f$ Heisenberg ferromagnet, in which the ferromagnetic coupling – provided a high crystalline quality – can be tuned by biaxial lattice strain. Moreover, the magnetic oxide EuO is perfectly suited as a spin-functional tunnel contact for silicon spintronics. However, up to now a challenging bulk and interface chemistry of EuO and Si has hampered a seamless integration into functional silicon heterostructures.

In order to investigate fundamental aspects of the magnetic and electronic structure of ultrathin EuO, in the first part of this thesis, we synthesize EuO thin films on conductive YSZ substrates from bulk-like thicknesses down to one nanometer by oxide molecular beam epitaxy (MBE). The EuO thin films are of textbook-like single-crystalline quality, and show bulk-like magnetic properties. We control the stoichiometry of buried EuO thin films by hard X-ray photoemission spectroscopy (HAXPES); even a 1 nm ultrathin EuO film exhibits no valence change or interface shifts. Furthermore, we conduct an advanced magnetic characterization by the magnetic circular dichroism (MCD) of Eu core-levels in photoemission, this gives us insight into the intra-atomic exchange coupling of EuO thin films. The MCD reveals large asymmetries of up to 49% in the well-resolved Eu $4d$ photoemission multiplet. Thus, ultrathin EuO coherently grown on conductive YSZ allows us to explore fundamental magnetic and electronic properties of a $4f$ magnetic oxide.
Biaxial lateral strain applied to single-crystalline EuO is of fundamental interest, since it alters the electronic structure and magnetic coupling in a controlled way. We apply +4.2% tensile biaxial strain to EuO by epitaxial EuO/$LaAlO_3$ (100) heterostructures. EuO seamlessly adapts the lateral lattice parameter of $LaAlO_3$, while the perpendicular parameter of EuO is the unchanged EuO bulk value, thus the strained EuO thin film shows a Poisson ratio of $\nu_{\mathrm{EuO}} \approx 0$. The tensile strain reduces the Curie temperature significantly by 12.3 K. The MCD effect provides an advanced magnetic characterization: the MCD asymmetries in Eu core-level photoemission reveal a larger reduction due to the tensile strain than obtained from bulk-averaging SQUID measurements. Thus, the mechanism of tensile strain on intra-atomic exchange (indicated by MCD) is significantly different than on the spin order of the $4f^7$ shell (indicated by SQUID). Experiments on EuO by MCD, thereby, reveal exciting perspectives for studying fundamental magnetic properties of EuO.

In the second part of this thesis, we explore how to integrate EuO directly with Si (001). We focus on interface engineering of structural and chemical properties of the EuO/Si (001) spin-functional heterointerface. In response to the extremely high chemical reactivity and pronounced surface kinetics of Eu, EuO, and Si during EuO synthesis at elevated temperatures, we initially conduct a thermodynamic analysis of the EuO/Si interface. In this way, we decide to investigate three *in situ* passivation techniques for the Si (001) surface, in order to prevent metallic and oxide contaminations at the EuO/Si interface – both being main antagonists for spin-selective tunneling. We conduct a comprehensive optimization study of the EuO/Si heterointerface by tuning the passivation parameters of the Si (001) surface and the growth parameters of EuO. Using HAXPES, we evaluate Si and Eu core-level spectra and determine the minimum of interface contaminants as $d_{\mathrm{opt}}(SiO_x) = 0.69$ nm concomitant with $d_{\mathrm{opt}}(EuSi_2) = 0.20$ nm, both of which are clearly in the subnanometer regime.
In conclusion, our ultrathin EuO/Si (001) heterostructures reveal a high chemical quality of the spin-functional interface, combined with magnetic properties of the EuO layer akin to bulk. By selected interface passivation methods, we achieve a reduction of residual contaminations to clearly below a closed interface coverage. Thus, we could confirm a heteroepitaxial integration of EuO on Si (001), which is the experimental basis for possible band-matched coherent tunneling. This is the first time that a direct integration of high quality EuO on silicon was experimentally realized – without insertion of additional oxide buffer layers. Such optimized EuO/Si (001) heterointerfaces are paving the pathway for near-future spin-functional devices using EuO tunnel contacts.

Contents

1. Introduction 1

2. Theoretical background 5
   2.1. The challenge of stabilizing stoichiometric europium oxide 5
   2.2. Electronic structure of EuO 8
      2.2.1. The open shell $4f^7$ 9
      2.2.2. Valence band, band gap, and conduction bands 10
   2.3. Magnetic properties of EuO 11
      2.3.1. The Curie temperature of EuO 14
      2.3.2. Thin film effects in EuO 15
      2.3.3. Spin filter tunneling in EuO 16
   2.4. Hard X-ray photoemission spectroscopy 18
      2.4.1. The three-step model of photoemission 19
      2.4.2. Spectral features and their interpretation 23
      2.4.3. Implications of hard X-ray excitation 25
   2.5. Magnetic circular dichroism in core-level photoemission 29
      2.5.1. Atomic multiplet theory including MCD 29
      2.5.2. Coupling schemes of angular momenta in Eu^{2+} core-levels 31

3. Experimental details 35
   3.1. Molecular beam epitaxy for oxides 35
   3.2. *In situ* characterization techniques 38
      3.2.1. Reflection high-energy electron diffraction 38
      3.2.2. Low-energy electron diffraction 40
      3.2.3. Auger electron spectroscopy 41
   3.3. Experimental developments at the Oxide-MBE setup 42
   3.4. *Ex situ* characterization techniques 45
      3.4.1. Superconducting quantum interference device magnetometry 45
      3.4.2. X-ray diffraction methods 46
      3.4.3. Hard X-ray photoemission spectroscopy 48
      3.4.4. Depth-selective profiling with HAXPES 51
      3.4.5. Hard X-ray circular magnetic dichroism in photoemission 55

4. Results I: Single-crystalline epitaxial EuO thin films on cubic oxides 57
4.1. Coherent growth: EuO on YSZ (100) 60
4.1.1. Thickness-dependent magnetic properties of EuO thin films 64
4.1.2. Preparation on conductive YSZ substrates 66
4.1.3. HAXPES core-level spectra of single-crystalline EuO/cYSZ 68
4.1.4. Magnetic circular dichroism of single-crystalline EuO/cYSZ 71
4.2. Lateral tensile strain: EuO on $LaAl_3$ (100) 74
4.3. Lateral compressive strain: EuO on MgO (100) 79
4.4. Summary 84

5. Results II: EuO integration directly on silicon 85
5.1. Chemical stabilization of bulk-like EuO directly on silicon 86
5.2. Thermodynamic analysis of the EuO/Si interface 96
5.3. Interface engineering I: Hydrogen passivation of the EuO/Si interface 105
5.4. Interface engineering II: Eu passivation of the EuO/Si interface 111
5.5. Interface engineering III: SiO_x passivation of the EuO/Si interface 117
5.6. Summary 121

6. Conclusion and Outlook 123

A. Appendix 126
A.1. EuO-related phases and cubic oxide substrates 126
A.2. *In situ* analysis of the Si (001) surface by AES 130

Bibliography 132

Software and Internet Resources 149

List of own publications 150

List of conference contributions 152

List of Figures

2.1. Phase diagram of single crystal EuO synthesis 6
2.2. Schematics of an Ellingham diagram 7
2.3. The rare earth electronic structure as a shell scheme for Eu metal. 9
2.4. Band structure of EuO calculated in the LSDA+U approximation 10
2.5. Temperature-dependent scheme of the EuO band gap 10
2.6. Calculated Eu 5*d* conduction bands 11
2.7. Ionic radii of Lanthanide ions 11
2.8. Ferromagnetism in ultrathin EuO films 15
2.9. Schematics of spin filter tunneling into a semiconductor 16
2.10. Schematic band structure of EuO for different directions k 18
2.11. The three step model of photoemission 19
2.12. Momentum conservation during photoexcitation 21
2.13. Photoemission from a solid 22
2.14. Schematics of photoemission spectroscopy 23
2.15. Photoemission cross-sections of hard X-ray excitation 26
2.16. Comparison of the intensity profiles of elastic photoelectron forward diffraction 27
2.17. Calculated Debye-Waller factors for valence-level photoemission 27
2.18. Universal curve of photoemission from solids 28
2.19. MCD components m_J for 2*p* level photoemission with dominant SO interaction 31
2.20. Reduced m_j sublevel energies for *p*-shells and *d*-shells dependent on spin–orbit or exchange coupling 32

3.1. Surface tensions between substrate and deposited film 36
3.2. Transmission electron micrograph of SiO_2 grown by low temperature silicon dry oxidation 38
3.3. RHEED working principle 39
3.4. Illustration of the layer-by-layer growth observed by RHEED 39
3.5. LEED working principle 40
3.6. Cylindrical mirror analyzer 41
3.7. Details of the Oxide-MBE setup at PGI-6 42
3.8. Geometrical arrangement of oxygen nozzles in the Oxide-MBE 43
3.9. Thermal hydrogen cracker 44
3.10. Measurement principle of a SQUID 45
3.11. The measurement geometry of a two-axis X-ray diffraction 47
3.12. Reciprocal space mapping and its interpretation 47
3.13. An extra-wide photoemission survey by HAXPES 48
3.14. HAXPES experiment at KMC1 with HIKE endstation 49
3.15. Schematics of the beamline P09 at PETRA III 50
3.16. HAXPES experiment at the P09 beamline (PETRA III) 51
3.17. Photoelectron excitation and damping in a three-layer heterostructure 52

3.18. Photoelectron yield for low or high kinetic energy and off-normal emission . . 53
3.19. HAXPES probe of a buried interface (schematics) 53
3.20. Geometrical setup for the HAXPES measurement of the MCD effect 56

4.1. Ellingham diagram for Eu oxides and realistic ranges of the oxygen partial pressure 58
4.2. Electron diffraction pattern for EuO thin films under oxygen variation 61
4.3. Bulk and interface morphology of EuO on conductive YSZ (100) observed by HR-TEM 62
4.4. EuO thin film magnetic properties with M measured in-plane and out-of-plane 63
4.5. Electron and X-ray diffraction of a 1 nm-thin EuO film 64
4.6. Thickness dependent magnetic properties in single-crystalline EuO thin films 65
4.7. Conductive YSZ characterized by high- and low-energy electron diffraction . . 66
4.8. Origin of metallicity in e-beam treated YSZ observed by HAXPES 67
4.9. Layer-by-layer growth of EuO/cYSZ (100) observed with the RHEED specular intensity 67
4.10. Hard X-ray photoemission spectroscopy of EuO: Survey 68
4.11. Hard X-ray photoemission spectroscopy of single-crystalline EuO/cYSZ (100) . 69
4.12. HAXPES of ultrathin single-crystalline EuO/cYSZ (100) at 63 K 70
4.13. MCD-PE in core-level photoemission of single-crystalline EuO/cYSZ (100) . . 72
4.14. MCD-PE for ultrathin EuO coherently grown on cYSZ (100) 73
4.15. EuO/LAO (100): process of strained EuO deposition observed by electron diffraction 75
4.16. EuO/LAO (100) perpendicular lattice parameter and layer thickness and roughness 75
4.17. EuO/LAO(100) in-plane and out-of-plane structure 76
4.18. Axial and transversal elasticity of EuO on LAO (100) 77
4.19. Magnetic bulk properties of epitaxial EuO on LAO (100) 78
4.20. MCD-PE for ultrathin EuO under tensile strain on LAO (100) 79
4.21. EuO/MgO (100): EuO deposition under large compressive strain observed by electron diffraction 80
4.22. EuO/MgO (100): different epitaxial arrangements 81
4.23. Magnetic bulk properties of epitaxial EuO on MgO (100) 82

5.1. Magnetic properties of ultrathin EuO directly on HF-Si 86
5.2. HAXPES information depths calculated for a EuO/Si heterostructure 87
5.3. Ultrathin EuO directly on HF-Si investigated by HAXPES 89
5.4. Valence bands of Al, Al_2O_3, and Si in comparison with Eu $4f$ PES multiplets . 90
5.5. Ultrathin EuO directly on HF-Si investigated by HAXPES: Eu4s Eu4d 93
5.6. Si $2p$ core-level photoemission spectra for stoichiometric EuO and oxygen-rich EuO 95
5.7. Ellingham diagram for Eu oxide phases and SiO_2 96
5.8. Three growth regimes of EuO illustrated in a Eu–O–Si Gibbs triangle 97
5.9. Gibbs free energies of formation for EuO, H-Si (001), and $EuSi_2$ 98
5.10. Resulting Gibbs free energies of EuO/Si interface reactions involving $EuSi_2$ . . 99
5.11. Resulting Gibbs free energies of EuO/Si interface reactions regarding SiO_2 in the initial growth stage of EuO 100

5.12. Resulting Gibbs free energies of EuO/Si interface reactions involving SiO_2 during EuO synthesis . . . 101
5.13. Resulting Gibbs free energies of EuO/Si interface reactions involving Europium hydroxide . . . 102
5.14. Free energy of nucleation $\Delta G(j)$ for different saturations $\Delta\mu$ . . . 103
5.15. Surface processes for a magnetic oxide on Si deposition . . . 104
5.16. Si (001) surface reconstructions . . . 105
5.17. Hydrogen termination of the clean Si (001) surface . . . 106
5.18. Surface and interface structure of EuO on Si (001) and on H-passivated Si (001) 107
5.19. The EuO/H-Si interface analyzed by peak fitting of the HAXPES Si 2*p* core-levels 109
5.20. Quantitative results of the EuO/H-Si silicide analysis . . . 110
5.21. Magnetic properties of EuO on H-Si dependent on synthesis temperature . . . 110
5.22. Eu monolayers on top of the Si (001) surface under surface diffusion . . . 112
5.23. The EuO/Eu-Si interface analyzed by RHEED and HAXPES of Si 2*p* and 1*s* core-levels . . . 113
5.24. Quantitative results of the SiO_x analysis in EuO/Eu-Si . . . 114
5.25. The EuO/Si interface with a combined minimization of silicides and SiO_x . . . 115
5.26. The EuO/Si interface: summary of silicide, SiO_x, and the combined minimization 117
5.27. Magnetic properties of EuO on passivated Si (001) under controlled addition of silicide . . . 118
5.28. Consistent peak fit analysis of the SiO_x-passivated EuO/Si (001) interface using Si and Eu core-levels . . . 119
5.29. Quantification of the SiO_x passivation and silicides at the EuO/SiO_x-Si interface by HAXPES . . . 120
5.30. Magnetic properties of epitaxial EuO/Si hybrids with SiO_x passivation . . . 121

A.1. EuO in relation to the substrates YSZ (001), MgO (001), LAO (100), and Si (001) 127
A.2. Structure and (001) plane of yttria-stabilized zirconia (YSZ) . . . 129
A.3. Rhombohedral and pseudo cubic structure of LaAlO3 (LAO) . . . 129
A.4. In situ Auger analysis of the Si (001) surface with different types of hydrogen passivation . . . 131

List of Tables

2.1. Photoemission final states of Eu np shells with spin–orbit coupling 32
2.2. Photoemission final states of Eu nd shells in jj-coupling and LS-coupling . . . 33
2.3. Photoemission final states of Eu ns^2 shells couple via exchange coupling with the ${}^8S_J$ open shell 34
2.4. Photoemission final states of Eu $4f$ shells in LS-coupling 34

3.1. Surface energies of silicon, oxidic substrates, Eu, and metals 37

4.1. Parameters for stoichiometric EuO on cubic substrates by Oxide MBE 59
4.2. Parameters set for creation of conductive YSZ by e-beam treatment 68

5.1. Binding energies and Eu^{3+} valency ratios for stoichiometric EuO and oxygen-rich Eu_1O_{1+x} by Eu $3d$ core-level and $4f$ valence-level spectra 91
5.2. Binding energies and Eu^{3+} valency ratios for stoichiometric EuO and oxygen-rich Eu_1O_{1+x} by Eu $4s$ and $4d$ semi core-level spectra 94

A.1. Eu compounds chemically adjacent to EuO and their properties at a glance . . 127
A.2. Cubic oxides as substrate: lattice parameters and strain when in epitaxial relation with EuO 128

1. Introduction

Smart and powerful electronic devices enrich our daily life. Computers, mobile phones and entertainment devices are performing gigantic amounts of logical operations and saving Terabytes of data. This stunning development of modern information technology largely relies on intelligent device concepts and functional materials. First and foremost, semiconductors are used for logic operations, i. e. the manipulation of charge currents, which enable electrical switching in transistors, diodes, etc. Ferromagnets, in contrast, provide the non-volatile spin degree of freedom, which is the basis for long-term data storage in computer hard disks.

A milestone for information technology was the discovery of the giant magnetoresistance (GMR),[1] which gave birth to the prospering field of *spintronics*.[2] By a combination of ultrathin ferromagnetic and non-magnetic (NM) layers, the GMR allows one to electrically read out magnetic information.[2,19] Substituting the NM layer by an insulating tunnel barrier has significantly increased the magnetoresistance in these ferromagnetic multilayer structures.[3] In this way, the tunnel magnetoresistance (TMR) is the basis for nowadays devices, such as hard disk read heads or magnetic random access memory (MRAM).[4] The significant technological impact of these spintronic devices impressively illustrates the recent progress of spintronics research.

A further important step in spintronics is the integration of ferromagnets with semiconductors, which exploits the non-volatile memory functionality of ferromagnets and the ability to process information of semiconductor logics in a single device. A model system for this combination is the spin-field effect transistor (spin-FET), which has been proposed by Datta and Das (1990).[5] The spin-FET concept relies on the injection of spin-polarized electrons through a ferromagnet into silicon and their subsequent electrical manipulation and detection. Economically, this is advantageous, since switching the spin information is expected to cost much less energy than switching a conventional charge-based transistor. This makes *silicon spintronics*[6,7] a potentially energy saving alternative information technology.

Materials with high electron spin polarization are the key for efficiently operating spintronic devices. In particular, ferromagnetic insulators can provide a spin-polarization of up to 100% when utilized as spin-functional tunnel contacts.* Thus, magnetic tunnel contacts integrated with silicon provide one possible route towards high-efficiency spin-FETs in silicon spintronics. For spin-functional tunneling, a magnetic tunnel contact must have particular properties: (*i*) The magnetic oxide has to provide an unoccupied conduction band above the Fermi level, which is spin-split by exchange interaction. This permits spin-dependent tunneling by the so-called spin filter effect.[10] (*ii*) When combining a ferromagnetic oxide with Si, one has to account for its thermodynamic stability. This requires the control of interface oxidation and diffusion between these highly reactive compounds. (*iii*) Spin injection into silicon using metallic ferromagnets is of negligible efficiency due to a large conductance mismatch.[11]

*Recent endeavors are pushing forward ferromagnetic insulators for all-oxide spintronics in which ferromagnetic and ferroelectric properties may be functionally interrelated.[8,9]

Ferromagnetic oxides closely match the electronic resistance with the silicon electrode. This is one important prerequisite for high-efficiency spin injection. (*iv*) An advanced transport concept is coherent tunneling, which relies on symmetry selection for spin-dependent tunneling and requires a matching of the Bloch states at the interface with the electrode.[12,13] This requires single-crystallinity of the magnetic oxide and epitaxial integration with the electrode.

Which materials fulfil this demanding set of requirements? Only few magnetic oxides are known in nature (e. g. $NiFe_2O_4$, $CoFe_2O_2$, $BiMnO_3$, or $Y_3Fe_5O_{12}$). Those materials provide ferromagnetism and spin filter tunnel functionality at the same time. Among this material class, we choose the binary magnetic oxide, Europium (II) oxide (EuO), which is an ideal model system for a spin-functional magnetic oxide. EuO, in particular, is the only binary magnetic oxide predicted to be thermodynamically stable in direct contact with silicon.[14] The exchange splitting of the lower conduction band ($2\Delta E_{ex} \approx 0.6$ eV) is largest in EuO among the magnetic Europium chalcogenides (EuO, EuS, EuSe). Furthermore, a band match with silicon is feasible due to the comparable bands gaps of EuO (1.12 eV) and Si (1.10 eV). Moreover, the electronic conductance of EuO can be largely tuned[15] by a precise compositional control of the synthesis by molecular beam epitaxy (MBE), which permits a conductance match with silicon. Using MBE growth, EuO thin films have shown single crystalline quality on various cubic substrates, even with large lattice mismatches up to 20%.[16] Thus, the moderate lateral lattice mismatch between EuO and Si (001) of 5.5% is a promising starting point for a heteroepitaxial integration of EuO tunnel contacts with Si. However, during EuO synthesis at elevated temperatures, interdiffusion of Eu atoms with the silicon surface as well as chemical reactions with oxygen will chemically degrade the functional EuO/Si interface. Consequently, EuO directly on Si has revealed a polycrystalline or at best textured structure until now.[17] This motivates our experimental study targeting on high-quality spin-functional EuO/Si interfaces.

From a more fundamental perspective, EuO is a model system of a Heisenberg ferromagnet.[18,19] The half-filled $4f^7$ shell exhibits a full spin alignment below T_C, and is highly localized inside the ionic Eu^{2+} core. A nearest-neighbor interaction between the $4f^7$ shells via $5d$ bands is the origin of the ferromagnetic order, which is an example of localized $4f$ ferromagnetism. This is very rare in nature, and indeed, the existence of ferromagnetic insulators was controversial until the mid-1950s. Until now, several indirect exchange mechanism have been proposed theoretically for the magnetic coupling between the Eu^{2+} ions of EuO. Experimentally, this coupling can be tuned by either external parameters like pressure and biaxial strain, or internal factors like electron doping.* Taking advantage of the well-established single-crystalline growth of EuO thin films on lattice-matched substrates,[15,16,22,23] we decide to propel the research on single-crystalline EuO in the direction of inducing biaxial strain to epitaxial EuO thin films. In this way, we focus on the expansion and compression of the lateral lattice parameter of EuO by biaxial tension from selected underlying cubic substrates. Thereby, we alter the electronic structure and inter-atomic exchange of the EuO single-crystal in a controlled way – this provides insight into fundamental ferromagnetic properties of EuO.

*Very recently, magnetization modulation in EuO by ferroelectric polarization pinning has been reported for strained ferromagnetic–ferroelectric EuO/$BaTiO_3$ heterostructures.[20,21]

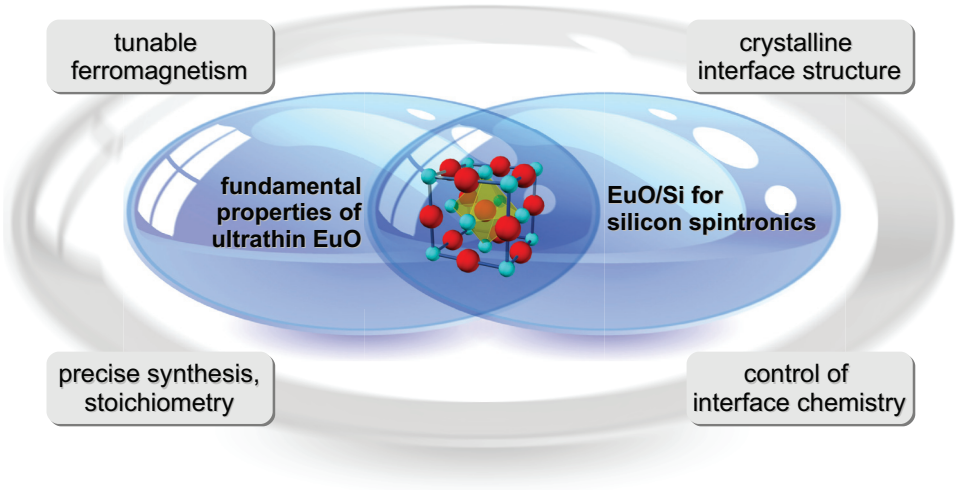

In the thesis at hand, we first address the fundamental properties of the magnetic oxide EuO. In particular, we introduce its electronic structure and discuss the origin of the ferromagnetism of EuO in **Chapter 2**. Next, we present an introduction to photoemission spectroscopy and X-ray circular dichroism as two major experimental techniques applied in this thesis.

The challenge of a high-quality synthesis of EuO – a metastable oxide – lies in controlling its high affinity to oxygen and water. In order to grow single-crystalline and stoichiometric EuO, we take advantage of the oxide molecular beam epitaxy (MBE), which is perfectly suited for a careful control of every growth parameter. We discuss the synthesis of EuO thin films via Oxide-MBE on cubic substrates and methods for their throughout characterization in **Chapter 3**. Given the necessity of protective capping layers, the electronic and magnetic properties of EuO ultrathin films are analyzed as buried layers and interfaces. Thus, there is an experimental need for a spectroscopy technique with a sufficiently large information depth. Therefore, hard X-ray photoemission spectroscopy (HAXPES) is our method of choice, in order to elucidate the electronic structure, chemical information and the magnetic circular dichroism (MCD) of ultrathin EuO heterostructures with buried interfaces.

We optimize and discuss the characteristics of single-crystalline EuO thin films grown by Oxide-MBE in **Chapter 4** of this thesis. For EuO thin films on the lattice-matched YSZ (001) substrate with thicknesses ranging from the bulk down to one nanometer, we investigate the surface structure, the interface to the substrate, and the magnetic properties. We use HAXPES to quantify the precise chemical composition and electronic structure of Eu core-levels in EuO ultrathin films. In this way, we compile a picture of EuO on YSZ (001) with textbook-like quality, and conclude on the essential parameters for a successful synthesis. We proceed our study by an advanced strain engineering of EuO on cubic oxide heterostructures, in order to investigate the impact of biaxial tension on the electronic structure and magnetism of epitaxial EuO thin films. Therefore, we conduct a throughout characterization of ultrathin epitaxial EuO heterostructures on $LaAlO_3$ and MgO substrates providing tensile and compressive biaxial strain, respectively. In this way, we compile a detailed picture of the strained

EuO heterostructures by means of their crystalline structure and averaged magnetic properties, and correlate these with the local intra-atomic exchange properties, as determined by the MCD effect in hard X-ray photoemission spectroscopy.

In the second part of this thesis, we investigate ultrathin EuO films directly on silicon, with the goal to establish spin-functional EuO tunnel barriers for application in spin filter contacts to silicon. Establishing high-quality interfaces between the magnetic oxide EuO to Si is by no means trivial, as we discuss in **Chapter 5**. Ferromagnetic tunnel junctions with additional oxide barriers to avoid diffusion are known,[24–27] however, this approach increases the thickness of the tunnel barrier significantly. Therefore, our objective is a seamless integration of EuO directly with silicon, with focus on realizing a chemically clean and structurally sharp functional interface. First, we synthesize EuO directly on HF-cleaned Si as a prototype for an integration of EuO directly on Si. In order to engineer structurally sharp and chemically clean EuO/Si interfaces, we conduct a comprehensive thermodynamic analysis of possible reactions of the three-constituent system Eu–O_2–Si at the functional interface, and conduct three *in situ* passivation techniques for the Si (001) surface. Remarkably, these chemical surface passivations allow for a heteroepitaxial integration of subsequent EuO layers. We quantify the residual chemical interface reaction products of the passivated EuO/Si interface by HAXPES. Finally, we correlate the optimized chemical interface properties with the crystalline structure and magnetic properties of the ultrathin EuO layer.

We conclude our research on the fundamental properties of ultrathin EuO films and on the integration of EuO tunnel contacts directly with Si (001) in **Chapter 6**.

2. Theoretical background

> ... The hero is a metal atom with strong personal magnetism, whose special properties may vary strongly with the environment.
>
> *(Prof. P.-O. Löwdin in the ceremony speech for the Nobel Prize for P. W. Anderson, Sir N. F. Mott, and J. H. van Vleck[28])*

Europium oxide is one of the very few magnetic insulators,* whose ferromagnetism arises from localized spin-only moments. Moreover, the ferromagnetic oxide EuO is perfectly suited as spin-functional tunnel contact in the field of silicon spintronics.[10] In this thesis, we aim towards an understanding of the fundamental *magnetic* and *electronics properties* of EuO thin films, and towards a successful *integration with silicon* technology. As a fundament for our investigations, we discuss the basic properties of EuO as well as principles of advanced probing techniques used in this thesis.

For the present experimental work on EuO including its meticulous preparation (see Ch. 3), it is obligatory to point out its chemical characteristics which feature a high affinity to oxygen and water. Therefore, at first we provide an introduction to the thermodynamic analysis of reactions which may appear during the MBE-synthesis of EuO (see Ch. 4), and in particular at the EuO/Si interface (see Ch. 5).

We proceed with a discussion of the electronic structure of EuO with focus on valence and conductions bands, as well as the open shell $4f$, which is the origin of the magnetic order in EuO. Subsequently, we describe the ferromagnetism of EuO: the Heisenberg model and couplings to nearest and next-nearest neighbors are briefly introduced, as well as the tuning of T_C and possible applications of EuO as a spin filter oxide.

In order to investigate the electronic structure and to quantify chemical phases of EuO thin films, photoemission spectroscopy is the method of choice. We discuss the physical mechanism of the photoemission process, the interpretation of characteristic spectral features, and finally the specificities of hard X-ray excitation (HAXPES). Finally, we introduce the magnetic circular dichroism (MCD) effect in photoemission, which provides insight into magnetic properties of EuO in terms of the intra-atomic coupling of core-level final states with the magnetic open shell.

2.1. The challenge of stabilizing stoichiometric europium oxide

EuO crystallizes in the face-centered cubic rock-salt structure (*fcc*) with a lattice parameter of 5.144 Å[31] at room temperature.† In order to produce bulk EuO single crystals, very high temperatures of about 1800 °C under an exact stoichiometric supply of Eu and oxygen

*Indeed, ferromagnetism in an insulator was even severely disputed up to the mid-1950s.[29]

†An overview of structural data of EuO and possible substrates as epitaxial seed is given in Appendix A.1.

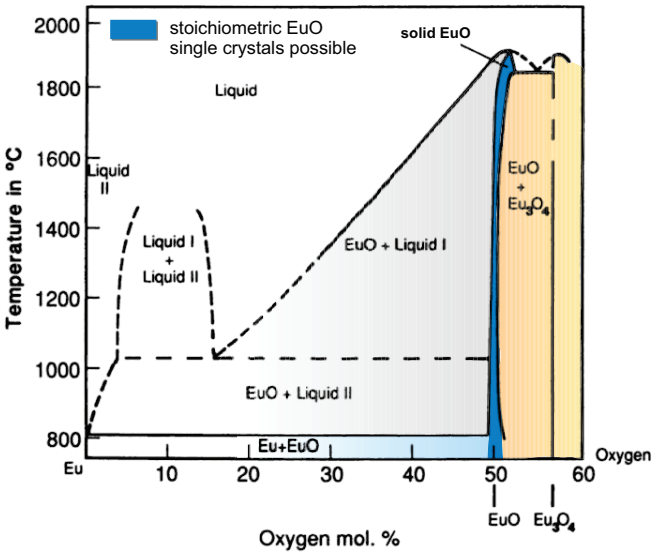

Figure 2.1.: Phase diagram for the synthesis of EuO single crystals. Stoichiometric EuO single crystals are obtained only in an extremely narrow parameter regime of oxygen and at high temperatures. After Morss and Meyer (1991).[30]

are necessary, as depicted in Fig. 2.1. Any slight deviation from the extremely confined parameters set for stoichiometric EuO results in the formation of either Eu vacancies, oxygen vacancies, Eu clusters, Eu_3O_4, or Eu_2O_3 phases.*

Hence, alternative techniques to grow single-crystalline EuO are of high interest. Among them are the oxidation of metallic Eu, and conversely, the reduction of Eu_2O_3. Both methods, however, yield polycrystalline EuO with a chemical mixture of phases. Since 2002, the EuO distillation growth mode has been established by Steeneken (2002).[22] This method is suitable for EuO thin film growth, which offers the benefit of well-defined growth rates and requires ultrahigh vacuum. At a moderate temperature of synthesis ($T_S \sim 400\,°C$), the Eu distillation growth allows one to obtain epitaxial EuO thin films of single-crystalline quality from few nanometers thickness (ultrathin) up to several hundreds of nanometers (bulk).[15,23,32] Recent works refer to this technique as "adsorption-controlled" EuO synthesis, since the oxygen supply during the reactive MBE synthesis is limited to extremely low partial pressures, thus limiting the adsorption of EuO.[25,27,33]

Worth mentioning is the chemical affinity of EuO to oxygen, carbon, and water – one of the largest among the rare earth compounds. Several higher coordinated Eu oxides, carbides, and hydroxides will immediately form, when Eu metal or the metastable EuO is exposed to air.* Thus, we emphasize that best UHV conditions and ultra-clean oxygen and Eu constituents are necessary in order to obtain chemically clean and stoichiometric EuO.

Thermodynamic potentials

For a predictive thermodynamic analysis of solid state reactions, such as the stabilization of the metastable EuO, we introduce the Gibbs free energy G. Depending on a reduction or

*EuO and chemically competing phases are summarized in Tab. A.1 in Appendix A.1.

increase of Gibbs free energy, we can discriminate whether a reaction will proceed ($dG < 0$) or not ($dG > 0$). Its differential is given by

$$dG = -S\,dT + V\,dp + \mu\,dN, \tag{2.1}$$

where S is the entropy, V the volume, and μ the chemical potential. One recognizes that T, p, and N are the natural state variables of G. The Gibbs free energy is a suitable thermodynamic measure for chemical reactions at fixed pressure and fixed temperature. Thus, the Gibbs free energy is perfectly suited to describe the EuO growth by MBE, which is a quasi-equilibrium system. In thermodynamic equilibrium, there is no total transfer of entropy: $\Delta S = 0$. This implies in terms of the variables for G for two subsystems A and B (e. g. two competitive EuO phases):

$$T_A = T_B$$
$$p_A = p_B$$
$$\mu_A = \mu_B$$

Since the temperature T and pressure p are constant, the only driving force out of the equilibrium is a possible difference in chemical potential $\Delta\mu = \mu_A - \mu_B$. Provided a constant atomic flux dN in MBE, the Gibbs free energy (2.1) depends then only on the specific $\Delta\mu$ of materials. Those material-specific Gibbs free energies are tabulated in databases like the CRC Handbook or Landolt-Börnstein,[34,35] and a comparison allows for a prediction of quasi-equilibrium reactions as during MBE synthesis.*

Ellingham diagrams

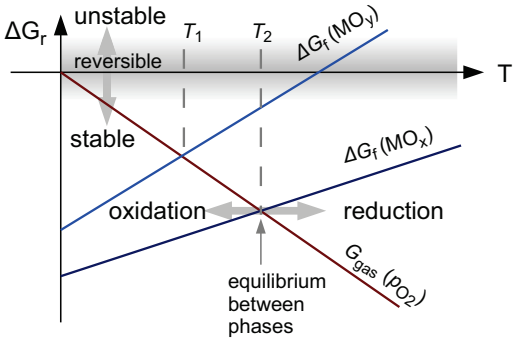

Figure 2.2.: Ellingham diagram.
Once the material-specific Gibbs free energies of formation and the gas lines are included, one can determine the principle thermodynamic stability ($\Delta G_r \gtrless 0$) and regions of oxidation or separation of metal and oxygen. These regions are separated by equilibria at the intersections, which determine a set of oxygen partial pressure $p(O_2)$ and temperature T.

For oxide growth using MBE, we want to elucidate the question of oxidation reactions, which is conveniently achieved by Ellingham diagrams. An Ellingham diagram is a compilation of Gibbs free energies of oxide compounds of interest, with the addition of "gas lines". One characteristic is the normalization of $G_f(T)$ to one mole of gaseous oxygen O_2; this rule perfectly describes the adsorption-controlled EuO synthesis, in which the growth progress only depends on the limited and constant oxygen supply. This weighting of $G_f(T)$ curves to one

*Further reading in the field of molecular thermodynamics is found in Dickerson (1969).[36]

mole of O_2 makes all reactions immediately comparable among each other. The curves in an Ellingham diagram are

$$G_f(T) = H_f - TS. \tag{2.2}$$
$$G_{gas}(T) = -R_{gas} T \ln p(O_2). \tag{2.3}$$

Here, R_{gas} denotes the gas constant, and $p(O_2)$ is the oxygen partial pressure given in mbar.

There are three main uses of the Ellingham diagram:*

1. Determine the relative probability of reducing a given metallic oxide to metal,†
2. determine the partial pressure of oxygen that is in equilibrium with a metal oxide at a given temperature, and
3. determine the ratio of metal oxide phases (e. g. oxidation numbers II, III, or IV) at a given temperature.

As a rule of thumb, if ΔG_r is more negative than −60 kJ/mol, the reaction is considered to be completed in oxidation direction, and if more positive than +60 kJ/mol, it will not proceed at all. Reactions inside this interval around zero are considered to be reversible (shaded in Fig. 2.2). We note, that this approach is purely thermodynamic, and the predicted chemical products may form slowly or may even be prevailed by growth kinetics and activation energies. In this thesis, we use Ellingham diagrams to distinguish thermodynamic conditions, by which the EuO synthesis at elevated temperatures in direct contact with a Si (001) wafer will proceed to either higher oxides or silicon compounds.

2.2. Electronic structure of EuO

The main properties of EuO investigated in this thesis, i. e. the chemical and magnetic properties, all rely on details of the electronic structure. First, we discuss the nature of the chemical bonding, then we proceed to the origin of ferromagnetism in EuO, which is the magnetic Eu $4f$ orbital. Finally, we elucidate the arrangement of valence level, band gap, and conduction bands. Their radial distribution is sketched in Fig. 2.3. Deep core-levels, as observed on photoemission experiments, are discussed in Ch. 2.5.2.

Among the 61 electrons of the Eu(II) ion in EuO, 54 saturate orbitals giving the Xe configuration; the seven remaining ones are in the configuration $4f^7 (5d\,6s)^0$. The Eu–O bonding is mainly of an ionic nature, which means that the two $(5d\,6s)^2$ electrons are transferred to the p orbitals of oxygen. This explains why the europium chalcogenides are insulators, with the valence band built of the p states of the anion, and a conduction band composed of empty $6s$ and $5d$ states of the cation.

*A useful webtool for Ellingham diagram creation is available online.[220]

†Technologically, the points 1) and 3) are used in the smelting industry, to reduce e. g. Fe from hematite (iron ore).

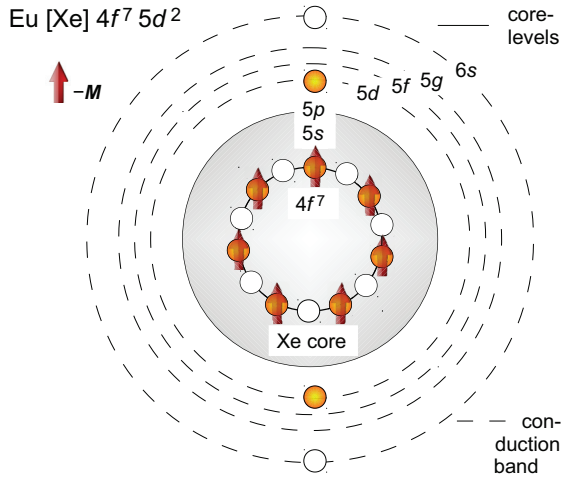

Figure 2.3.: The rare earth electronic structure as a shell scheme for Eu metal.
The open shell $4f^7$ and conduction electrons of Eu are highlighted. The conduction band is composed of the $5d$ and $6s$ levels. The Eu $4f^7$ levels are highly localized inside the [Xe] core. In ferromagnetic $Eu^{2+}O$, the seven f electrons carry the spin-only magnetic moment $\boldsymbol{M}$. After Dionne (2009).[37]

2.2.1. The open shell $4f^7$

The half-filled Eu $4f^7$ orbitals constitute valence-like levels near the Fermi edge in EuO which are often represented as bands, as depicted in Fig. 2.4. However, the $4f$ levels do not take part in the ionic bondings. The narrow radial distribution of $n = 4$ shells is responsible for the highly localized character of the $4f$ shell.[38] These properties justify a treatment of the Eu $4f$ orbital as core-level rather than a valence band, in particular with regard to core-level photoemission (see Ch. 2.4). In Eu $4f$, the spin–orbit interaction is weak and the electron exchange strong. This justifies the Russel-Saunders-coupling (LS) for which the Hund's Rules predict the filling of the $4f^7$ level as follows:

1. The spin multiplicity $\mathcal{S} = 2S + 1$ is maximal.
   $S_{4f^7} = \sum s_i = 7/2 \quad (\mathcal{S} = 8)$, in the FM state due to spin alignment.
2. With given spin multiplicity, the total angular momentum L is largest.
   Due to Pauli's exclusion principle, there is only one way to distribute seven electrons with parallel spins in an f shell: $\ell_i = -3 \ldots +3, \quad L_{4f^7} = \sum \ell_i = 0$.
3. For a half-filled shell, the total angular momentum is $J = L + S$.
   For Eu $4f^7$: $J_{4f^7} = 0 + 7/2 = 7/2$.

Thus, the Eu $4f$ orbital is in the initial state with ferromagnetic order in a ${}^8S_{7/2}$ configuration.* The ferromagnetic moments in EuO originate from the ${}^8S_{7/2}$ spin-only states of the $4f$ orbital. Correlations between the localized magnetic states $4f^7$ and the itinerant electrons† are the cause of the ferromagnetic exchange, as discussed in Ch. 2.3. The correlations in the $4f$ shell are further discussed in literature.[18,39–42]

*This is the term symbol notation, ${}^{\mathcal{S}}L_J$. The spin multiplicity $\mathcal{S} = 2S + 1$ quantifies the amount of unpaired electron spins.

†Of course, in EuO there are no itinerant electrons. However, interactions between Eu^{2+} sites work via $4f$ spins and virtual excitations to $5d$ conduction bands, often referred to as d–f interaction, or as s–f model in which s denotes the virtual itinerant electron in the conduction band.

2.2.2. Valence band, band gap, and the 5*d* 6*s* conduction bands

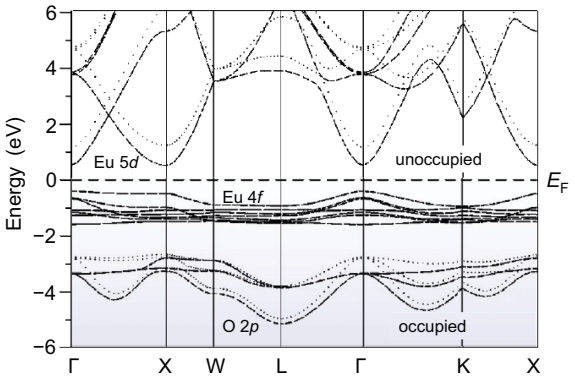

Figure 2.4.: Band structure of EuO calculated in the LSDA+U approximation.
The Eu 5*d* conduction band and the top of the Eu 4*f* band are indicated. The 4*f* band is narrow in energy and shows almost no dispersion, it is clearly distinguishable from the O 2*p* level at $E_B \approx -4.5$ eV. Adapted from Ghosh et al. (2004).[41]

EuO, as an ionic crystal, possesses the valence band O 2*p*, and the conduction bands (5*d* 6*s*). Between the lower edge of the conduction band and the O 2*p* valence band is an electrical gap of ~5 eV, thus, conduction levels and the anionic O 2*p* level are well separated. The optical gap between Eu 4*f* and the conduction band has been determined by optical absorption to be 1.12 eV.[29,43]

Spin-splitting of the conduction band

As one of the most noteworthy properties of a ferromagnetic insulator, EuO exhibits an exchange spitting of the conduction bands due to exchange coupling with the aligned spin state $^8S_{7/2}$ of the $4f^7$ orbital. This splitting was first determined by Wachter (2011) and confirmed by Steeneken et al. (2002) ($2\Delta E_{exch} \approx 0.6$ eV) and is depicted schematically in Fig. 2.5.[29,45]

In order to obtain an image of the spin-split conduction band of ferromagnetic EuO, Fig 2.6 shows the calculated one-electron Bloch density of states (B-DOS) for the first five conduction bands in Eu^{2+} of the majority spin system.[44] They are of 5*d* character. Below T_C, the $m = 1$ peak is shifted by about 1 eV to lower energies. This spin-selective shift of conduction bands is the basis for electronic transport effects in EuO: (*i*) spin-selective tunnel transmission be-

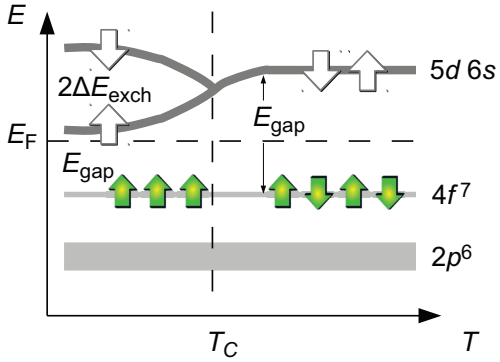

Figure 2.5.: Temperature-dependent scheme of the EuO band gap. If $T < T_C$, the exchange interaction arising from the aligned 4*f* spins splits the conduction band and lowers the band gap. Adapted from Wachter (2011).[29]

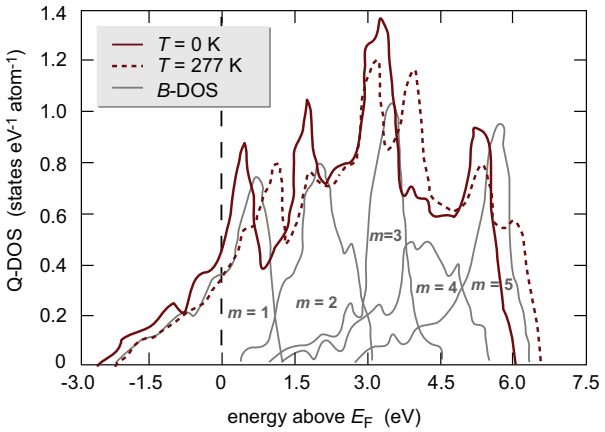

Figure 2.6.: Calculated Eu 5*d* conduction bands. The calculated DOS of the first five conduction bands in the quasiparticle model (Q-DOS) for spin-up electrons, and the one-electron Bloch density of states (B-DOS). After Nolting et al. (1987).[44]

comes possible through the EuO 5*d* majority conduction band, or (*ii*) the lowered conduction bands overlap with donor levels or trap states of oxygen vacancies near the Fermi level. In that case one observes an insulator-to-metal transition (IMT, also: Mott transition), when cooling down the sample below the ferromagnetic ordering temperature. This effect was first reported by Oliver et al. (1970).[15,23,46–52]

2.3. Magnetic properties of EuO

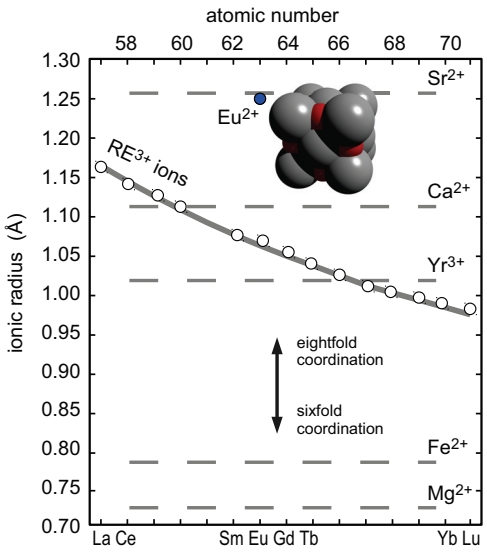

Figure 2.7.: Plot of ionic radii versus atomic number for lanthanide ions (La–Lu). For comparison, the ionic radius of divalent Eu is highlighted, and the inset shows a space-filled image of the EuO unit cell. Additionally, Sr^{2+}, Ca^{2+}, and Y^{3+} ions are included, which represent the cations in important oxide substrates for EuO growth. The regular decrease of ionic radii of the lanthanides is called the lanthanide contraction. Remarkably, the ionic radii of the lanthanides are much larger than for Fe^{2+} or Mg^{2+}. After Atwood (2013).[53]

The magnetic order in ferromagnetic insulators is induced by indirect exchange interactions

such as superexchange,[37] and is thus of a different origin than the itinerant electron ferromagnetism of the elemental 3*d* ferromagnets. In EuO, the strong ferromagnetic coupling is directly related to unique crystal features, the large ionic radius (see Fig. 2.7), combined with a high density of magnetic Eu^{2+} ions* (inset) both ensure a strong long-range ferromagnetic order. In the following, we briefly discuss the microscopic origin of the magnetic coupling in EuO, including competing exchange interactions. Finally, we show up tuning possibilities for T_C and the benefits of EuO for an application as a spin filter tunnel barrier.

Weiss' mean field model

We begin with a simple model for the magnetic order of EuO, in which the molecular mean field is proportional to the macroscopic magnetization. This mean field model considers a local magnetic moment interacting with the mean magnetic field of the crystal. In EuO, the Eu^{2+} ions carry a magnetic moment of $7\mu_B$ (see Ch. 2.2.1) which is interacting with the effective magnetic field of the EuO crystal. The reduced magnetization σ can be expressed in a simple form,

$$\sigma \equiv \frac{m(T)}{m(T=0)} \propto (T_C - T)^{\beta}, \quad \text{where } \beta = \frac{1}{2}. \tag{2.4}$$

The Weiss molecular field is responsible for the long-range interatomic magnetic order and its magnitude determines the Curie temperature.[54] However, experimentally $\beta = 0.37$ instead of 1/2 was found.[55] For a better description of the magnetic coupling between the localized Eu^{2+} ions, the Heisenberg model is applied.

Heisenberg models for the magnetization of EuO

The Heisenberg model suggests that a spontaneous magnetization arises from the exchange interactions between spins moments of neighboring atoms. In EuO, the $4f^7$ spin magnetic moment of a Eu^{2+} ion interacts with the $4f^7$ spin moments of its nearest neighbors. Since the $4f^7$ orbital has maximum spin multiplicity $\mathcal{S} = 8$ and $L = 0$ (term symbol $^8S_{7/2}$) in the ferromagnetic ground state,† it is of spherical *s*-like symmetry. Thereby, the exchange is considered isotropic, and one effective Hamiltonian is sufficient to describe the nearest neighbor interaction:

$$\mathcal{H} = -J_{ex} \sum_{<i,j>} \boldsymbol{S}_i \cdot \boldsymbol{S}_j \tag{2.5}$$

$\mathcal{H}$ denotes the Heisenberg Hamiltonian which sums up the spins over nearest neighbors, where J_{ex} is the positive exchange energy describing a pure ferromagnetic interaction. Although there is no exact solution of eq. (2.5), the Bloch $T^{3/2}$ law was found,[54]

$$\sigma \equiv \frac{m(T)}{m(T=0)} = 1 - \frac{0.0587}{S \cdot Q}\left(\frac{k_B T}{2J_{ex}S}\right)^{\frac{3}{2}}, \quad Q = \begin{cases} 1 & \text{sc structure,} \\ 2 & \text{bcc structure,} \\ 4 & \text{fcc structure.} \end{cases} \tag{2.6}$$

*Remarkably, the density of Eu^{2+} ions in *fcc* EuO is 44% larger than in *bcc* Eu metal, and comparable to the density of Gd ions in ferromagnetic Gd metal.[22]

†The occupation of the $4f^7$ orbital is described in Ch. 2.2.1.

which fits the experimental data very well. The three-dimensional Heisenberg model provides a power law for temperatures below the magnetic phase transition:[56]

$$\sigma \propto (T_C - T)^{\beta}, \quad \text{where } \beta = 0.36. \tag{2.7}$$

For EuO an experimental value $\beta = 0.37$ was found,[55,57] thus EuO is considered as a clear realization of a 3D Heisenberg ferromagnet. In the Weiss-Heisenberg mean field model, the most-used temperature dependence of the spontaneous magnetization σ follows a Brillouin function $\mathcal{B}_J(x)$.[58] This behavior can be derived from the mean field theory for ideal paramagnets by substituting the external field B_{ext} by the Weiss molecular field βH_{Weiss}. Then, at constant H_{Weiss}, the temperature dependence is

$$\sigma \propto \mathcal{B}\left(\sigma \frac{3J}{J+1} \frac{T_C}{T}\right). \tag{2.8}$$

A more complex Heisenberg model has been proposed by Mauger and Godart (1986) including two exchange interactions J_1 and J_2 for the EuO magnetic order, which are the nearest neighbor and next-nearest neighbor Eu^{2+}–Eu^{2+} interactions, respectively.[18] The nearest neighbors interaction is ferromagnetic with an experimental value of $J_1 = \sim 5.3 \times 10^{-5}$ eV.[59] The next-nearest neighbor exchange J_2 is more complex and still under debate, one experimental value being $J_2 \sim 1.05 \times 10^{-5}$ eV.[59] The ordering temperature T_C is expressed via the mean field approach

$$T_C = 2S(S+1) \cdot \frac{12J_1 + 6J_2}{3k_B}, \tag{2.9}$$

where S is the total spin of the EuO magnetic shell ($4f^7$). The dominant interaction J_1 acts between the $4f$ orbitals of the 12 nearest neighbors via a virtual exchange involving the unoccupied $5d$ conduction states for transfer. Between the six next-nearest neighbors, the J_2 interaction is of mainly super-exchange nature and involves different mechanisms. Until now, the nature of the J_2 interaction is not clear – is it antiferromagnetic or ferromagnetic in EuO? Several mechanisms are currently discussed in order to describe the J_1 and J_2 parts of the magnetic coupling in EuO, and we summarize the most established ones in the following.

Competing exchange interactions in EuO

The microscopic origin of the exchange interaction is still under discussion. Proposed by Kasuya (1993),[42] several competing exchange mechanisms exist in EuO:

Nearest neighbor exchange A $4f$ electron is excited to the $5d$ band where the electrons are itinerant, is then influenced by the exchange interaction of the $4f$ spins of the nearest neighbors, and falls back to the initial state. This indirect interaction leads to ferromagnetism. This idea is first proposed by Mauger and Godart (1986).[18]

The Kramers-Anderson superexchange An f electron is transferred via oxygen to an f orbital of a neighboring atom. This exchange is antiferromagnetic and very small.

Superexchange via the *d–f* interaction Oxygen electrons are transferred to the d orbitals of neighboring Eu atoms, where they influence the $4f$ spins via the d–f exchange. This leads to an antiferromagnetic exchange.[60–62]

Hybridization of the 5*d* and 2*p* orbitals Via hybridization, bonding and antibonding molecular orbitals are formed between Eu 5*d* and O 2*p* ligands. An oxygen electron is excited from the bonding to the antibonding 5*d*–2*p* molecular orbital, which experiences exchange interaction with both Eu spins. Its place is filled by a Eu 4*f* electron, and a 5*d* electron falls into the 4*f* hole. This could lead to ferromagnetic exchange.

From the Heisenberg theory (large J_1 coupling) and Kasuya (1993) it is evident, that the ferromagnetic nearest neighbor exchange between $4f^7$ via 5*d* states is most dominant. This emphasizes the important role of the nearest neighbor distance and the 5*d* conduction band with its possible population with donor electrons – both of which can easily be tuned by suitable synthesis parameters.

2.3.1. The Curie temperature of EuO

Stoichiometric EuO is ferromagnetic below the Curie temperature of $T_C = 69.3\,\mathrm{K}$.[63] Many studies have been devoted to increase this transition temperature.

One approach is the introduction of biaxial strain to heteroepitaxial EuO thin films by underlying substrates. In this way, decreasing the lateral lattice parameters of EuO is an ideal method to increase the Curie temperature T_C due to enhanced nearest neighbor coupling. Ingle and Elfimov (2008) find by their first principles calculation,[64] that the semiconducting gap closes at a 6% in-plane lattice compression for epitaxial EuO. This value thus constitutes an upper limit of compressive strain on EuO, if EuO shall remain insulating. However, the biaxial lateral forces are likely compensated by expansion or reduction in the perpendicular *z* dimension for most oxides, thus conserving the volume of a unit cell. For EuO, this perpendicular compensation is extremely small,[64] thus biaxial forces should have a large effect on the total expansion or compression of the EuO unit cell, giving rise to a tuned magnetic coupling. Therefore, we investigate biaxial strain and the elasticity of heteroepitaxial EuO thin films in Ch. 4.

Another approach of tuning T_C of EuO involves electron doping. This is indeed the most common method and does not require epitaxial integration of the EuO thin films. A model system for electron doping in EuO is the substitution of Eu^{2+} by Gd^{2+}, thereby one 5*d* electron is provided. Initially, an RKKY model[18] suggested the support of the *d*–*f* exchange between Eu ions. A more recent model by Kasuya (1993) proposes that the donor electron is trapped at the Gd ion building up a bound magnetic polaron together with the surrounding Eu^{2+} ions.[42] The increase of T_C is then proportional to the Gd doping concentration for low doping ($\leqslant 3\%$). An optimum Gd concentration ($\sim$4%) for highest T_C ($\sim$125 K) has been experimentally determined.[65] In a similar way, the Curie temperature could be increased by La and Lu doping up to 200 K due to comparable effects,[66,67] thus rendering EuO as the rare earth magnetic insulator with the highest Curie temperature.
Extra electrons are also provided by oxygen vacancy sites in EuO_{1-x}. For an oxygen vacancy, one Eu^{2+} ion provides two conduction electrons to the crystal. This yields a weak magnetization tail up to 150 K, whose origin is subject to discussions. The magnetization above 69 K may be induced by antiferromagnetic Eu metal clusters.[15,23,68] A recent study, however, proposes magnetic polarons to increase T_C of EuO_{1-x}.[60] Moreover, oxygen vacancies in EuO_{1-x} induce metallic conductivity, as discussed in Ch. 2.2.2, and are undesired in this thesis in

order to maintain the insulating nature of EuO tunnel contacts. An exotic method to provide itinerant $5d$ electrons in EuO_{1-x} is by light doping using a laser irradiation of $h\nu \approx 2$ eV.[23]

Finally, if chemical constituents with different ionic radii are incorporated into the crystal, this gives rise to isotropic strain (chemical pressure). This chemical pressure is supposed to vary the f–f and d–f exchange interactions.[69]

2.3.2. Thin film effects in EuO

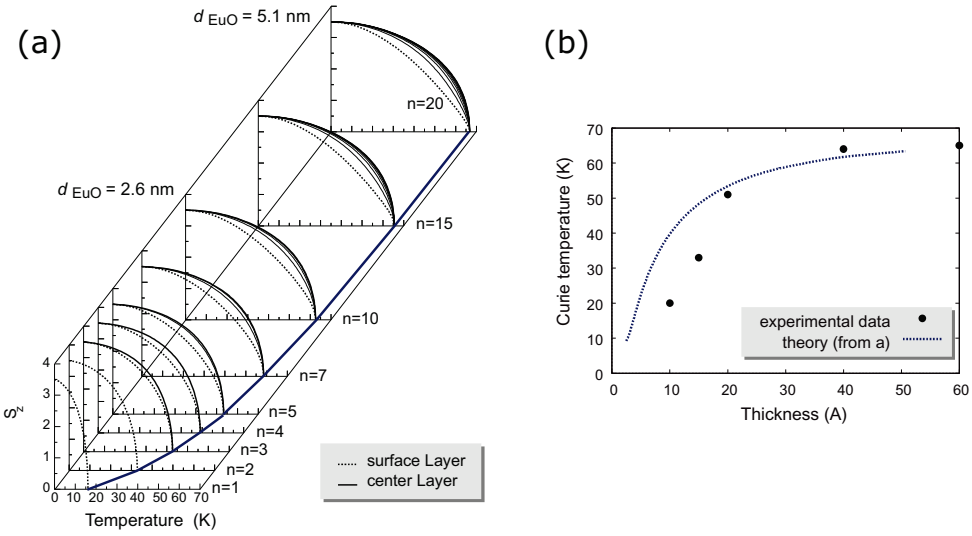

Figure 2.8.: Ferromagnetism in ultrathin EuO films. In (*a*), the Curie temperature is calculated by a ferromagnetic Kondo-lattice model and seen to be reduced with decreasing number of EuO monolayers. Adapted from Schiller and Nolting (2001).[70] Polycrystalline EuO thin films show a decrease in T_C (*b*), that roughly matches the calculation depicted in (*a*). Adapted from Müller et al. (2009).[48]

Since we investigate mainly ultrathin EuO films ($d \leqslant 5$ nm) in this thesis, the behavior of the magnetic moment and T_C in dependence on the thickness is of fundamental interest. The ferromagnetism in *fcc* EuO depends on the inter-atomic exchange coupling of the $4f$ orbitals. This coupling will be affected by reduced dimensions, e. g. in ultrathin EuO films. Schiller and Nolting (2001) calculated the electronic structure of one up to 20 monolayers of single-crystalline EuO as a function of temperature and thickness in a Kondo-lattice model.[70] In their study, the averaged spin moment of the $4f$ begins to reduce when the EuO thickness drops below 2.5 nm, as depicted in Fig. 2.8a. For one monolayer EuO, they found a T_C of 15 K. Remarkably, the temperature-dependent magnetization curves of center layers follow a Brillouin function, while surface layers show a lower magnetization. This can be explained by the Heisenberg model: Eu^{2+} ions in center layers can couple to 12 neighbors, while surface ions only to 8 nearest neighbors. Experimental evidence of the reduction of the Curie temperature is shown in Fig. 2.8b, where the T_C values of polycrystalline EuO match Schiller's model very

well. However, an experimental study of magnetic properties of *ultrathin single-crystalline* EuO is still missing and discussed in the thesis at hand.

In ultrathin films of EuO, moreover, the *shape anisotropy* will usually dominate over the *crystalline anisotropy* which is very small due to the spherical symmetry of the magnetic $^8S_{7/2}$ ground state. We investigate the shape anisotropy of ultrathin single-crystalline EuO in Ch. 4.

2.3.3. Spin filter tunneling in EuO

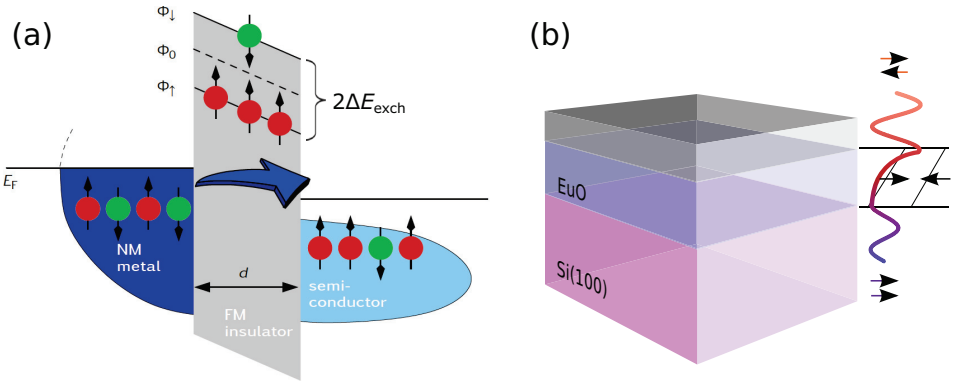

Figure 2.9.: Schematics of spin filter tunneling into semiconductor. Unpolarized electrons from a non-magnetic electrode (*a*, *left*) can tunnel through a tunnel barrier of the magnetic oxide EuO (*a*, *center*). Due to a exchange-split conduction band in EuO, the spin-up electrons have a much larger transmission probability, thus yielding a spin-polarized current which is injected into silicon (*a*, *right*), adapted from Moodera et al. (2007).[10] EuO tunnel contacts of the structure depicted in (*b*) are investigated in this thesis.

EuO offers the fruitful combination of magnetic exchange and electrical insulation, this yields a spin-selective tunnel path through the lower conduction bands of EuO thin films (see Figs. 2.5 and 2.6). For tunnel transmission through ferromagnetic EuO, the barrier height Φ is spin-dependent and expressed as

$$\Phi_{\text{tunnel}} \overset{\text{spin-split}}{=} \Phi_{\uparrow\downarrow} = \Phi_0 \pm \Delta E_{\text{exch}}. \tag{2.10}$$

This spin-dependent potential height of the tunnel barrier allows for a spin-selective electron transmission, as depicted in Fig. 2.9. Electrons travel to the opposite side of the tunnel barrier with the tunnel transmission probability described as:

$$T_{\uparrow\downarrow}(E) = T_0 \exp\left(-2d\sqrt{\frac{2m}{\hbar^2}\left(\Phi_{\uparrow\downarrow} - E\right)}\right), \tag{2.11}$$

where d denotes the thickness of the insulating barrier, and m is the effective mass of the electron. Remarkably, the transmission probability drops exponentially with the tunnel path d and with the barrier height Φ, these define the two crucial parameters of the tunnel barrier.

For spin-selective tunneling due to different barrier heights $\Phi_{\uparrow\downarrow}$, spin polarizations up to 100% are expected theoretically. In practice, spin selection by using a magnetic insulator was first reported by Moodera et al. (1988) for the magnetic tunnel barrier EuS. The europium chalcogenide EuS – the electronic equivalent to EuO – has shown a spin polarization of ∼86%.[71] In an initial experiment of polycrystalline EuO tunnel contacts a metal electrode, a spin polarization of 29% has been observed by Santos and Moodera (2004).[72] Recently, Miao and Moodera (2012) have realized polycrystalline EuO/MgO/Si magnetic tunnel junctions.[73] We, however, follow the approach to integrate EuO directly on Si with high crystalline quality, thus keeping the tunnel path minimal and well-defined.

Benefits of EuO for spin filter tunneling

We decide to use the magnetic oxide EuO out of the set of magnetic insulators, because EuO brings unique benefits for a possible application as spin-functional tunnel contact to silicon.

For EuO, the lower edge of the conduction band is exchange-split by $2\Delta E_{ex} \approx 0.6$ eV – almost double the value of EuS. Moreover, the Curie temperature of EuO is four times higher than for EuS. This renders the fundamental properties of EuO, among the Eu chalcogenides, best suitable for future spin filter tunnel barriers.

An integration of the magnetic insulator EuO with silicon combines established semiconductor technology with spin functionality. EuO provides fundamental prerequisites for this approach: it is the only binary magnetic oxide which is thermodynamically stable in direct contact with silicon.[14] This, in principle, already allows the fabrication of functional EuO tunnel contacts directly on silicon, thus paving the tunneling pathway for spin electronic devices like a spin-FET.[7] Moreover, EuO can resistively be tuned over a large range by means of electron doping. This reduces Schottky barriers at the spin injection interface,[74] and allows for a conductance match between EuO and silicon. This is one requirement for high-efficiency spin injection into silicon.[11]

Finally, comparable band gaps of EuO (1.12 eV) and Si (1.1 eV) allow for a possible band matching at the spin injection interface. In this way, an epitaxial integration of EuO on Si (001) with a crystalline interface quality is promising for an advanced tunneling approach in the framework of symmetry bands: coherent tunneling of spin-polarized electrons directly into Bloch states of the silicon electrode.

An advanced possibility: coherent tunneling in EuO

An advanced tunnel approach exploits the matching of majority or minority symmetry bands of the magnetic oxide with the Bloch states of the electrodes. This allows for efficient spin filter tunneling, referred to as “coherent tunneling”.

A well-known example is the lattice-matched epitaxial Fe/MgO/Fe trilayer. Here, high TMR values could be observed by spin filtering through Δ symmetry bands by Yuasa et al. (2004) and Parkin et al. (2004).[12,13] Recently, predictions of spin filtering by symmetry bands for EuO have been reported.[75,76] In EuO, both the real and complex bands are spin-dependent (Fig. 2.10). The studies conclude that spin filter tunneling will occur mainly via Δ_1 symmetry bands in EuO/*bcc* metal interfaces. In particular, in epitaxial Cu/EuO/Cu tunnel junctions (Fig. 2.10b), a coherent tunnel efficiency of ∼100% is predicted.[76]

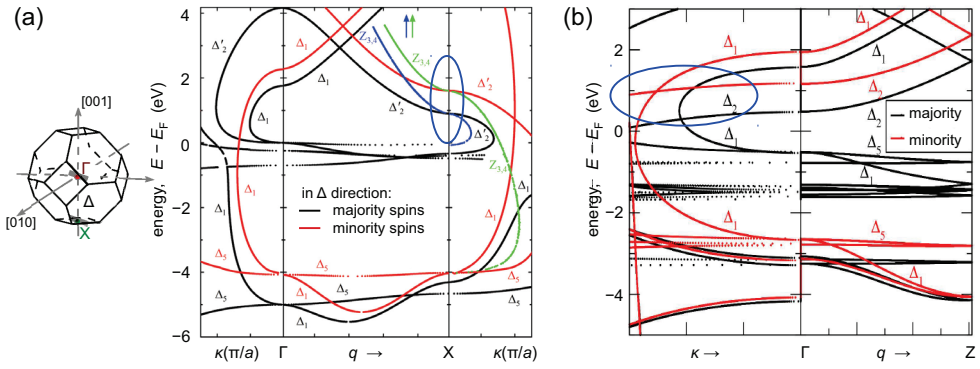

Figure 2.10.: Schematic band structure of EuO for the Δ direction in k space (*a*, *left*). For coherent tunneling, evanescent waves in the imaginary part κ need to match the real band structure q of the EuO conduction band. Majority and minority spins band are at different energy heights, as highlighted in (*a*).[75] Evanescent waves in the imaginary part exhibit different decays rates in the electrode for majority and minority spins, as emphasized in (*b*).[76] These differences are the basis for spin-selective coherent tunneling.

In practice, the spin injection interface must be crystalline and epitaxial in order to allow for a matching of symmetry bands. EuO thin films can be grown epitaxially with single-crystalline structural and magnetic properties by reactive MBE on cubic oxides,[25,27,32] thus forming a basis for a possible coherent tunnel functionality. This may also be achieved on cubic silicon crystals. Therefore, we investigate EuO directly on silicon with the demand of high interface quality in Ch. 5.

Moreover, to date, no band structure for coherent tunneling is reported for tunnel contacts of epitaxial EuO on Si (001). This motivates spin-dependent density functional theory calculations of EuO symmetry bands matching Bloch states of Si (001), in order to compare the spin filter efficiency of experimental epitaxial EuO tunnel contacts with models in the frame of band structures.

2.4. Hard X-ray photoemission spectroscopy

A characterization of buried EuO layers and interfaces is necessary in order to understand their chemical and electronic properties. In response to the experimental need for a large and tunable probing depth, we select a specialized spectroscopic technique in this thesis. Hard X-ray photoemission spectroscopy (HAXPES) is perfectly suited to characterize our EuO heterostructures, which we introduce in the following.

The story of photoemission already began in 1887, when Heinrich Hertz observed the emission of electrons by light from solids,[77] which was not compatible with Maxwell's equations describing a continuous wave theory. Later in 1905, this photo-induced electron emission

was interpreted by the quantum nature of light in which the "light particles" possess an energy $h\nu$ dependent on frequency,[78] a discovery for which Albert Einstein was honored with the Nobel Prize in 1921. After a continuous development of theoretical and experimental techniques, photoemission spectroscopy is nowadays the most important experimental technique for studying the electronic structure of occupied electronic states in a solid.[79] The high-energy variant of photoemission, HAXPES, is employed to investigate the electronic properties of buried layers and interfaces of EuO heterostructures in this thesis. In order to interpret the core-level photoemission spectra, we discuss the basic photoemission theory in the framework of the three-step model. Later, spectral features besides the main core-level lines are discussed by means of intra-atomic interactions. Finally, we discuss the characteristics of hard X-ray excitation including the important benefit of increased information depth.

2.4.1. The three-step model of photoemission

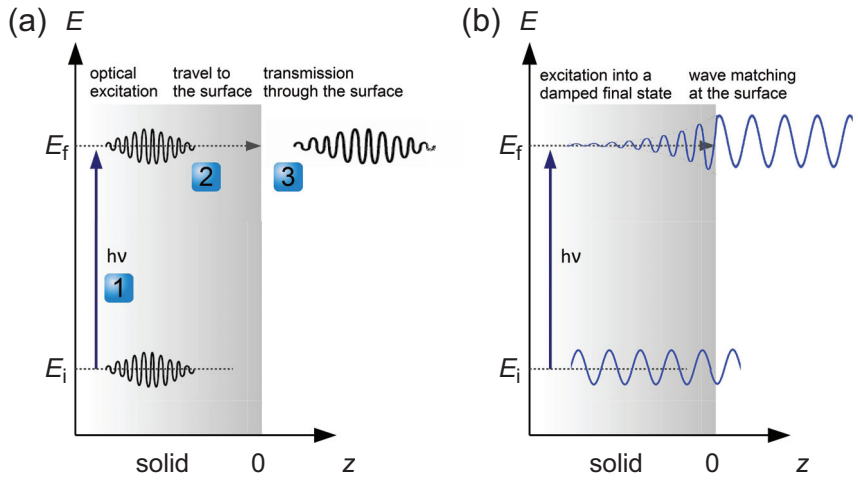

Figure 2.11.: The three step model of photoemission (*a*). It connects Bloch states (plane waves) of the photoelectron in three independent steps. For comparison, the one-step model (in *b*) includes the electronic waves of the initial state, and the (eventually damped) final state, and matches with the wave departed from the solid in one formalism.[80]

An intuitive, yet simplified approach to the photoemission process is the three-step model, introduced by Berglund and Spicer (1964).[81] This model divides the photoemission process into three independent events and assumes Bloch functions in a one-electron picture for both the initial and final states of the photoelectron. The successive events are discussed in the following[82] and schematically sketched in Fig. 2.11a. Finally, we briefly mention the exhaustive description of photoemission by the one-step theory, which uses the inverse LEED state as final state, as sketched in Fig. 2.11b.

1. Excitation of the electron into unoccupied states The interaction of the electron with a time-dependent electromagnetic field $\mathbf{A}(\mathbf{r}, t)$ (from the plane wave of the incoming light) in

the single-electron picture is expressed as

$$\mathcal{H} = H_0 + H^S = \frac{1}{2m}\left(\frac{\hbar}{i}\nabla - \frac{e}{c}\mathbf{A}(\mathbf{r})\right)^2 + V(\mathbf{r}), \tag{2.12}$$

here, H_0 is the Hamiltonian of the unperturbed system, H^S is the perturbation operator, $\mathbf{p} = \hbar/i\,\nabla$ denotes the momentum operator, and $V(\mathbf{r})$ is the potential within the solid from the ionic cores. The single Hamiltonians are written as

$$H_0 = -\frac{\hbar^2}{2m}\nabla^2 + V(\mathbf{r}), \qquad H^S = \frac{1}{2m}\left(-\frac{e\hbar}{ic}(2\mathbf{A}\nabla + (\nabla\mathbf{A})) + \frac{e^2}{c^2}|\mathbf{A}|^2\right). \tag{2.13}$$

Here, we approximate $|\mathbf{A}|^2 \approx 0$ for small electromagnetic field strengths, and the gradient $\nabla\mathbf{A} \approx 0$, because the field changes within the crystal only very slowly (X-ray penetration of the crystal).

The ansatz for $\mathbf{A}$ is a plane wave with wave vector $\mathbf{k}_\gamma$, the amplitude A_0, and $\mathbf{r}$ is the unit vector in direction of the electric field:

$$A(\mathbf{r}, t) = A_0 e^{i\mathbf{k}_\gamma \mathbf{r}} \qquad \Rightarrow \quad H^S = -\frac{e}{mc}A_0 e^{i\mathbf{k}_\gamma \mathbf{r}}\mathbf{p}. \tag{2.14}$$

The wave vector $k_\gamma = \frac{2\pi}{\lambda}$ is small with respect to the size of a typical Brillouin zone up to the XPS regime, therefore $e^{i\mathbf{k}_\gamma \mathbf{r}} \approx 1$, which simplifies the perturbation Hamiltonian in the dipole approximation as

$$H^S = -\frac{e}{mc}A_0 \cdot \mathbf{p}. \tag{2.15}$$

We remark that for high-energetic photons (HAXPES), the dipole approximation may be insufficient and higher order transitions (electric quadrupole E2, or magnetic dipole M1) are emerging.* The Hamiltonian (2.15) depends only on the momentum transfer $\mathbf{p}$ between the plane wave (light) and the electron, which is to be determined now. It is used in Fermi's golden rule, which expresses the probability per time that the system is excited by a photon of the energy $h\nu$,

$$w_{i\to f} = \frac{2\pi}{\hbar}\left|\left\langle f\middle|H^S\middle|i\right\rangle\right|^2 \cdot \delta(E_f - E_i - h\nu) \tag{2.16}$$

Here, $|i\rangle$ denotes the electron's initial state with the energy eigenvalue E_i, and $|f\rangle$ is the final state in the single particle model with energy E_f, as depicted in Fig. 2.11a. The δ-function ensures the energy conservation. The transition matrix element in Fermi's golden rule, M_{if}, depends on the symmetries of the final and initial state as

$$M_{if} = \left\langle f\middle|H^S\middle|i\right\rangle \propto \langle f|\mathbf{p}|i\rangle. \tag{2.17}$$

Besides the energy conservation, also the conservation of the momentum ($\propto \mathbf{k}$, the wave

*The E2 or M1 distributions occur for very short wavelength photons ($h\nu \gg 1$ keV) and for the ejection of electrons in very large orbits. However, these distortions only alter the angular dependence of photoemission. Since we conduct angle-integrated HAXPES only at fixed emission angles, the inclusion of higher order transitions is negligible in this thesis.

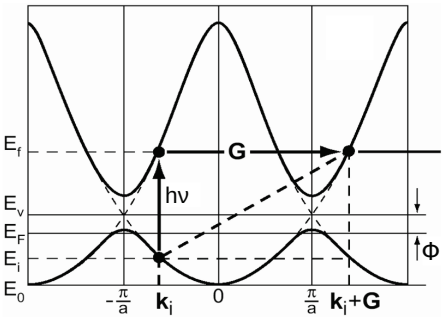

Figure 2.12.: Momentum conservation during photoexcitation in a reduced zone scheme inside a solid. For X-ray excitation, transitions are mainly vertical, i.e. shifted only by the photon energy $h\nu$. Free states must be available at the energy E_f and in the momentum space at $\mathbf{k}_f = \mathbf{k}_i + \mathbf{G}$.

vector) has to be fulfilled for photoexcited electrons within the solid,

$$\mathbf{k}_f = \mathbf{k}_i + \mathbf{k}_\gamma + \mathbf{G}, \tag{2.18}$$

where $\mathbf{k}_f$, $\mathbf{k}_i$, and $\mathbf{k}_\gamma$ denote the wave vectors of the electron's initial state, its final state, and the photon's wave vector, respectively. $\mathbf{G}$ is a reciprocal lattice vector of the crystal, as sketched in Fig. 2.12. Concluding, we can write the photocurrent I *inside* the crystal, taking into account the transition probability (2.16) and the momentum conservation (2.18), as follows:

$$I(h\nu) \propto \sum_{i,f,\mathbf{G}} \left| M_{if} \right|^2 \cdot \delta(E_f - E_i - h\nu) \cdot \delta(\mathbf{k}_f - \mathbf{k}_i - \mathbf{G}). \tag{2.19}$$

2. Transfer of the electron to the surface of the solid What happens during the travel of the excited electron through the solid to the surface? A fraction of the electrons experiences collisions with other electrons and phonons. The material parameter describing inelastic electron scattering of electrons in a specific solid is the inelastic mean free path (IMFP). The IMFP is a measure how far a photoelectron can travel through a solid before an inelastic scattering events changes its energy information. The IMFP value is strongly dependent on the kinetic energy of the photoelectron. IMFPs for common solids in practice are estimated by the the modified Bethe-equation (TPP-2M formula) derived by Tanuma et al. (1994),[83]

$$\lambda = \frac{E_{\mathrm{kin}}}{E_{\mathrm{p}}^2 \left(\beta \ln(\gamma E_{\mathrm{kin}}) - \frac{C}{E_{\mathrm{kin}}} + \frac{D}{E_{\mathrm{kin}}^2} \right)}, \tag{2.20}$$

where E_{kin} is the electron energy, E_{p} is the free-electron plasmon energy, and β, γ, C, and D are material-specific parameters. In this thesis, we use recalculated values for hard X-ray excitation from Tanuma et al. (2011).[84]

3. Transfer of the photoelectron through the surface into the vacuum The third step considers the transfer of the photoelectron through the surface of the solid into a vacuum state. Only those electrons can leave the solid by dispensing energy of the value of the work function ϕ_0, which have a sufficiently high kinetic energy. Escaping electrons, thereby, have the kinetic energy

$$E_{\mathrm{kin}} = E_f - \phi_0 = h\nu - E_{\mathrm{bin}} - \phi_0. \tag{2.21}$$

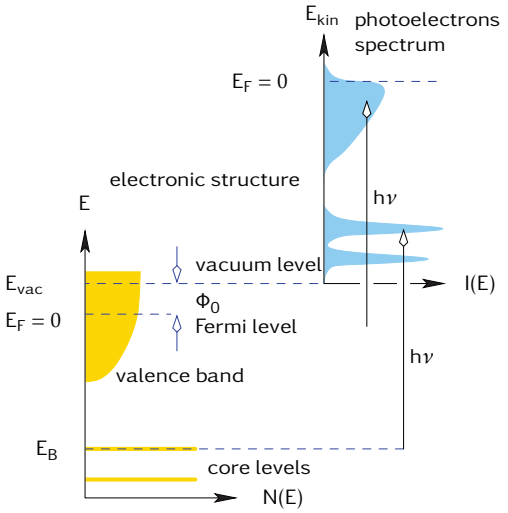

Figure 2.13.: Photoemission from a solid. The photoemission process translates the electronic density of states of the specimen into a photoemission spectrum, if a single-electron picture is assumed. The intensity of the photoelectrons as a function of the binding energy, the so-called energy distribution curve (EDC), shows the density of occupied electronic states in the solid. After Hüfner (2010).[80]

Here, E_f is the final state energy relative to the Fermi level E_F, E_bin denotes the binding energy of the electron, and ϕ_0 is the work function of the solid which equals the difference between the Fermi level and the vacuum level (4–10 eV). The final states are free electron states in the vacuum and generally not relevant, and the photoemission intensity is proportional to the density of initial states of energy E_i. Thus, in the one-electron picture, photoemission spectroscopy images the occupied density of states (DOS) of the solid. The exit process of the photoelectron and the resulting spectrum (energy distribution curve) is sketched in Fig. 2.13.

Exciting the sample involves diffraction (i. e. a change of $\mathbf{k}_\perp$) at the potential barrier of the crystal surface. In core-level photoemission in the XPS and HAXPES regime ($h\nu > 1$ keV), however, the so-called *XPS limit* can be applied: for most materials at room temperature, the combined effects of phonons and angular averaging in the spectrometer yield photoemission spectra that are directly related to the matrix element-weighted density of states (MW-DOS).[85] This means, in HAXPES, the $\mathbf{k}$ dependence in eq. (2.19) is negligible. Furthermore, element-specific atomic cross-sections can be used to weight the MW-DOS for quantitative evaluations.[86] which the simplified three-step model does not account for.

The one-step theory of photoemission

An exhaustive treatment of the photoemission process is provided in a the one-step theory.[80,87,88] It contains the Golden Rule equation with proper wave functions of the initial and final states, and the dipole operator for the interaction of the electron with the incoming light. Inverse LEED wave functions are used for the final state of the photoelectrons and the wave functions are expanded as Bloch functions in the periodic crystal, as sketched in Fig. 2.11b. This allows one to discriminate between different scenarios of matching types between the free electron wave in the vacuum and the Bloch function in the crystal. This matching can be (*i*) simply inside the crystal, (*ii*) in a band gap yielding an "evanescent wave", or (*iii*) in a band-to-band photoemission for small escape depths. Damping due to inelastic

losses is introduced by using an imaginary part of the momentum, $k_\perp = k_\perp^{(\mathrm{real})} + ik_\perp^{(\mathrm{im})}$. Since we are interested only in binding energies and chemical shifts of deep core-levels (negligible **k** dependence), a basic picture according to the three-step model is sufficient for this thesis.

2.4.2. Spectral features and their interpretation

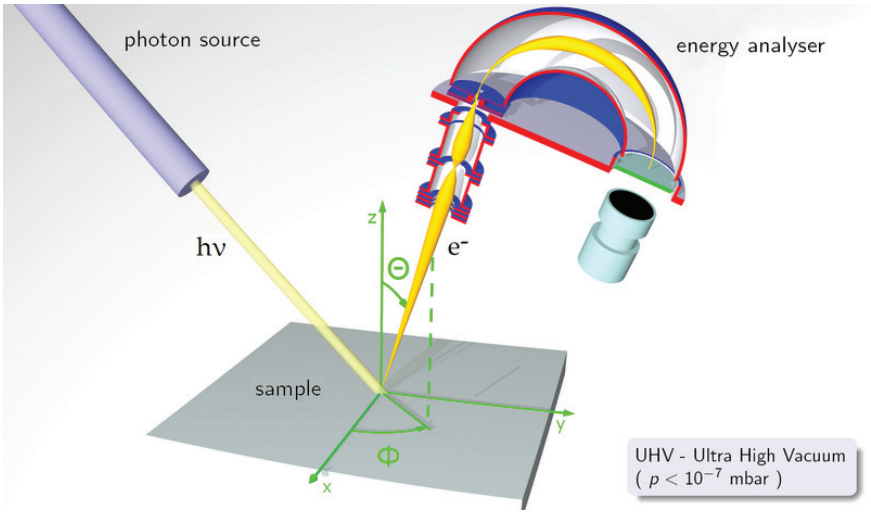

Figure 2.14.: Schematics of photoemission spectroscopy. After Saiht (2009).[221]

In photoemission spectroscopy, a solid sample is irradiated by monochromatic photons which excite electrons from occupied states in the solid. If the photoelectrons have a large enaugh kinetic energy, then they can be detected by an electron energy analyzer (Fig. 2.14). A photoemission spectrum usually comprises peaks which correspond to the kinetic energy of the photoelectrons, $E_{\mathrm{kin}} = h\nu - E_{\mathrm{bin}} - \phi_0$, where $h\nu$ is the energy of the light, ϕ_0 denotes a work function which the photoelectrons have to overcome in order to reach a free electron state in the vacuum, and E_{bin} is the binding energy of the electron's initial state in the solid.

While the description of photoemission spectra by the three-step model can be very successful, the one-electron approximation neglects many body interactions in the final state, as well as surface effects or intra-atomic exchange interactions. We are leaving the one-electron picture here, and subsequently introduce selected spectral features due to multiple electron interactions in the final states, which are relevant to EuO core-level spectra.

Intrinsic satellites of core-levels. After emission of the photoelectron from orbital k, the remaining $N-1$ electrons will reorder to minimize their energy. This includes final state configurations in which the $(N-1)$ system of the core-level interacts with electron near the Fermi level. The transition matrix element must then be calculated by summing over all possible final states. In a photoemission spectrum, the core-level line appears then asymmetric,

or even comprises distinguishable additional satellite lines.[80] Intrinsic photoemission satellites may occur due to the reduced Coulomb interaction from the $(N-1)$ core-level, so that the valence level can accept one more electron. This "apparent valence change" due to the photoexcitaiton is included in the observable final state, and referred to as shake-up satellite at higher binding energy. A discussion on the intrinsic satellites of Eu $3d$ photoemission in given in Ch. 5.1.

Plasmons One class of extrinsic loss events is the excitation of a free electron gas in the sample by photoelectrons. In this case, a photoelectron dissipates a fraction of its kinetic energy to collective excitations with the plasma frequency ω_0 in metallic layers. These are of characteristic energy and referred to as plasmons. The plasmon excitation probability is dependent on the photoelectron's kinetic energy as calculated in Inglesfield (1983): for high kinetic energy (hard X-ray excitation), plasmon losses have a reduced probability.[89] In this thesis, fast photoelectrons from Eu core-levels excite plasmons in Al and Si layers which are well known in literature,[90,91] and thus can easily be included into a quantitative evaluation of the core-level spectra (Ch. 5.1).

Chemical shifts In photoemission, we are interested in the chemical states of the thin film material. This information is provided by the chemical energy shift, first explained by Fadley et al. (1967) – interestingly on the example of native europium oxide.[92] By measuring this energy shift (generally 0.2–10 eV) one can investigate the initial state valency in ionic crystals. The chemical shift ΔE_{bin} of core-level binding energies between two chemical phases A and B in a solid is given by

$$\Delta E_{\text{chem}}(A,B) = K \cdot (Q_A - Q_B) + (V_A - V_B). \tag{2.22}$$

Here, K is the coupling constant from the Coulomb interaction between valence and core electrons, and Q denotes the charge transfer on the particular ion (e. g. +2 for an oxidized cation). Thus, the first term in eq. (2.22) describes the difference in the electron–electron interaction between the core orbital and the valence charges in a certain ionic bounding. The second term $(V_A - V_B)$ represents the interaction of the atoms A and B with the remaining crystal. For oxides, this is a Madelung-type energy.[80] As a rule of thumb, ions with higher coordination number (e. g. octahedral vs. tetrahedral) or with larger charge transfer (e. g. Eu^{2+} vs. Eu^{3+}) exhibit also a larger chemical shifts to higher binding energy.

Surface core-level shifts. Energetic shifts can also arise from an altered electronic configuration in the surface layers of a solid. For low-energetic photoelectrons, the escape depth is in the range of the surface layers, and surface shifts are likely to be observed. This is approximately the case for the deeply bound Eu $3d$ photoelectrons analyzed in this thesis. However, surface shifts are usually small ($\leqslant 3$ eV) and less pronounced in HAXPES experiments due to the predominant bulk character of the photoelectrons.

Spin–orbit coupling. During photoionization of a core-level, a core hole is created with spin $s^* = 1/2$. A dominant spin–orbit coupling assumed, a doublet peak is eminent due to the final states coupling $j = \ell \pm s^*$ in orbitals with an angular momentum $\ell \geqslant 0$ (i. e. the p, d, f,

etc. shells). The branching ratio of the two final state peaks is calculated as

$$\frac{I_{\ell-s^*}}{I_{\ell+s^*}} = \frac{2\left(\ell-\frac{1}{2}\right)+1}{2\left(\ell+\frac{1}{2}\right)+1} = \frac{\ell}{\ell+1}. \tag{2.23}$$

This reveals intensity ratios of 1:2 for p shells, 2:3 for d shells, and 3:4 for f shells. The spin–orbit splitting is realized prefereably for heavy elements and deep core-levels. In this thesis, the deeply bound Eu 3d peak structure is well described by a spin–orbit doublet, but Eu 4d and lower core-levels require other coupling schemes, as will be discussed in section 2.5.2.

Core-hole polarization. Core-level photoemission always produces a final state with spin and angular momentum. If the system has a valence state configuration ℓ^n with corresponding spin and orbital momenta, the coupling with the core-hole orbital and angular momenta leads to different final states. For an s^1 final state, the photohole has a spin of $s^* = 1/2$. This spin can be either parallel or antiparallel to the net spin S of the valence shell. The exchange splitting is then

$$\Delta_{\text{exch}}(s, \ell, S) = \left(\frac{2S+1}{2\ell+1}\right) G^{\ell}(s, \ell), \tag{2.24}$$

where $G^{\ell}(s, \ell)$ is the exchange integral.[93] Thereby, the Eu 4s and 5s core-levels exhibit a double-peak structure which is well-described by this model.[80] Remarkably, this exchange splitting is largest in the 4s levels of Eu, Gd,* and Tb, thus rendering that effect of fundamental interest.[95]

2.4.3. Implications of hard X-ray excitation

Conventional X-ray photoemission spectroscopy (XPS) is limited to a probing depth of a few surface atomic layers. Modern solid state and material science research, however, often requires the selective probe of buried layers or interfaces in a depth of several hundred Ångström from the surface. A solution for these experimental needs is the use of hard X-ray excitation, exceeding the limited probing depth of common XPS experiments.
The first hard X-ray photoemission experiment at $h\nu = 17.4$ keV using a Mo anode was carried out by Nordling, Sokolowski, and Siegbahn[96] in 1957. However, the energy resolution and brilliance were not sufficient to resolve small chemical shifts or multiplet fine structures. Subsequently, low energy anodes with Al $K\alpha$ and Mg $K\alpha$ radiation were subsequently established, and synchrotron light up to 1.5 keV enabled a success story of XPS. Nowadays, highly brilliant synchrotron hard X-ray sources[85,97,98] offer a wealth of experimental opportunities with an energy resolution down to 0.2 eV.[98,99]
An excitation of photoelectrons with hard X-rays implies major differences in view of conventional XPS. We discuss (*i*) changed photoemission cross-sections and (*ii*) Debye-Waller factors for photoemission, both of which directly affect the photoexcitation process. Finally (*iii*), hard X-ray-excited photoelectrons offer a largely increased inelastic mean free path in the solid, which is a major experimental benefit of HAXPES.

*Gd 4s and 5s core-hole polarization was recently discussed in Tober et al. (2013).[94]

I. Photoemission cross-sections Due to the large energy difference between exciting X-rays and the binding energy of the initial state electrons in the solid, in particular for valence band photoemission, the photoionization cross-section σ for hard X-ray excitation is small. For an individual orbital $(n\ell j)$, it is continuously reduced as

$$\sigma_{n\ell j}(h\nu) \propto \begin{cases} (E_{\mathrm{kin}})^{-7/2}, & \text{for } s \text{ subshells, and} \\ (E_{\mathrm{kin}})^{-9/2}, & \text{for } p, d, \text{ and } f \text{ subshells.}\,[100] \end{cases} \tag{2.25}$$

The significant decrease of atomic cross-sections for hard X-ray photoelectron excitation is shown in Fig. 2.15 (inset).

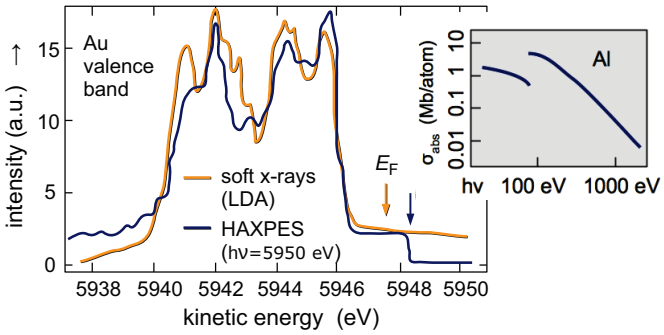

Figure 2.15.: Photoemission cross-sections for hard X-ray excitation. Au valence levels in HAXPES deviate significantly from soft X-ray photoemission.[85] The inset exemplifies the drop of photoemission cross-section with excitation energy for Al.[101]

II. Forward scattering and Debye-Waller factors for photoemission Only unscattered or coherently elastically scattered photoelectrons contribute to an analyzable spectrum. Elastic scattering events can deflect the photoelectrons which are emitted in direction of the surface normal away from that direction. For high excitation energies ($h\nu$ = 5–15 keV), Thompson and Fadley (1984) have shown[102] that the forward scattering (i. e. within 90° in direction of the original emission direction) becomes significantly narrower for photoemission *from surface layers* (Fig. 2.16). This reduces the directional anisotropy of the photoelectrons which is advantageous for angular-resolved PES. Moreover, the narrow emission plume of photoelectrons can be better approximated by a simple expression for the electron's effective attenuation length,* and thus allows one to predict information depths of a HAXPES experiment more accurately.[86] The photoemission process *inside a solid* can be thought of as a scattering process of the photoexcited ion inside the crystal.[80] Thus, the photoelectrons reflect the effect of the lattice vibrations of the crystal in a way similar to that in X-ray diffraction or neutron scattering, which is described by the Debye-Waller factor. The Debye-Waller factors for photoemission intensities are strongly dependent on temperature and on the excitation energy: an increase of temperature leads to a decreased intensity of coherently scattered photoelectrons. A calculated example is shown in Fig. 2.17, from which we clearly see that low sample temperatures are advantageous, and for larger X-ray excitation energies the Debye-Waller factor significantly drops. In practice, at a fixed excitation energy, the cooling of the sample will significantly increase the analyzable intensity (i. e. unscattered or coherently scattered photoelectrons).

*The effective attenuation length, λ^*, is introduced by eq. (2.26) on page 28.

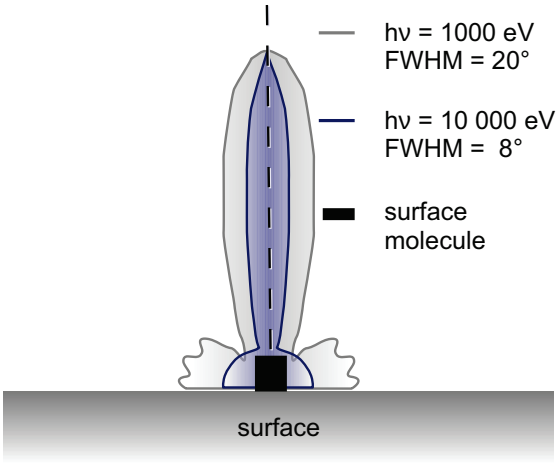

Figure 2.16.: Comparison of the intensity profiles of elastic photoelectron forward diffraction.
The intensity plumes are drawn as expected for C 1*s* photoemission at $h\nu = 1$ keV or $h\nu = 10$ keV from a vertical CO molecule on the surface. Adapted from Thompson and Fadley (1984).[102]

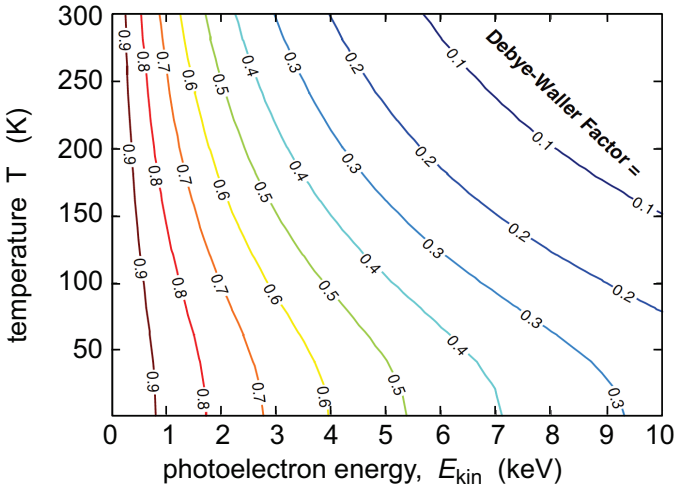

Figure 2.17.: Calculated Debye-Waller factors for valence-level photoemission.
The values are strongly dependent on the photoelectron kinetic energy. At high kinetic energy, cooling well below room temperature reveals significantly larger Debye-Waller factors. Adapted from Plucinski et al. (2008).[103]

III. The inelastic mean free path A critical parameter for the probing depth in any photoemission experiment is the inelastic mean-free path (IMFP) λ of hot electrons in a solid. Calculated curves of λ versus E_{kin} are depicted in Fig. 2.18. The similarity in the slope for many elemental solids justifies the use of the term "universal" curve. We recognize that with energies of 10 keV IMFPs of up to 200 Å can be reached.

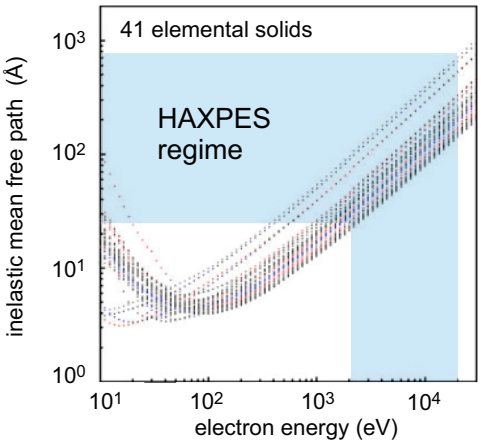

Figure 2.18.: Universal curve of photoelectron emission in solids. The inelastic mean free path (IMFP) λ is the key parameter to describe inelastic scattering of photoelectrons in solids.
Extending the escape depth of the photoelectrons up to several tens of nanometers (with $\lambda \propto E_{\mathrm{kin}}^{0.78}$),[85] the HAXPES regime is perfectly suited to investigate the electronic properties of buried interfaces or bulk properties. This recent calculation of IMFPs is from Tanuma et al. (2011).[84]

It is evident that, in reality, the IMFP curves can be very different depending on the physical properties of an individual material. Density, dielectric function and band gap of the solid as well as the elastic scattering can also alter the trajectory of a photoexcited electron. If these effects are included into λ, one obtains the effective attenuation length (EAL). One can then express a mean escape depth down to which unscattered photoelectrons can be expected as

$$\lambda^* = \lambda_{\mathrm{EAL}}(E_{\mathrm{kin}}) \cdot \cos\alpha, \tag{2.26}$$

where λ_{EAL} denotes the experimentally determined effective attenuation length,[80] and α the off-normal exit angle of the photoelectron.

As evident from eq. (2.26), the bulk-vs-surface sensitivity of the photoemission measurement can be controlled the kinetic energy or by varying the photoelectron's off-normal exit angle α. The behavior is determined by cosine, which gives e. g. a halving of the mean escape depth at $\lambda^*(60°) = \frac{1}{2}\lambda^*(0°)$. This phenomenon is extremely useful, since simply by tilting the sample one can obtain depth-resolved information,[86] which we apply for chemical depth profiles of EuO/Si in Ch. 5. Most intuitive for depth-selective measurements, however, is the information depth ID, from which 95% of the detected photoelectrons originate. This definition coincides, in practice, with the detection limit for chemical species in buried layers (see Ch. 5.1), and equals approximately $\mathrm{ID}_{95\%} \approx 3\lambda^*$.

Concluding, hard X-ray excitation offers the advantage of a largely tunable probing depth up to tens of nanometers, thus allowing to investigate buried layers and functional interfaces. Minor drawbacks are reduced photoemission cross-sections and Debye-Waller factors. Those, however, can be compensated by nowadays highly brilliant hard X-ray radiation sources, as introduced in Ch. 3.4.3.

2.5. Magnetic circular dichroism in core-level photoemission

Dichroism is derived from Greek and means the "effect of two colors", originally used for natural materials showing two colors due to surface effects. The *magnetic circular dichroism* (MCD) uses circularly polarized light for excitation and is caused by a directional symmetry breaking. This can be a magnetic order in the solid. In contrast to itinerant ferromagnets (e. g. Fe), the "magnetic" open shell in EuO is localized and treated as a core-level in terms of photoemission spectroscopy. The well-understood core-level photoemission and the completely available MCD theory render the MCD effect in Eu core-level photoemission an ideal tool for investigations of tunable effects on the magnetic interaction in EuO thin films: biaxial strain, stoichiometry, etc. By using hard X-ray photoemission, the MCD effect can be analyzed at a selected information depth down to 20 nm, thus providing insight into buried magnetic layers and interfaces.

In this section, we first introduce the basic theory of MCD in photoemission. We proceed with a simple example: MCD in $2p$ core-level photoemission. Finally, coupling schemes of the angular momenta of the Eu photoemission final states are discussed, as a first step for a future determination of the line strengths in MCD of Eu core-level photoemission spectra.

2.5.1. Atomic multiplet theory including MCD

In order to understand the MCD effect in photoemission, we need to analyze the photoemission process excited by circularly polarized light, thus including the magnetic quantum number M. During the photoemission process, an electron from a core-level with w electrons of orbital momentum ℓ is excited into a free electron state $|\epsilon\ell'\rangle$ with an orbital momentum ℓ' and energy ϵ. Finally, $w-1$ electrons are left in the final state configuration $|\ell^{w-1}\rangle$:

$$\underbrace{\left|\ell^{w}\right\rangle}_{|J,M\rangle} \overset{\Delta J,\Delta M}{\longrightarrow} \underbrace{\left|\ell^{w-1};\,\epsilon\ell'\right\rangle}_{|J',M'\rangle}. \tag{2.27}$$

The final states $|J', M'\rangle$ emerge via the dipole selection rules,* according to:

$$\Delta J = 0, \pm 1 \qquad\qquad \Delta M = 0, \pm 1. \tag{2.28}$$

The photoemission spectrum is composed of the core final states $|\ell^{w-1}\rangle$ and transferred to the detector by the photoelectron $|\epsilon\ell'\rangle$. In order to quantify the MCD effect, a theoretical prediction of photoemission line strengths is desirable. A formal description of the MCD in core-level photoemission considers two interactions,[104] (*i*) intra-atomic exchange coupling, which connects core-level spins with the magnetically aligned spins of an open shell, and (*ii*) the spin–orbit interaction, which couples the orbital "magnetic" momentum of the circularly polarized photon to the system of magnetically aligned spins of the sample. We discuss the analytical derivation, as published in Starke (2000),[105,106] in a shortened form in the following.

First, the total photoemission intensity is described by Fermi's golden rule, similar to core-level photoemission with unpolarized light (Ch. 2.4). However, for an MCD experiment, we

*Herein, $\Delta J = 0$ is only possible if $J \neq 0$, due to the enforced momentum change of the photohole ℓ^{w-1}.

must distinguish between the different polarizations q of the light, with $q = M' - M$. Therefore, we choose the basis $|J, M\rangle$ including the magnetic quantum number, and the final states $|J', M'\rangle$, using the electric dipole operator P_q. A summation over all light polarization q yields the total photoemission intensity as

$$\sigma^{JJ'} \propto \sum_q \sigma_q^{JJ'} = \sum_q \left| \left\langle J', M' \right| P_q \left| J, M \right\rangle \right|^2, \tag{2.29}$$

where P_q denotes the q component of the electric dipole moment $P_q = \sqrt{4/3\,\pi}\, r \cdot Y_\ell^q(\theta, \varphi)$, expressed by the spherical harmonics $Y_\ell^q(\theta, \varphi)$.

We focus on transitions with $\Delta M = -q = \pm 1$ according to the angular momentum q of the circularly polarized light. The transition probability $\sigma^{JJ'}$ can be divided into two factors which can be treated separately: (*i*) the line strength $S_{JJ'}$ for every allowed transition $J \to J'$, and (*ii*) the algebra of angular momenta which includes the change of M due to q and the dipole selection rules. Applying the Wigner-Eckart theorem yields

$$\begin{aligned} \sigma_q^{JJ'} &\overset{(2.29)}{=} \left| \left\langle J', M' \right| \mathbf{P}_q \left| J, M \right\rangle \right|^2 \\ &= \underbrace{\left| \left\langle J' \right| \mathbf{P} \left| J \right\rangle \right|^2}_{S_{JJ'}} \cdot \underbrace{\begin{pmatrix} J & 1 & J' \\ -M & q & M' \end{pmatrix}^2}_{3j\text{-symbol}} . \end{aligned} \tag{2.30}$$

The $3j$-symbol vanishes for $q = M' - M = 0$, which means, that the key prerequisite in order to obtain an MCD is the transfer of the angular momentum of circularly polarized light onto the final state M'. The line strength $S_{JJ'}$ shows only a non-vanishing MCD difference spectrum, if the different sub-levels for every M are unequally populated.

The MCD spectrum is defined as

$$I_{\mathrm{MCD}} = \sum_{J'} \left(\sigma_{q=-1}^{JJ'} - \sigma_{q=+1}^{JJ'} \right) \quad \propto \quad \left\langle M \right\rangle_{k_\mathrm{B}T} , \tag{2.31}$$

whereas $\langle M \rangle_{k_\mathrm{B}T}$ is the Boltzmann average (at temperature T) which is proportional to the macroscopic magnetization $|\mathbf{M}(T)|$. In this approximation, the MCD spectrum I_{MCD} is a measure for the macroscopic magnetization.

Example of an MCD spectrum by core-level photoemission

We discuss the MCD in Fe $2p$ core-level photoemission, which was initially experimentally observed by Baumgarten et al. (1990) prior to the development of the MCD theory.[108] In Fe $2p$, the spin–orbit interaction is dominant. Hence, a good approximation is the use of $|j, m_j\rangle$ spin–orbit final states as a basis.[106] Then, the MCD spectrum can be described by

$$I_{\mathrm{MCD}}(j, m_j) = \sum_{\ell' s'} \left(\sigma_{q=-1}^{\ell' s'} - \sigma_{q=+1}^{\ell' s'} \right). \tag{2.32}$$

Here, ℓ' and s' denote the final state angular and spin momenta of the photo-ionized p^5 shell. The sum in eq. 2.32 runs over the six spin–orbit lines as indicated in Tab. 2.1. Radial matrix

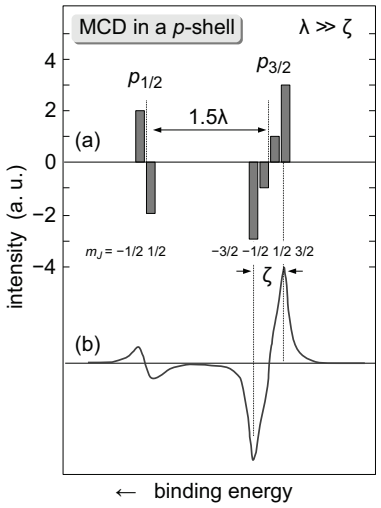

Figure 2.19.: *Right*: MCD components m_J for $2p$ level photoemission with dominant spin–orbit interaction. In (*a*), the lines correspond to p^5 final states in the limit of dominant SO interaction. (*b*) MCD simulation including lifetime broadening. The energy separation between the pure spin components $m_J = \pm 3/2$ is always equal to the exchange coupling strength ζ.

Bottom: MCD of p-level photoemission components for dominant spin–orbit interaction λ. They depend on radial matrix elements $\Delta = 1/3(2R_2^2 - R_0^2 + \tilde{R}_0\tilde{R}_2)$.[107] Adapted from Starke (2000).[105]

j	m_j	$I_{\mathrm{MCD}}(j, m_j)$
3/2	3/2	3Δ
3/2	1/2	Δ
3/2	−1/2	−Δ
3/2	−3/2	−3Δ
1/2	−1/2	−2Δ
1/2	1/2	2Δ

elements from literature[107] allow one to express the resulting MCD intensities $I_{\mathrm{MCD}}(j, m_j)$ for every final state $|\, j, m_j \,\rangle$, as shown in Fig. 2.19.

In this example, the spin–orbit-only MCD final states of the Fe $2p$ photoemission can be analytically quantified. A prediction of MCD line strengths is also desirable for Eu core-levels, which would allow for a direct comparison of the magnetic coupling in epitaxial EuO under different biaxial strain. For EuO core-levels, however, the intra-atomic coupling is more complex, being a composition of spin–orbit and exchange interaction. As a first step, we discuss the possible intra-atomic couplings schemes of Eu core-levels in the following section.

2.5.2. Coupling schemes of atomic angular momenta in Eu^{2+} core-level photoemission final states

Now, we consider the single photoemission final states of the Eu core-levels, which are the basis for a further analysis yielding MCD line strengths. In order to obtain information on the core hole final state $|\, \ell^{w-1} \,\rangle$, one has to decouple the photoelectron from the total photoemission final state $|\, \ell^{w-1}; \epsilon\ell' \,\rangle$. In case of the electronically similar system Gd $4f$, the decoupling of the photoelectron final state has been conducted analytically by Starke (1999).[106] However, for the MCD in Eu core-level photoemission, this decoupling and an evaluation of $\sigma_q^{JJ'}$ of eq. (2.30) has not been published to date. Therefore, as a first step we discuss possible coupling schemes of the angular momenta in order to obtain J and m_J in the following.

The Eu deep core-levels couple via exchange interaction with the $4f^7$ open shell, which we denote as ${}^8S_J$ using the term symbol. With the initial state orbital $n\ell^v$, the final states are created via

$$\left|n\ell^v\right\rangle \quad \overset{\text{photoionization}}{\longrightarrow} \quad \left|n\ell^{v-1}; {}^8S_J; \varepsilon\ell\right\rangle. \tag{2.33}$$

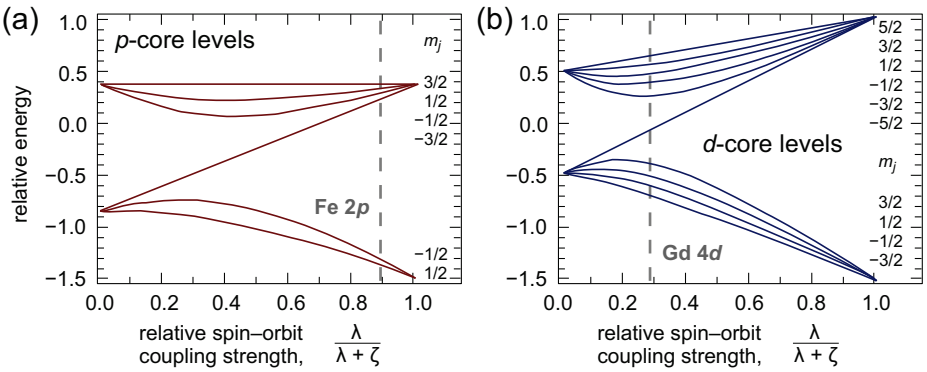

Figure 2.20.: Reduced m_j sublevel energies for p-shells and d-shells dependent on spin–orbit coupling λ or intra-atomic exchange coupling ζ. For dominant λ (jj coupling), the projections m_j are indicated. Adapted from Henk et al. (1999).[87]

The question is, how the spin and orbital angular momenta of the photoionized core and the photoelectron couple to the observable projections m_J of the total angular momentum J of the final states.

In order to include spin–orbit and intra-atomic exchange interaction, we use the single-particle Hamiltonian for core-shells,

$$\mathcal{H} = \lambda(\boldsymbol{\ell}\cdot\boldsymbol{\sigma}) + \zeta\sigma_z, \tag{2.34}$$

where λ denotes the spin–orbit coupling constant for the core-level, and the second term quantifies the exchange interaction between core and valence-level along a quantization axis, usually $\mathbf{z} \parallel \mathbf{M}$. In Fig. 2.20, the reduced sublevel energies of p and d core-level multiplets are displayed in dependence on the relative strength of the spin–orbit (SO) coupling. For dominant SO interaction ($\frac{\lambda}{\lambda+\zeta} \approx 1$), the jj coupling scheme is suitable. If the SO is small ($\frac{\lambda}{\lambda+\zeta} \approx 0$), then the LS-coupling is preferred. If both couplings are present, one may select the intermediate coupling scheme.[109] There exist simple cases, in which e. g. the Fe $2p$ orbital is clearly split by the dominant SO interaction (in Fig. 2.20a), this yielding a doublet with groups of four and two final states, respectively. More ambivalent is the d orbital (in Fig. 2.20b). Here, the SO interaction may be dominant, then the m_J projections as indicated

only spin–orbit $j = \ell + s^*$.			
core hole			projection
s^*	ℓ	j	m_j
$+\frac{1}{2}$	1	3/2	3/2
			1/2
			−3/2
			−3/2
$-\frac{1}{2}$	1	1/2	1/2
			−1/2

Table 2.1.: Photoemission final states of Eu np shells with spin–orbit coupling. Only intra-orbital spin–orbit splitting is considered, which is applicable for Eu $3p$.

will occur in two groups with six and four final states, respectively. In between the limits of dominant or negligible spin–orbit interaction ($\lambda \gg \zeta$, or $\lambda \to 0$), the intermediate coupling scheme is suited to describe the total angular momenta, as seen for the complex example of Gd 4*d*. In the following, we express the final state momenta m_J for the Eu core orbitals either via *jj* or *LS*-coupling, dependent on their classification on λ in Fig. 2.20.

We begin with a simple orbital: the Eu np^6 shell. In Tab. 2.1, the six final final states are derived under assumption of a pure spin–orbit coupling of the photoionized p^5 orbital. For the Eu 3*p*, the spin–orbit splitting is clearly dominant ($\Delta E_{SO} = 135$ eV, $E_B = 1500$ eV), and exchange interaction is negligible.

Table 2.2.: Photoemission final states of Eu *nd* shells in *jj*-coupling (*a*) and *LS*-coupling (*b*) with the ${}^8S_{7/2}$ open shell. In this work, we consider orbitals with principal quantum number $n = \{3; 4\}$.

(a) *jj*-coupling. $j = \ell + s$, $J = \sum j_i$.

core hole s^*	$m_j(nd^9)$	$m_j(4f^7)$	m_J of final state
$+\frac{1}{2}$	5/2	7/2	6
	3/2	7/2	5
	1/2	7/2	4
	−1/2	7/2	3
	−3/2	7/2	2
	−5/2	7/2	1
$-\frac{1}{2}$	3/2	7/2	5
	1/2	7/2	4
	−1/2	7/2	3
	−3/2	7/2	2

(b) *LS*-coupling. $L = \sum \ell_i$, $S = \sum s_i$, $J = L + S$.

core hole s^*	m_L	m_S	m_J of final state
$+\frac{1}{2}$	2	4	6
	1	4	5
	0	4	4
	−1	4	3
	−2	4	2
$-\frac{1}{2}$	2	3	5
	1	3	4
	0	3	3
	−1	3	2
	−2	3	1

We proceed with the Eu nd^{10} orbitals, which show a characteristic multiplet structure in Eu[110,111] and Gd[112] compounds. In Tab. 2.2 (a), we discuss the final states for *jj*-coupling, which is a good assumption for the deeply bound Eu 3*d* core-levels due to their large spin–orbit interaction of $\Delta E_{SO} = \sim 30$ eV and deep binding ($E_B = 1125$ eV). In the 4*d* core-levels, however, which are more weakly bound at ∼120 eV, the spin–orbit interaction is weaker. Thus, a suitable model for the Eu 4*d* level is the *LS*-coupling (Tab. 2.2 (b)) showing two parts of the multiplet, from $m_J = 2 \ldots 6$ in the low binding energy part and $m_J = 1 \ldots 5$ at higher binding energy. The best description for the Eu 4*d* spectra, however, is the more complex intermediate coupling. For a comprehensive discussion on the 4*d* final states, we may refer to literature.[112–115]

A significant spectral separation due to intra-atomic exchange splitting can be observed in the Eu ns^1 orbital of the photoemission final state. Due to the effect of core polarization (as described in Ch. 2.4.2), the core hole with spin s^* can be aligned either parallel or antiparallel with respect to the spin-aligned ${}^8S_J$ open 4*f* shell.[116] This yields two spectral features, which can be practically observed for Eu 3*s* (weak), 4*s* and 5*s* photoemission, as listed in Tab. 2.3. In this work, we show only the Eu 4*s* orbital due to its large cross-section and exchange splitting.

Finally, we consider the Eu $4f^7$ level. Upon 4*f* photoemission, the finals states are created as

$$\left|4f^7; {}^8S_J\right\rangle \overset{\text{photoionization}}{\longrightarrow} \left|4f^6; {}^7F_J; \varepsilon\ell\right\rangle. \tag{2.35}$$

LS-coupling. $L = \sum \ell_i$, $S = \sum s_i$, $J = L + S$.				
core hole			m_J of	
s^*	m_L	m_S	final state	term symbol
+1/2	0	8/2	8/2	$^9S_4$
−1/2	0	6/2	6/2	$^7S_3$

Table 2.3.: Photoemission final states of Eu ns^2 shells couple via exchange coupling with the ^8S_J open shell.

In the final state of the photoionized core (we consider $4f^6$ also as "core"), the term symbol shows the angular momentum F. This is due to Hund's second rule, which lets L be maximal under the precondition of 6 parallel spins in $4f^6$. Thus, the Eu $4f$ core final states consist of the ^7F_J multiplet with $m_J = 0, \ldots, 6$.[117] The splitting between the spin–orbit states of different J is approximately 0.1 eV, and therefore one observes an unresolved single peak in high-energy photoemission spectroscopy. Beyond this simple model, electronic correlation effects may be included by the model proposed by Gunnarsson and Schönhammer,[118] which includes an interplay of strong intra-atomic Coulomb correlations between $4f$ electrons and predicts hybridization of the $4f$ states with the conduction states. The ground and excited states can be then described by a mixing of several $4f$ configurations. For details on $4f$ correlations in EuO, we may refer to literature.[40,119,120]

LS-coupling. $L = \sum \ell_i$, $S = \sum s_i$, $J = L + S$.			
$n-1$			m_J of
spins	m_L	m_S	final state
$+\frac{6}{2}$	3	3	6
	2	3	5
	1	3	4
	0	3	3
	−1	3	2
	−2	3	1
	−3	3	0

Table 2.4.: Photoemission final states of Eu $4f$ shells in *LS*-coupling. In this work, we consider the $4f$ orbitals as core-level shell.

3. Experimental details

> Die Pläne hab' ich bereits im Kopf! Ich muss nur noch einen passenden Apparat konstruieren.
>
> *(Daniel Düsentrieb)*

The fabrication and detailed investigation of functional magnetic oxide heterostructures requires suitable experimental methods. First, their synthesis by reactive molecular beam epitaxy is illustrated in detail, focusing on *in situ* passivation techniques for silicon surfaces and specifications of the growth of magnetic oxide thin films. In a second step, insights into the surface crystal structure can be obtained from *in situ* electron diffraction techniques, and the surface chemical properties (e. g. the silicon oxidation) are controlled by Auger electron spectroscopy. Finally, a variety of *ex situ* methods covering superconducting quantum interference device magnetometry, X-ray diffraction techniques, hard X-ray photoemission spectroscopy, and the MCD effect in photoemission allow one to compile a detailed picture of the magnetic properties, crystal structure, and electronic structure of the surface, buried interfaces, and the bulk of magnetic oxide heterostructures.

3.1. Molecular beam epitaxy for thin magnetic oxide films

In order to fabricate high quality thin films or coatings for electronic and semiconductor technologies, molecular beam epitaxy (MBE) was invented in the 1960s at Bell Telephone Laboratories. Nowadays it is used mainly for the fabrication of transistors, diodes, solar cells, and for fundamental thin film research. MBE is a very fine-controllable deposition technique, which provides the opportunity to grow epitaxial thin films with a low deposition rate (typically < 1 nm/s) such that a monolayer-controlled growth is possible.

Thin films growth modes

An essential advantage of the MBE technique is its ability to achieve layer-by-layer growth of epitaxial thin films. This highest-quality growth mode, however, needs several key prerequisites. First, the mean free path ℓ of the emitted particles should be larger than the distance from the effusion cell to the substrate surface,

$$\ell = \frac{k_\mathrm{B} T}{\sqrt{2}\pi\, p\, d^2} \overset{!}{\geqslant} 40\ \mathrm{cm}, \tag{3.1}$$

with k_B: Boltzmann's constant, T: the system temperature, p: the chamber pressure, and d: the diameter of the particle. This limits the residual gas pressure to roughly 10^{-5} mbar. Nevertheless, UHV conditions in the 10^{-10}–10^{-11} mbar range are required in order to maintain the purity of chemical composition of the film – or in other words – to keep the ratio of contaminants $\leqslant 10^{-5}$.

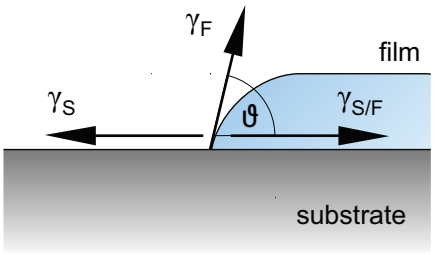

Figure 3.1.: Surface tensions between substrate and film. After Lüth (2010).[79]

Moreover, the substrate plays a crucial role in epitaxial growth as it initially influences the arrangement of the atomic species of the growing film. Regarding the substrate, we distinguish coherent growth (e. g. EuO on YSZ (100)), in which the film will be single crystalline, from an incoherent growth mode (e. g. EuO on MgO (100)), in which the film may be also polycrystalline. Depending on a geometrical consideration of surface tensions between the substrate and the deposited film (Fig. 3.1), different growth modes can be modeled[121] by a balance of the surface tensions,

$$\gamma_S = \gamma_{S/F} + \gamma_F \cos\vartheta, \tag{3.2}$$

where γ_S denotes the tension between substrate and vacuum, γ_F between film and vacuum, and $\gamma_{S/F}$ between substrate and film. Depending on the angle ϑ between $\gamma_{S/F}$ and γ_F, three classic modes of thin film growth are distinguished:

1. In the layer-by-layer (*Frank-Van der Merwe*) growth mode, the adatoms are more strongly bound to the substrate than to each other. With $\vartheta = 0$, we obtain $\gamma_S \geqslant \gamma_{S/F} + \gamma_F$, which means that the wetting of adatoms on the substrate is large, because its surface energy γ_S is less than that of the substrate. The layered growth is possible even if there is a slight lattice mismatch, indicating that a strained-layer epitaxy is feasible.

2. The three-dimensional (3D) island growth (*Volmer-Weber*) occurs, if adatoms are more strongly bound to each other than to the substrate, so that they form films consisting of 3D islands. With $\vartheta > 0$, we obtain $\gamma_S < \gamma_{S/F} + \gamma_F$, which means that the large interface tensions γ_F and $\gamma_{S/F}$ induce the island growth mode. Island growth is very probable if the lattice mismatch is large, and can even occur without any lattice mismatch.

3. The layer-plus-island growth (*Stranski-Krastanov*). In this intermediate case, a formation of one or more layers is energetically favorable in the initial growth stages. However, island growth becomes dominant in the subsequent stages.

4. *Step-flow growth* occurs at very high temperatures (non-equilibrium) when the surface diffusion length of adatoms exceeds the average terrace width. Adatoms in this case migrate to the step edges, which causes the step edges to "flow".

Surface energies of compounds used for EuO heterostructures in this thesis are compiled in Tab. 3.1. Remarkably, the system Eu/YSZ is best-suited for layer-by-layer deposition, since Eu has the smallest and YSZ the largest surface energy of our selection.

Table 3.1.: Surface energies γ of materials used for magnetic oxide heterostructures in this thesis, i. e. silicon, oxides for substrates, Eu as constituent for the EuO synthesis, and metals used as capping or top electrodes. Remarkably, Eu has the lowest and YSZ the largest surface energy, this heterosystem thus likely forms a smooth Van der Merve interface. The same is true for Eu/Cu and Eu/Si, but here the wetting of Eu implicates a large reactivity.

material	application	$\gamma\ (\mathrm{Jm^{-2}})$	method	reference
Eu(100)	EuO constituent	0.46	density functional theory	D. Sander and H. Ibach (2002)[122]
Eu(111)	EuO constituent	0.524	density functional theory	D. Sander and H. Ibach (2002)[122]
Gd	magnetic	0.9	cleavage experiments	Himpsel et al. (1998)[123]
YSZ (9%)	substrate	1.63	multiphase equilibrium*	Tsoga and Nikolopoulos (1996)[124]
MgO(100)	substrate	1.15	cleavage experiments†	D. Sander and H. Ibach (2002)[122]
CaF_2(100)	substrate	0.45	cleavage experiments†	D. Sander and H. Ibach (2002)[122]
CaO	substrate	0.75	equilibrium with H_2O	Paisley et al. (2011)[125]
Si(100)	substrate	1.2	cleavage experiments	Himpsel et al. (1998)[123]
Al_2O_3	spacer oxide	1.4	cleavage experiments	Himpsel et al. (1998)[123]
Al	capping	1.1	cleavage experiments	Himpsel et al. (1998)[123]
Cu	electrode	1.52	cleavage experiments‡	D. Sander and H. Ibach (2002)[122]
Au	electrode	1.41	cleavage experiments‡	D. Sander and H. Ibach (2002)[122]

* at $T = 450\,°\mathrm{C}$ † at $T = 77\,\mathrm{K}$ under HV ‡ at elevated T under HV

In situ ultrathin thermal oxidation of silicon

Surface treatments of Si are often necessary to engineer electric properties and tune the chemical reactivity and diffusion behavior, as investigated in Ch. 5. A thermal oxidation of single-crystalline silicon is the most common process in semiconductor technology in order to create a thin layer of silicon dioxide. During thermal oxidation of Si, molecular oxygen diffuses into the Si surface and reacts to SiO_2, which has been found to be ∼46% below and ∼54% above the surface of the original Si wafer.[222] Our approach aims at growing *ultrathin* silicon dioxide ($d_{SiO_2} \leqslant 2\,\mathrm{nm}$) as a chemical passivation layer directly on clean Si (001), which is clearly thinner than native SiO_2 that forms on Si wafers upon exposure to air.

Synthesis of ultrathin silicon oxide by Oxide-MBE is not well-described by the steady state model[126] which is established for thermal oxidation of silicon in the semiconductor industry. For ultrathin thermal SiO_2 growth on Si, Krzeminski et al. (2007) propose a time-dependent reaction rate approach to model the oxidation kinetics for $Si + O_2 \xrightarrow{K} SiO_2$.[127] Including the diffusivity D, the reaction rate constant K and the concentrations n, the oxidation reaction is then described by rate equations (i. e. changes by time),

$$\frac{\partial n_{O_2}}{\partial t} = \nabla\left(D \times \nabla n_{O_2}\right) - K \times n_{O_2} \times n_{Si} \tag{3.3a}$$

$$\frac{\partial n_{Si}}{\partial t} = -K \times n_{O_2} \times n_{Si} \tag{3.3b}$$

$$\frac{\partial n_{SiO_2}}{\partial t} = K \times n_{O_2} \times n_{Si} \tag{3.3c}$$

which correspond to the diffusion of molecular oxygen (3.3a), the reaction with silicon (3.3b), and finally the creation of SiO_2 (3.3c). As a result, this model reveals that the O_2 coverage on the silicon surface behaves like $n_{O_2} \approx 0.2\,\frac{p}{T}$, which clarifies that at a given oxygen

pressure p the oxygen coverage is significantly larger for lower temperatures T. At higher temperatures $T_{Si} \geqslant 800\,°C$, however, the diffusion into the silicon wafer is significantly increased. Thus, the temperature is an essential parameter for successful *in situ* oxidation of Si surfaces. Experimentally, the model of the reaction rate approach is verified for ultrathin SiO_2 on single-crystalline Si (001) synthesized at $T_{Si} = 725\,°C$ (Fig. 3.2), which shows a time-dependent behavior $n_{SiO_2} \propto t^{0.8}$ for the oxide growth.[127]

Aiming towards a controllable SiO_2 growth on Si with ultrathin oxide thickness in this work, we adopt this parameter set from the low end of the temperature range for thermal oxidation ($T_{Si} \sim 700\,°C$) and in the linear time behavior of oxide formation ($\partial n_{SiO_2} \propto t$). However, the presented approach (eqs. (3.3)) is confirmed only for Si oxide thicknesses greater than 1 nm. Thus, the desired *ultrathin* Si oxide layers for Si surface passivation ($0 < d_{SiO_x} \leqslant 2\,nm$) motivate a detailed determination of the growth characteristics* using the Oxide-MBE.†

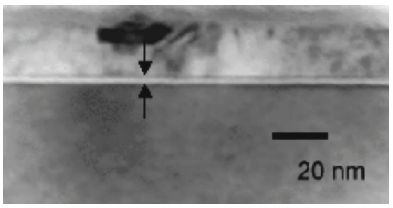

Figure 3.2.: Transmission electron micrograph of 19 Å SiO_2 grown on Si at 720 °C for 10 min by thermal silicon dry oxidation.[127]

3.2. *In situ* surface characterization

Chemical and structural characterizations of magnetic oxide heterostructures can be obtained directly *in situ* before, during and after synthesis of thin films by MBE. Elastic scattering or diffraction of electrons is the standard technique to obtain structural information about crystalline surfaces. Before and after process steps like substrate passivation or thin film growth, the two-dimensional surface crystal structure can be characterized by Low-energy electron diffraction (LEED). In order to confirm the substrate quality and to monitor the thin film surface of the magnetic oxide during the *in situ* synthesis, we use a reflection high-energy diffraction (RHEED) system. Finally, the chemical properties of the silicon or magnetic oxide surface can be investigated by Auger electron spectroscopy (AES).

3.2.1. Reflection high-energy electron diffraction (RHEED)

A powerful *in situ* surface characterization technique is provided by RHEED, which allows one to monitor the surface crystal quality before, during, and after the MBE growth process.

In RHEED, a focused electron beam accelerated to several keV impinges on a flat sample at grazing incidence to investigate the surface crystalline structure. Due to the small sampling depth of RHEED, the surface can be approximated as a two-dimensional layer. Every reciprocal lattice rod leads to a reflection, which is depicted in the Ewald construction in Fig. 3.3. Since the radius of the Ewald sphere ($k_0 = 2\pi/\lambda$) is much larger than the reciprocal lattice

*Such SiO_2 passivation of the Si (001) surface has been conducted by S. D. Flade[128] together with the author and is presented in Ch. 5.

†A characterization of the Oxide-MBE setup is given in Ch. 3.3.

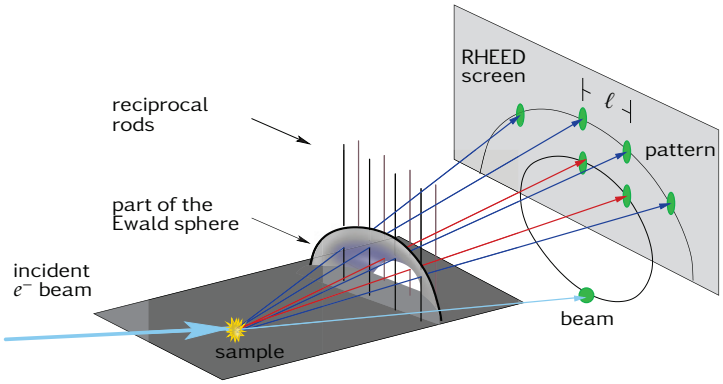

Figure 3.3.: RHEED working principle.

parameter ($k = 2\pi/d$, for cubic lattices), the intersection between both is not very sharp and the diffraction condition

$$\mathbf{k} - \mathbf{k}_0 = \mathbf{G}_{\parallel}(hkl) \tag{3.4}$$

is fulfilled over a range of vertical angles θ. This leads to streaks instead of points on the fluorescence screen. Based on the Bragg equation $n\lambda = 2d\sin\phi$, the *in-plane* cubic lattice parameter d can easily be extracted from the distance ℓ between two reciprocal streaks,[129]

$$d = 2\lambda \cdot \frac{L}{\ell}$$

L: distance sample–screen $\quad \ell$: distance between neighboring rods,

$$\text{with } \lambda = \lambda^{e^-}_{\text{deBroglie}} = \frac{hc}{\sqrt{E_{\text{kin}}(2E_0^{e^-} + E_{\text{kin}})}} \overset{E_{\text{kin}}=10\text{ keV}}{=} 0.12\text{ Å}.$$

If the sample surface is flat on an atomic scale, the diffraction pattern consists of well-defined parallel lines. If the surface structure is three-dimensional due to island growth, these parallel lines shorten to elongated dots, and many orders of these dots are observable. If, however, an extremely flat and ideal surface is probed (e. g. flashed Si under best UHV condition) and

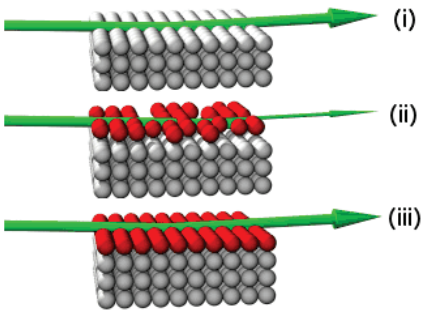

Figure 3.4.: Illustration of layer-by-layer growth observed by high-energy electron diffraction (RHEED).
A maximum reflection of the specular RHEED spot occurs for an atomically flat surface (*i*), whereas the intensity is damped when deposition has reached half a monolayer (*ii*). Once the deposition of a monolayer is completed (*iii*), the maximum reflection is observed again.[223]

a very good electron focusing is achieved, one can observe very sharp diffraction spots of only one order rather than elongated rods. Some inelastically scattered electrons penetrate the bulk crystal and can be detected besides the surface diffraction pattern. If they fulfill Bragg diffraction conditions in the bulk, they are observed as diagonal Kikuchi pattern connecting the intense surface diffraction points.[130] If there is no pattern at all or if it consists of concentric circles, the surface is not well ordered or even polycrystalline.

Recording RHEED intensity oscillations of the specular reflex with time allows one to quantify the number of monolayers grown in MBE, if the Van-der-Merve growth mode is predominant, as illustrated in Fig. 3.4. The Oxide-MBE system at PGI-6 is equipped with a self-constructed RHEED system having a VARIAN 981 e-gun source in the main deposition chamber.

3.2.2. Low-energy electron diffraction (LEED)

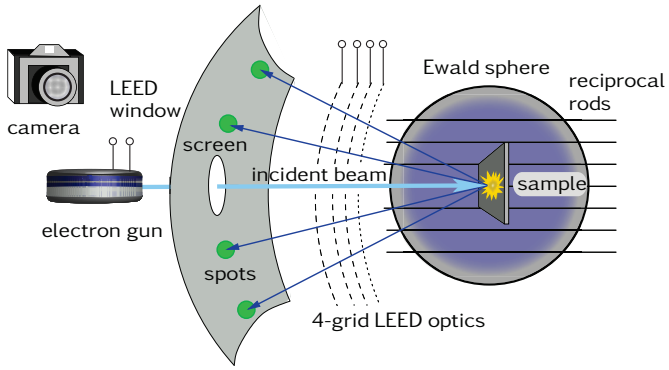

Figure 3.5.: LEED working principle.

Low-energy electrons with energies from about 20 to 500 eV are ideal probes for surface studies, because they are mainly elastically scattered by atoms. According to the de Broglie relation, $\lambda = \sqrt{150.4/E_0^{e^-}}$ ($[\lambda] = $ Å, $[E] = $ eV), typical LEED wavelengths are of the same magnitude as interatomic distances in crystals and comparable with that used in X-ray diffraction (see Sec. 3.4.2). The Ewald sphere intersects only the lattice rods at particular points that fulfill the Laue diffraction condition eq. (3.4), and the resulting LEED pattern consists of an ordered arrangement of spots. All surface diffraction patterns show a symmetry reflecting that of the crystal class and are centrally symmetric. The scale of the diffraction pattern depends on the electron energy and the size of the surface unit cell as

$$\frac{2\pi}{d} \propto \sqrt{\frac{2mE}{\hbar^2} - |\mathbf{G}_{\parallel}|^2}, \tag{3.5}$$

where d is the real space lattice parameter, and $\mathbf{G}_{\parallel}$ a reciprocal lattice vector in the surface plane.[79,131]

In the experimental work, a LEED image shall exhibit a sharp pattern and low background intensity. Defects and crystallographic imperfections will broaden spots and increase the

diffuse background, due to scattering from statistically distributed centers. Since the area on a sample surface in which constructive diffraction occurs is smaller than the coherence width of the electron beam, which amounts to ~100 Å, a LEED probe is point-like.[79] Thus, LEED probes a microscopic area, while with RHEED one can "scan" the entire surface of the sample. In this work, LEED investigations are used to monitor the surface crystal structure by a qualitative comparison with simulated patterns of the LEEDpat software.[224] In practice, we use a three mesh VG Microtech RVL 640 Rear View LEED system.

3.2.3. Auger electron spectroscopy (AES)

Whenever functional heterostructures with the highest chemical quality of interfaces and surfaces are designed, an *in situ* analysis of the chemical composition and a quantification of surface oxidation or possible carbon contamination is essential. Among the non-destructive and element-selective chemical probing techniques, the Auger electron spectroscopy (AES) is well-established for analyzing the kinetic energy of secondary electrons. For light elements ($Z \leqslant 30$), the Auger-Meitner cascade is the dominant emission process, when surface atoms are excited by X-rays or electrons. The external excitation leaves an electron core-hole (A), which is filled by an upper shell electron (B). This recombination energy is characteristic for the particular elemental atom and is used to emit an outer shell electron (C) carrying the characteristic kinetic energy

$$E_{\text{kin}} = E_A - E_B - E_C - E_{\text{vac}}.$$

The specific Auger processes are named by the participating shells, e. g. KLM for transitions between the *s* and *p* orbitals and an emission from the *d* shell.

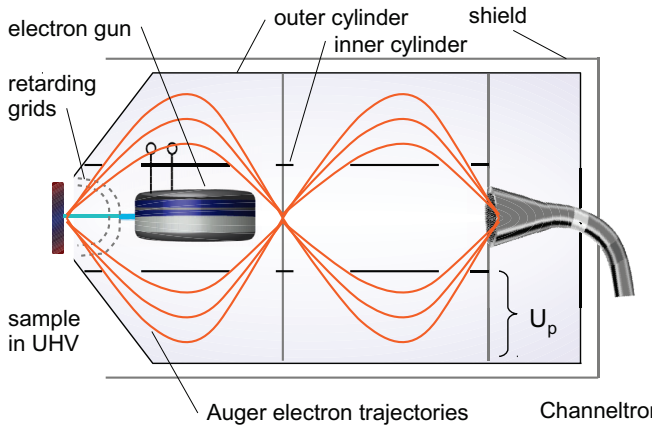

Figure 3.6.: Cylindrical mirror analyzer for Auger electron spectroscopy. The pass energy E_0 and voltage U_p between the two cylinders are related by $E_0 = eU_p/0.77\ln(b/a)$, with a and b denoting the radii of the inner and the outer cylinders.[79]

A cylindrical mirror analyzer (CMA) is used for Auger electron spectroscopy. The Auger electrons are focused from an entrance point into a certain cone by two concentric cylindrical

electrodes onto an image point, where a Channeltron detector is positioned. The electric field determining the pass energy is a radial field between the two concentric electrodes, as schematically shown in Fig. 3.6. For AES, a non-retarding mode is used in which the electrons pass through the analyzer with their initial kinetic energy, and the energy range being swept by varying the potential on the outer cylinder. With this geometry, an energy resolution of 0.6% of the electron kinetic energy can be reached, which is limited by the angular deviation of the incoming electron trajectories (see Lüth (2010)).[79]

In this work, AES is employed to routinely check the surface quality by means of chemical cleanliness, and to quantify the thickness of the *in situ* oxidation of silicon. A VARIAN cylindrical mirror analyzer is used with electrons of $E_{\mathrm{exc}} = 3$ keV from a VARIAN 981 e-gun source. In practice, the energy resolution is ~1 eV due to the sweep generator.

3.3. Experimental developments at the Oxide-MBE setup

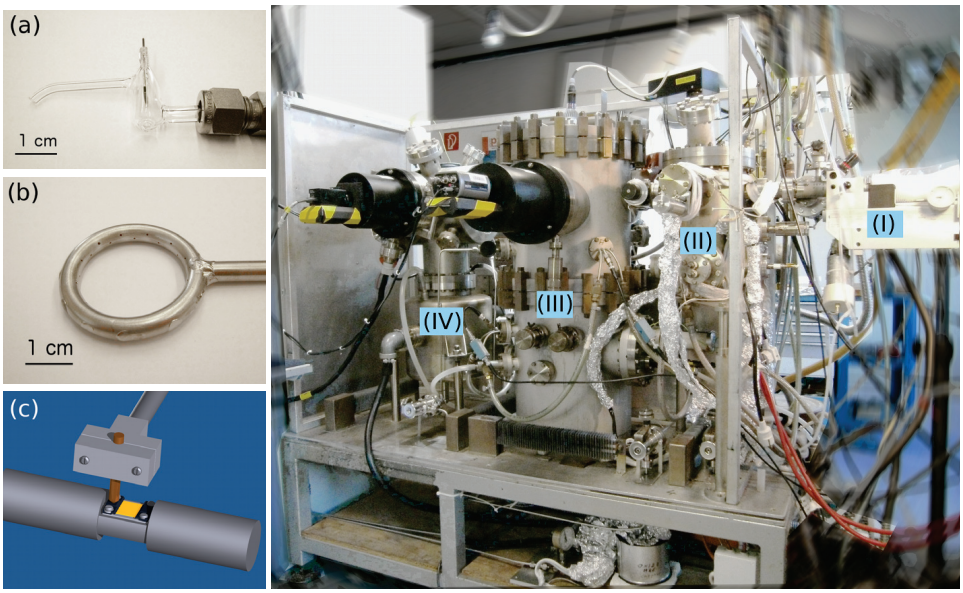

Figure 3.7.: Details of the Oxide-MBE setup at PGI-6. (*a*): Atomic gas supply with robust tungsten filament in a high pressure cracking bulb. (*b*): Oxygen nozzles which are located 10 mm in front of the sample surface and the mass spectrometer filament. (*c*): Flashing stage for Si wafer pieces. *Right*: Oxide-MBE setup at PGI-6 equipped a drive-through fast load lock system (I), a preparation chamber (II), the main deposition chamber (III), and an analysis chamber (IV).

The Oxide-MBE setup utilized in the frame of this thesis allows for the deposition of magnetic oxide heterostructures in conjunction with oxides or silicon substrates. Historically, mainly metallic three-layer structures have been fabricated in this system since the 1980s in order to explore novel electronic effects. In particular, in 1988 Fe/Cr/Fe structures showed an "en-

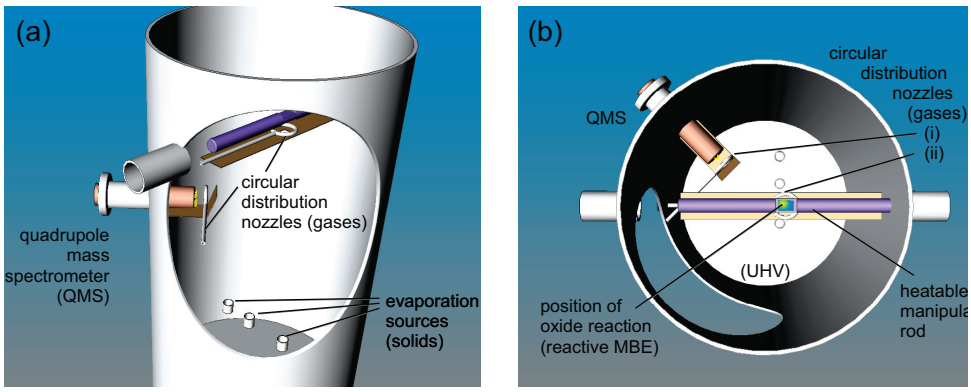

Figure 3.8.: Geometrical arrangement of oxygen nozzles inside the Oxide-MBE. Drawing *(a)* illustrates the bisection of gas supply with respect to the sample manipulator and the mass spectrometer. A top view in drawing *(b)* illustrates the position of oxide reaction on the manipulator.

hanced magnetoresistance"[1] which established as the giant magnetoresistance (GMR) effect.* This discovery was awarded with the Nobel Prize for P. Grünberg and A. Fert in 2007.[219]

In the Peter Grünberg Institut (PGI-6 "Electronic Properties"), the MBE system comprises three UHV chambers and a drive-through fast load lock system (Fig. 3.7 I), which are connected by a fully rotatable and heatable sample manipulator. First, a pre-chamber (II) allows for a fast deposition of metallic layers (e. g. Al) and contains gas nozzles, by which the *in situ* silicon oxidation or hydrogen termination with partial pressures up to the 10^{-2} mbar regime are conducted. Second, providing best vacuum conditions of $\sim 10^{-11}$ mbar, the main deposition chamber (III) is equipped with three electron beam evaporation guns which permits one to evaporate up to five different target materials. The atomic flux rate can be monitored parallel by two quartz crystal microbalance systems. Here, the magnetic oxide deposition takes place under a meticulous control of Eu flux and oxygen partial pressure. Controlling the crystalline surface structure during deposition is feasible by a RHEED system. Finally, the analysis chamber (VI) contains the surface analysis tools, i. e. LEED for imaging the surface reciprocal lattice and Auger electron spectroscopy for chemical surface investigations. In order to match the special needs for the synthesis and investigation of ultrathin oxide films, three special developments have been introduced into the system. Therefore we refer to it as a specialized *Oxide-MBE*.

First, to allow for a meticulous control of the oxygen supply necessary for the magnetic oxide synthesis, two nozzles of a symmetric circular shape (Fig. 3.7b) distribute the process O_2 gas equally to a quadrupole mass spectrometer as well as to the surface of the sample. This local gas supply provides the advantage that the remaining chamber is spared from gas adsorption: the highly reactive Eu reservoir as well as filaments benefit from this.

*The GMR uses the inter-layer exchange interaction between the adjacent magnetic layers separated by a thin nonmagnetic spacer which favors an anti-ferromagnetic configuration of the magnetic layers. Due to spin-dependent scattering in the three-layer system, the resistance of the antiparallel magnetic configuration in remanent state is much larger than in a parallel configuration under external H field. Nowadays, this is the basis for hard disk read heads or miniaturized H field sensors.

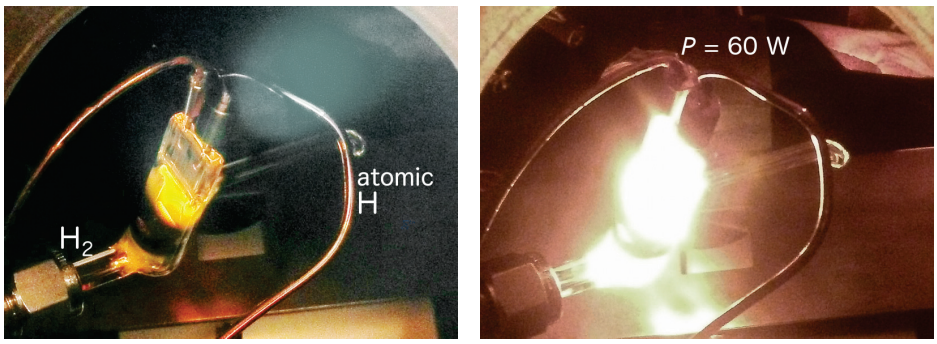

Figure 3.9.: Thermal hydrogen cracker for *in situ* substrate treatments, for example silicon surfaces. *Left*: degas mode. *Right*: cracking mode with H_2 supply ($T_{fil} \approx 2000$ K).

In order to provide chemically clean and atomically sharp silicon surfaces, we treat Si wafer pieces by an *in situ* thermal flashing procedure. A flashing sample holder consisting of tantalum clamping, tungsten fixation screws, and alumina isolation spacers enables the effective thermal cleaning of Si pieces by a direct current heating. We constructed the flashing stage according to the textbook of Yates (1998)[132] and under practical advice from Westphal (2011).[133] The thermal flashing procedure takes place in the main chamber under the best UHV conditions (Fig. 3.7c), and substrate temperatures of $T_{Si} \geqslant 1100$ °C are easily reached for low-doped silicon ($\rho_{Si} \geqslant 3$ kΩ cm).

Atomic hydrogen is suited for the surface passivation of silicon dangling bonds, which we provide *in situ* in order to ensure chemical cleanliness and to cover a broad range of supply parameters. For H_2 crackers using a tungsten hot surface, the efficiency of H production is proportional to $(p_{H_2})^{1/2}$ in a regime $p_{H_2} > 10^{-5}$ mbar, and commercial H_2 crackers work at $p_{H_2} \approx 10^{-2}$ mbar in the tungsten cracking capillary.[132] Using a white glowing tungsten surface ($T_W \geqslant 2000$ °C), a dissociation efficiency of 0.3 per H_2 collision with W was reported.[134] In order to match these efficiency parameters and considering the limited space in the pre-chamber, we developed a source for atomic hydrogen and mounted it to the pre-chamber. It is fabricated from a high-power halogen lamp (Fig. 3.7a).* Ultraclean (99.999%) molecular hydrogen gas is leaked by a dose valve into the cracking bulb, in which the tungsten filament is heated with a power of ∼60 W. While a hydrogen partial pressure in the chamber of 10^{-3} mbar is found to optimally passivate the clean Si, we estimate the hydrogen pressure in the cracking bulb to be in 10^{-1} mbar regime, in agreement with the reported working pressure of commercial crackers. Moreover, the cracking bulb architecture with a short nozzle protects the sample surface from unwanted evaporation of the hot cracking filament.

For this work, only a persistent high chemical and structural quality of the EuO heterostructures permits one to systematically investigate a tuning of composition, strain, or interface structure. The presented specializations of the Oxide MBE setup render high quality growth of EuO thin films possible on various oxide substrates (as shown in Ch. 4). Moreover, advanced treatments of clean Si crystals are applicable in order to apply atomically thin passi-

*Fabrication from high-power halogen lamps suggested by F.-J. Köhne.

vations to the surface (as presented in Ch. 5).

3.4. *Ex situ* characterization techniques

In addition to the *in situ* synthesis and characterization of magnetic oxide heterostructures, we apply a variety of *ex situ* characterization methods which permit an in-depth analysis of magnetic properties, crystalline structure and the electronic structure. After a brief introduction of bulk-sensitive SQUID magnetometry and X-ray diffraction techniques, photoemission spectroscopy with advanced analysis methods are discussed, which allows for a depth-selective profiling. We present a model to determine the information depth by HAXPES and derive a formula to quantify chemical species located at a buried interface. We introduce the HAXPES beamlines and endstations where the photoemission experiments were conducted. Finally, we present the photoemission experiment conducted with circularly polarized X-ray light, which allows to investigate the magnetic circular dichroism effect in magnetized thin films.

3.4.1. Superconducting quantum interference device (SQUID) magnetometry

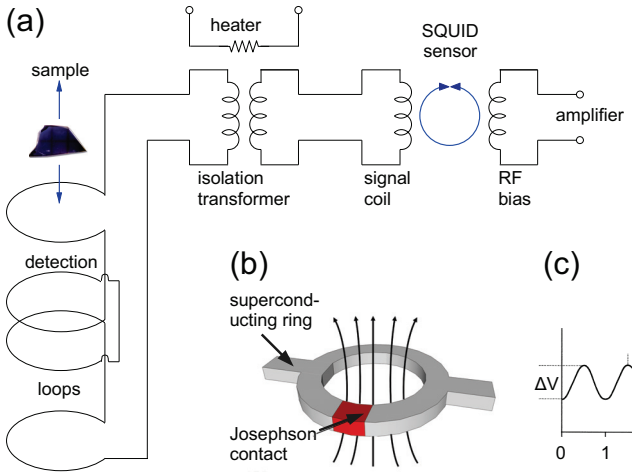

Figure 3.10.: Measurement principle of a superconducting quantum interference device (SQUID). The thin film sample is reciprocating through the superconducting detection loops (*a*). Variations of the flux Φ (*b*) are converted by a Josephson contact into an RF signal (*c*).

In order to characterize the bulk magnetic properties of thin magnetic oxide films, SQUID magnetometry is perfectly suited, as it provides a sensitivity down to the nano emu regime.* Moreover, a He atmosphere prevents the degradation of the air-sensitive samples. The probing of the sample magnetization takes place in the SQUID sensor, which consists of a superconducting ring interrupted by one Josephson contact. Due to the fundamental magnetic flux quantization (Meißner-Ochsenfeld effect), only a magnetic flux of multiples of $\Phi_0 = \frac{h}{2e}$ is allowed to pass through the area of the ring. During measurement, a magnetic sample

*The electromagnetic notation "emu" measures magnetic moment in the Gaussian cgs system. It converts to SI as: 1 emu = 10^{-3} Am^2 = 10^{-3} J/T.

is moved through the ring (Fig. 3.10a), which induces a ring current. At the same time, the magnetic flux through the ring has to result in an integer multiple of Φ_0. To fulfill this condition, the Josephson contact generates voltage oscillations with the time period of one $\Delta\Phi_0$ (Fig. 3.10b, c). These voltage oscillations are detected by an RF coil and further processed (see Fig. 3.10).

In practice, when $\widetilde{m}(T)$ denotes a measured magnetization, $\widetilde{m}_{\mathrm{off}}$ the magnetization offset from zero when only a vanishing signal is expected (i. e. at $T \gg T_{\mathrm{C}}$), $\widetilde{m}_0 = m(T \to 0)$ the measured saturation magnetization, and m_{theo} the theoretically expected magnetization, then the magnetic moment m in μ_{B} per magnetic formula unit can be expressed as

$$m(\widetilde{m}(T)) = \frac{\widetilde{m}(T) - \widetilde{m}_{\mathrm{off}}}{f\,\mu_{\mathrm{B}}} \cdot \frac{V_{\mathrm{cell}}}{A\,d}, \qquad \text{or} \tag{3.6a}$$

$$d = \frac{\widetilde{m}_0 - \widetilde{m}_{\mathrm{off}}}{f\,\mu_{\mathrm{B}}\,m_{\mathrm{theo}}} \cdot \frac{V_{\mathrm{cell}}}{A}. \tag{3.6b}$$

Here, μ_{B} denotes Bohr's magneton, $V_{\mathrm{cell}} = a^3$ the volume of the cubic unit cell of the magnetic oxide, f the number of magnetic units per cubic cell, A the area and d the thickness of the magnetic thin film. Application of eq. (3.6a) with known geometry of the magnetic thin film reveals the specific magnetic moment m. Alternatively, by assuming an optimum sample with reference magnetization $\widetilde{m}_0 = m_{\mathrm{theo}}$, the thin film thickness d can be obtained from eq. (3.6b).

In this work, a Quantum Design MPMS XL SQUID magnetometer is used to determine the magnetic properties of magnetic oxide thin films. The magnetization $m(T)$ is recorded as field warm curve at a minimum saturation field (usually ~100 Oe), which we determined by hysteresis measurements for every thin film sample.

3.4.2. X-ray diffraction methods (XRD, XRR, RSM)

Based on the Bragg equation $n\lambda = 2d\sin\theta$, X-ray diffraction (XRD) is a versatile technique which allows for the determination of structural properties such as the distance between crystal lattice planes, the thickness of layers, interface and surface roughness, texturing, and mosaicity, to mention the most common properties.

In a simple Bragg-Brentano setup, in which one axis (2θ) is moved in order that the sample surface is always at $\omega = \theta$, a standard 2θ–ω diffractogram is obtained (Fig. 3.11). Here, only crystallites oriented parallel to the surface contribute to the diffraction peak. The observable peaks directly arise from the diffraction after Bragg's law, and the exact peak position on the 2θ scale allows to calculate the distance between diffracting planes (c: out-of-plane lattice parameter). The width of those peaks provides information about the orientation distribution of the crystallites, i. e. the mosaicity. Thus, already simple XRD diffractograms provide information about orientation and quality of thin films with good crystallinity.[135]

Using small angle scattering in the 2θ–ω setup, also known as X-ray reflectivity (XRR), a simulation of Kiessig fringes using the Parratt model[136] allows for the determination of the thickness of several layers from roughly two up to hundreds of nanometers. Moreover, from the damping of these fringes, the interface and surface roughness can be modeled.

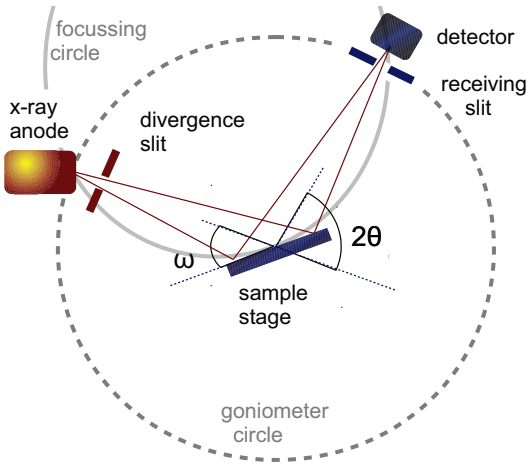

Figure 3.11.: The measurement geometry of a two-axis X-ray diffraction. In the Bragg-Brentano geometry, the focus of the X-ray tube, the detector and the sample are situated on a focussing circle with a radius scaling down with larger diffraction angles.

Coherent areas of the reciprocal space can be recorded with two-dimensional reciprocal space maps (RSM). In the neighborhood of a selected diffraction peak, a series of ω–2θ scans is conducted such that a two-dimensional area is scanned by the stepwise variation of ω. The coordinates in reciprocal space q are expressed as

$$q_{\parallel} = R_{\text{Ewald}}\Big(\cos\omega - \cos(2\theta - \omega)\Big) \tag{3.7}$$

$$q_{\perp} = R_{\text{Ewald}}\Big(\sin\omega + \sin(2\theta - \omega)\Big), \quad [q] = \text{rlu} = \text{reciprocal lattice units} \tag{3.8}$$

where $R_{\text{Ewald}} = 2\pi/\lambda \overset{\text{Cu}K_\alpha}{=} 40.7\ \text{nm}^{-1}$ is the radius of the Ewald's sphere. We obtain an interpretation of structural deviations from a perfect crystal by reflex broadening with respect to the scattering vector $\mathbf{q}$ (see Fig. 3.12). Moreover, a quantitative evaluation of parallel and perpendicular lattice components i with respect to the surface can be obtained, if the reciprocal

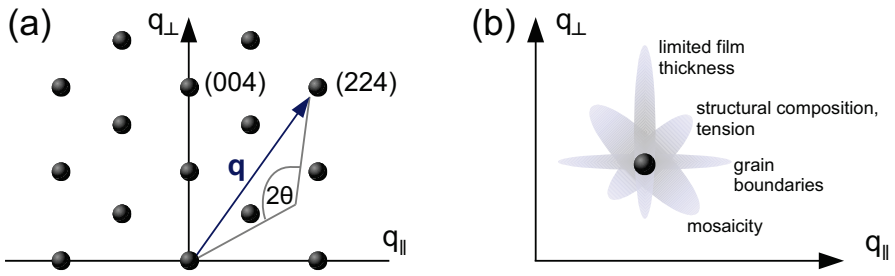

Figure 3.12.: Reciprocal space mapping. *(a)* An asymmetric reflex provides information of $q_{\parallel}$ as well as $q_{\perp}$. *(b)* Broadening effects of an asymmetric reflex and its structural interpretation.[135]

coordinates q_i are converted into real space distances with Miller's indices m_i,

$$d_i = \frac{1}{q_i} \cdot m_i, \qquad m_i = \begin{cases} h \text{ or } k, & \text{for } i \text{ parallel,} \\ l, & \text{for } i \text{ perpendicular.} \end{cases} \tag{3.9}$$

In this work, all X-ray diffraction experiments are conducted with a four-cycle Phillips MRD Pro using monochromatized Cu $K\alpha$ radiation.

3.4.3. Hard X-ray photoemission spectroscopy (HAXPES)

Quantifying the element-specific electronic properties of a multilayer system is impossible when using surface-sensitive soft X-ray photoemission due to its limited probing depth. The major limiting factor is the inelastic scattering of free electrons in solids. For an electron with energy $E_{\text{kin}} = \frac{\hbar^2 k^2}{2m}$, the inelastic mean free path (IMFP) can be expressed as $\lambda = \left(\frac{\hbar k}{m}\right)\hbar\tau_{\text{inel.}}$, where $\tau_{\text{inel.}}$ denotes the lifetime due to inelastic scattering processes. A removal of unwanted top layers with argon etching and subsequent soft X-ray PES provides access to buried layers, however, this approach significantly changes the surface morphology and hampers a further investigation of highly reactive functional layers such as EuO.

Since the last decade, however, the hard X-ray regime ($h\nu \geqslant 2$ keV) has become available to photoemission – an energy range complementary to the established soft X-rays. This extends the escape depth of the photoelectrons up to several tens of nanometers according to the estimation $\lambda \propto E_{\text{kin}}^{0.78}$, as depicted in Fig. 2.18.[84,85] Thus, HAXPES with photon energies up to 10 keV is perfectly suited to investigate the electronic properties of buried interface or bulk properties. Hard X-ray excitation, however, implies also drawbacks such as reduced photoemission cross-sections and Debye-Waller factors, as discussed in Ch. 2.4.3. Fortunately, since

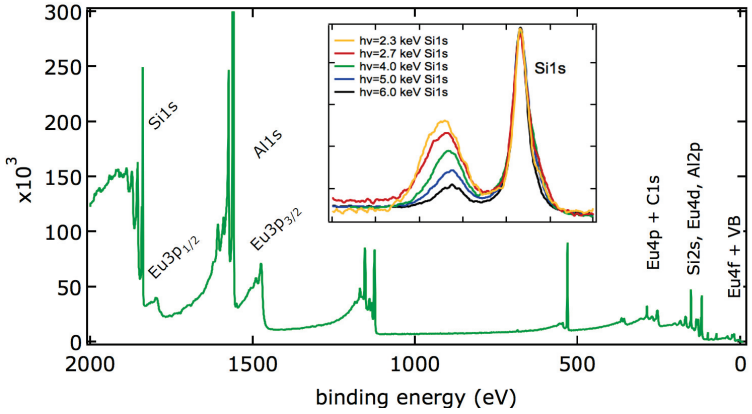

Figure 3.13.: An extra-wide photoemission spectrum by HAXPES. Deep core-levels are accessible and valence-like levels have reduced cross-sections, as illustrated in a survey spectrum taken at $h\nu$ = 4 keV. The spectrum of a buried SiO_x interface layer *(inset)* varies in observable SiO_x fraction with excitation energy.

highly brilliant synchrotron light sources are available (e. g. PETRA III), the reduced photoemission cross-sections can be compensated by high-intensity hard X-ray radiation: photoemission spectra with a wide range of electron kinetic energies are thus available (example in Fig. 3.13). This, in turn, fulfills the key prerequisite for depth profiling of the electronic properties in multilayer structures including buried layers and interfaces, by analyzing photoelectrons of largely different kinetic energies.

The HAXPES experiment at KMC1 beamline in the BESSY II storage ring

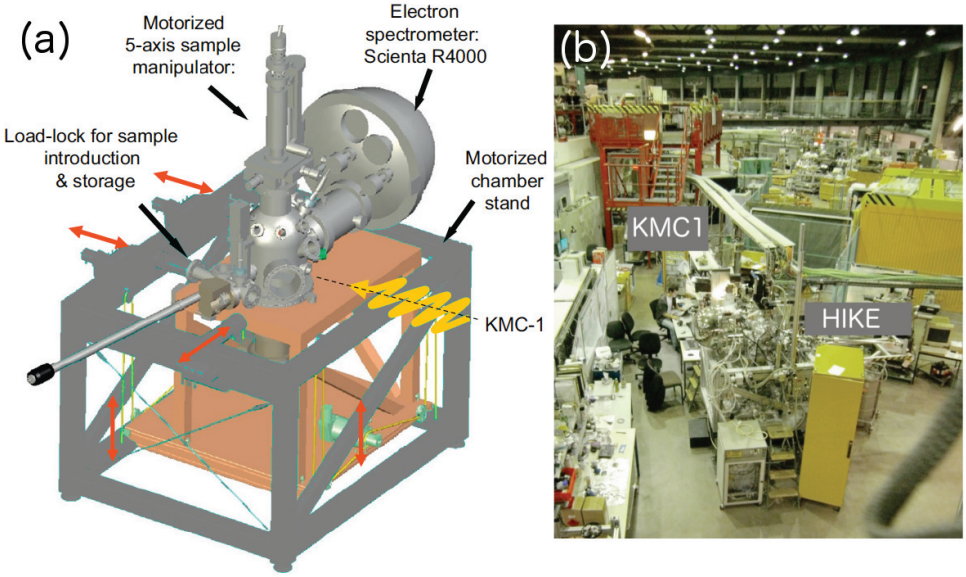

Figure 3.14.: The HIKE endstation (*a*) is located at the KMC1 dipole magnet beamline (*b*) at the BESSY II storage ring in Berlin.

Since 1994, the third generation synchrotron light source of the Helmholtz-Zentrum Berlin (Germany) provides access to a variety of experiments employing highly brillant X-ray light. Electrons are accelerated up to an energy of 1.7 GeV and are injected into the storage ring BESSY II. A variety of X-ray sources (undulator, wiggler and dipole magnet sources) with high energy resolution are in operation.

The KMC-1 beamline disperses light from a dipole light source, and is coupled to the HIKE endstation with a SCIENTA R4000 electron spectrometer. Spectroscopy experiments can be conducted with a high energy resolution and an excitation energy up to 12 keV. A two-crystal Si monochromator provides mono-energetic light, achieving an overall energy resolution of 200 meV. Very high resolution is achieved around 2, 6 and 8 keV photon excitation energy due to an optimal Bragg reflection of the monochromator crystals. The instrumental resolution of the spectrometer can be better than 40 meV at 6 keV (Gorgoi et al. (2009)).[98] As depicted in Fig. 3.14a, the R4000 analyzer is positioned at an angle of 90° with respect to the incoming X-ray light. Thus, the excitation is at grazing incidence which lets the photo-

electron emission be normal to the surface in the standard setup. This provides the largest escape depth of the photoelectrons and, moreover, lets the X-ray penetration depth match the electron escape depth, which minimizes the inelastic background of photoemission spectra. In this work, magnetic oxide on silicon heterostructures are investigated by high-resolution HAXPES measurements at the HIKE endstation.

The HAXPES experiment at P09 beamline at PETRA III

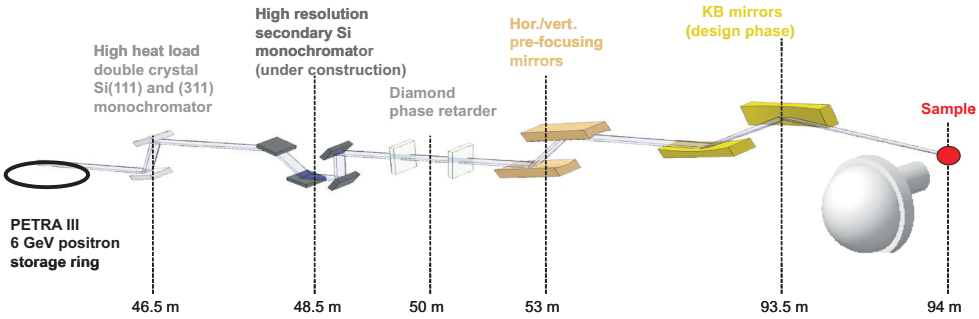

Figure 3.15.: Schematics of the beamline P09 at PETRA III. Courtesy Gloskovskii et al. (2012).[97]

Since 2010, a very high photon brilliance due to its small emittance of 1 nm rad at 6 GeV makes X-ray light of the Positronen-Elektronen Tandembeschleunigeranlage (PETRA III storage ring) in Hamburg (Germany) perfectly suited for spectroscopic techniques requiring high energy resolution and high intensity.

At the hard X-ray beamline P09 (Fig. 3.15), the energy adjustment of highly coherent light is provided by a two-meter undulator followed by a Si-crystal primary monochromator. For experiments requiring elliptically polarized light, a double-stage diamond phase retarder can be moved into the beam path in order to generate either linear or circularly polarized X-ray light. In order to allow for magnetization-dependent measurements of the magnetic circular dichroism effect*, a permanent magnet can be approached by a non-magnetic ultrathin-walled feedthrough. In this way, we apply a large magnetic induction ($B_{\mathrm{max}} \geqslant 1$ T) to the thin film sample, which remains then remanently magnetized.

A high-resolution HAXPES setup using a SPECS Phoibos 225 HV delay line detector is installed as the spectroscopy endstation. The detector is situated along the dispersive direction of the spectrometer, which permits a detector resolution of 30 meV at 10 keV.[97] Figure 3.16 illustrates the arrangement of analysis chamber, the energy analyzer, and optionally magnetized thin film sample.

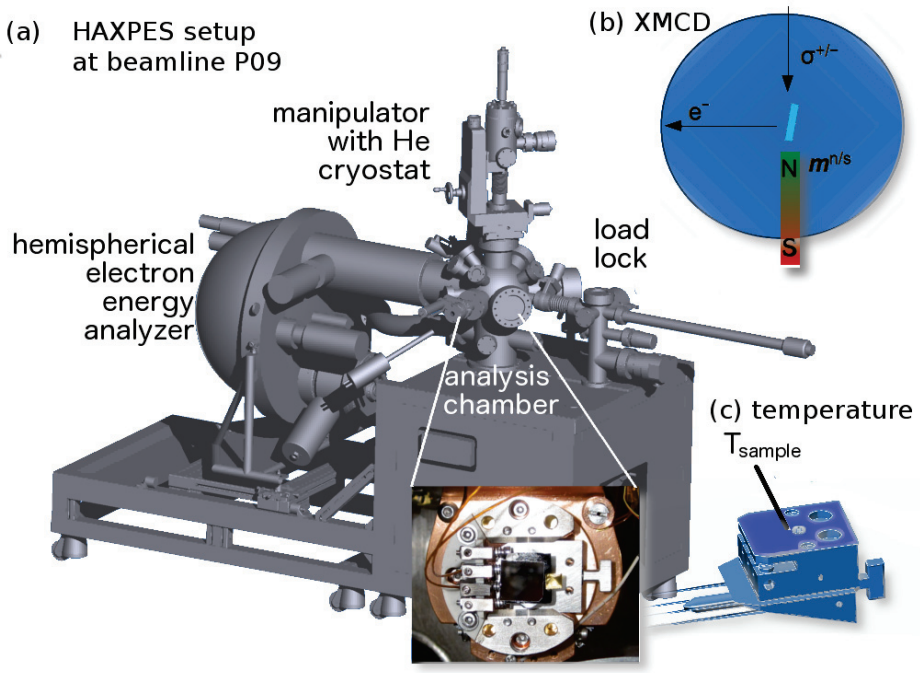

Figure 3.16.: HAXPES experiment at the P09 beamline at PETRA III (*a*). (*b*): Geometry of an MCD measurement. A remanent magnetization of the thin film parallel or antiparallel with respect to the incoming light is induced by a removable permanent magnet. (c): The sample temperature is directly measured at the sample plate using a thermocouple (design courtesy F. Okrent).

3.4.4. Depth-selective profiling with HAXPES

A suitable measure of the sampling depth in solids from which photoelectrons carry information to the detector is based on the so-called information depth (ID). We define the information depth as the probing depth from which 95% of the emitted photoelectrons originate, thus $I(\lambda,\alpha)|_{\mathrm{ID}}^{\mathrm{top}} \Big/ I(\lambda,\alpha)|_{\infty}^{\mathrm{top}} \leqslant 95\%$, whereas

$$I(\lambda,\alpha)\big|_{\mathrm{bottom}}^{\mathrm{top}} = C \sum_{\mathrm{layers}\ i} \int_{\mathrm{bottom}\ i}^{\mathrm{top}\ i} \exp\left(\frac{-z}{\lambda_i \cos\theta}\right) dz, \tag{3.10}$$

where I denotes the spectral intensity, z the depth in the heterostructure from the surface, λ the effective attenuation length,[84] θ the off-normal emission angle, and C a sample-specific parameter. For example, using an excitation energy $h\nu = 4$ keV, we can obtain an information depth of approximately 20 nm for valence level photoemission peaks.

*see MCD results in Ch. 4.

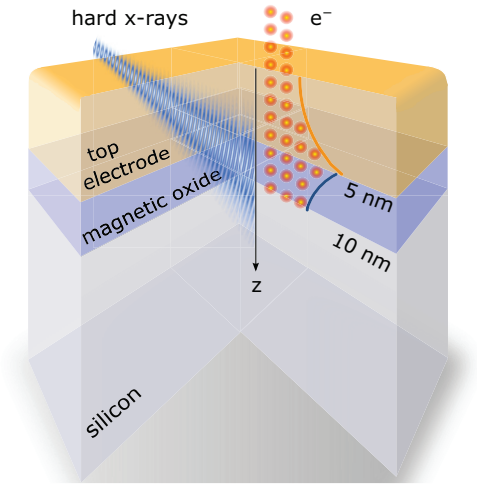

Figure 3.17.: Schematics of hard X-ray photoelectron excitation and damping in a three-layer heterostructure. Taking advantage of the largely tunable excitation energy of the hard X-ray synchrotron radiation, the resulting information depth is the essential parameter for a depth-selective probe of multilayer structures.
As an example, the excitation takes place in the buried magnetic oxide and the electron yield is damped by the metallic overlayer.

An essential application of HAXPES is the determination of non-destructive depth profiles of specific elements with Ångström resolution. Photoelectron excitation and damping in dependence on the depth z is illustrated in Fig. 3.17. The detected intensity I can be expressed in dependence on the density n of an element x which reveals a profile in z,

$$I_x = \frac{I_x^\infty}{N_x^\infty \lambda(E_{\mathrm{kin}}) \cos\theta} \cdot \int_a^b n_x(z) \exp - \frac{z}{\lambda(E_{\mathrm{kin}}) \cos\theta} \, dz, \tag{3.11}$$

where N_x^∞ denotes the density of an element x in the bulk and $n_x(z)$ the density profile of x. The function $n_x(z)$ can be unraveled by a series of photoemission measurements of element x with different kinetic energies of the photoelectrons (procedure conducted e. g. by Rubio-Zuazo and Castro (2008)).[137]

In this work, however, the determination of a continuous density profile is replaced by two representative values. First, bulk-sensitive measurements are conducted by using a large kinetic energy of the photoelectrons, thus λ is large, too. As a complementary second measurement, the kinetic energy is tuned down by using the minimum excitation energy provided by the beamline, thus the information depth is tuned to a minimum and the experiment is surface-sensitive. Alternatively, changing the emission geometry of the photoelectrons to a large off-normal emission angle also reduces the mean escape depth according to $\lambda(E_{\mathrm{kin}})\cos\alpha$ (see Fig. 3.18).

Thickness determination of buried layers by HAXPES

The depth sensitivity of HAXPES not only allows the determination of the chemical state of a thin buried layer, but also its *thickness*. The thickness of buried oxide tunnel barriers, though, is a key parameter for oxide spintronics.[85] Considering a layer stack, in which a toplayer of thickness c is of interest on top of a substrate, a simple formula can be derived[138] and applied[139] for such a two-layer system. As an example, the thickness of a silicon surface

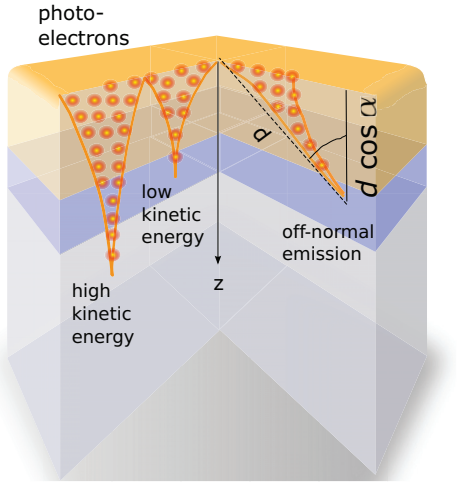

Figure 3.18.: Photoelectron yield for low or high kinetic energy and off-normal emission. In case of a high kinetic energy of the photoelectrons, the escape depth is large due to less probable inelastic scattering. Low-kinetic energy electrons experience inelastic scattering more likely on their escape, such that the depth of unscattered photoelectron is smaller. Off-normal emission reduces the escape depth by $\cos\alpha$ and renders this configuration surface-sensitive, too. For an off-rotation of $\alpha = 60°$, the photoelectrons travel two times the normal emission path to escape the solid.

oxide on top of a silicon wafer calculates as

$$c = -\lambda_{ox}\cos\alpha \cdot \ln\left(\frac{I_{ox}}{I_{Si}} \cdot \frac{\lambda_{Si} n_{Si}}{\lambda_{ox} n_{ox}}\right). \tag{3.12}$$

Here, λ denotes the effective attenuation length,[84] α is the off-normal emission angle, n is the density of the element from which the spectra arise (e. g. Si), and I are the measured spectral weights of either the bulk material or the surface layer of interest.

However, if the thin layer of interest is buried under multiple top layers (e. g. EuO and a capping), we have to extend the derivation of eq. (3.12) in order to obtain a model for a three-layer system: this includes intensities of a substrate, a thin buried reaction layer, and accounts for the exponential damping of the photoelectrons by top layers. First, we consider the photoelectron intensities I of the substrate (sub) and a possible reaction layer (rl) as depicted in

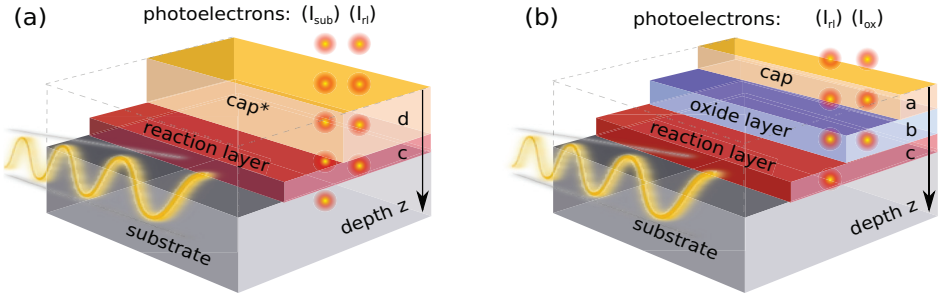

Figure 3.19.: HAXPES probe of a buried interface. The photoelectrons from either the substrate element are evaluated (a), or from an element of the tunnel barrier (b).

Fig. 3.19a,

$$I_{\mathrm{rl}}(c,d,\lambda) = e^{-\frac{d}{\lambda_{\mathrm{cap}}\cos\alpha}} \int_{d}^{d+c} e^{-\frac{x}{\lambda_{\mathrm{rl}}\cos\alpha}}\, dz, \text{ and} \tag{3.13}$$

$$I_{\mathrm{sub}}(c,d,\lambda) = e^{-\frac{d+c}{\lambda_{\mathrm{cap}}\cos\alpha}} \int_{d+c}^{\infty} e^{-\frac{x}{\lambda_{\mathrm{sub}}\cos\alpha}}\, dz. \tag{3.14}$$

In the next step, we express the fraction of spectral contribution of the reaction layer f_{rl} with respect to the bulk intensity. Here, the measured intensities I have to be normalized by λ and the density n of contributing atoms in the particular layer,

$$\frac{I_{\mathrm{rl}}(c,d,\lambda)}{I_{\mathrm{sub}}(c,d,\lambda)} \overset{\mathrm{calc}}{=} f_{\mathrm{rl}} \overset{\mathrm{meas}}{=} \frac{I_{\mathrm{rl}}}{I_{\mathrm{sub}}} \cdot \frac{\lambda_{\mathrm{sub}} n_{\mathrm{sub}}}{\lambda_{\mathrm{rl}} n_{\mathrm{rl}}}. \tag{3.15}$$

This equation (3.15) contains the thickness of the buried reaction layer c. Because it is not analytically solvable, a Taylor expansion of c to the 2nd order is applied which lets c be expressed as

$$\begin{aligned} c = {} & \frac{\lambda_{\mathrm{rl}}\lambda_{\mathrm{cap}^*}\lambda_{\mathrm{sub}}\cos\alpha}{\lambda_{\mathrm{sub}}\lambda_{\mathrm{cap}^*} - 2\lambda_{\mathrm{sub}}\lambda_{\mathrm{rl}} - 2\lambda_{\mathrm{rl}}\lambda_{\mathrm{cap}^*}} + \frac{e^{\frac{d}{\lambda_{\mathrm{rl}}\cos\alpha}}\lambda_{\mathrm{sub}}\cos\alpha\sqrt{\lambda_{\mathrm{rl}}\lambda_{\mathrm{cap}^*}}}{\lambda_{\mathrm{sub}}\lambda_{\mathrm{cap}^*} - 2\lambda_{\mathrm{sub}}\lambda_{\mathrm{rl}} - 2\lambda_{\mathrm{rl}}\lambda_{\mathrm{cap}^*}} \cdot \\ & \sqrt{\frac{2f_{\mathrm{rl}}\lambda_{\mathrm{cap}^*}\lambda_{\mathrm{sub}}e^{\frac{d}{\lambda_{\mathrm{rl}}\cos\alpha}} - 4f_{\mathrm{rl}}\lambda_{\mathrm{rl}}\lambda_{\mathrm{sub}}e^{\frac{d}{\lambda_{\mathrm{rl}}\cos\alpha}} - 4f_{\mathrm{rl}}\lambda_{\mathrm{rl}}\lambda_{\mathrm{cap}^*}e^{\frac{d}{\lambda_{\mathrm{rl}}\cos\alpha}} - \lambda_{\mathrm{rl}}\lambda_{\mathrm{cap}^*}e^{\frac{d}{\lambda_{\mathrm{sub}}\cos\alpha}}}{-e^{\frac{d}{\lambda_{\mathrm{sub}}\cos\alpha}}\left(e^{\frac{d}{\lambda_{\mathrm{rl}}\cos\alpha}}\right)^2}}. \end{aligned} \tag{3.16}$$

In order to determine the thickness of possible reaction layers of EuO on a silicon surface (SiO_x or $EuSi_2$), this expression is applied to Si 1s or Si 2p HAXPES spectra of EuO/Si heterostructures investigated in this work.

A consistent chemical characterization of the reaction layer at the functional EuO/Si interface can be achieved by the additional evaluation of HAXPES spectra from the magnetic oxide layer in direct contact with the Si substrate. Here, the photoelectrons from the bottom layer in the EuO oxide (ox) layer carry information about the electronic structure of a possible reaction layer (rl). Hence, the HAXPES intensities are modeled according to Fig. 3.19b as

$$I_{\mathrm{rl}}(a,b,c,\lambda) = e^{-\frac{a+b}{\lambda_{\mathrm{cap}^*}\cos\alpha}} \int_{a+b}^{a+b+c} e^{-\frac{x}{\lambda_{\mathrm{rl}}\cos\alpha}}\, dz, \text{ and} \tag{3.17}$$

$$I_{\mathrm{ox}}(a,b,\lambda) = e^{-\frac{a}{\lambda_{\mathrm{cap}}\cos\alpha}} \int_{a}^{a+b} e^{-\frac{x}{\lambda_{\mathrm{ox}}\cos\alpha}}\, dz. \tag{3.18}$$

The measured photoelectron spectra have to be normalized (similar to eq. (3.15)), and this fraction is compared with the modeled fraction, so that $\frac{I_{\mathrm{rl}}(a,b,c,\lambda)}{I_{\mathrm{ox}}(a,b,\lambda)} \overset{\mathrm{calc}}{=} f_{\mathrm{rl}} \overset{\mathrm{meas}}{=} \frac{I_{\mathrm{rl}}}{I_{\mathrm{ox}}} \cdot \frac{\lambda_{\mathrm{ox}} n_{\mathrm{ox}}}{\lambda_{\mathrm{rl}} n_{\mathrm{rl}}}$ can be solved analytically to extract the thickness c of the reaction layer as

$$\begin{aligned} c = {} & -\lambda_{\mathrm{rl}} \ln\left(f_{\mathrm{rl}}\frac{\lambda_{\mathrm{ox}}}{\lambda_{\mathrm{rl}}} e^{-\frac{a\lambda_{\mathrm{ox}} + a\lambda_{\mathrm{cap}} + b\lambda_{\mathrm{cap}}}{\lambda_{\mathrm{cap}}\lambda_{\mathrm{ox}}\cos\alpha}} + e^{-\frac{(a+b)\left(\lambda_{\mathrm{cap}^*} + \lambda_{\mathrm{rl}}\right)}{\lambda_{\mathrm{rl}}\lambda_{\mathrm{cap}^*}\cos\alpha}} - f_{\mathrm{rl}}\frac{\lambda_{\mathrm{ox}}}{\lambda_{\mathrm{rl}}} e^{-\frac{a\left(\lambda_{\mathrm{ox}} + \lambda_{\mathrm{cap}}\right)}{\lambda_{\mathrm{cap}}\lambda_{\mathrm{ox}}\cos\alpha}} \right) \cdot \cos\alpha \\ & + \frac{a\lambda_{\mathrm{rl}} + b\lambda_{\mathrm{rl}} + a\lambda_{\mathrm{cap}^*} + b\lambda_{\mathrm{cap}^*}}{-\lambda_{\mathrm{cap}^*}}. \end{aligned} \tag{3.19}$$

This expression is applied to determine the thickness of a possible reaction layer in EuO/Si heterostructures (e. g. $EuSi_2$) by the evaluation of Eu core-level spectra by HAXPES in this work.

Choosing the excitation energy and a background treatment

In the experiment, the excitation energy should be selected in a way to optimally investigate the buried interface of the EuO/Si heterostructures. In order to limit the information depth of Si photoemission to the top layer of the Si substrate, a reduced excitation energy is applied (e. g. the beamline minimum of the HAXPES endstation), while a high photon energy ($h\nu \geqslant 4$ keV) is chosen to fully record the photoemission of buried Eu atoms at the bottom of the EuO slab.

Inelastic processes of photoelectrons in the solid generate secondary electrons and thereby generate a broad background intensity. Only photoelectrons carry the initial state information which are not inelastically scattered. In order to evaluate sharp peaks of unscattered photoelectrons quantitatively, it is necessary to define and subtract a realistic background of inelastically scattered photoelectrons. Therefore, we use the approach of Tougaard (1988) in this thesis, to simulate the inelastic background of secondary electrons, which is best suitable for inelastic backgrounds of rare earth compounds.[141–143]

3.4.5. Hard X-ray circular magnetic dichroism in photoemission

Magnetic circular dichroism using hard X-ray photoemission spectroscopy (MCD-PE) combines the element-selective sensitivity with a magnetic contrast (intra-atomic exchange interactions: MCD) and a largely selective information depth up to ~20 nm. Hence, MCD-PE is perfectly suited to probe buried interfaces of ultrathin magnetic layers.

If a core-level shows an unequal population for every M quantum number, and the solid has magnetic order, then the magnetic circular dichroism (MCD) effect can occur.* The photoemission variant of MCD is attractive, because it does not involve a spin-polarization analysis of the photoelectrons, but only a measurement of their intensity. Unlike X-ray absorption experiments, photoemission spectroscopy is usually (at least partially) constrained to certain emission angles. The geometry of an MCD experiment in photoemission is completely described by four vectors,

$$\{\mathbf{q}, \mathbf{M}, \mathbf{k}^{e^-}, \mathbf{n}\}, \tag{3.20}$$

where $\mathbf{q}$ and $\mathbf{M}$ are the magnetic directions of the circularly polarized light and the sample, respectively. $\mathbf{k}^{e^-}$ is the photoelectron wave vector and $\mathbf{n}$ denotes the surface normal. The question, whether an MCD asymmetry in photoemission is observable at all, is answered by a rule given by Feder and Henk (1996):[144]

> MCD in photoemission can exist, if there is no space-symmetry operation which only reverses the magnetization $\mathbf{M}$ but leaves the system unchanged otherwise.

A discussion on forbidden geometries in order to observe MCD in photoemission is given in Starke (2000),[105] it comes out that only normal incidence combined with normal emission

*for an introduction of the MCD effect, please see Ch. 2.5.

does not fulfill the above-mentioned rule. We remark moreover, that the MCD amplitude depends on the direction of the $\mathbf{k}^{e^-}$ vector, for this we refer to literature.[145] Here, we focus on the geometry used in this thesis: the electron wave vector $\mathbf{k}^{e^-}$ is in 10° off-normal emission, and the axial vector of the light polarization $\mathbf{q}$ is either parallel or antiparallel to the in-plane sample magnetization $\mathbf{M}$. In this setup, every symmetry operation (i. e. rotation of the sample by the $\mathbf{n}$-axis or mirroring by planes normal to the surface) which changes $\mathbf{M}$ also alters $\mathbf{k}^{e^-}$. Thus, the rule of Feder allows one to observe the MCD effect in photoemission.

In a photoemission spectrum including MCD, the intensity of a peak changes when the polarization of the incoming light is changed from left-circularly polarized light (LCP) to right-circularly polarized light (RCP), or as an alternative the magnetization of the sample is reversed. The MCD asymmetry is defined as

$$\mathrm{MCD} \equiv \frac{I(\sigma^+, \mathbf{M}) - I(\sigma^-, \mathbf{M})}{I(\sigma^+, \mathbf{M}) + I(\sigma^-, \mathbf{M})} = \frac{I(\sigma^+, +\mathbf{M}) - I(\sigma^+, -\mathbf{M})}{I(\sigma^+, +\mathbf{M}) + I(\sigma^+, -\mathbf{M})}. \tag{3.21}$$

The MCD photoemission experiment is conducted with hard X-rays at the HAXPES beamline P09 at the high brilliance storage ring PETRA III (see Ch. 3.4.3). In practice, a constant helicity of the incoming light (e. g. σ^+) is used, and to obtain the MCD asymmetry in eq. (3.21), the magnetization of the thin film is altered to be either parallel or antiparallel with respect to the $\mathbf{k}$ vector of the incoming light (see Figs. 3.20, and 3.16 on p. 51). This offers a high experimental consistency: neither a modification of the X-ray beam (by changing the diamond phase retarder) nor a rotation of the sample position (by 180°) is needed in order to reverse the MCD effect.

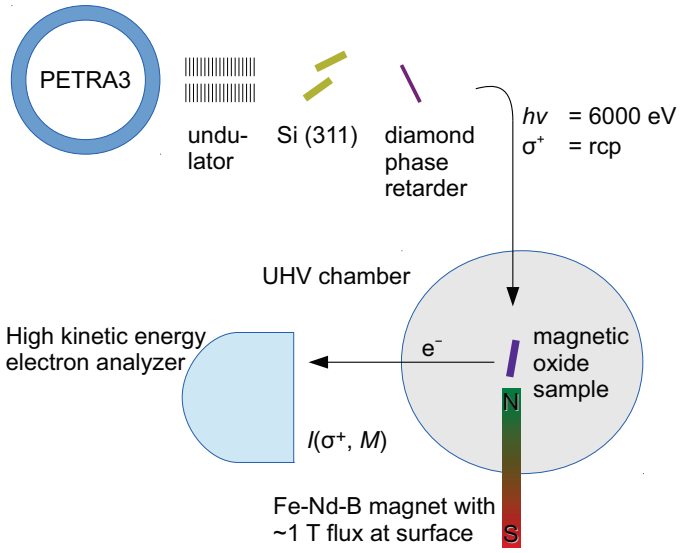

Figure 3.20.: Geometrical setup for the HAXPES measurement of the magnetic circular dichroism effect (MCD).

4. Results I: Single-crystalline epitaxial EuO thin films on cubic oxides

> Researchers engineering oxide heterostructures and layer-by-layer film growers [...] can dramatically accelerate the rate at which new functional oxides are discovered, enabling innovative materials for spintronics or new energy technologies.
>
> *(after J. Chakhalian, 2012[146])*

A key prerequisite of functionalizing magnetic oxides as spin filter materials is a high-quality stoichiometric synthesis, which ensures a bulk-like ferromagnetism.
In this chapter, we discuss the synthesis of ultrathin EuO and investigate the impact of different cubic substrates on the electronic properties of epitaxial EuO thin films. First, we investigate a system with perfect lattice match, EuO on yttria-stabilized zirconia (YSZ). This system is perfectly suited to study and optimize the growth of single-crystalline EuO thin films, since it allows for coherent growth. Second, we characterize electron beam-treated YSZ with unaltered crystal structure and a certain electrical conductivity. This "conductive YSZ" substrate opens up the possibility to perform electron diffraction and photoelectron emission experiments on otherwise insulating oxides.
Aiming towards ultrathin EuO films in the nanometer regime for application as tunnel barriers, we investigate the magnetic behavior of single-crystalline epitaxial EuO from bulk thickness down to one nanometer. We confirm the stoichiometry and chemical cleanliness of EuO on conductive YSZ, and investigate the depth-dependent chemical homogeneity by high resolution HAXPES core-level spectra. Finally, taking advantage of the MCD in photoemission, we investigate the spin-dependent electronic structure of ultrathin magnetic EuO films.
Tuning the lateral lattice parameter of thin EuO films is not only of interest from the synthesis point of view, but also fundamentally changes the magnetic behavior of the EuO film under the tensile or compressive force of the underlying lattice. We discuss epitaxially grown EuO on $LaAlO_3$ (100) which provides a moderate tensile strain, and investigate magnetic properties by SQUID and hard X-ray magnetic circular dichroism. Finally, we investigate a large compressive strain in the heteroepitaxial system EuO on MgO (100).

Key parameters for stoichiometric single-crystalline EuO growth on oxides

First, we discuss a route how to stabilize thin films of the metastable magnetic oxide EuO by reactive MBE. Stoichiometric EuO is divalent and formed with comparable thermodynamic probability as the Eu oxides with higher valency, as recognized from the Ellingham diagram* depicted in Fig. 4.1a. The Gibbs free energies of all possible Eu oxide phases are located left to an intersection (out of range) with the gas line of $p(O_2) = 1 \times 10^{-9}$ mbar (dashed line) which reveals that the oxidation reaction of Eu + O_2 is favored and stable for nearly all temperatures and oxygen pressures. Since the mixed-valent Eu_3O_4 and the trivalent native Eu_2O_3 compounds have complex non-cubic structures and are not ferromagnetic, they

*The thermodynamic potentials and the Ellingham diagram are introduced in Ch. 2.1.

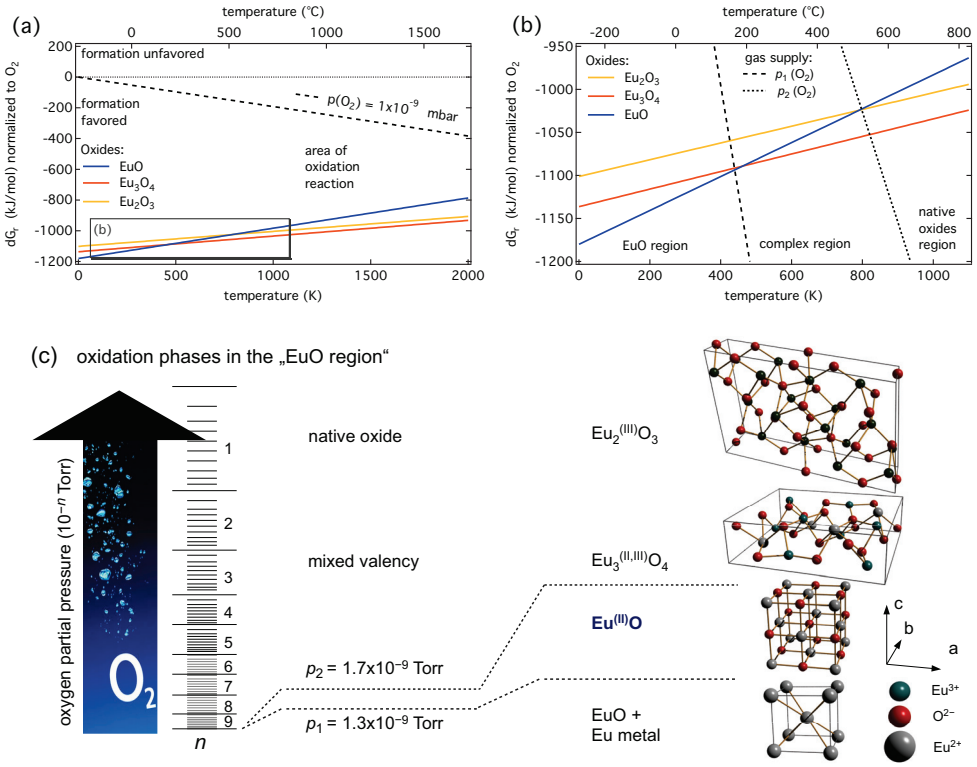

Figure 4.1.: Ellingham diagram for Eu oxides and realistic ranges of the oxygen partial pressure. Eu oxide phases are formed under any oxygen partial pressure (*a*). A zoom into the temperature range of EuO synthesis (*b*) uncovers intersections between EuO and higher oxides. They define three regions of different thermodynamic stability of the Eu oxides. The region borders coincide with certain oxygen partial pressures (dashed lines). A realistic range of $p(O_2)$ and resulting Eu oxide phases are sketched in (*c*).

are undesired phases. A zoom into the Ellingham diagram in Fig. 4.1b elucidates the changing probabilities of formation for the particular Eu oxides in different temperature regions. While at $T_S \leqslant 200\,°C$ divalent EuO is most favorable ("EuO region"), there is a "complex region" between 200 °C and 500 °C in which all three Eu oxide phases coexist with varying thermodynamic stability. Above $T_S = 550\,°C$, Eu oxides comprising trivalent ions are favorably formed. Since high crystalline quality and epitaxy is only guaranteed at elevated temperatures of EuO synthesis,[23,32] our growth parameters of EuO are situated in the "complex region" in Fig. 4.1b. Gas lines defining the borders of the complex region have experimentally been evaluated to correspond both to the 10^{-9} mbar regime, as depicted in Fig. 4.1c. Hence, the EuO synthesis must take place under ultra-high vacuum. We successfully established an *in situ* synthesis of stoichiometric EuO by reactive MBE and present the procedure in the following.

Table 4.1.: Parameters for stoichiometric EuO on cubic substrates by Oxide MBE. UHV conditions are required and gas nozzles are employed. YSZ provides oxygen to the initial EuO layers.

substrate	EuO growth initiation	T_S	flux density of Eu	partial pressure O_2	EuO growth termination
YSZ (9%)	30–60 s Eu	350–450 °C	2.77×10^{13} Eu/cm^2 s	$1.3–1.7 \times 10^{-9}$ Torr	10–60 s Eu
cYSZ, LAO, MgO	0–30 s Eu	350–450 °C	2.77×10^{13} Eu/cm^2 s	$1.3–1.7 \times 10^{-9}$ Torr	10–60 s Eu

Substrates of cubic oxides (YSZ, LAO, or MgO) are cleaned in iso-propanol, followed by an *in situ* annealing step at elevated temperature (T_S = 600 °C) under O_2 supply. In this way, we obtain atomically smooth surfaces, for which RHEED pattern confirm the expected cubic (100) surface structure. A consistent application of the Eu distillation condition,[32,45] in which at elevated temperature any excess Eu metal is evaporated, ensures a stoichiometric composition of the EuO thin film during MBE synthesis. For this approach, Eu metal (purity 99.99%) is e-beam evaporated with a constant flux density ($\Phi_{Eu} = 2.77 \times 10^{13}$ Eu/cm^2 s) under ultra-high vacuum ($p_{base} \leqslant 1 \times 10^{-10}$ mbar) onto the surface of the heated oxide substrate (T_S = 350–450 °C).

A limited supply of molecular oxygen (purity 99.999%), which is leaked into the main deposition chamber via specialized oxygen distribution nozzles (described in Sec. 3.3 on p. 42), initiates the reaction to EuO, this approach is referred to as "adsorption-controlled deposition".[25] Stoichiometric EuO is obtained by the supply of O_2 in the range $1.3–1.7 \times 10^{-9}$ Torr. In order to obtain chemically well-defined interfaces, before and after the adsorption-controlled deposition of EuO, we supply excess Eu in the monolayer regime as a seed for epitaxial EuO and as an oxidation protection after O_2 supply has been terminated.

Finally, we apply an air-protective metallic cap, prefereably Al or Si.

4.1. Coherent growth: EuO on YSZ (100)

> The difficulty lies in obtaining high quality, stoichiometric, ultrathin EuO films.
>
> *(J. S. Moodera on EuO, 2007)*

In order to provide high-quality ultrathin EuO films without any strain or chemical intermixing, first we stabilize EuO on yttria-stabilized zirconia (YSZ), as discussed in the following.*

In response to the extremely narrow parameter regime in which the stoichiometric phase of EuO can be obtained via reactive MBE, the O_2 supply has to be under a meticulous control. In Fig. 4.2, we investigate EuO thin films synthesized in an O_2 pressure range around the stoichiometric EuO phase by electron diffraction and SQUID magnetometry. All oxygen partial pressures lie in the lower 10^{-9} Torr range, coinciding with the stability region for all Eu oxide phases in the Ellingham diagram (Fig. 4.1 on p. 58).

Overoxidized $Eu_{1-x}O_x$ phases form next to EuO, if 3×10^{-9} Torr oxygen partial pressure is supplied (Fig. 4.2a). Here, the $Eu_{1-x}O_x$ film is insulating as observed in LEED, and the magnetization exhibits mainly paramagnetic contributions of Eu_2O_3 which are identified by a tail below 5 K.[147–149]

Stoichiometric EuO. A slight reduction of the oxygen partial pressure to values below 1.7×10^{-9} Torr yields stoichiometric EuO, which exhibits the expected *fcc* rocksalt lattice and magnetization curves with a Brillouin shape as expected for a Heisenberg ferromagnet (Fig. 4.2b–d). We identify this oxygen partial pressure (1.7×10^{-9} Torr) as the limit, at which stoichiometric EuO can be obtained (Fig. 4.2b). No excess Eu for the Eu distillation condition is left in order to ensure the EuO stoichiometry. This is reflected by the formation of a small fraction of higher oxidized $Eu_{1-x}O_x$ phases in the RHEED pattern of Fig. 4.2b, as well as in the small paramagnetic feature of the magnetic moment at $T \to 0$ K. In the range of mainly stoichiometric EuO and Eu distillation growth, we establish the growth at 1.5×10^{-9} Torr for stoichiometric EuO with a perfect *fcc* structure and a magnetization curve identical with a Brillouin function. Thus, the oxygen supply as presented in Fig. 4.2c is considered as the optimum for stoichiometric EuO.

Europium-rich EuO_{1-x}. A further reduction of the oxygen partial pressure also yields mainly stoichiometric EuO (Fig. 4.2d). We observe even an improved surface crystal structure, as indicated by the LEED pattern, probably due to the high mobility of the excess Eu during Eu-rich growth. Nonetheless, this composition does not match the exact stoichiometry of EuO: in the SQUID characterization, we observe a paramagnetic feature near $T = 0$ K and a magnetization tail extending up to $T_C(EuO_{1-x}) = 150$ K – both indications of metallic Eu contributions in the EuO thin film.[15,23]

*A summary of substrates suited for epitaxial integration with EuO, including strain, is found in Tab. A.2 on p. 128.

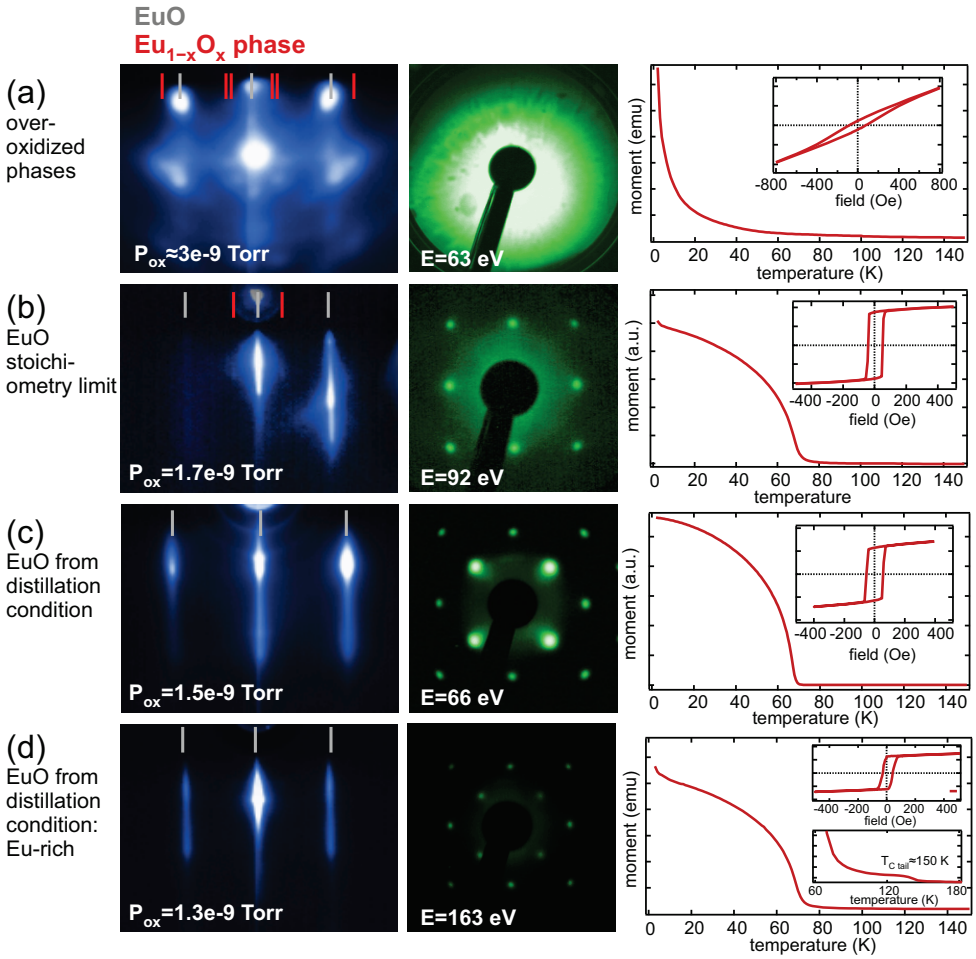

Figure 4.2.: Electron diffraction pattern for EuO thin films for different oxygen partial pressures during growth. From (*a*) to (*d*), the oxidation of EuO during synthesis is reduced, and RHEED (*blue*), LEED (*green*), and SQUID results display the effects of stoichiometry variation. The EuO films are synthesized on annealed YSZ (100) at T_S = 400 °C and are ~20 nm thick.

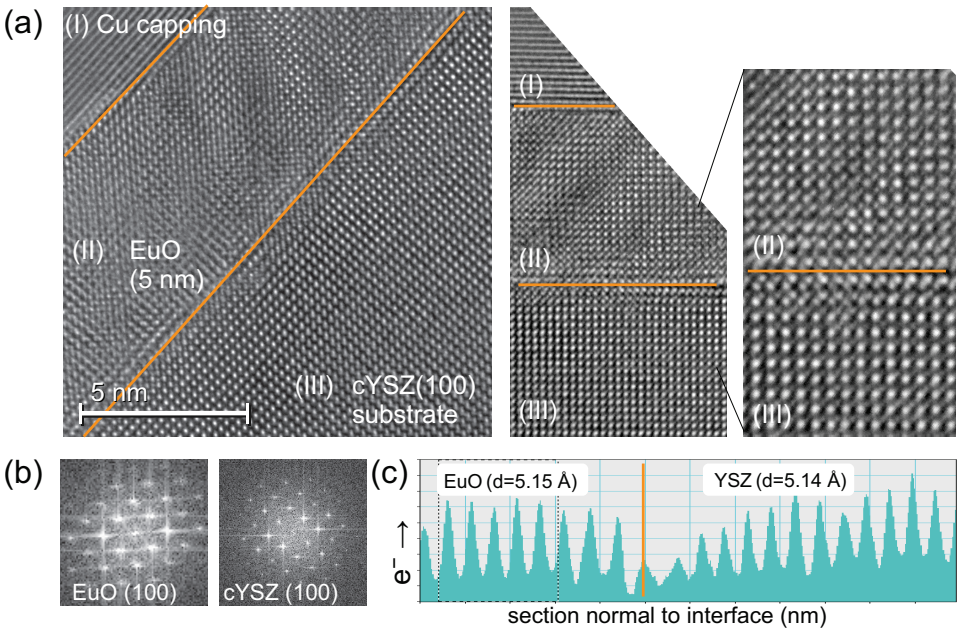

Figure 4.3.: Bulk and interface morphology of EuO on conductive YSZ (100) observed by transmission electron microscopy. (*a*) A region of the perpendicularly cut lamella of a Cu/EuO/cYSZ heterostructure. A magnification of the EuO/cYSZ interface is included in the right panel. In (*b*) fast Fourier transforms of the EuO film and the cYSZ substrate depict the reciprocal lattice. (*c*) shows the intensity profile of a section normal to the EuO/cYSZ interface which allows to determine the lattice parameter.

Next, we investigate the crystalline homogeneity of the magnetic oxide (5 nm EuO) and the structure of the EuO/cYSZ (100) interface.* High resolution electron transmission microscopy pictures (HR-TEM) of a representative Cu/EuO/YSZ(100) heterostructure are depicted in Fig. 4.3. Sharp interfaces between EuO and the YSZ substrate as well as between EuO and the metallic Cu capping are found in the entire heterostructure. We see no structural defects in the EuO magnetic oxide layer, and a clear *fcc* reciprocal lattice is found by a fast Fourier transformation of the electron micrograph. Finally, an intensity profile perpendicular to the EuO/YSZ interface reveals a homogeneous spacing of the EuO net planes which exhibit the same lattice parameter as the YSZ. This is a confirmation of the structural homogeneity of EuO in growth direction. In lateral direction (parallel to the interface), Eu sites of EuO match the YSZ cubic lattice sites, which is an evidence for cube-on-cube epitaxy. Remarkably, also the Cu/EuO (100) interface shows the lateral lattice planes in same directions. This may be a promising route for a future epitaxial integration of Cu with EuO (100).†

*This heterostructure uses already the conductive YSZ substrate (cYSZ), which permits one to use high-electron yield techniques without charging issues. This is discussed in the following section.

†Epitaxial EuO/Cu may be a promising system for coherent tunneling in the frame of symmetry band structures. See Ch. 2.3.3.

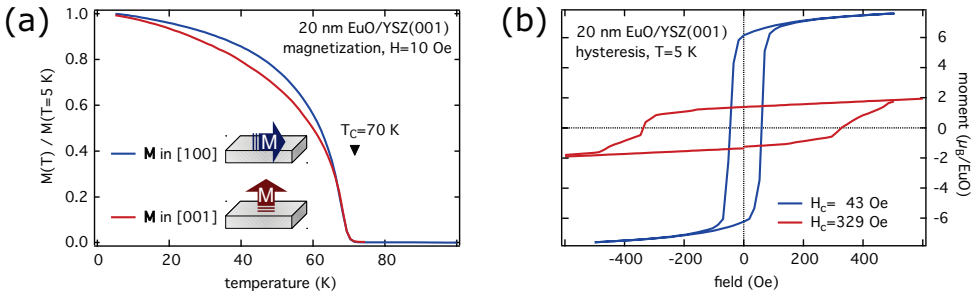

Figure 4.4.: Magnetic properties of a 20 nm single-crystalline EuO (100) film with M measured in-plane and out-of-plane. The measurement was conducted by B. Zijlstra.

All EuO lattice parameters agree well with bulk EuO. In conclusion, we confirm a seamless coherent growth of EuO on conductive YSZ (100) by HR-TEM.

A key property of EuO is its ferromagnetic behavior. In Fig. 4.4, the temperature dependent magnetization curves and the hysteresis curves are depicted for a 20 nm EuO thin film coherently grown on YSZ (100). Both in-plane and out-of-plane magnetization curves follow the shape of a Brillouin function. A large difference is observed in the magnetic switching behavior: the coercive field for in-plane magnetic switching along the [100] direction shows a low value of $H_c = 43$ Oe which is indicative for a good crystallinity of EuO. For the out-of-plane direction, in contrast, the coercive field exhibits an eight times larger value of $H_c = 329$ Oe, and the saturation magnetization cannot be reached. The reduced magnetization in out-of-plane direction can be explained by the significant fraction of interface and surface layers of EuO with reduced nearest neighbor coordination, as predicted by Schiller and Nolting (2001).*

Mainly three different anisotropy contributions determine the magnetic switching: crystalline anisotropy, shape anisotropy and pinning by defects. The crystalline anisotropy is weak in EuO, and the shape anisotropy is dominant. We distinguish between in-plane and out-of-plane anisotropy. A measure for the magnetic anisotropy is the anisotropy constant in first order K_1, expressed as[54]

$$K_1 = -1/2\, H_{an}\, \sigma_{sat}. \tag{4.1}$$

Here, H_{an} denotes the anisotropy field which is necessary to saturate the magnetic sample to the saturation moment σ_{sat} in the magnetic easy direction, to which H_{an} is parallel. For our single-crystalline EuO thin film, we determine the out-of-plane anisotropy as $K_1^{\perp}(\text{cryst. film}) = -0.851 \times 10^5$ erg/g. We compare this out-of-plane anisotropy with a polycrystalline EuO thin film ($d = 100$ nm) from literature,[150,151] for which $K_1^{\perp}(\text{poly. film}) = -9.3 \times 10^5$ erg/g was found. The large difference of magnetic anisotropy between polycrystalline and single-crystalline EuO thin films can be explained by magnetic pinning: while in polycrystalline EuO the pinning of magnetic moments due to crystalline defects is omnipresent, in single-crystalline EuO without defects, one would expect this pinning effect to vanish. Indeed, in single-crystalline EuO the shape anisotropy is smaller by a factor of ten than for the polycrystalline EuO film.

*For EuO thin film effects, please see Fig. 2.8 on p. 15.

Now, we ask ourselves, which mechanisms increase the coercive field in perpendicular direction of our single-crystalline EuO thin film. One microscopic origin may be anisotropy of the magnetic Eu $4f$ orbitals, which have recently been shown to be *not* spherically symmetric and thus provide a working point for local pinning in EuO.[152] During layer-by-layer growth of EuO, the structural neighborhood parallel vs. perpendicular (i. e. in surface normal) to growth direction may be slightly different, in particular due to the initially and finally deposited Eu seed layers. These in-plane antiferromagnetic Eu environments may lead to stronger magnetic pinning. This would yield a larger out-of-plane anisotropy.

We summarize, that the crystal quality of EuO plays a crucial role in magnetic switching behavior, such that in a single-crystalline thin film the out-of-plane anisotropy is approximately ten times smaller than for a polycrystalline sample. The out-of-plane saturation moment cannot be reached with small external field. For the application side, the desired soft magnetic switching and easily reached saturation magnetization only show up when magnetic fields are applied in the surface plane (e. g. in [100] direction) of the single-crystalline EuO thin film.

4.1.1. Thickness-dependent magnetic properties of EuO thin films

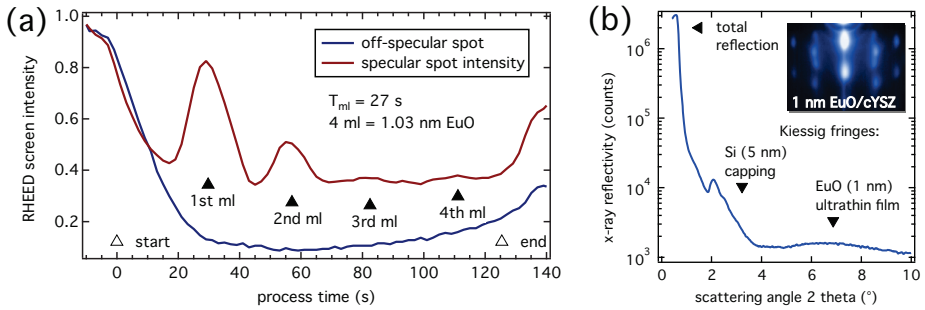

Figure 4.5.: Electron and X-ray diffraction of a 1 nm-thin EuO film. RHEED oscillations are a measure for completed atomically smooth net planes (red in (*a*)), the off-specular intensity indicates begin and end of synthesis. XRR (*b*) shows an EuO Kiessig fringe corresponding to 1.25 nm EuO.

The investigation and optimization of single-crystalline EuO in the thickness regime of few nanometers is essential as a reference for fundamental studies regarding interfacial strain effects* and for EuO employed as ultrathin spin-functional tunnel barriers.† While bulk-like magnetic properties of thick single-crystalline EuO films ($d \geqslant 20$ nm) were confirmed in the last section, now we proceed towards growth and characterization of *ultrathin* EuO layers with the aim to provide the same single-crystalline quality. As an evidence for the successful growth of ultrathin EuO, RHEED oscillations and XRR Kiessig fringes identify four perpendicular net planes of EuO ($d_{\mathrm{EuO}} = 1.25$ nm) in Fig. 4.5. This means, single-crystalline EuO thin films ranging from one nanometer up to several tens of nanometers (bulk) are available by our Oxide-MBE synthesis with persistently high structural quality.

*as discussed in upcoming chapters 4.2 and 4.3 of epitaxial EuO on the cubic oxides $LaAlO_3$ and MgO.
†For the integration of EuO on Si, please see Ch. 5.

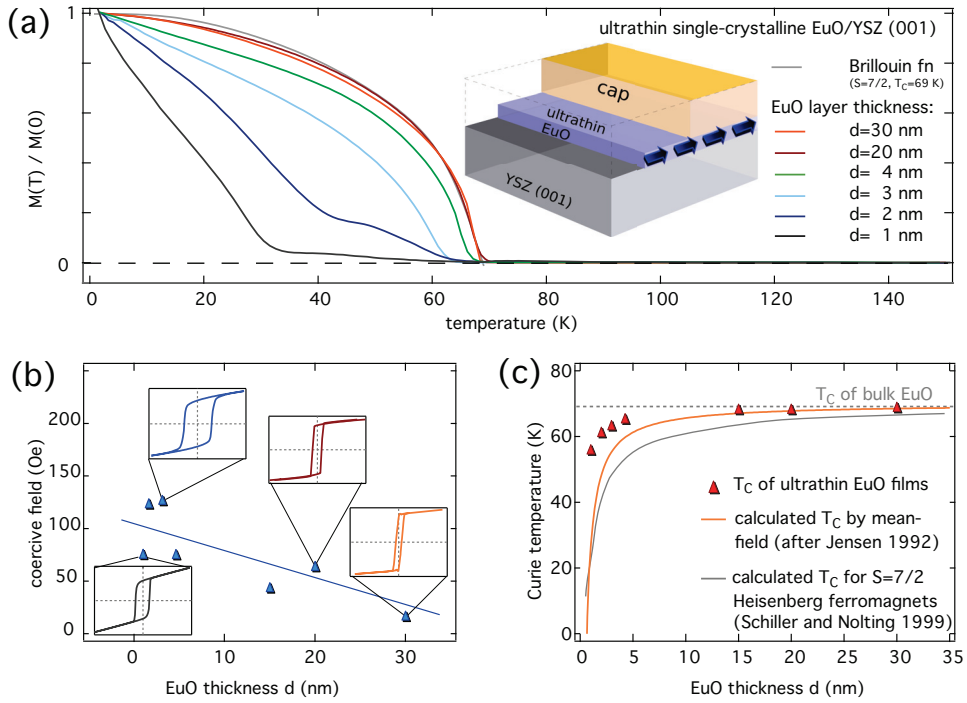

Figure 4.6.: Thickness dependent magnetic properties in single-crystalline EuO thin films. (*a*) depicts the in-plane magnetization under applied saturation field. (*b*) shows the coercive field for every thickness of EuO, with the original hysteresis loop as insets. (*c*) summarizes the Curie temperature for every EuO thickness, together with model predictions.

Starting with bulk-like EuO, for the EuO thickness d = 20–30 nm no change in the magnetization curves is observable, as depicted in Fig. 4.6, and a bulk-like saturation and Curie temperature is observed. If the EuO thickness is reduced, the coercive field increases from an optimum value of 23 Oe of the bulk-like EuO film up to ~130 Oe for an ultrathin (d = 2 nm) EuO film (Fig. 4.6b). This variation of coercivity with thickness also has been found in Suran et al. (1995) for soft ferromagnetic thin films.[153] A reduction of the EuO thickness to d = 15 nm does not affect the Curie temperature, but the magnetization curve is altered from the shape of a Brillouin function to a reduced magnetization (Fig. 4.6a). The field dependence changes towards a mixture of ferromagnetic (rectangular-shaped hysteresis) and paramagnetic (linear response) behavior. This trend is continued in the course of a further reduction of EuO thickness down to d = 2 nm. Bulk-near magnetic ordering temperatures (T_C = 64 K) are maintained down to d = 2 nm and the saturation magnetization is still approximately half the bulk EuO value for this thickness. Finally for 1 nm EuO, the magnetization curve strongly deviates from the Brillouin shape and we estimate T_C as 18 K. In this case, the remanence is near zero and the field dependence is mainly paramagnetic.

We conclude, that the threshold for establishing sizable ferromagnetic properties of coher-

ently grown single-crystalline EuO lies between one and two nanometers film thickness. In particular, obtaining a bulk-like T_C down to 2 nm is remarkable, and more robust than for polycrystalline EuO films.[48] This thickness dependence* can be described by a mean field model after Jensen et al. (1992) or the Heisenberg model by Schiller and Nolting (1999) with no need for corrections due to interface intermixing as presented in Fig. 4.6c.[154,155]

4.1.2. Preparation on conductive YSZ substrates

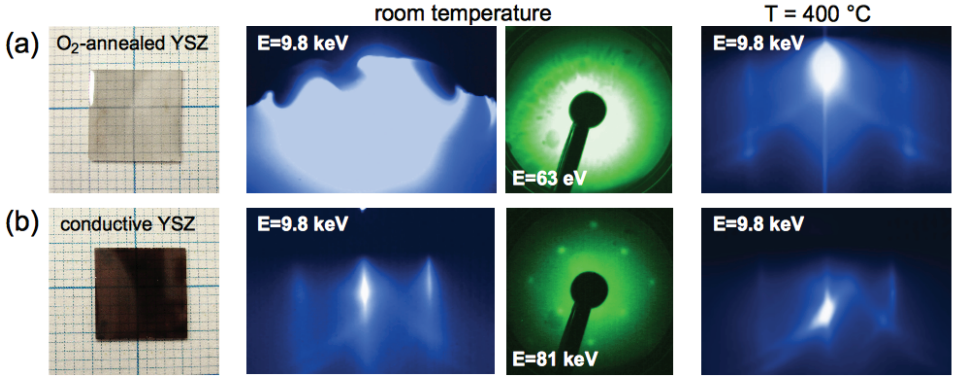

Figure 4.7.: Conductive YSZ characterized by high- and low-energy electron diffraction. LEED (green) is only observable after an e-beam treatment of YSZ.

Coherent growth of EuO on YSZ (100) provides the advantages of single-crystalline EuO thin films with bulk-like magnetic properties. However, any investigation based on high-energy electrons – either by electron scattering or electron emission techniques – is usually hampered by charging of YSZ, as depicted in Fig. 4.7a. Since magnetic oxides like EuO on top of YSZ are also insulating, there arises an experimental need for a certain electrical conductivity in YSZ (100) substrates.

The physical origin of a finite electrical conduction in otherwise highly insulating YSZ is usually described by ionic conduction in literature,[156] however this effect is working only at elevated temperatures (usually above $T = 500$ °C). For a large concentration of oxygen vacancies, electronic defect bands may form which allow for a metallic conduction.[157] This conductive effect of metallic donor bands is particularly predicted for Ti-doped YSZ,[158] which renders Ti-doped YSZ promising as a future substrate which might combine electrical contact with a coherent seed for epitaxial EuO thin films. In the frame of this work, however, doped YSZ (100) substrates were not available, and we developed a treatment with the aim to increase the electronic conduction in otherwise insulating YSZ.

Conductive YSZ (we refer to is as cYSZ) with a large oxygen deficiency is created as a conductive substrate for EuO heterostructures. For this, we bombard a cleaned and oxygen-annealed YSZ substrate with hot electrons from a tungsten filament with an energy of $U = 1000$ eV

*We remark, that our experimental investigation of the Curie temperature does not provide a highly resolved curve from which we can judge a best fitting model. The included models serve as a guide for the eye.

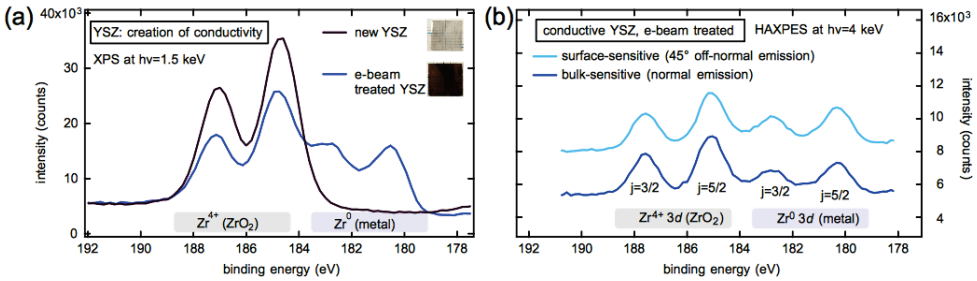

Figure 4.8.: Metallicity in e-beam treated YSZ observed by HAXPES. The Zr 3*d* doublet is best suited for a determination of metallic Zr in ZrO_2 (=oxygen vacancies).

from 5 mm distance onto the back side of the substrate. In this way, a low electron emission current of 10–20 mA is persistently applied for two hours. The result is a black YSZ substrate, indicative of a reflective behavior typical for conductive oxides. A successive three hours annealing step under UHV *without* oxygen supply leads to an atomically smooth *fcc* surface possible, which can easily be verified by electron diffraction, as depicted in Fig. 4.7b.

Photoemission studies (XPS and HAXPES) of untreated and electron-bombarded YSZ substrates (cYSZ) reveal a significant change in the oxidation state of the zirconia compound. In Fig. 4.8a, the Zr 3*d* photoemission doublet is compared for YSZ before and after the conductivity treatment. While in the untreated YSZ we identify only the chemically shifted Zr^{4+} oxidation states of ZrO_2, in cYSZ one third of the zirconium spectral weight has changed to Zr^0 indicating Zr metal. A depth-sensitive investigation by HAXPES (Fig. 4.8b) confirms the homogeneity of the metallicity within the cYSZ substrate for the accessible probing depth down to 20 nm.

Does the e-beam-treated cYSZ provide a surface quality comparable to untreated YSZ? During EuO growth on cYSZ, intensity oscillations of the RHEED specular spot are a direct proof of a layer-by-layer growth of MBE-deposited films, and they only appear, if structurally smooth and chemically clean substrates are used. In Fig. 4.9, persistent intensity oscillations

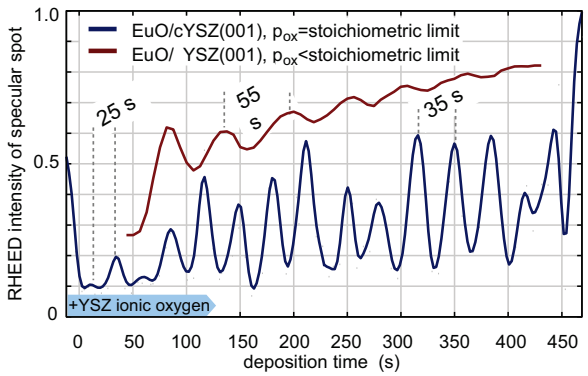

Figure 4.9.: Layer-by-layer growth of EuO on YSZ (100) and on cYSZ (100) observed by RHEED specular intensity. Every oscillation maximum represents one finished EuO monolayer of height 2.57 Å. The first 4–5 oscillations exhibit a different period due to the oxygen diffusion from the YSZ substrate (*blue curve*). The oscillation period of sustained growth depends on the oxygen partial pressure (*red* vs. *blue curve*).

Table 4.2.: Parameters set for creation of conductive YSZ by e-beam treatment.

substrate	surface pre-annealing	e^- treatment	post-annealing	possible techniques
YSZ (9%)	2 h in vacuo at 600 °C + 1×10^{-7} mbar O_2	3 h e-beam with U = 1000 eV, I_{em} = 10–20 mA	3 h in vacuo at T_S = 700 °C	RHEED, LEED, XPS, HAXPES, TEM, SEM,…

of a EuO thin film on cYSZ are observed. As zirconia substrates supply ionic oxygen through lattice diffusion in the first five monolayers of EuO growth,[16] the time period of one monolayer EuO is shorter in this initial phase. For cYSZ, however, every second oscillation in the initial stage of EuO growth shows a reduced intensity which we ascribe to the significantly reduced oxygen supply of the cYSZ underlayer. Moreover, if EuO is grown well below the stoichiometric limit in the Eu distillation condition, the RHEED oscillations are equidistant and homogeneously damped in time. If, however, the EuO growth is at the stoichiometric limit, the time period for one monolayer EuO is 36% shorter and the intensity of some oscillations is sensitive to manual re-adjustments of the Eu flux rate.

We conclude, that EuO can be synthesized on cYSZ (100) with comparable crystal quality as for insulating YSZ (100). This renders EuO/cYSZ heterostructures accessible to investigations using high-energy electrons, for example RHEED, TEM, or HAXPES.

4.1.3. Core-level spectra by hard X-ray photoemission spectroscopy of single-crystalline EuO thin films on cYSZ

After a successful substrate treatment, synthesis of the magnetic oxide, and control of structural properties, we now proceed with the investigation of the electronic structure of single-crystalline EuO thin films. The heterostructures under investigation are Si/EuO/cYSZ (100). Different thicknesses of the single-crystalline EuO layer are investigated: bulk-like 20 nm EuO, and 4 nm EuO as typical for a tunnel barrier, and also 1 nm EuO representing a quasi two-dimensional layer. The magnetic oxide EuO is buried under Si capping, and requires a probing technique with sufficiently large information depth. HAXPES reveals information about the entire EuO slab, as depicted Fig. 4.10. In the following, we present a study of selected core-level peaks of EuO, which are best-suited for analysis in this work.

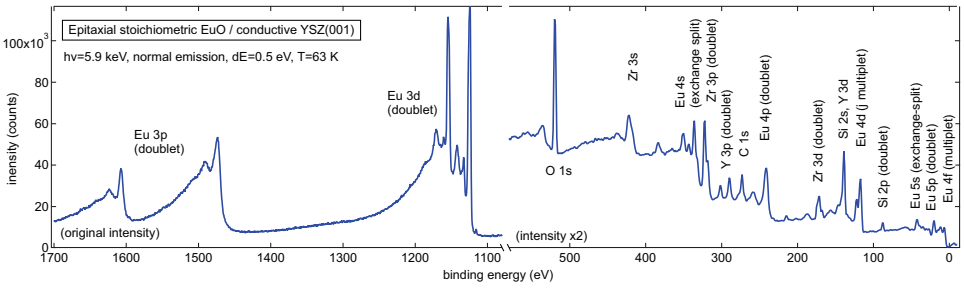

Figure 4.10.: Hard X-ray photoemission spectroscopy of EuO/cYSZ (100). All accessible core-levels of EuO, Si, and YSZ are are showing in a survey spectrum.

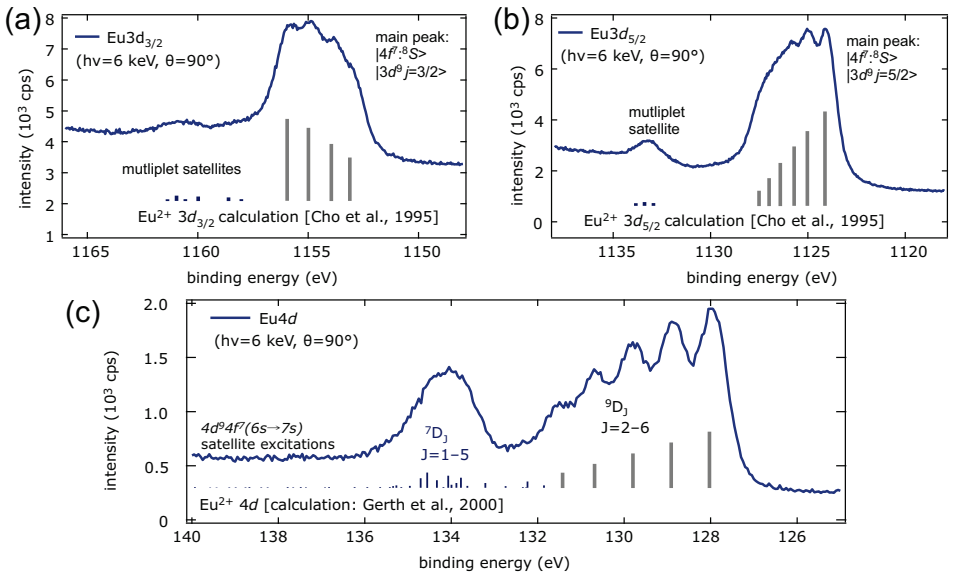

Figure 4.11.: Hard X-ray photoemission spectroscopy of 20 nm single-crystalline EuO/cYSZ (100). The Eu 3*d* in (*a*, *b*) and the Eu 4*d* (*c*) photoemission spectra are well-suited for an electronic structure analysis of EuO thin films. The calculated multiplet lines are taken from literature.[110,114]

With the largest photoionization cross-section and one of the best separated doublet structures among the Eu core-levels, according to the survey in Fig. 4.10, the Eu 3*d* photoemission is perfectly suited for a characterization regarding chemical character and electronic states of the EuO layer. The Eu 3*d* final state (Fig. 4.11a, b) shows $3d_{5/2}$ and $3d_{3/2}$ groups, separated by a large spin-orbit splitting of 29.2 eV, in agreement with literature.[159] The peak of low intensity in the center is assigned to collective excitations of Eu 3*d* photoelectrons in the Si layer, a so-called extrinsic plasmon with a kinetic energy loss of 17 eV.[90] For stoichiometric EuO, one main peak is observable in the Eu $3d_{5/2}$ and $3d_{3/2}$ groups which originates from the Eu^{2+} initial state (Fig. 4.11a, b).

The observed asymmetry in the line shapes is perfectly consistent with theoretical calculations of the divalent Eu 3*d* multiplet[110] which is described by the $\left|4f^7\text{:}\,{}^8S_{7/2}\right\rangle \left|3d^9\text{:}\, j=\frac{5}{2},\, j=\frac{3}{2}\right\rangle \left|\epsilon\ell\right\rangle$ final states, where $\epsilon\ell$ denotes the photoelectron. The multiplet structure of the final state has its origin in the core-hole interaction with the 4*f* open shell. A satellite peak in the high binding energy region of the $Eu^{2+}3d_{5/2}$ ($Eu^{2+}3d_{3/2}$) multiplet, which is separated by 7.8 eV (6.3 eV) from the main peak is also attributed to the $\left|3d^9\,4f^7\right\rangle$ final state multiplet.[111] Both energy splitting and intensity ratios compare well with previous reports on calculated and measured multiplet spectra of divalent Eu compounds.[110,159,160]

The Eu 4*d* core-levels are found at a relatively low binding energy of 126 eV and are therefore photoelectrons of high kinetic energy (Fig. 4.11c). The Eu 4*d* photoemission final states extend to the binding energy of 160 eV.[114,115] In this work, however, we focus on the two

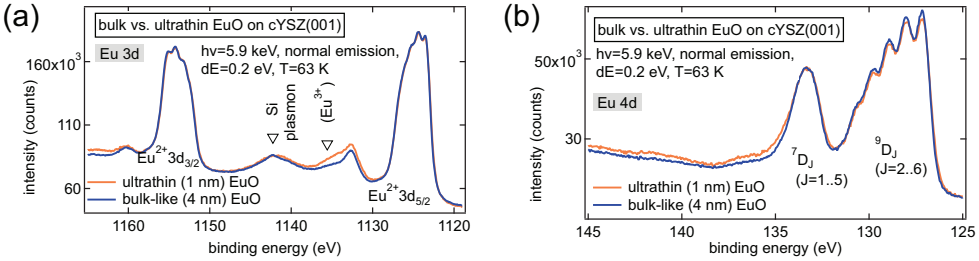

Figure 4.12.: HAXPES of ultrathin single-crystalline EuO/cYSZ (100) recorded at 63 K. Large cross-sections of Eu 3*d* and 4*d* levels in (*a*) and (*b*) permit one to resolve even small intensity changes in the multiplet structure.

peaks at low binding energy, as depicted in Fig. 4.11c. They resolve a complex multiplet structure. The 4*d* orbital shares the same principal quantum number with the 4*f* valence level which involves a strong *d*–*f* exchange interaction due to radial overlap. Therefore, we cannot separate 4*d* spectra into $4d_{J=3/2}$ and $4d_{J=5/2}$ components, but rather to a $J = L - S$ multiplet splitting, and assign the peaks to the ^7D_J and ^9D_J multiplets, respectively.[114,115] Eu 4*d* final states are well described by the intermediate coupling scheme (**LSJ**) in which both spin-orbit and exchange splitting are treated as perturbations.[112] This leads to an intensity ratio of about 1:3 for the septet to the nonet peaks[161] of the final state configuration $\left|4f^7{:}\,^8S_{7/2}\right\rangle\left|4d^9{:}\,^9D_J, {}^7D_J\right\rangle\left|\epsilon\ell\right\rangle$. Once more, we observe a clear Eu^{2+} valency in EuO, indicative for the integral divalent state of EuO.

In the HAXPES spectrum (Fig. 4.11c), the fine structure of the ^7D final state is not resolved, whereas the J = 2–6 components in the ^9D state are easily identified. Energy losses due to the excitation of the 5*p* or the 4*f* electrons during photoemission are predicted to lead to satellites at 5–10 eV higher binding energy from the main line.[162]. Furthermore, smaller contributions of the ^7D final state exist at up to 20 eV higher binding energy than the ^7D main peak.[114] However, these higher binding energy features overlap within intensities of an extrinsic plasmon of silicon and the background of inelastic electron scattering.

In a further step, we investigate the two core-levels from *ultrathin* single-crystalline EuO, and compare a bulk-like EuO thin film (4 nm) with a quasi-two dimensional EuO layer (1 nm). Such thicknesses are typical for tunnel barriers in future spin-selective tunnel contacts. In Fig. 4.12a, b, the HAXPES spectra of Eu 3*d* and Eu 4*d* core-levels are taken at LN_2 temperature in order to reduce thermal broadening. We observe a line shape of the core-level spectra comparable with thicker EuO, even the multiplet splitting originating from the single atomic angular momenta J is resolved with an identical distribution of spectral weight.
In the spectra of 1 nm EuO, a small deviation can be observed at 8 eV shift towards higher binding energy with respect to the main multiplet features. We observe this small feature consistently in both the Eu 3*d* and 4*d* spectra, and identify this as chemical shift of Eu^{3+} ions.[1] An explanantion may be ionic oxygen provided by the cYSZ substrate, to which the ultrathin EuO layer reacts sensitively with oxidation.

In conclusion, we investigated Eu core-levels of heterostructures with single-crystalline EuO thin films in the range 1–20 nm by HAXPES. We selected the Eu 3*d* and the 4*d* orbitals for

an investigation at low temperature yielding high resolution spectra. Multiplet structures (J final states splitting) in agreement with literature were resolved, and exclusively the Eu^{2+} oxidation state and an unaltered multiplet structure was observed for EuO films of 20, 4 and 1 nm thickness (with a small deviation for 1 nm EuO). Here, the HAXPES analysis of buried EuO thin films proves its potential to characterize the chemical properties and detailed multiplet structure of a buried layer of a spin-functional magnetic oxide.

4.1.4. Magnetic circular dichroism of single-crystalline EuO/cYSZ (100)

Magnetic circular dichroism is of fundamental interest, as its analysis can elucidate the intra-atomic interaction between core-levels and the magnetic open shell. Moreover, its Boltzmann-averaged amplitude is a direct measure for the magnetization of the EuO thin film. This section summarizes the first successful X-ray magnetic circular dichroism experiment in core-level photoemission (MCD-PE) on EuO thin films. We investigate single-crystalline epitaxial EuO thin films on conductive YSZ (100). This system allows one to investigate a magnetic oxide with $4f$ spin-only magnetic order, textbook-like crystalline quality and chemically well-defined and atomically sharp interfaces.

Magnetically oriented ${}^8S_J$ states in the Eu $4f$ orbital form the basis of ferromagnetism in the magnetic oxide EuO. These oriented spins interact via d–f exchange with core-levels like $4d$ and $3d$, both of which showing a resolvable final state multiplet structure. The J final state components of these core-levels are of largely different strength, as presented in the last section. This is the basis for the observation of magnetic circular dichroism in photoemission final states of these core-levels, as introduced theoretically in Ch. 2.5. We conducted MCD-PE measurements of Eu $3d$ and $4d$ core-levels at beamline P09 of the high-brilliance facility PETRA III (see Ch. 3.4.3). The polarization vector of the circularly polarized light $\boldsymbol{q}$ and the magnetization of the thin film $\mathbf{M}$ are collinear during the photoemission experiment.

In Fig. 4.13, MCD-PE spectra of Eu $3d$ and $4d$ core-levels are summarized. The spectra clearly resolve the single final states of $m_J = 2..5$ and $m_J = 1..6$ for the $3d_{3/2}$ and $3d_{5/2}$ mutliplets, where jj-coupling is assumed.* The most dominant splitting of single angular momenta is observed in the $4d$ final states ${}^9D_J$, $J = 2..6$, where LS-coupling is assumed. The resolved J components match the energy positions of calculated values from literature very well, as illustrated with grey markers.[110,114,115]

Consistently in the MCD of Eu $3d$ and $4d$ core-levels, we identify the largest MCD asymmetry for the final state components with largest m_J. The MCD difference can be interpreted as the product of core-shell angular momentum $\boldsymbol{\ell}$ after photoexcitation with the spin moment $\mathbf{S}$ of the open $4f$ shell, therefore $\langle \boldsymbol{\ell}, \mathbf{S} \rangle$. When we identify the sign of the MCD asymmetry as vector of $\boldsymbol{\ell}$, then we can correlate its direction with the fixed spin moment of $\mathbf{S}_{4f}$, which is indicated in the MCD spectra (Fig. 4.13). We recognize, that the multiplet lines with largest m_J have parallel angular orientation with $\mathbf{S}_{4f}$. At a minimum temperature of the sample ($T_{\mathrm{min}} = 33\,\mathrm{K}$), maximum MCD asymmetries of 44% for Eu$3d$ and 49% for Eu$4d$ could be observed for these maximum J lines. The alignment of multiplet lines reverses with lower J: The $m_J = 1..4$ lines and the multiplet satellite of $3d_{\frac{5}{2}}$ are antiparallel with respect to $\mathbf{S}_{4f}$

*For intra-atomic coupling of angular momenta in Eu core-levels, please see Ch. 2.5.2.

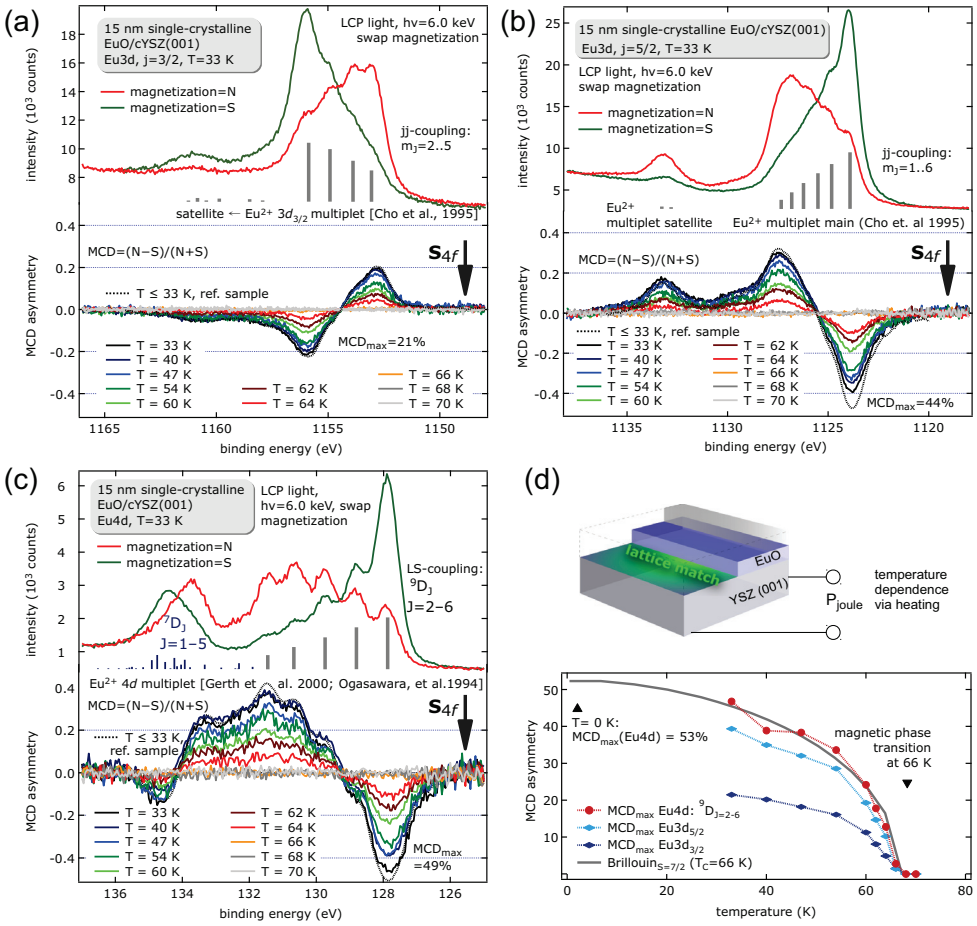

Figure 4.13.: X-ray magnetic circular dichroism in core-level photoemission of single-crystalline EuO/cYSZ (100). Core-levels with largest cross-sections Eu 3*d* in (*a*, *b*) and Eu 4*d* in (*c*) resolve every component of the angular momentum *J*. The MCD is quantified by its amplitude and plotted in dependence on the sample temperature (*d*). The vector $\mathbf{S}_{4f}$ denotes the orientation of the aligned spins of the magnetic 4*f* shell, it can be compared with the photoexcited core hole angular momentum, which corresponds to the sign (+ or −) of the MCD difference.

(Fig. 4.13b). In the 4*d* high-spin peak ^9D_J, the multiplet component with $m_J = 2..4$ are antiparallel to $\mathbf{S}_{4f}$. A further analysis regarding the coupling of single core-level final states with $\mathbf{S}_{4f}$ is subject to present work.

A temperature-dependent series of the magnetic circular dichroism reveals, that the MCD asymmetry vanishes under the noise threshold at $T \geqslant 66$ K, as observed in Fig. 4.13d. The MCD follows the shape of a Brillouin function, as expected for the magnetic order of a Heisenberg ferromagnet. For all temperatures, the MCD of the Eu4*d* $^9D_{J=6}$ final state remains largest, followed by Eu3$d_{5/2}$ and 3$d_{3/2}$ multiplets. Assuming the Heisenberg model for EuO, we extrapolate the Brillouin function to $T = 0$ and obtain a maximum MCD asymmetry of 53%. This value is obtained for the $m_J = 6$ component of the ^9D high spin peak of the Eu 4*d* orbital. We remark, that the polarization of the circular-polarized light was ~60% during the measurement at PETRA III at the end of 2012.

We conclude, that we observed magnetic circular dichroism in Eu core-level photoemission of single-crystalline epitaxial EuO films for the first time. Hard X-ray excitation permits one to probe the entire film thickness (15 nm) of EuO. Large MCD asymmetries are found in Eu 3*d* and 4*d* core-levels. The maximum measure amplitude is 49% which is extrapolated to 53% at $T = 0$ K. Final states with largest m_J are parallel to the 4*f* spin, this behavior switches for lower m_J in both core-levels. The MCD amplitude follows a Brillouin function and is thus a good measure for the magnetization of the EuO thin film.

Ultrahin EuO coherently grown on cYSZ (100): MCD of a reference sample

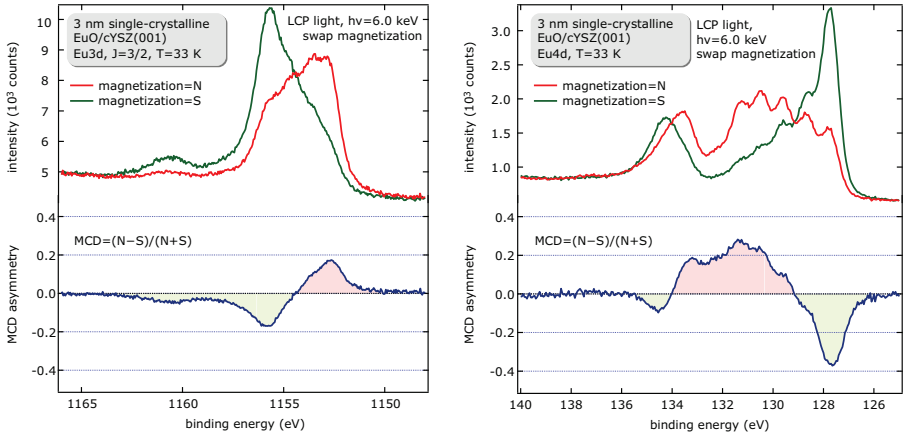

Figure 4.14.: MCD-PE of Eu 3*d* and 4*d* core-levels for ultrathin EuO coherently grown on cYSZ (100).

In the following, we investigate the lower thickness regime of EuO, in particular 3 nm single-crystalline EuO on cYSZ (100). This heterostructure is coherently grown without any strain, and thus represents a reference system for the MCD in photoemission of ultrathin EuO. Later, we will compare it with strained EuO thin films.

The multiplets of Eu 3$d_{3/2}$ and 4*d* photoemission are well-resolved, as depicted in Fig. 4.14. A good characterization of the MCD is the maximum amplitude by the final states with largest

m_J. For 3 nm single-crystalline EuO/cYSZ (100), this maximum MCD difference is 18% for Eu3$d_{3/2}$ and 38% for Eu4d. These MCD values reach 95% of those measured from a 15 nm thin film of single-crystalline EuO presented in Fig. 4.13. Thus, a bulk magnetization of the EuO ultrathin film is almost realized, if we assume that the MCD amplitude is a good representation of the macroscopic magnetization.

Here, we have presented a reference for single-crystalline unstrained EuO, which we will compare with EuO under biaxial tensile strain and biaxial compressive strain in the following sections 4.2 and 4.3.

4.2. Lateral tensile strain: EuO on $LaAlO_3$ (100)

Although the bulk properties of the EuO films are well-known, lateral strain from the interface will significantly alter the electronic structure of epitaxial oxide heterostructures.[163] Biaxial lateral strain inherited from the underlying substrate has recently inspired several experimental studies on epitaxial EuO, which conclude small changes in T_C upon small (∼2%) tensile strain.[27,33,64] Small lateral strain on EuO has been also applied by Liu et al. (2012). They found a change (±2 K) of T_C due to the underlying substrate, either CaF_2 or MgO.[61] However, the authors investigated mainly polycrystalline EuO, making a systematic comparison of the lattice strain difficult.

Taking advantage of the adsorption-controlled EuO synthesis ensuring the stoichiometry and single-crystallinity (as presented in the last section), in the following we investigate single-crystalline EuO layers epitaxially integrated with $LaAlO_3$ (100) substrates (LAO) by an unchanged synthesis.* This induces 4.2% biaxial tensile strain to EuO, thus extending the Eu^{2+} nearest-neighbor distance in the lateral dimension. First, we investigate the structural characteristics of the strained epitaxial EuO top layer. Furthermore, we present the magnetic behavior of EuO under lateral tension by LAO (100) using SQUID magnetometry. Finally, we investigate Eu core-levels of the EuO/LAO (100) heterostructure by an analysis of magnetic circular dichroism in core-level photoemission (MCD-PE).

Structural characterization of epitaxial EuO on LAO (100)

First, we investigate the structural quality of EuO which is deposited on $LaAlO_3$ (100) using the adsorption-controlled growth by Oxide-MBE. The LAO crystal is usually referenced with a large rhombohedral unit cell with $a = b = 5.36$ Å, these lattice parameters span the cubic surface plane and provide 4.2% tensile strain to the EuO top layer. A pseudocubic representation lattice is used for the quantitative analysis by X-ray diffraction presented in the following, the conversion is illustrated in the appendix (Ch. A.1).

In Fig. 4.15, the *in situ* characterization of 16 nm EuO/LAO (100) is summarized. Before EuO growth, we anneal the LAO (100) substrate similarly to the YSZ substrates (last section) but with a temperature reduced below the structural displacement transition of LAO at ∼540 °C.[164] This yields a flat and single-crystalline cubic surface as indicated by sharp

*A summary of substrates suited for epitaxial integration with EuO, including strain, is found in Tab. A.2 on p. 128.

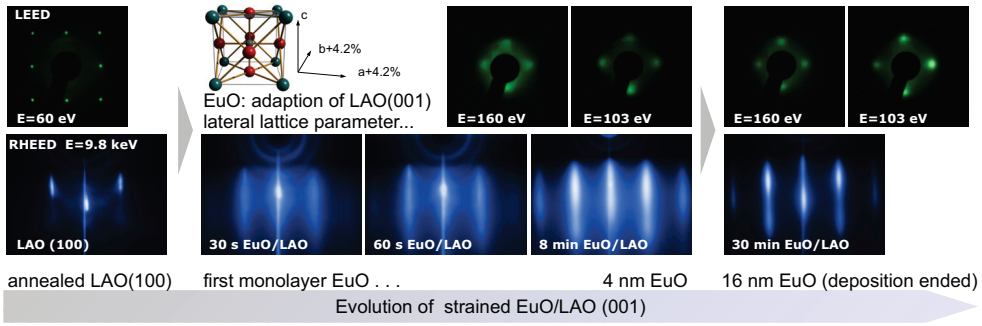

Figure 4.15.: EuO/LAO (100): process of strained EuO deposition. On oxygen-annealed LAO (100), EuO is grown via the Eu distillation condition. Beginning from one monolayer, EuO adapts the in-plane lattice parameter of LAO. LEED and RHEED pattern confirm the EuO/LAO (100) heteroepitaxy and display an *fcc* lattice for every stage of a sustained EuO growth.

LEED and RHEED pattern. Applying the Eu-distillation condition with limited oxygen supply (adsorption-controlled growth), a 16 nm-thick EuO film is grown onto annealed LAO (100). Beginning from the very first monolayer of EuO – thus showing no interstitial stages - – the RHEED streaks indicate a smooth and crystalline surface at every stage of EuO growth, and the RHEED patterns show the same reciprocal space distance as for the LAO (100) surface. This is an evidence for the adaption of the LAO lateral lattice parameter by the EuO layer. LEED patterns were recorded after growth of a 4 nm and of a 16 nm EuO thick film. Both indicate a good crystallinity of the EuO *fcc* lattice without any other phases. These electron diffraction results prove that it is possible to grow epitaxial and single-crystalline EuO on LAO (100).

X-ray diffraction of the 16 nm epitaxial EuO layer (Fig. 4.16a) shows exclusively the cubic

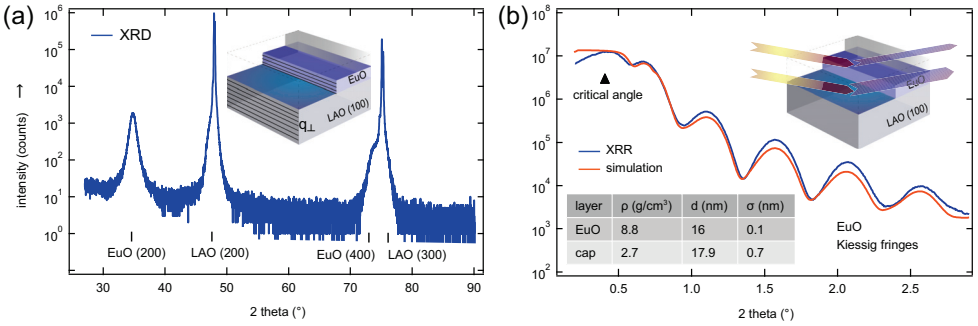

Figure 4.16.: EuO/LAO (100) investigation of the perpendicular lattice parameter, and layer thickness and roughness. In (*a*), a 2θ wide scan reveals the perpendicular lattice parameter of the LAO (100) substrate and single-crystalline EuO (100). This multilayer structure is characterized by X-ray reflectivity (*b*) which reveals density ρ, thickness d, and roughness σ of each slab.

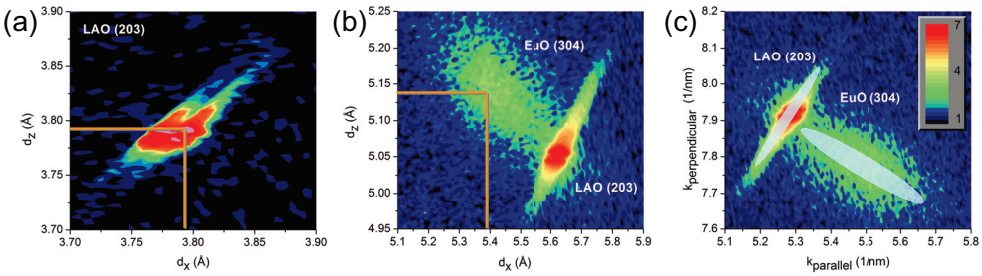

Figure 4.17.: EuO/LAO (100) in-plane and out-of-plane crystal structure determined by reciprocal space maps. The pseudocubic lattice parameter of LAO (100) is confirmed by the asymmetric (2 0 4) reflex both in-plane and out-of-plane (*a*). Close to the LAO reflex, the asymmetric EuO (3 0 4) diffraction peak allows one to determine the lattice parameters of the EuO film (*b*): in-plane, EuO adapts the LAO (100) lattice spacing. The broadening (highlighted grey in *c*) of the LAO (2 0 3) and EuO (3 0 4) diffraction features in reciprocal space allow to identify a small structural inhomogeneity for LAO and an in-plane mosaicity for EuO.

(h 0 0) diffraction pattern. The EuO diffraction peaks are located at $2\theta = f(q_\perp)$ positions which correspond to the perpendicular lattice parameter of $d_\perp = 5.14$ Å, in agreement with the literature value of bulk EuO. A simulation to fit X-ray reflectivity of the EuO/LAO multilayer structure (Fig. 4.16b) reveals a thickness of 16 nm, a mean roughness of the EuO surface of only 1 Å, and a density of EuO of 8.8 g/cm^3. This result underlines the high-quality MBE growth of EuO yielding smooth interfaces. However, the slightly increased density of the EuO layer (+6%) can be explained by excess Eu clusters in the film arising from the Eu-rich distillation growth condition.

Further information regarding the crystal structure of the strained EuO thin film is obtained from a reciprocal space mapping, a two-dimensional X-ray diffraction technique. In Fig. 4.17, we scanned the reciprocal space around the asymmetric EuO (3 0 4) and the LAO (2 0 3) diffraction peaks. This provides information about in-plane and out-of-plane lattice parameters and the crystal quality in these dimensions. A sharp diffraction peak confirming the LAO pseudo cubic lattice parameter can be identified in Fig. 4.17a, here the two features with comparable intensity distribution originate from the two lines of the Cu $K\alpha_{1,2}$ radiation of the X-ray anode. A conversion of the reciprocal vectors to real space distances* reveals the in-plane lattice parameter of EuO as 5.39 ± 0.02 Å, in agreement with the LAO (100) lattice parameter. The perpendicular lattice parameter of EuO is almost unchanged ($d_z = 5.140 \pm 0.010$ Å).

A specific material parameter describing volume elasticity under an axial strain is the Poisson ratio, defined as

$$\nu = -\frac{\mathrm{d}\varepsilon_{\mathrm{trans.}}}{\mathrm{d}\varepsilon_{\mathrm{axial}}} \overset{\text{1st order approx.}}{=} -\frac{\Delta\ell_{\mathrm{trans.}}}{\Delta\ell_{\mathrm{axial}}} = \frac{d_z^{\mathrm{RSM}} - d_z^{\mathrm{ref.}}}{d_{xy}^{\mathrm{RSM}} - d_{xy}^{\mathrm{ref.}}}. \tag{4.2}$$

For epitaxial EuO/LAO (100) which reveals lateral tensile strain, we evaluate a Poisson ratio

*The conversion between reciprocal coordinates and the real space is shown in Ch. 3.4.2. A well-explained example of RSM to analyze effects of strain and relaxation is published in Liu and Canonico (2004).[165]

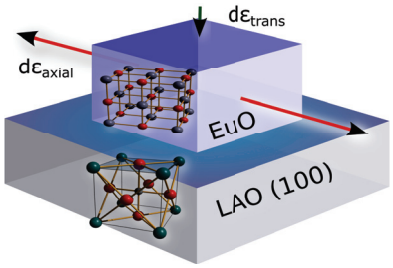

Figure 4.18.: Axial and transversal elasticity of EuO on LAO (100). The Poisson ratio ν can be calculated as the ratio of axial and transversal change of length in the crystalline thin film, in first order approximation.

for the 16 nm EuO thick film of $\nu_{\mathrm{EuO}}^{16\,\mathrm{nm}} = (0.01 \pm 0.04)$. The uncertainty arises from the broadening of the RSM peak of EuO/LAO (100) in Fig. 4.17b. Within the error bars, we consider the Poisson ratio to be positive but near zero. When compared to other oxides (e. g. bulk SiO_2, $\nu = 0.2$), this small Poisson ratio is a remarkable feature of a strained EuO thin film epitaxially integrated on LAO (100). Using the definition (4.2), we can state, that the volume elasticity of the strained EuO thin film is extremely small ($\approx$0).

The broadening of the two-dimensional diffraction peaks (Fig. 4.17c) allows one to judge the crystal quality (according to Fig. 4.17 on p. 47). For LAO (2 0 3), the broadening is caused by a certain structural inhomogeneity, yet we consider this value as small due to the very high-quality surface of LAO as observed by *in situ* electron diffraction. A broadening is also observed for the EuO (3 0 4) peak, which is interpreted as in-plane mosaicity. This means, crystal domains are rotated with respect to neighboring domains by a small angle around an axis normal to the surface. However, this broadening is as small as for the LAO substrate which qualifies the mosaicity of EuO to be small, too.

In conclusion, our structural investigations of the strained epitaxial EuO/LAO (100) heterostructures prove the superior crystal quality of EuO. EuO/LAO (100) constitutes a magnetic model system which is stretched by 4.2% biaxial strain exclusively in two dimensions and unchanged in the z dimension.

Magnetic characterization of epitaxial EuO thin films on LAO (100)

A magnetic characterization of the EuO/LAO (100) heterostructure by SQUID is given in Fig 4.19 for two thicknesses of EuO, $d = 4$ nm and bulk-like $d = 30$ nm. The temperature dependent magnetization shows a Brillouin-shaped curve without any features of antiferromagnetic or paramagnetic phases. For ultrathin (4 nm) EuO/LAO (100), the Curie temperature is clearly determined at 57 K, which is a reduction of 12 K according to the bulk value of single-crystalline EuO/YSZ (100). This reduction is due to the lateral strain effect rather than reduced dimensionality of the EuO slab, which is easily recognized when compared with the thickness dependence of unstrained EuO/YSZ (see Fig. 4.6 on p. 65). The switching of the magnetic moment due to magnetic field reversal is a measure for the crystal homogeneity. For the strained EuO/LAO (100), the coercive field is 74 Oe which is double the minimum value obtained for optimum EuO/YSZ (100). One explanation can be the in-plane mosaicity determined by the reciprocal space map analysis. Moreover, the magnetization switches gradually, as indicated by the rounded shape of the hysteresis, while for unstrained EuO/YSZ rectangular shapes of the hysteresis are observed (see Fig. 4.6). A magnetic saturation moment of nearly the bulk EuO value ($7\mu_B$ expected) is observed at $T = 2$ K.

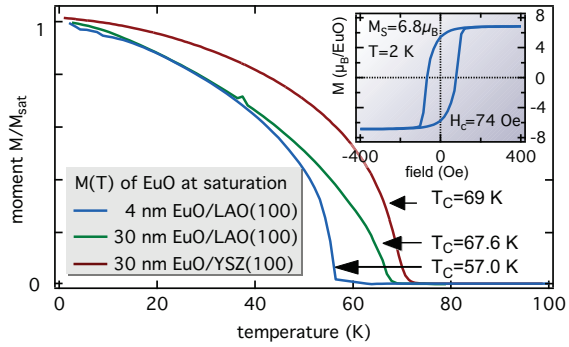

Figure 4.19.: Magnetic bulk properties of epitaxial EuO on LAO (100).
A Brillouin-shaped magnetization curve is observed for EuO/LAO (100) heterostructures with 4.2% biaxial tensile strain. The ordering temperature for 4 nm EuO/LAO (100) is reduced by 12 K with respect to coherently grown epitaxial EuO/YSZ.

A reduced dimensionality of the ultrathin EuO/LAO heterostructure may also affect the magnetic ordering temperature, and thus we additionally investigate a bulk-like 30 nm EuO/LAO (100) heterostructure, for which we have confirmed a persistent adaptation of the LAO lateral lattice parameter, by SQUID (green curve in Fig. 4.19). The shape of the temperature-dependent magnetization coincides with that of ultrathin EuO/LAO (100), however, the T_C is determined at 67.6 K, a reduction of 1.4 K with respect to unstrained bulk-like EuO/YSZ. Thus, the reduction of long range magnetic order can almost completely be compensated in laterally expanded EuO, when the unstrained z dimension is provided with a bulk-like thickness of 30 nm.

Summarizing, the magnetic behavior of ultrathin EuO under 4.2% lateral tensile strain is comparable to the bulk EuO behavior, only the T_C is reduced by 12 K, which mainly originates from the reduced J_1 coupling (eq. (2.9)) due to the increased distance of in-plane nearest neighbors. This reduction can almost completely be compensated if a bulk-like thickness in the unstrained vertical dimension is provided.

X-ray magnetic circular dichroism of epitaxial EuO on LAO (100)

Finally, we investigate 3 nm single-crystalline EuO on LAO (100) by means of the MCD effect in core-level photoemission spectroscopy. In Fig. 4.20, the multiplets of Eu $3d_{3/2}$ and $4d$ photoemission are well-resolved, similar to the reference sample EuO/cYSZ (100) (in Fig. 4.14 on p. 73). The maximum MCD amplitude is determined by the final states with largest m_J and is 8% for Eu $3d_{3/2}$ and 22% for Eu $4d$. We compare these MCD amplitudes directly with the reference heterostructure EuO/cYSZ of the last section, and find that the current strained EuO/LAO heterostructure shows 44% and 58% maximum MCD of Eu $3d$ and $4d$ core-levels with respect to the unstrained reference heterostructure. Thus, by tensile strain the intra-atomic coupling of Eu^{2+} ions in EuO is more reduced in $3d^9$ final states than in $4d^9$. This may be explained by the weaker exchange coupling between $3d^9$ and the magnetic open shell $4f^7$ with configuration ${}^8S_{7/2}$.

Moreover, from magnetization curves by SQUID, we obtain a ratio of magnetization at T = 33 K of 84% when EuO/LAO (100) is compared with the reference sample EuO/YSZ (100) (as seen from Figures 4.19 and 4.6). Thus, the MCD asymmetry (less than 50% with respect to the reference sample) responds more sensitively on lateral tensile strain than the averaged

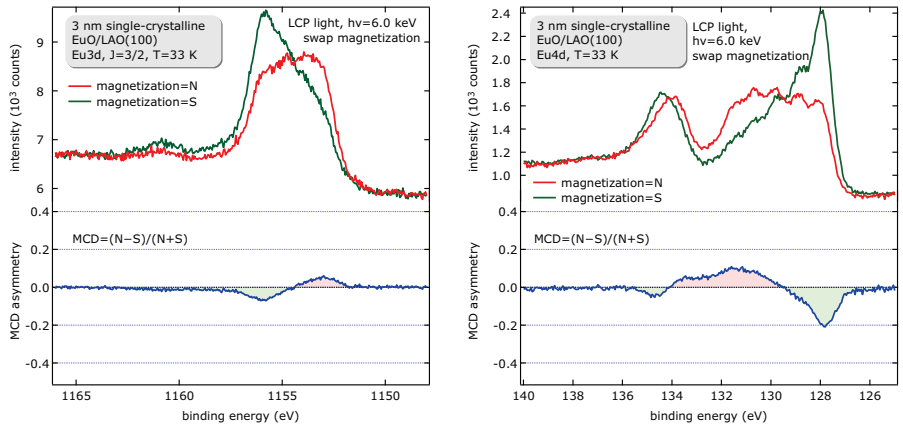

Figure 4.20.: MCD-PE of Eu 3*d* and 4*d* core-levels for ultrathin EuO under tensile strain on LAO (100).

magnetization in the EuO/LAO (100) heterostructure. This may partly be explained by a small applied field during SQUID measurements, while during photoemission for the MCD-PE measurement, the EuO thin film is magnetized only remanently. Apart from this, SQUID measures the averaged spin alignment of the $4f^7$ orbitals, thus the macroscopic magnetization. MCD-PE probes the photoemission final states of a core hole which is under exchange interaction with $4f^7$. Thereby, under external strain the intra-atomic exchange may be significantly altered, while the spin alignment itself (i. e. the origin of the magnetization) of the $4f^7$ is mainly unaltered. This may explain the largely reduced MCD signal. A further analysis of single final state J components is subject to present work.

Here, we have presented the MCD effect in a EuO/LAO (100) heterostructure with 4.2% tensile strain. The MCD asymmetry shows a large reduction with respect to an unstrained reference sample. This reduction is even larger than expected from SQUID measurements, and outlines changes in intra-atomic exchange interactions.

4.3. Lateral compressive strain: EuO on MgO (100)

Lateral compressive strain can be induced by substrates with a smaller cubic lattice parameter than EuO. Magnesium oxide (MgO) has a smaller lattice parameter of $a = 0.42$ nm of the cubic unit cell. Thus, EuO on MgO (100) is exposed to 18% compressive biaxial strain in the lateral dimension.*

Several works have reported the successful growth of EuO/MgO (100), where epitaxy and a bulk-like magnetization of EuO has been observed.[32,166] However, these EuO films on MgO (100) were thick by means of many tens of nanometers, and the initial stages of growth and the properties of strained EuO in the few-nanometer regime were not adressed yet. A recent

*A summary of MgO and other substrates regarding lattice parameters and strain can be found in Tab. A.2 on p. 128.

study[27] investigates ultrathin EuO directly on MgO (100) and finds that epitaxial EuO can be observed only after 2 nm of EuO deposition. This study also reveals a formation of EuO on MgO (100) in the monolayer regime without oxygen supply, a similar effect as observed for YSZ,[32,45] which supplies ionic oxygen at elevated temperatures. Facing the problem of "interrupted epitaxy", Swartz et al. (2012) focus on an additional oxide interlayer in order to integrate the EuO unstrained lattice with the MgO substrate.[27]

In this section, we focus on high-quality epitaxial EuO grown directly MgO (100) in order to investigate structural and magnetic effects of the large lateral compressive strain.

Structural characterization of epitaxial EuO on MgO (100)

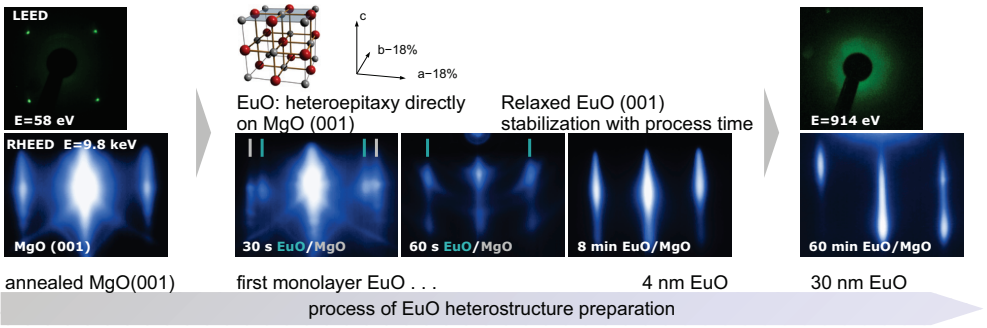

Figure 4.21.: EuO/MgO (100): EuO deposition under large compressive strain. Beginning from one monolayer, EuO shows its native in-plane lattice parameter. A seamless EuO/MgO heteroepitaxy is observed by RHEED, accompanied by a small fraction of polycrystalline EuO as indicated by circular intensities. From 4 nm EuO on, reciprocal pattern improve towards largely single-crystalline EuO; however, the accumulated roughness prevents the observation of the EuO surface structure by LEED after growth.

In Fig. 4.21, the *in situ* deposition of EuO directly on MgO (100) is monitored by electron diffraction. The annealed MgO substrate shows sharp RHEED and LEED pattern indicating a single-crystalline and smooth surface. Accounting for possible oxygen diffusion from the substrate, one monolayer of Eu metal is deposited onto the heated MgO just before EuO growth as a seed preventing over-oxidized EuO phases. When EuO growth begins, for 1–2 monolayers EuO we observe a RHEED pattern of MgO and EuO simultaneously without any polycrystalline or amorphous phase. This is the first time, that a good heteroepitaxy of EuO directly on MgO (100) without any non-crystalline stages is achieved. The observed RHEED streaks of the first monolayer EuO exhibit the native EuO lattice parameter, thus large areas of unstrained and epitaxial EuO have formed directly on MgO. Proceeding with the EuO synthesis, from two monolayers EuO on, a small polycrystalline fraction indicated by circular intensities next to the unstrained EuO pattern is observed in the RHEED photograph. Thus, a small fraction of disorder or cracks must be present to allow the unstrained EuO to arrange heteroepitaxially directly on MgO (100). From two monolayers EuO until the end of EuO deposition, the surface crystal structure improves, and only EuO *fcc* pattern are observable when EuO growth is finished ($d = 15$ nm). However, inherited from the initial polycrystalline

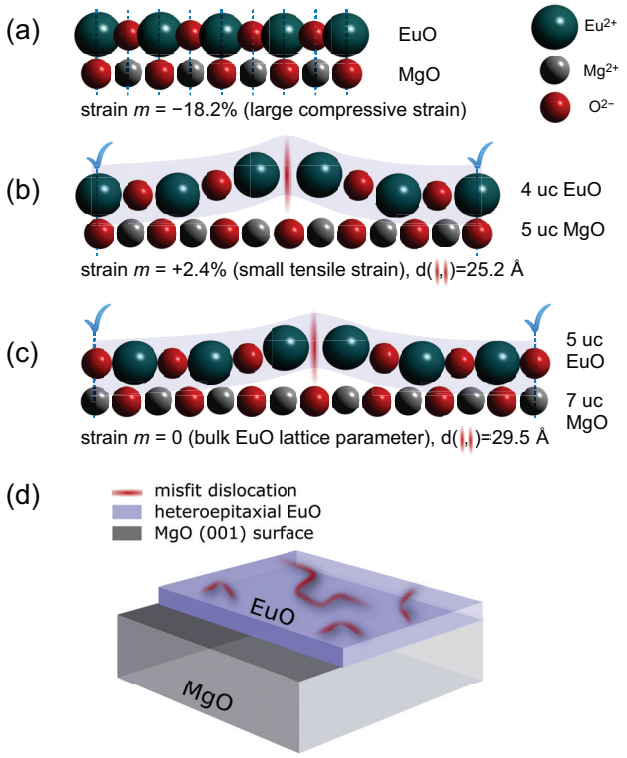

Figure 4.22.: EuO/MgO (100): different epitaxial arrangements. In (*a*), a cube-on-cube relation is illustrated inducing large compressive strain to EuO. In the EuO/MgO 4:5 configuration, a minimum lateral strain of +2.4% acts on EuO (*b*). If however, EuO keeps its native lattice parameter (*c*), no simple cube-on-cube relation is realized and electrostatic distortions will readily occur.

fraction, a certain roughness remains and hampers observation of a surface crystal structure in low energy electron diffraction.

We elucidate the observed initial polycrystalline fraction and the quasi-relaxed EuO growth at the EuO/MgO (100) interface in terms of geometrical and electrostatical aspects: In Fig. 4.22, three configurations of the EuO/MgO (100) heteroepitaxy are illustrated assuming different lateral lattice parameters (e. g. in [010] direction) of the initial EuO layers. From our structural investigation, we can exclude the direct cube-on-cube heteroepitaxy (in Fig. 4.22a) comprising large compressive strain, which can be explained as follows: the deposition of one atomically flat EuO layer on an MgO (100) surface is equivalent to a substitution of the Mg atoms of the top layer. Here, the ion-size difference[167] forms different sizes of the Mg–O and the Eu–O bond: in the MgO surface, replacing the Mg^{2+} ion with a Eu^{2+} ion changes the cation ionic diameter to 0.234 nm and increases the O–O nearest neighbor bond by 22% from 0.298 nm to 0.363 nm.[168] In such a case, the ion-size difference would force the Eu or O atoms to find equilibrium positions in a roughened structure.[27] Considering a second configuration, a EuO/MgO lateral arrangement of 4:5 as sketched in Fig. 4.22b has a lateral strain with a minimum value of +2.4%. From an electrostatic view point, strong Coulomb repulsion between O^{2-}–O^{2-} and Eu^{2+}–Mg^{2+} ions at alternating position would certainly lead to structural roughening at the interface. From our electron diffraction results, we observe in-

dications for a third configuration: relaxed epitaxial EuO/MgO (100) with a small fraction of EuO crystal defects at the interface, as observed in the 60 s-RHEED photograph in Fig. 4.21. Here, the in-plane heteroepitaxy is maintained, however no simple integer relation of EuO and MgO lattices can be realized, as sketched in Fig. 4.22c. Starting from an EuO on MgO matching point, after several unit cells of relaxed EuO a structural distortion likely occurs in order to newly arrange a EuO/MgO ionic match. This leads to misfit dislocations in the initial layers of the EuO crystal and is observed as polycrystalline fraction next to epitaxial relaxed EuO in RHEED. As a result, no compressive strain is acting on the EuO layer, but rather structural dislocations which are observed in the first two nanometers of heteroepitaxial EuO/MgO (100).

In conclusion, we observe a good heteroepitaxy of unstrained EuO on MgO (100) beginning with one monolayer EuO, which initially comprises a fraction of crystal defects and develops towards EuO single-crystalline quality. The following magnetic measurements investigate EuO/MgO (100) heterostructures of different EuO thickness to elucidate the relative effect of misfit dislocations from interfacial EuO on the magnetic properties.

Magnetic bulk characterization of epitaxial EuO on MgO (100)

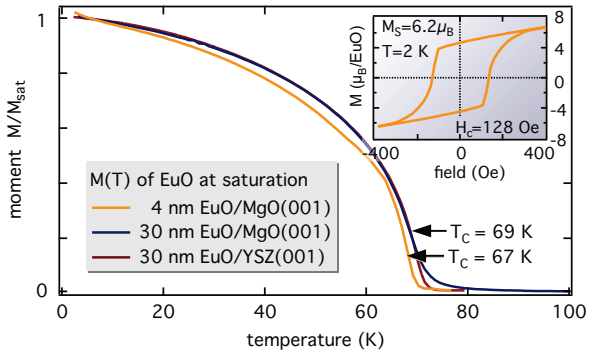

Figure 4.23.: Magnetic properties of heteroepitaxial EuO on MgO (100).
A Brillouin-shaped magnetization curve is observed for all heteroepitaxial EuO/MgO (100) layer structures. The ordering temperature for 4 nm-thin EuO/MgO is comparably reduced as for coherently grown epitaxial 4 nm EuO/YSZ.

We investigate the influence of the MgO (100) substrate with a large lateral mismatch on the magnetic properties of heteroepitaxial EuO films by SQUID magnetometry, as depicted in Fig. 4.23. An ultrathin EuO/MgO (100) heterostructure exhibits a magnetization curve with a deviation from the optimum EuO/YSZ curve less than 5%. Here, the Curie temperature is reduced to 67 K, which is 2 K below the bulk value of optimum EuO/YSZ. These small deviations from bulk are caused by an interplay of reduced dimensionality (only 4 nm EuO) and the crystal distortions of interface-near EuO as discussed above. However, the hysteresis loop encloses a rectangular area with a well-defined switching point as expected for a ferromagnetic film, but the coercive field is double the value of an optimum EuO/YSZ heterostructure. This highlights the difference in crystalline quality: coinciding with the polycrystalline fraction of EuO in RHEED, these structural defects may contribute to pinning of magnetic domains in EuO.
For EuO/MgO (100) of bulk-like thickness, however, we observe a bulk-like magnetization curve similar to that of a coherently grown reference sample EuO/YSZ (100). In conclusion, the magnetic properties of EuO/MgO are relatively robust against structural misfit disloca-

tions. Even ultrathin EuO exposed to a large lateral mismatch by the MgO (100) surface deviates only in a weakly from the magnetization curve of bulk EuO. These results are published in Caspers et al. (2013).[2]

In order to investigate the effect of large compressive strain and resulting structural rearrangements EuO/MgO (100) heterostructures, we conducted an MCD experiment using hard X-ray photoemission spectroscopy. However, no MCD asymmetry above the noise level could be observed (not shown). Since the EuO ultrathin film on MgO (100) is only of 3 nm thickness, the polycrystalline crystal structure may be responsible for a reduced T_C, which lets the EuO layer be in the paramagnetic phase during the experiment. We assume experimental issues, for example a local warming of the heterostructure during the spectroscopy. One reason might be the incident X-ray beam, which excites the MgO resulting in a white glowing fluorescence. Further studies of biaxial compressive strain on epitaxially integrated EuO are desirable.*

*A summary of alternative substrates regarding lattice parameters and strain can be found in Tab. A.2 on p. 128.

4.4. Summary

In order to provide high-quality ultrathin EuO for our fundamental studies, we synthesized EuO thin films from bulk-like thicknesses down to one nanometer by reactive molecular beam epitaxy specialized for oxide growth (Oxide-MBE).

The EuO thin films are of textbook-like single-crystalline quality, as confirmed by electron diffraction techniques. We developed a procedure to obtain a certain metallicity in YSZ substrates ("conductive YSZ"), which allows for experimental techniques involving high electron yields, e. g. hard X-ray photoemission spectroscopy (HAXPES) or transmission electron microscopy (TEM). On conductive YSZ, we confirmed epitaxial layer-by-layer growth of EuO. A sharp and well-defined EuO/cYSZ interface as well as a homogenous crystallinity of the EuO film are observed by high-resolution TEM. Our magnetic oxide EuO thin films exhibit a bulk-like magnetization down to 2 nm thickness. The stoichiometric chemical quality of EuO in Si/EuO/cYSZ (100) heterostructures was confirmed by HAXPES for various thicknesses. Even for 1 nm ultrathin EuO, no valence change or interface shifts are identified from Eu core-level peaks. We conducted an advanced magnetic characterization by magnetic circular dichroism (MCD) in core-level photoemission, providing insight into the intra-atomic exchange coupling of EuO. This reveals large MCD asymmetries of up to 44% in the Eu 3*d* and 49% in the Eu 4*d* photoemission multiplets. The temperature dependence of the MCD describes a Brillouin function with $T_C = 64$ K. Thus, EuO thin films on conductive YSZ provide a fundament for ideal EuO heterostructures of reference quality. This allows to explore advances of selected physical properties of ultrathin EuO layers – like a tuned ferromagnetism.

Biaxial lateral strain applied to single-crystalline EuO is of fundamental interest, since it alters the electronic structure and magnetic coupling in a controlled way. In order to investigate epitaxial EuO under 4.2% tensile biaxial strain, we synthesized high quality EuO/LAO (100) heterostructures by Oxide-MBE. A seamless heteroepitaxy of EuO is observed by electron diffraction. For 16 nm epitaxial EuO/LAO (100), reciprocal space maps reveal the adaption of the lateral LAO lattice parameter, while the perpendicular parameter c of EuO is the unchanged EuO bulk value, which corresponds to a Poisson ratio of $\nu_{EuO} \approx 0$. While the magnetization of 4 nm EuO/LAO (100) heterostructures shows a Brillouin-shape as expected for a Heisenberg ferromagnet with a bulk-like saturation moment, the Curie temperature is reduced by 12.3 K with respect to the EuO reference value. However, a EuO/LAO (100) heterostructure of bulk thickness shows a T_C reduction of only 1.7 K. Therefrom we anticipate, that a large thickness in the unstrained z dimension provides sufficient long range magnetic exchange for a bulk-like Curie temperature in laterally expanded EuO. MCD asymmetries in Eu 3*d* and 4*d* core-level photoemission multiplets show a maximum asymmetry of 58% relative to the unstrained EuO reference. This reduction is significantly larger than expected from SQUID measurements, which we interpret as a larger effect of the tensile strain on intra-atomic exchange (MCD) than on the long range order of the $4f^7$ magnetic moments (SQUID).

5. Results II: The integration of the magnetic oxide EuO directly on silicon

The interface is *still* the device.

(H. Y. Hwang and J. M. Chakhalian, Nat. Mat. editorial, 2012[146,169,170])

Despite its tremendous potential as tunnel contacts with spin functionality, the successful stabilization of stoichiometric EuO thin films directly on silicon without any buffer layer is not reported to date. At present, a number of studies have used interfacial barriers of several nanometers thickness, which prevent diffusion and serve as epitaxial seed for EuO synthesis on silicon.[7,25,27] This, however, largely extends the tunneling path, as the total thickness of the oxide barrier and the magnetic oxide EuO can easily exceed 5 nm. This may result in hopping transport and scattering of spin-polarized electrons rather than tunnel transmission. Therefore, our goal is the integration of ultrathin EuO on Si (001) without any buffer layer. This study is based on the predicted thermal stability of the magnetic oxide EuO in contact with silicon.[14] A moderate lateral strain of 5.6% provided by Si (001) to the EuO lattice is in the usual range which allows for heteroepitaxy of oxides on semiconductors. Remarkably, this lattice mismatch is clearly lower than for the dielectric oxide HfO_2 epitaxially integrated with Si (strain = 6.9%), which is presently attracting great interest. Having established a high quality EuO synthesis on cubic oxides (Ch. 4) with single crystalline quality and bulk-like magnetism, now we proceed stepwise towards the application side: epitaxial integration of EuO directly on Si (001). This system combines lattice strain with a challenging interface chemistry.

We start the study with a chemically well-defined system: polycrystalline EuO on HF-passivated Si. Herein, EuO is grown with the well-established EuO distillation growth mode as used for oxide substrates, yielding a bulk-like EuO thin film. A detailed picture of the valence state of Eu ions in EuO and the electronic structure depending on the chemical composition is still missing. A major reason is the difficulty to probe this highly reactive compound by conventional surface-sensitive photoelectron spectroscopy, due to the necessity for a protective capping layer in EuO/Si hybrid structures. Here, we control the chemical integrity of the buried EuO bulk and surface layers by hard X-ray photoemission (HAXPES) experiments carried out at the high brilliance synchrotron light source PETRA III.

In the next step, we prepare and investigate ultrathin EuO on atomically smooth Si (001). We remove any oxides and contaminations from the Si substrate by *in situ* flashing procedures. For the system EuO directly on Si, the interface chemistry is the crucial challenge, as all the constituents Eu, O_2, and Si easily react to either metallic silicides, various oxides or over-oxidized EuO phases. Thus, we dedicate one section explicitly to a thermodynamic analysis of the EuO/Si interface. For different regimes of EuO synthesis, we identify the most probable interface reaction products and quantify balanced interface reactions by means of their resulting Gibbs free energies. In this way, we derive three different passivation meth-

ods of the Si (001) surface. The three types of interface engineering of the functional EuO/Si hybride structures include (*i*) hydrogen termination of Si dangling bonds, (*ii*) Eu coverage of Si in the monolayer regime, and (*iii*) passivation of Si by ultrathin silicon oxide. We apply these treatments *in situ* in the Oxide-MBE and control the surface crystal quality by electron diffraction. A quantitative chemical investigation of the ultrathin EuO films and the EuO/Si interface is carried out by HAXPES. Finally, we provide an optimum set of parameters for the minimization of metallic and oxidic interfacial reaction products.

5.1. Chemical stabilization of bulk-like EuO directly on silicon

A first step towards functional EuO/Si tunnel contacts is the chemical stabilization of ultrathin EuO films directly on silicon. EuO is predicted to be the only binary magnetic oxide thermodynamically stable in contact with Si.[14] For this reason, we fabricate EuO/Si heterostructures using the established technique of EuO synthesis presented in Ch. 4.

In this study, we investigate two complementary EuO systems: (*i*) stoichiometric EuO and (*ii*) oxygen-rich Eu_1O_{1+x}. The films are grown by Oxide-MBE under UHV with residual partial pressures of $p_{res} \leqslant 1 \times 10^{-10}$ mbar. We etch Si (001) substrates in diluted hydrofluoric acid (2% HF) in order to remove the native SiO_2 layer and to prepare a (H-Si)-terminated surface. For EuO on Si, the same adsorption-controlled EuO synthesis using the Eu distillation condition is employed,[15,32,45] similar to our study of EuO on oxide substrates.* In this way, we fabricate 45 Å-thick EuO films with different stoichiometries (*i*) and (*ii*) using a constant O_2 partial pressure in the range $p_{ox}^{partial} = 2\text{–}4 \times 10^{-9}$ Torr at an elevated substrate temperature of $T_S = 350$ °C. This yields mainly polycrystalline EuO as verified by X-ray diffraction. The EuO samples were capped by a 40 Å-thick Al film to prevent oxidation in air.

Magnetic properties

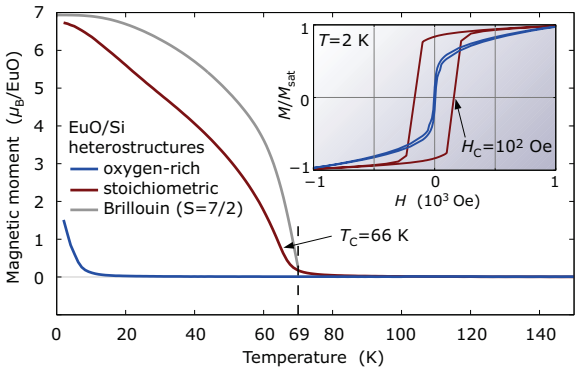

Figure 5.1.: Magnetic properties of ultrathin EuO films (d = 45 Å) grown directly on HF-Si. By SQUID magnetometry, the saturation field is determined by field-dependent hysteresis loops (*inset*) and applied for temperature-dependent magnetization measurements. The magnetization $M(T)$ shows a (S = 7/2) Brillouin-like curve for EuO compound (*i*).

First, we present the magnetic properties of both types of EuO/Si heterostructures (*i*) and (*ii*), measured by SQUID magnetometry. The magnetization $M(T)$ and hysteresis $M(H)$ characteristics for both stoichiometric EuO (*i*) and oxygen-rich Eu_1O_{1+x} (*ii*) thin films on silicon

*as described in Ch. 4 on p. 57.

are depicted in Fig. 5.1. In stoichiometric EuO (*i*), $M(T)$ roughly follows a Brillouin function, as expected for a Heisenberg ferromagnet with spin angular momentum $S = 7/2$.[18] We can observe a magnetic saturation moment of $M_S = 6.7\,\mu_B$, close to the bulk value of $7\,\mu_B$ per Eu^{2+} as expected for a $4f^7$:$^8S_{7/2}$ system. Likewise, the normalized $M(H)$ characteristics taken at 2 K (see inset of Fig. 5.1) displays a clear square-like ferromagnetic hysteresis with a coercive field of $H_c \approx 100$ Oe of the (*i*) stoichiometric EuO/Si (001) heterostructure. This magnitude of coercive field is characteristic for polycrystalline EuO.
The complementary EuO/Si heterostructure (*ii*) comprising oxygen-rich EuO, in contrast, reveals an $M(T)$ curve in Fig. 5.1 which is almost completely suppressed. Here, a reduced magnetic saturation moment $M_S = 1.5\,\mu_B$ is detected at 2 K, caused by a dominant fraction of paramagnetic Eu^{3+} cations in Eu_3O_4 or Eu_2O_3 phases, which instantly form under any oxygen excess. This mainly paramagnetic behavior is also reflected in the $M(H)$ curve (inset) of oxygen-rich EuO, in which a hysteretic behavior of remaining EuO is hardly identified.
The complete alteration of the magnetic behavior due to an oxygen partial pressure change of only 2×10^{-9} Torr underlines that the oxygen supply is an extremely important parameter during EuO synthesis, in order to obtain EuO/Si structures of stoichiometric type (*i*) instead of Eu_1O_{1+x} (*ii*).*

HAXPES: Analysis of the Eu 4*f* valence level

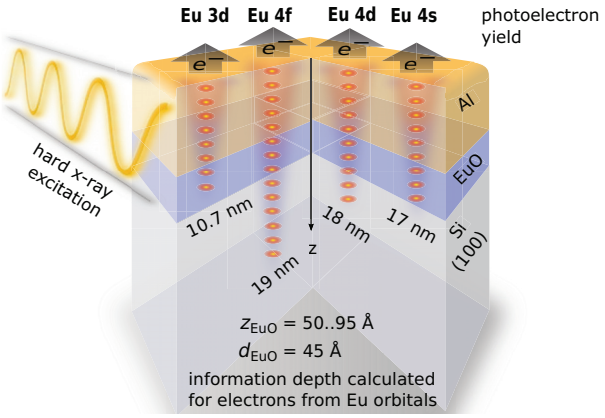

Figure 5.2.: Photoemission information depths z, as calculated for the particular EuO/Si heterostructures and core-levels investigated in this study under hard X-ray excitation of $h\nu = 4.2$ keV.

A straightforward analysis of the EuO chemical state is feasible by the analysis of the hard-dray photoemission spectra of the Eu 4*f* orbital. Due to the highly localized character of the 4*f* valence band with an energy dispersion limited to 0.3 eV,[41,171] hybridization with other ligand states is weak and photoemission from the deeper bound oxygen 2*p* valence band becomes well distinguishable, as indicated† by a recent LDA+U band structure of EuO[41]. In contrast to photoemission spectroscopy of deep core-levels, final state screening effects of the 4*f* photo-hole are negligible here. Depending on the Eu_1O_{1+x} stoichiometry, Eu cations will be either in a divalent Eu^{2+} initial state with half-filled $4d^{10}4f^7$ shell and a ferromagnetic moment of $7\,\mu_B$, or exist as trivalent Eu^{3+} occupying a $4d^{10}4f^6$ level, which is chemically

*One may want to compare this oxygen paramater with the synthesis of stoichiometric EuO on cubic oxides in Ch. 4.1 on p. 60.
†as depicted in Fig. 2.4 on p. 10.

shifted towards higher binding energies by reduced Coulomb repulsion and couples antiferromagnetically; this $4f^6$ configuration will exhibit more complex final-state multiplet effects that have been studied e. g. by Lang et al. (1981).[172]

HAXPES experiments were carried out at the undulator beamline P09 at PETRA III (DESY Hamburg) using a photon excitation energy of 4.2 keV. The spectra were recorded at room temperature in normal emission geometry with an energy resolution of 0.5 eV.* The binding energy scale was calibrated to the metallic Fermi edge of an Au foil in contact with the sample. A Shirley-type background was subtracted from the raw data to correct inelastic photoelectron scattering.

Eu $4f$ valence band spectra in normal emission geometry are depicted in Fig. 5.3a and c for both EuO compounds (*i*) and (*ii*). A center of spectral weight is located 1.8 eV below E_F in both spectra, which can be clearly identified as electron emission from the divalent Eu^{2+} initial state in a $4f^7 \rightarrow 4f^6$ final state configuration. The Eu^{2+} peak agrees well with the calculated divalent Euf $4f$ multiplet depicted in Fig. 5.3e.[173] Moreover, a doublet peak centered at ~4.8 eV below E_F is assigned to the emission from O $2p$ orbital, which originates from both EuO and Al_2O_3. The absence of a second multiplet in the higher binding energy region in Fig. 5.3a indicates, that the Eu cations in compound (*i*) are mainly of divalent valency, as expected for stoichiometric EuO.

In contrast, the $4f$ spectrum of the EuO compound (*ii*) in Fig. 5.3c shows a large additional multiplet structure in the binding energy region from 5–13 eV below E_F, which corresponds to the $4f^6 \rightarrow 4f^5$ final state multiplet of trivalent Eu^{3+}. The broad Eu^{3+} final state structure is in accordance with previous experimental studies on oxidized Eu compounds[159,160,174,176] and with calculated multiplet lines[172,175] (Fig. 5.3e). Due to over-oxidation in compound (*ii*), the contribution of the overlapping O $2p$ peak has significantly increased. From the presence of both $4f^6$ and $4f^5$ final state multiplets, we anticipate, that the initial state valency of Eu in compound (*ii*) is of mixed divalent and trivalent nature, which is indicative for the Eu_3O_4 oxidation phase.

A necessary criterion to identify the stoichiometry of the magnetic oxide EuO is its initial state valency. Therefore, we quantify the spectral contributions of divalent ($n = 7$) and trivalent ($n = 6$) Eu cations from the respective $4f^{n-1}$ peak intensities. However, the EuO surface electronic structure may significantly differ from that of bulk EuO, due to changes in local atomic geometry or coordination in direct proximity to the Al/Al_2O_3 capping layer. Thus, surface-shifted and bulk-like final states may contribute to the Eu photoemission peak, shifted in binding energy E_B by $\delta_S = E_B^{surface} - E_B^{bulk}$. To discriminate between surface and bulk-related photoemission, we vary the depth sensitivity of the HAXPES experiment by recording spectra in normal emission (*ne*) and 43° off-normal emission (*oe*) geometry. From our calculated energy and angle-dependent information depths ID_{4f} of photoelectrons,† we expect an enhanced surface sensitivity of 30% for $4f$ photoemission in (*oe*) geometry compared to the bulk-sensitive (*ne*). Depth-dependent information can be extracted from Fig. 5.3b and d, which display the difference intensity curves of the normalized and background-corrected $4f$ spectra recorded in (*oe*) and (*ne*) geometries, $\Delta I^*_{4f} = I^*_{oe} - I^*_{ne}$. In these plots, $\Delta I^* < 0$ (> 0) correspond to contributions from bulk (I^*_B) (surface (I^*_S)) photoemission. For

*We refer to Ch. 3.4.3 on pp. 48 for details on the beamline and the electron analyzer.

†see Ch. 3.4.4 on p. 51, or references Powell et al. (1999), Tanuma et al. (2011).[84,179]

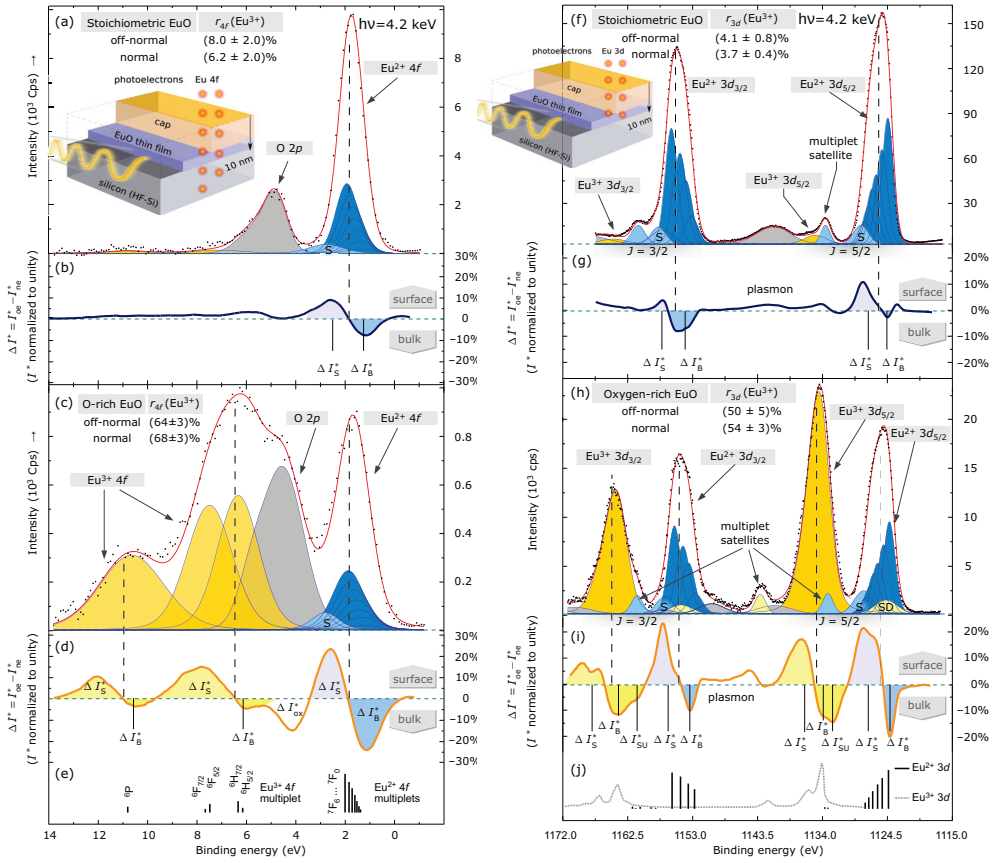

Figure 5.3.: Ultrathin EuO films (d = 45 Å) directly on HF-Si investigated by HAXPES.
For the Al/EuO/HF-Si heterostructures, HAXPES spectra of the Eu 4f valence level (a–d) and of the Eu 3d deep core-level (f–i) are analyzed by quantitative peak fitting. Plotting the difference of spectral weight in grazing and normal emission geometries (b, d and g, i) exploits any surface and bulk contributions of the EuO thin film. For curve fitting, calculated Eu^{2+} and Eu^{3+} multiplets[110,111,172,174,175] (e and j) serve as reference of binding energies for the photoemission final states.

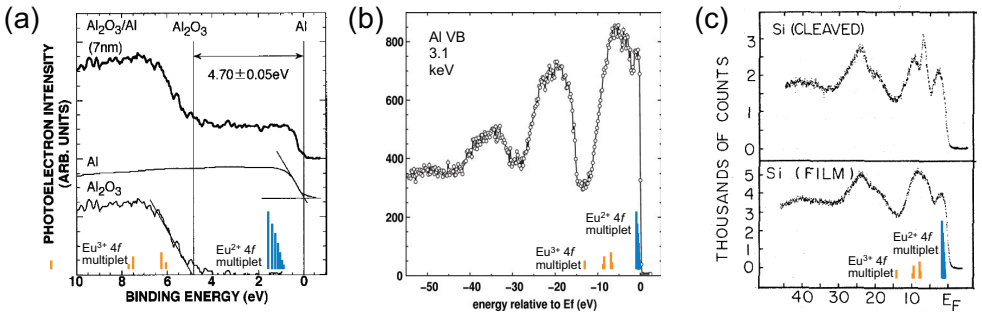

Figure 5.4.: Valence bands of Al_2O_3, Al and Si in comparison with Eu $4f$ PES multiplets. From Miyazaki (2001), Drube (2012) and Ley et al. (1972).[99,177,178]

both EuO compounds (*i*) and (*ii*) we observe a redistribution in peak intensity within the divalent Eu^{2+} $4f^6$ final state from the lower binding energy side ($-\Delta I_B^*$) towards the higher binding energy side ($+\Delta I_S^*$). This result suggests, that the $4f^6$ final state multiplet of both EuO compounds is composed of a bulk component *B*, located at a binding energy of $E_B \cong 1.8$ eV, and a surface component *S* shifted towards higher binding energy due to the contact with Al/Al_2O_3. The Eu^{2+} $4f$ surface shifts for the EuO compounds (*i*) and (*ii*) are determined as $\delta_S^{(i)} = 1.2$ eV and $\delta_S^{(ii)} = 1.3$ eV, respectively. A quantitative analysis of the Eu^{3+} $4f$ interface shift is impeded by the overlap with the O $2p$ states.

In order to quantify the chemical states of the Eu $4f$ photoemission peak in Fig. 5.3a and c, we fit the $4f^{n-1}$ multiplets using convoluted Gaussian-Lorentzian curves. Three tunable parameters were employed for least-squares fitting, namely the energy separation between the divalent and trivalent Eu contributions, their intensity ratio and the spectral width (FWHM) for every species. For Eu^{2+}, a multiplet fine structure serves as reference for binding energy in accordance with theoretical calculations by Cho et al. (1995). Least-squares best-fit curves are shown by the solid curves in Fig. 5.3a and c, which match the experimental data points very well, and the resulting intensity ratios and energy positions of Eu^{2+} and Eu^{3+} species are summarized in Tab. 5.1. From the integrated spectral intensities *A* of the Eu^{2+} and Eu^{3+} components, we derive the relative fraction of trivalent Eu as $r^{Eu^{3+}} = A^{Eu^{3+}}/(A^{Eu^{2+}} + A^{Eu^{3+}})$. For the EuO compound (*i*), we determine mainly an integral divalent chemical state of the Eu cations (trivalent contribution $r_{4f}^{Eu^{3+}} = 7.4\%$). For the EuO compound (*ii*), in contrast, a mixed initial valency with a trivalent contribution of $r_{4f}^{Eu^{3+}} \approx 66\%$ is derived. Thus, we confirm EuO compound (*i*) as *stoichiometric* EuO and (*ii*) as *oxygen-rich* Eu_1O_{1+x}.

A comparison of contributions to the valence level from the entire Al/EuO/Si heterostructure is given in Fig 5.4. In Fig. 5.4a, the Al_2O_3 valence band[177] coincides mainly with Eu^{3+} PES final states. The metallic Al valence band[99] (*b*) and the Si valence band[178] (*c*) coincide with both Eu^{2+} and Eu^{3+} PES multiplets.[110,111,172,174,175] Thus, the oxidation state and thickness of the Al overlayer influences the spectral weight observed at the energy position of Eu $4f$ final states. Our Eu^{3+} spectral fit does not include any Al $3s$ and Al^{3+} $3s$ contributions[177] from the cap layer or the Si valence band[178] from the substrate in this energy region, which may lead to a slight over-estimation of $r_{4f}^{Eu^{3+}}$.

HAXPES: Analysis of the Eu 3*d* deep core-levels

Now we proceed with spectra of the more deeply bound Eu 3*d* core-levels, which helps to provide a consistent quantification of the initial state valency in conjunction with the Eu 4*f* results. We note, that analyzing the 3*d* core-level spectra has a significant advantage for the determination of the initial state Eu valency compared e. g. to the 4*d* core-levels, because the 3*d* states show a much weaker multiplet splitting and larger photoexcitation cross section. Moreover, the kinetic energy of Eu 3*d* photoelectrons is reduced by about 1150 eV, thus the probe is more surface sensitive within the EuO layer, as sketched in Fig 5.2.

Eu 3*d* photoemission spectra for EuO compounds (*i*) and (*ii*), recorded in normal emission geometry, are depicted in Fig. 5.3f and h. The spectra consist of a main peaks, the spin–orbit-like final state groups $3d_{j=5/2}$ and $3d_{j=3/2}$, which are clearly separated by a large spin–orbit coupling of 29.2 eV in agreement with previous studies.[159] The broad structure in the center is assigned to extrinsic plasmon excitations caused by high energy 3*d* photoelectrons, which dissipate the plasmon energy in the electron gas of the metallic Al top layer.[173] The plasmons are located at the expected energy loss (16 eV) from the $3d_{5/2}$ peak and the $3d_{3/2}$ peak.

Stoichiometric EuO (*i*) shows one main peak in each of the Eu $3d_{5/2}$ and $3d_{3/2}$ groups in Fig. 5.3f. Within the two spin–orbit split groups, the distribution of final states m_J is asymmetrically shaped, in perfect agreement with theoretical calculations of the divalent Eu 3*d* multiplet, as depicted for comparison in Fig. 5.3j.[110] A satellite peak in the high binding energy region of the Eu $3d_{5/2}$ (and $3d_{3/2}$) multiplet separated by 7.8 eV (6.3 eV) from the main peak belongs to the divalent Eu^{2+} multiplet of the $3d^9 4f^7$ final state. Energy splitting as well as intensity ratios of the satellites agree with previous reports on calculated and measured multiplet spectra of divalent Eu compounds.[110,111]

Evaluating the oxygen-rich EuO compound (*ii*) in Fig. 5.3h, we observe prominent double peak structures in the $3d_{5/2}$ ($3d_{3/2}$) regions, which are separated by 10.45 eV (10.90 eV). We assign these features to divalent Eu^{2+} ($3d^9 4f^7$ final state) and trivalent Eu^{3+} ($3d^9 4f^6$ final state) spectral contributions. Similar with the divalent Eu structure, the Eu^{3+} 3*d* multiplet consists of a doublet whith a satellite peak appearing at 6.9 eV higher binding energy below the $3d_{5/2}$ main peak. The Eu^{3+} $3d_{3/2}$ satellite structure is broadly distributed (not shown). The energy positions and shape of the Eu^{2+} and Eu^{3+} 3*d* multiplet final states agree well with previous experiments[176,180,181] and theoretical calculations,[110,111] as illustrated in Fig. 5.3j.

For a depth-sensitive analysis of the 3*d* core-levels, we calculate the energy and angle-depen-

Table 5.1.: Binding energies E_B and Eu^{3+} valency ratios $r^{Eu^{3+}}$ for (*i*) stoichiometric EuO and (*ii*) oxygen-rich Eu_1O_{1+x}, as obtained by least-squares fitting of the Eu 4*f* and 3*d* spectra.

Eu 4*f*	$E_B^{Eu^{2+}}$			$E_B^{Eu^{3+}}$			$r_{4f}^{Eu^{3+}}$	
(i) EuO	1.8 eV			7.0–11.1 eV			7.4 ± 1.2%	
(ii) EuO_{1+x}	1.64 eV			7.0–11.1 eV			66 ± 2%	
Eu 3*d*	$E_B^{Eu^{2+}}$ (eV)			$E_B^{Eu^{3+}}$ (eV)			$r_{3d}^{Eu^{3+}}$	
j =	5/2	3/2	ΔE_{SO}	5/2	3/2	ΔE_{SO}	5/2	3/2
(i) EuO	1124.9	1154.1	29.2	1134.7	1164.4	29.7	4.1%	3.2%
(ii) EuO_{1+x}	1125.0	1154.3	29.3	1134.8	1164.5	29.7	59%	49%

dent information depths as $\mathrm{ID}_{3d}^{ne} \approx 10.7\,\mathrm{nm}$ and $\mathrm{ID}_{3d}^{oe} \approx 7.3\,\mathrm{nm}$, indicating an increase in surface sensitivity of 43% for both emission geometries compared to $4f$ photoemission. The Eu $3d$ difference intensity curves $\Delta I_{3d}^{*} = I_{oe}^{*} - I_{ne}^{*}$ for both stoichiometric and oxygen-rich EuO compounds are given in Fig. 5.3g and i. While in the $4f$ spectra the Eu^{2+} ions show a symmetric shift from bulk to surface states, we observe a larger imbalance in intensity transfer of Eu^{2+} photoemission in the $3d$ spectra such that the surface contribution is clearly dominant, $|-\Delta I_{\mathrm{B}}^{*}| \leqslant |+\Delta I_{\mathrm{S}}^{*}|$. This spectral intensity from more surface-like states is explained by the significantly enhanced surface sensitivity of the $3d$ photoelectrons. Only for oxygen-rich EuO (*ii*) we find this accumulation of divalent ions in the surface region of the EuO layer, this effect coincides with "divalent surface states" of trivalent EuO compounds in literature.[111]

In order to quantify the Eu $3d$ multiplet, we use convoluted Gaussian-Lorentzian lines with consistent intensity ratios, peak widths and energy differences. The Eu^{2+} multiplet is in accordance with Cho et al. (1995).[110] For the Eu^{3+} $3d$ line shapes, we employ single Gaussian-Lorentzian peaks, respectively, since the explicit fine structure of the trivalent Eu $3d$ multiplet is not published to date. Two satellite features are included besides the Eu^{2+} and Eu^{3+} main $3d$multiplets. They may be interpreted as follows: due to a photoionization of the $4f$ valence level, the rearrangement of $4f^6$ electrons permits the acception of a conduction electron and is observed as an "apparent $Eu^{(III)}$ configuration" of the initial state, $4f^6\,5d^1$. This yields a so-called shake-up satellite at about 6.5–7.0 eV higher binding energy with respect to the main divalent Eu photoemission peak, $3d^9 : 4f^7\,5d^0$.[180] Moreover, we include contributions from a well-known $Eu^{(III)}$ $3d$ final state effect[180] referred to as shake-down (SD and Δ_{SD}^{*} in Fig. 5.3g and i). Here, unoccupied $4f$-subshells are lowered in energy by the potential of the $3d$ photohole, which allows a conduction electron to occupy these $4f$-subshells. This increases the occupation of $4f$-subshells, corresponding to an "apparent change of the initial valence" as observable in the photoemission energy region of $Eu^{(II)}$ $3d$. Thus, the shake-down satellite transfers intensity on the low binding energy side of the main photoemission peak,[176] and can be described within the Anderson impurity model.[182] Furthermore, for both Eu^{2+} $3d$ and Eu^{3+} $3d$ main peaks, a small surface spectral contribution S is included on the higher binding energy side. The best fit of the least-squares fitting is shown as solid line in Fig. 5.3f and h in very good agreement with the experimental spectra.

We determine the relative fraction of Eu^{3+} cations as $r_{3d}^{\mathrm{Eu}^{3+}} \approx 3.7 \pm 0.4\%$ for EuO compound (*i*) and $r_{3d}^{\mathrm{Eu}^{3+}} \approx 55 \pm 4\%$ for EuO of type (*ii*). This result is in good agreement with the quantitative analysis of the $4f$ valence states, as summarized in Tab. 5.1. Our quantification reveals the excellent chemical quality of the MBE-deposited EuO thin films, with a homogeneous depth distribution of Eu cations.

For (*ii*) oxygen-rich EuO, we extract an about 17% reduced fraction of Eu^{3+} cations from the more surface-sensitive $3d$ compared to the $4f$ emission. This underlines again a small accumulation of Eu^{2+} cations at the surface-near interface in contact with Al. The feature is consistently observed for both emission geometries in the Eu $4f$ and Eu $3d$ peak analysis and coincides with the grazing–normal emission difference intensity curves. Relating the formation energies[35,183] G_{f}°,

$$\mathrm{Eu_3O_4}\,(-2140\,\mathrm{kJ/mol}) \ll \alpha\text{-}\mathrm{Al_2O_3}\,(-1582\,\mathrm{kJ/mol}) < \mathrm{Eu_2O_3}\,(-1559\,\mathrm{kJ/mol})$$

we may identify the thermodynamically most probable origin of divalent Eu ions in compound (*ii*): the formation probability of Eu_3O_4 exceeds these for alumina (Al_2O_3) and europia (Eu_2O_3). Indeed, Eu_3O_4 is mixed-valent with 66% Eu^{3+} ions, and thus fits perfectly

to the valency quantification of the oxygen-rich Eu compound (*ii*). Thus, we estimate the mixed-valent Eu_3O_4 to be the origin of the Eu^{2+} signal in oxygen-rich Eu_1O_{1+x}, which may also explain the Eu^{2+} accumulation near the surface as a result of reduction by metallic Al from the capping layer. The results of this section are published in Caspers et al. (2011).[1]

HAXPES: Analysis of the Eu 4*s* and Eu 4*d* core-levels

In order to develop a consistent compositional analysis of the two complementary EuO/Si heterostructures (*i*) and (*ii*), we include the Eu 4*s* and 4*d* photoemission spectra into the quantitative analysis. In studying the 4*s* and 4*d* core-levels, one has to take into account the dominant exchange interactions with the magnetic $4f^7$ open shell. Fig. 5.5a–d shows the Eu 4*s* and 4*d* core-levels for (*i*) stoichiometric EuO and (*ii*) oxygen-rich Eu_1O_{1+x} on Si. A quantitative least-squares peak fitting analysis of the divalent and trivalent spectral contributions in the Eu 4*s* and 4*d* spectra is employed to quantify the EuO chemical composition.

First, we identify the individual spectral features in the Eu 4*s* core-level. Figures 5.5 (a) and (b) show the Eu 4*s* core-level spectra for both (*i*) and (*ii*) EuO compounds. A clear double-peak structure is caused by coupling of the 4*s* core-level electrons with the localized Eu 4*f* state, which leads to an exchange splitting $\Delta E = 7.4\,\mathrm{eV}$ of the 4*s* inner shell. The spins in the 4*s* photoemission final state $|4s^1\,4f^7:\,{}^9S\rangle\,|\epsilon\ell\rangle$ are predicted to antiparallel for the lower binding energy peak and parallel for the higher binding energy peak $\left(|4s^1\,4f^7:\,{}^7S\rangle\,|\epsilon\ell\rangle\right)$ with respect to 4*s* emitted spin.[94,184] For stoichiometric EuO (*i*), the 4*s* double-peak is assigned to divalent Eu^{2+} spectral contributions, whereas an additional overlapping double-peak feature appears in Fig. 5.5b, that is chemically shifted by 8.1 eV towards higher binding energy. This shifted structure corresponds to trivalent Eu^{3+} ions.

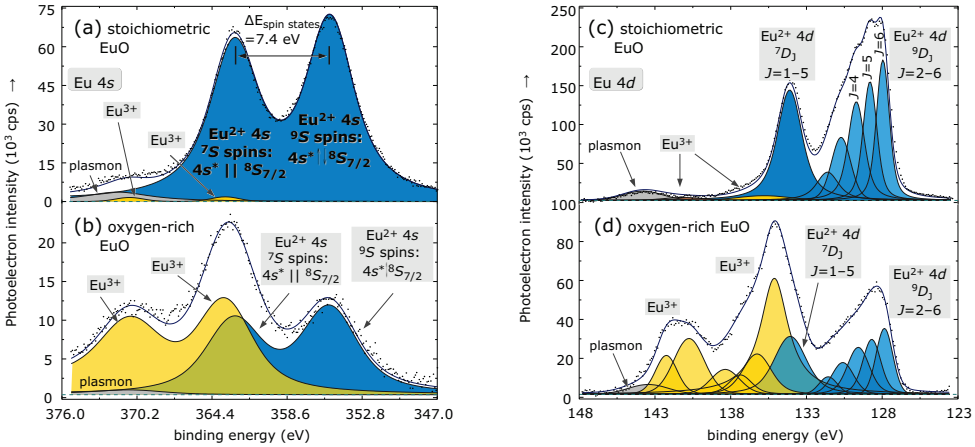

Figure 5.5.: Ultrathin EuO directly on HF-Si investigated by HAXPES. In Al/EuO/HF-Si heterostructures, HAXPES spectra of the Eu 4*s* core-level (*a*, *b*) and of the Eu 4*d* core-level (*c*, *d*) are analyzed quantitatively. For curve fitting, calculated Eu^{2+} and Eu^{3+} multiplets serve as reference for the final state binding energies.[110,111,172,174,175]

Proceeding with the most complex photoemission final state structure among the Eu core-levels, we present the Eu 4*d* core-levels in Fig. 5.5c and d. Their complex multiplet structure is distributed in a wide energy range from 125–170 eV and we focus on the most prominent double peak structure at lower binding energy. Due to the strong 4*d*–4*f* exchange interaction and much weaker 4*d* spin–orbit splitting, these two 4*d* peak shapes cannot be assigned $4d_{3/2}$ and $4d_{5/2}$ spin–orbit components. By assuming a $J = L - S$ multiplet splitting caused by the 4*d*–4*f* interaction, the two peaks are denoted as ^7D_J and ^9D_J multiplets, respectively.[112,114,115] The fine structure of the ^7D final state is not resolved, whereas the J = 2–6 components in the ^9D state are easily identified. In agreement with the other Eu core-levels, we clearly observe a mainly divalent Eu^{2+} valency in EuO (*i*), but significant spectral contributions from Eu^{3+} cations in oxygen-rich EuO (*ii*).

Finally, we performed a quantitative peak analysis by least-squares fitting of the spectral contributions with convoluted Gaussian-Lorentzian curves. The best fit is shown by the solid lines in Fig. 5.5a–d and matches the experimental spectra quite well. From the integrated spectral intensities of the divalent Eu^{2+} and trivalent Eu^{3+} components, we derive a relative fraction of Eu^{3+} cations of only 2.8% for stoichiometric EuO (*i*) and of 59% for oxygen-rich Eu_1O_{1+x} (*ii*), both in excellent agreement with the Eu 4*s* and 3*d* analysis, as summarized in Tab. 5.2. Again, the larger ratio of Eu^{3+} from the Eu 4*f* spectra is explained by the summation of Al and Si valence band spectral weight to the trivalent Eu peaks (as illustrated in Fig. 5.4 on p. 90).

Table 5.2.: Binding energies E_B and Eu^{3+} valency ratios $r^{Eu^{3+}}$ for (*i*) stoichiometric EuO and (*ii*) oxygen-rich Eu_1O_{1+x}, as obtained by least-squares fitting the Eu 4*s* and 4*d* spectra.

Eu 4*s*	$E_B(Eu^{2+})$			$E_B(Eu^{3+})$			$r_{4f}^{Eu^{3+}}$
4*s* spins	∥ 4*f*	↓↑ 4*f*	ΔE_{states}^{spin}	∥ 4*f*	↓↑ 4*f*	ΔE_{states}^{spin}	
(i) EuO	355.4 eV	362.7 eV	7.3 eV	363.5 eV	370.7 eV	7.2 eV	2.2%
(ii) EuO_{1+x}	355.4 eV	362.6 eV	7.2 eV	363.5 eV	370.7 eV	7.2 eV	53.0%
Eu 4*d*	$E_B(Eu^{2+})$			$E_B(Eu^{3+})$			$r_{3d}^{Eu^{3+}}$
$^{S+1}D_J$	^7D_J	$^9D_6$	ΔE_{states}^{spin}	^7D_J	$^9D_6$	ΔE_{states}^{spin}	$^7D_J + {}^9D_6$
(i) EuO	134.2 eV	128.0 eV	6.2 eV	141.9 eV	135.4 eV	6.5 eV	2.8%
(ii) EuO_{1+x}	134.3 eV	128.0 eV	6.3 eV	141.9 eV	135.4 eV	6.5 eV	59.0%

HAXPES: Impact of the EuO phases on the EuO/Si interface chemical state, observed by Si 2*p* photoemission

Having confirmed the stoichiometric quality of the EuO film on top of Si, we now proceed to study the chemical state of the interface formed between the EuO layer and the Si substrate, which is crucial for any electrical and spin transport. Here, we probe the local chemistry and bonding at the EuO/silicon transport interface by HAXPES. Photoemission from the Si 2*p* core-level was recorded in normal (0°) and off-normal (45°) emission geometry with hard X-ray ($h\nu$ = 4.2 keV) excitation. In this way, the information depth of the escaping photoelectrons is substantially varied between ∼18.4 nm and ∼13.2 nm, respectively, which allows to distinguish bulk and interface-like electronic states of the buried Si substrate.

In oxygen-rich EuO/HF-Si (*ii*), next to the well-resolved Si^0 2*p* peak, a broader feature can

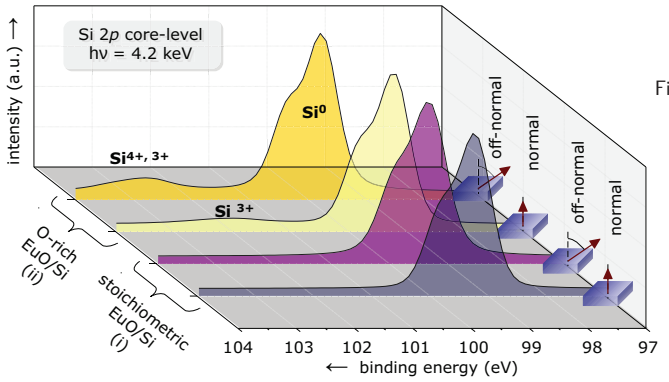

Figure 5.6.: Si 2*p* core-level photoemission spectra for stoichiometric EuO (*i*) and oxygen-rich EuO (*ii*), recorded at $h\nu = 4.2$ keV in normal ($\alpha \approx 0°$) and off-normal ($\alpha = 45°$) electron emission geometry.

be observed on the high binding energy side as depicted in Fig. 5.6. It is attributed to the emission from Si^{n+} 2*p* states, which indicates the presence of the silicon oxide, SiO_x. The chemical shift of $\Delta E \sim 3.0$ eV corresponds to Si^{3+} oxidation states, and $\Delta E \sim 4.0$ eV is the dioxide with Si^{4+} ions[139]. The Si^{4+} 2*p* spectral intensity is enhanced for off-normal emission, which confirms that the silicon dioxide signal mainly originates from the EuO/Si interface rather than deeper Si regions.

For stoichiometric EuO/HF-Si (*i*), we observe the well-resolved Si 2*p* doublet structure for both emission geometries, as depicted in Fig. 5.6. This doublet is indicative for an exclusively integral Si^0 valency both in the bulk and interface regions of the substrate. Any other valencies are absent in these Si spectra, which confirms the chemical stability of the EuO/HF-Si interface, which is in agreement with the predicted thermodynamic stability of EuO in contact with the Si surface.[14]

We finally conclude, that the chemical state of the EuO/HF-Si interface directly correlates with the specific EuO growth conditions at elevated substrate temperatures. In particular, any oxygen excess during EuO synthesis not only leads to the formation of antiferromagnetic EuO phases (favorably Eu_3O_4), but also promotes an oxidation of the EuO/Si interface. Only if the Eu distillation process and a precise oxygen supply is maintained, stoichiometric EuO thin films can be grown directly on Si without interface oxidation. The results of this section are published in Caspers et al. (2011, 2012).[3–5]

The highly sensitive interface chemistry observed for oxygen-rich EuO in contact with silicon motivates further investigations of the chemical interface properties of EuO on Si – both of which featuring high reactivity and and atomic mobility at elevated temperatures. Therefore, we conduct a thermodynamic analysis in order to elucidate the interface chemistry of the functional EuO/Si (001) heterointerface in the following section.

5.2. Thermodynamic analysis of the EuO/Si interface

In spite of the tremendous interest in EuO tunnel contacts on Si[7,25,74,185] and the well-established thin film synthesis of EuO*, no thermodynamic overview of possible EuO phases and reaction products in contact with silicon has been published to date. Such thermodynamic predictions are fruitful for experimentalists, particularly in the Eu distillation growth regime of EuO where reactions take place at elevated temperature and at constant pressure in a quasi-equilibrium. Given these conditions, we can compile the Gibbs free energies of formation G_f° from experimental studies[34,35,183,187–189] for possible compounds at the EuO/Si interface. In a further step, we extend our quantitative analysis to formation and disappearance reactions of possible interface reaction products during EuO-on-Si synthesis.†

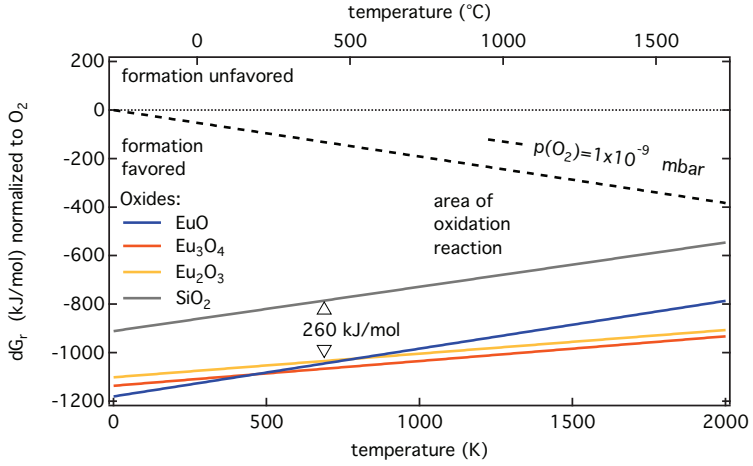

Figure 5.7.: Ellingham diagram for Eu oxide phases and SiO_2. The Gibbs free energies of formation of stoichiometric EuO, higher Eu oxides, and SiO_2 are normalized to a constant molar O_2 supply. All oxides are located in the stable oxide area situated left of an intersection with the oxygen curve $p(O_2)$.

First, we address a central question: may EuO exist in contact with Si, or will rather silicon dioxide form? While the static existence of (cold) EuO in contact with Si is already predicted[14], the synthesis under oxygen supply and under different temperatures has not been analyzed to date. To elucidate this question of oxidation, an Ellingham diagram is perfectly suited.† In order to evaluate the probabilities of formation for the experimentally most relevant interface compounds in comparison with EuO, we compiled Gibbs free energies of formation reactions $G_r(T)$ and a gas line for one representative O_2 pressure in Fig. 5.7.

We identify a narrow band of the Gibbs free energy in which all the $G_r(T)$ curves of Eu oxide phases are located. A zoom in and analysis of the different EuO phases is presented in Ch. 4 with the result that phase-pure EuO can be synthesized by Oxide-MBE. Here, we observe a

*Experimental challenges and solutions for phase pure EuO e. g. in [15,30,32,45,186].

†A systematic introduction to thermodynamics regarding the reaction potentials (like the enthalpy and Gibbs free energy) and Ellingham diagrams is given in the theory chapter, Sec. 2.1.

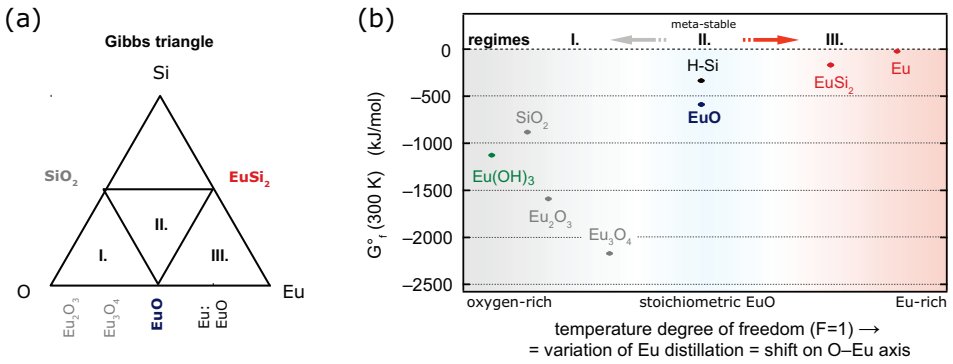

Figure 5.8.: Three growth regimes of EuO, illustrated in a Eu–O–Si Gibbs triangle (inset). (*I*) describes the oxygen-rich regime, (*III*) the Eu-rich EuO regime, and (*II*) can be referred to, when EuO is stabilized on (H-passivated) Si, as the stoichiometric EuO regime.

significant shift to lower Gibbs free energy from the Eu oxides to SiO_2 by 260 kJ/mol, which clearly exceeds energies of the Si surface or surface diffusion kinetics. This energy shift is nearly temperature independent. Thus we can conclude, that EuO is not only statically stable on Si, but is also under gaseous oxygen supply and under elevated temperature significantly more stable than the formation of SiO_2. We remark, that this prediction is of thermodynamic nature, thus the result (stable Eu oxides) may be reached after a long time or even mixed up by interface kinetics.

The Gibbs phase rule[36] connects the number of constituents C and resulting phases P with the degrees of freedom F of a system under constant pressure* as

$$F = C - P + 1. \tag{5.1}$$

In our system, the constituents are O_2–Eu–Si at constant and limited O_2 pressure, and the resulting phases are assumed to be SiO_2 + EuO + $EuSi_2$ during Eu distillation growth†. For this three-constituent system, a Gibbs triangle serves as a perfect visualization as depicted in Fig. 5.8a. The Eu–O–Si phase diagrams are constrained to contain only one, two, and at most three-phase regions. A one-phase region exists at the vertex of the triangle, e. g. Si. A two-phase region exists on any tie line where phases thermodynamically meet, e. g. Si and Eu. The interior of any triangle is a three-phase region, including probabilities for e. g. EuO + Eu + $EuSi_2$ in region III. Crossing tie lines are not allowed because at the point of their intersection the simultaneous coexistence of four phases would contradict the Gibbs phase rule, this for example negates the simultaneous existence of EuO + Eu + SiO_2 + $EuSi_2$ in thermodynamic equilibrium, as read from a fictitious crossing of lines SiO_2 → Eu with EuO → $EuSi_2$ from Fig. 5.8a. Hence, from the Gibbs triangle, we obtain a limit to three chemical regimes (I, II, and III) of resulting phases, which limits the number of co-existing phases to those being in the same subtriangle.

*The Gibbs phase rule for constant pressure is sometimes referred to as the "solid state phase rule". It is particularly suited for solid systems under low pressures in which one constituent is gaseous.

†as introduced in Ch. 4

What is the free parameter which drives the system into one of these regimes? The phase rule for constant pressures (5.1) evaluates $F = 1$, a degree of freedom in only one dimension. This degree of freedom is the temperature of synthesis T_S. Via this temperature, the Eu distillation condition during EuO synthesis is strongly affected by means of partial or complete re-evaporation of excess Eu, this corresponds to a shift along the O–Eu tie line in the Gibbs triangle. Therefore, the chemical phases can range from oxidized phases over stoichiometric EuO to metallic phases. This variation is plotted in Fig. 5.8b with different background colors revealing the chemical regimes (I), (II), and (III), all depending on the temperature degree of freedom.

We proceed with the quantitative analysis of EuO/Si interfacial reactions products. The reactions are evaluated by balancing the Gibbs free energies of formation,

$$\Delta G^\circ = \sum_{\text{products}} n G_f^\circ - \sum_{\text{reactants}} m G_f^\circ. \qquad \text{(after Hess' law)} \tag{5.2}$$

These balances are not limited to the comparison of bare formation energies $G_f(T)$ directly from the constituents as presented in the Ellingham diagram. We rather compare oxygen-rich (I) with Eu-distillation (II–III) chemical regimes during the EuO synthesis in the initial stage and during sustained growth. Herein, the distillation condition is persistently expressed by the term $(3\text{Eu} + \text{O}_2)$ and the oxygen-rich synthesis as $(\text{Eu} + 3/2\text{O}_2)$. First, we address the native metallic silicide $EuSi_2$, and then the silicon dioxide SiO_2. Among ternary compounds, we limit the discussion to $Eu(OH)_3$ which is the most probable europium hydroxide. In the case of a two-dimensional structure, we remark that the energy gain ΔG° is reduced compared to a volume reaction by the surface energy of the substrate: $\Delta G^\circ_{(1\times1)} = 113$ kJ/mol for (1×1)-Si (001), or $\Delta G^\circ_{(2\times1)} = 124$ kJ/mol for (2×1)-Si (001).[190]

Europium silicide reactions at the EuO/Si interface

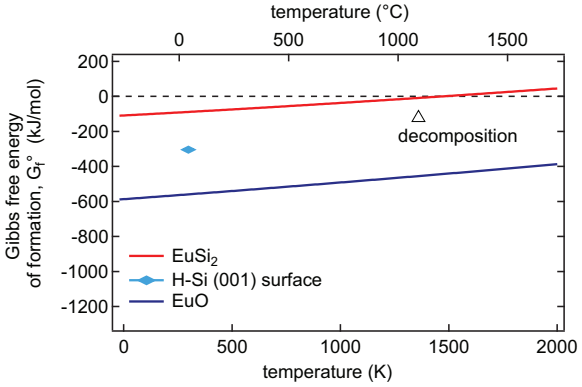

Figure 5.9.: Gibbs free energies of formation for EuO, the H-Si (001) surface, and $EuSi_2$. The silicide shows crossing to positive Gibbs free energy, which indicates a favorable decomposition at high temperature.

We begin with the thermodynamically least stable compound (Fig. 5.9), Europium silicide $EuSi_2$, notwithstanding being the most serious antagonist to any tunnel functionality due to its metallic conductivity and paramagnetic behvavior[191]. Despite the likely silicidation of Si surfaces, thermodynamic data for the native europium silicide $EuSi_2$ are still missing. Therefore, a calculation of the formation energy including the temperature dependence is

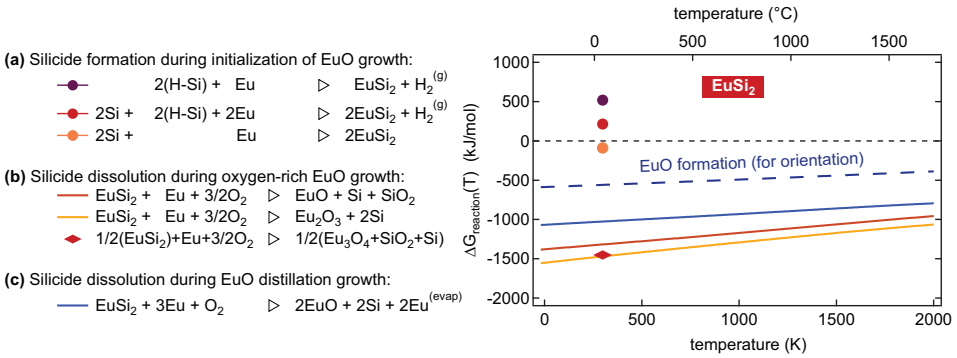

Figure 5.10.: Resulting Gibbs free energies of EuO/Si interface reactions involving $EuSi_2$.

needed. Such a calculation has been conducted by Rushchanskii (2012) and Ležaić (2011) using the harmonic approximation in density-functional perturbation theory (DFPT).* [191,192]

The chemical environment when beginning EuO synthesis is an Eu-rich seed layer for epitaxial growth on top of the hydrogen-passivated silicon surface, H-Si (001). These conditions reveal possible silicide formation reactions, as assembled in Fig. 5.10a. Their resulting Gibbs free energy is $\Delta G^{\circ}_{300\,\mathrm{K}} > 0$ (purple and red circles), which renders the silicide formation on H-Si unlikely. However, we analyze three different hydrogen coverages of the Si surface, complete passivation (purple circle), half surface passivation (red circle), and in case no hydrogen covers the Si surface surface, the asymptotic case of Eu + Si alloying (orange circle). It is evident, that only the complete hydrogen passivation of Si shows a large positive $G^{\circ}_{300\,\mathrm{K}} \gtrsim 500$ kJ/mol, while the results for fractional Si passivation follow $G^{\circ}_{300\,\mathrm{K}} \rightsquigarrow 0$, which is the thermodynamic threshold to a silicide formation probability. If no H passivation is left, the simple alloying reaction is thermodynamically favored to proceed ($G^{\circ}_{300\,\mathrm{K}} = -84$ kJ/mol). This underlines the importance of a complete hydrogen passivation of the Si (001) surface in order to prevent $EuSi_2$ formation.

Proceeding with the next stage of EuO synthesis on top of silicon, we analyze the two complementary EuO growth regimes (I) and (III), oxygen-rich growth in Fig. 5.10b and Eu distillation growth in Fig. 5.10c. During these EuO growth modes, EuO binds most of the supplied Eu, and any excess Eu is re-evaporated by the high synthesis temperature around the Eu sublimation point. Thus, during EuO synthesis silicides are thermodynamically unlikely formed (remember Fig. 5.9), and consequently we consider the disappearance of residual $EuSi_2$ from the initial Eu-rich stage of EuO growth. During oxygen-rich EuO growth (regime I. Red and yellow solid lines, red diamond in Fig. 5.10), the disappearance of $EuSi_2$ is very probable. Among the resulting phases, the formation of Eu_3O_4 and Eu_2O_3 are thermodynamically favored, yet not desired. During Eu distillation growth (regime III. Blue solid line in Fig. 5.10),

*Phonons of bulk $EuSi_2$ were calculated using DFPT [193] within local-density approximation [194] as implemented in Quantum-Espresso code. [225] A 6×6×6 k-point mesh was used for Brillouin-zone integration with a plane-wave kinetic energy cut-off of 30 Ha. For pseudopotential construction, the following valence-electron configurations were considered: $5s^2 5p^6 4f^7 6s^2$ for Eu and $3s^2 3p^2$ for Si. In the structural relaxation, the Hellman-Feynman forces were minimized to 2×10^{-4} Ry/Bohr. The thermodynamic potentials H and S were derived from the phonon density of state which was calculated at a 30×30×30 mesh in the Brillouin-zone.

the disappearance of $EuSi_2$ is still favorable and yields EuO, Si, and metallic Eu, altogether constituting a suited basis for further synthesis of high quality EuO by the Eu distillation condition. All $EuSi_2$ disappearance reactions show $G^{\text{dissol.}}_{EuSi_2}(T) \leqslant 2 \times G^{\text{f}}_{EuO}(T)$, thus being significantly more probable than the formation of EuO, given for orientation as dashed blue line in Fig. 5.10.

In conclusion, the only remaining condition when metallic europium silicide may be formed is the initial stage of EuO synthesis with excess of Eu and an incomplete passivation of the Si surface. Our thermodynamic prediction clearly prohibits a formation of $EuSi_2$ during EuO synthesis and in case of a complete hydrogen passivation of the Si surface. In short: the H-Si (001) surface is suited to provide a silicide-free EuO/H-Si hybrid structure.

Silicon dioxide reactions at the EuO/Si interface

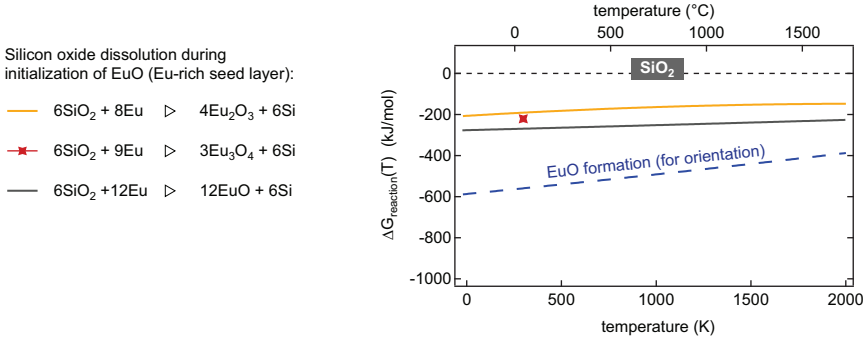

Figure 5.11.: Resulting Gibbs free energies of EuO/Si interface reactions regarding SiO_2 in the initial growth stage of EuO (Eu seed layer).

While employed as chemically stable dielectric in many semiconductor applications, our approach is the avoidance of polycrystalline SiO_2 at the Si surface in order to maintain a structurally sharp and chemically well-defined functional interface of EuO directly on Si. From the Ellingham diagram (Fig. 5.7) we have already derived that all Eu oxides phases are thermodynamically more stable than SiO_2, and this is true for any temperature. However, residual SiO_2 from the Si wafer may be located on the Si (001) surface, and due to diffusion and surface defects SiO_x may form even under EuO growth conditions. This renders an in-depth thermodynamic analysis of SiO_2 disappearance and formation reaction at the EuO/Si interface very reasonable.

First, we consider the Eu-rich start of EuO synthesis directly on top of the Si wafer. No oxygen is supplied for the Eu seed layer, and only disappearance of residual SiO_2 may occur, as compiled in Fig 5.11. We analyze disappearance reactions leading to all possible europium oxide valency phases: they are formed with almost comparable probability, but divalent EuO is thermodynamically most favorable (grey solid line) with the most negative $G^{\text{dissol.}}_{SiO_2}(300\,\text{K}) \approx -280\,\text{kJ/mol}$. Remarkably, once oxygen supply initiates EuO synthesis, the EuO formation (blue dashed line) shows more than double the gain in Gibbs free energy and thus displaces any initial SiO_2 disappearance reaction. Therefrom, only in the initial stage of Eu deposition as a seed layer the SiO_2 disappearance is considerable, leading with the largest probability to

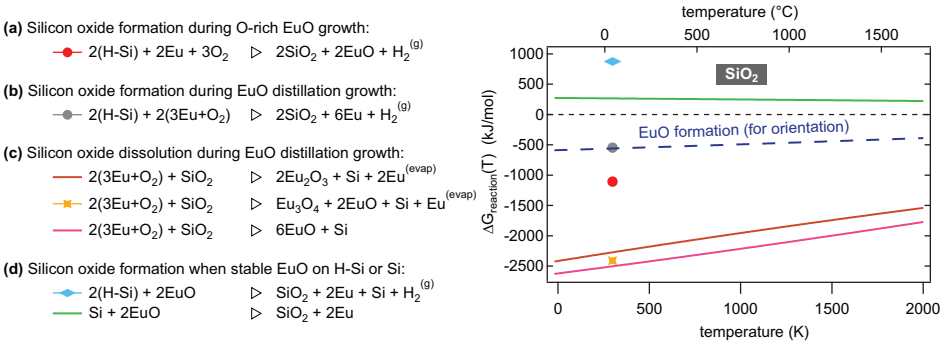

Figure 5.12.: Resulting Gibbs free energies of EuO/Si interface reactions involving SiO_2 during EuO synthesis, and for stable EuO on Si (001).

the divalent EuO phase.

In the next step, we proceed with reactions involving SiO_2 during EuO synthesis. First, the analysis of oxygen-rich EuO (regime I in the Gibbs triangle) growth is depicted in Fig. 5.12a and reveals in conjunction with divalent EuO a highly favorable formation of SiO_2 (red circle).* This denotes thus an exclusively oxidic result of the initial EuO layers without any metallic silicide or Eu. We proceed with the complementary EuO growth mode, the Eu-distillation growth (regime III in the Gibbs triangle) of EuO on H-Si as depicted in Fig. 5.12b–c. Herein, the resulting Gibbs free energy of the SiO_2 formation during Eu distillation growth equals almost the bare EuO formation energy. Which one is the thermodynamically favored result? If we analyze the energy gain of the EuO formation, we find it at $G^{\mathrm{f}}_{\mathrm{EuO}}(300\,\mathrm{K}) = -559\,\mathrm{kJ/mol}$, while the SiO_2 formation reaction results in $G^{\mathrm{f}}_{\mathrm{SiO_2}}(300\,\mathrm{K}) = -546\,\mathrm{kJ/mol}$, which is only 2% less gain of Gibbs free energy and thus a weak argument for a possible dominance of the EuO formation.

In order to elucidate the SiO_2 behavior from another viewpoint, we consider its disappearance during Eu distillation growth in Fig. 5.12c. We find, that the SiO_2 disappearance is very probable yielding all different EuO valencies, with an energy gain of $G^{\mathrm{dissol.}}_{\mathrm{SiO_2}}(300\,\mathrm{K}) \approx -2500\,\mathrm{kJ/mol}$. However, upon SiO_2 disappearance the most favorable products are the mixed-valent Eu_3O_4 and divalent EuO. This underlines the importance of minimization of any SiO_x at the EuO/Si interface, because SiO_2 may act as constituent for oxidation yielding antiferromagnetic higher Eu oxides. We remark, that disappearance reactions of SiO_2 need an activation energy and are more likely at elevated temperatures.

Finally, when layers of stoichiometric EuO have been grown on top of the Si surface, we investigate the thermodynamic stability of this system. In Fig. 5.12d, stable EuO on either bare Si (001) or hydrogen-passivated Si (001) are analyzed with respect to a possible SiO_2 formation. In case of H-Si as the substrate, the resulting Gibbs free energy is $G^{\mathrm{f}}_{\mathrm{SiO_2}}(300\,\mathrm{K}) = +900\,\mathrm{kJ/mol} \gg 0$ and thus extremely unfavored. Here, it is safe to state that EuO is thermodynamically stable directly integrated with H-Si (001), this coinciding with a previous thermodynamic prediction.[14] Furthermore, when we consider EuO on bare

*This is evident from the large gain of Gibbs free energy upon SiO_2 formation as already summarized in the introductory figure 5.7 on p. 96.

Si, $G^{f}_{SiO_2}(300\,K) \approx +200$ kJ/mol, which is in the range of the reconstruction energy of the Si (001) surface. Thus, under unpropitious conditions like surface contamination or roughness, some SiO_2 may form on thermodynamic average for bare Si (001). Again, we remark that the SiO_2 formation needs an activation energy, thus is likely only at elevated temperatures of several hundred °C.

From our thermodynamic balances, we conclude that in the oxygen-rich EuO growth regime the Si dioxide will form as well. Thus, the growth regime of choice is the Eu distillation growth mode. Here, EuO is thermodynamically more favored. Nonetheless, SiO_2 formation cannot be excluded because the resulting energy gain of EuO is larger only by 2% than for the SiO_2 formation. Fortunately, during ongoing Eu distillation growth, SiO_2 disappearance is evaluated to be extremely favorable. However, SiO_2 disappearance yields EuO and also higher Eu oxides. Finally, EuO on H-Si is confirmed to be clearly stable.

Europium hydroxide and silicates at the EuO/Si interface

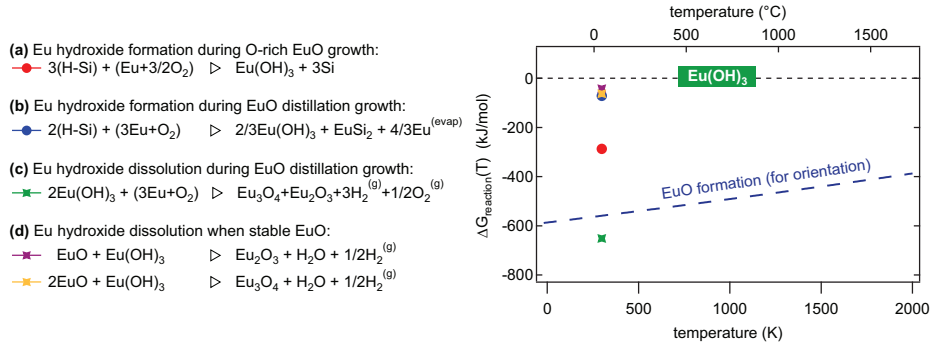

Figure 5.13.: Resulting Gibbs free energies of EuO/Si interface reactions involving Europium hydroxide.

In this section, we consider ternary phases at the EuO/Si interface, which are commonly formed in case of equilibrium, i.e. if every constituent is provided and the reactants may form in their standard state (solid). First, we analyze the most likely Europium hydroxide (often referred to as "the hydride") $Eu(OH)_3$ as depicted in Fig 5.13. Again, we start from preconditions of either or oxygen-rich EuO growth or Eu-distillation growth (regimes I or III, respectively), and we assume a hydrogen-passivated Si substrate. In case of oxygen-rich EuO synthesis (in Fig. 5.13a, red circle), Eu hydroxide may form with a gain of Gibbs free energy of $G^{form.}_{Eu(OH)_3}(300\,K) \approx -290$ kJ/mol, which is only half the gain for EuO formation. Still thermodynamically possible is the formation of $Eu(OH)_3$ during Eu distillation growth (in Fig. 5.13b, blue circle), however the energy gain is small ($\Delta G_r \approx -90$ kJ/mol). Moreover, during Eu-distillation growth, a disappearance of the hydroxide (green cross) is thermodynamically more favorable than the EuO formation itself. When we consider stable EuO together with $Eu(OH)_3$, we even find disappearance reactions to be thermodynamically favorable in the range $\Delta G_r \approx -60$ kJ/mol. All disappearance reactions, however, yield preferably higher oxidized Eu oxide phases rather than divalent EuO. For most lanthanide hydroxides, the hydroxide disappearance occurs at elevated temperatures ($T \geqslant 300$ °C) and is basically an evaporation of water.[195,196] While H-passivation of Si or different growth regimes of EuO

do not allow a clear prevention of hydroxide formation, two practical methods circumvent $Eu(OH)_3$: using bare Si instead of H-Si obviates the constituent H for $Eu(OH)_3$ formation. Any further hydroxide formation can be prevented by depriving any traces of H_2 or H_2O gas in the UHV system (Oxide-MBE).

For europium hydroxide, we conclude that neither hydrogen passivation of Si nor different EuO growth regimes are capable to prevent hydroxide formation. Nevertheless, the energy gains on formation are comparably small with respect to SiO_x or higher Eu oxides. The disappearance of $Eu(OH)_3$ is thermodynamically favored, yielding preferably trivalent Eu oxides. To practically prevent the Eu hydroxide, a H-Si surface as well as a H_2 atmosphere in the system of synthesis are to be avoided.

We exclude the following compounds from discussion due to their negligible formation probabilities: mineralic contaminations on top of the Si surface, like silicates, will form only at process temperatures of $T_S \geqslant 800$ °C ($Si(OH)_4$) or 1500 °C ($Eu_3^{(II)}SiO_5$).[197,198] Moreover, complicated silicide phases Eu_xSi_y are predicted[199] or experimentally investigated[200,201] in previous studies; here, we limit the discussion to the most probable native silicide, $EuSi_2$. Finally, silane phases (Si_nH_{2n+2}) are considered to be negligible due to their thermal instability.[196]

Nucleation probability and surface kinetics at the EuO/Si heterointerface

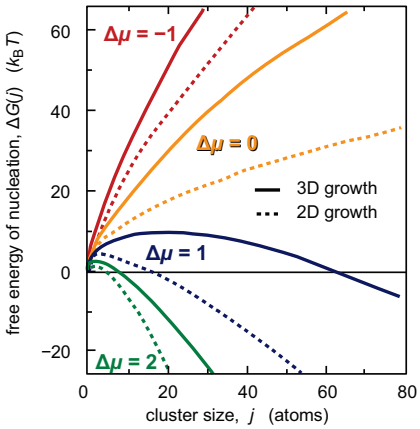

Figure 5.14.: Free energy of nucleation $\Delta G(j)$ for different saturations $\Delta\mu$.
At negative $\Delta G(j)$, nucleation of the deposit is thermodynamically favored to proceed. A maximum of the curvature in a positive energy regime constitutes a nucleation barrier. The curves are to scale for the surface free energy term $X = 4$, and for $\Delta\mu = -1,\ 0,\ 1,$ or 2. $\Delta G(j)$, $\Delta\mu$, and X are chosen to be in the unit k_BT in agreement with Weeks and Gilmer (1979).[202] Adapted from J. A. Venables (1999).[203]

Reaction balances are thermodynamic in nature and ignore reaction kinetics. Thus, processes that we have predicted to be favorable by the Gibbs free energy balances in Ellingham diagrams can still be slow – or be enhanced by molecular kinetics. Therefore, we expand our picture of the EuO/Si interface by means of the classical growth kinetics on surfaces: the nucleation theory.[203] For the substrate–deposit heterosystems, we revisit the concept of surface and interface energies.* The predictions of the classical nucleation theory are dependent on the knowledge of the saturation, the surface energies γ, and the geometry for each deposit. A measure for the thermodynamic probability of a cluster nucleation containing j atoms is the

*See section "MBE growth" in chapter 3.1.

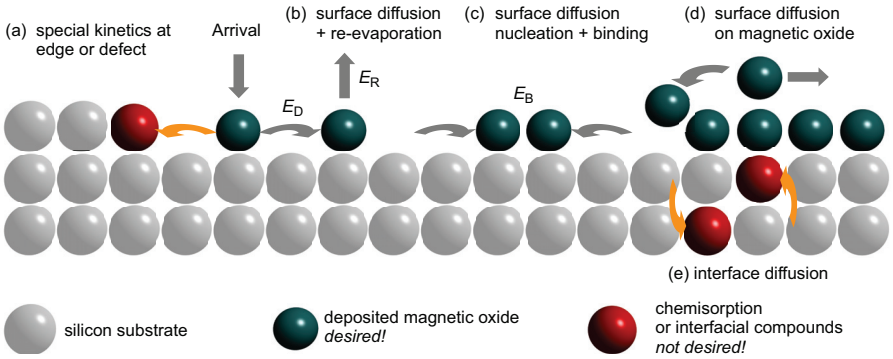

Figure 5.15.: Surface processes for a magnetic oxide (MO) on Si deposition. First, MO atoms are supplied and arrive on the Si surface. Either desired processes may proceed (b,c,d) which form a stoichiometric and heteroepitaxial MO layer; or undesired chemisorption or contaminations may form with the Si surface (a,e). Adapted from Venables (1994). [204]

nucleation energy,

$$\Delta G(j) = -j\,\Delta\mu + j^{2/3}X, \qquad X = \underbrace{\sum_k C_k\,\gamma_k}_{\substack{\text{surface energy of } k \\ \text{faces of the deposited cluster}}} + \underbrace{C_{SF}\,(\gamma^* - \gamma_F)}_{\substack{\text{interface energy} \\ \text{between substrate } S \\ \text{and film } F}} . \tag{5.3}$$

Herein, C_k and C_{SF} are geometrical constants depending on the shape of the cluster of size j. The saturation factor $\Delta\mu$ of the deposit is discriminated between

$$\Delta\mu \quad \begin{cases} < 0, & \text{undersaturation, and} \\ > 0, & \text{supersaturation of the deposit.} \end{cases}$$

Typical shapes of $\Delta G(j)$ curves for different $\Delta\mu$ are shown in Fig. 5.14. In case of an undersaturation of the deposit, nucleation is unfavored (red lines). If, however, a supersaturation is eminent ($\Delta\mu \gg 0$), the thermodynamic behavior of $\Delta G(j)$ predicts growth of clusters of the deposit. Thereby, the cluster size j allowing for a nucleation reduces to a few atoms.

Now, we apply the classical nucleation theory to obtain comparisons of cluster formation probabilities at the EuO/Si interface. In the EuO/Si heterosystem, however, for EuO and the interfacial contaminants $EuSi_2$, $Eu(OH)_3$, and SiO_2 the nanostructure of nucleation sites directly on Si (001) is unknown to date. This hampers a numerical evaluation of $\Delta G(j)$ by eq. (5.3), and thus predictions have to be taken with a grain of salt.

First, we consider the initial stage of EuO growth which is a Eu seed layer in the monolayer regime. This means supersaturation and a large $\Delta\mu$. Moreover, Eu has an extremely low surface energy* ($\gamma_{Eu} = 0.46\,J/m^2 < \frac{1}{2}\cdot\gamma_{Si}$). Thus, for Eu on Si (001), the factor X in eq. (5.3) is small and allows for negative energies $\Delta G(j)$ of the nucleation, independent from the cluster size j: Eu wets the Si surface.

*see Table 3.1 on p. 37.

Second, a possible H supply from a H-passivated Si surface motivates an analysis of the hydrate $Eu(OH)_3$. An extreme undersaturation of H far from equilibrium is given at the H-Si surface. Given $\Delta\mu \ll 0$ for H and $\Delta\mu \approx 0$ for limited O_2 supply, the nucleation theory predicts a large formation barrier for $Eu(OH)_3$ clusters (either 2D or 3D), corresponding to red or orange lines in Fig. 5.14. Thus, from the classical nucleation theory, $Eu(OH)_3$ is not predicted to form clusters.
Finally, the remaining compounds are the desired magnetic oxide EuO, and the interfacial contaminants $EuSi_2$ and SiO_2. However, as mentioned before, a nucleation of these compounds cannot be evaluated due to the lack of nano-structural and surface energy data.

Besides the classical nucleation theory, many kinetic surface effects between Si and the deposit will likely proceed at elevated temperatures of synthesis. These are sketched in Fig. 5.15. In particular, special kinetics at substrate imperfections and edges (the Ehrlich-Schwoebel barrier[205]), as well as interdiffusion of the deposit with Si layers change the stoichiometry, structure and even magnetism, and render themselves as major antagonists to a functional transport interface. This motivates a comprehensive experimental study, in which we determine conditions for which the functional EuO/Si interface remains structurally sharp and chemically clean: nowadays often referred to as *interface engineering*.[7]

5.3. Interface engineering I: Hydrogen passivation of the EuO/Si interface

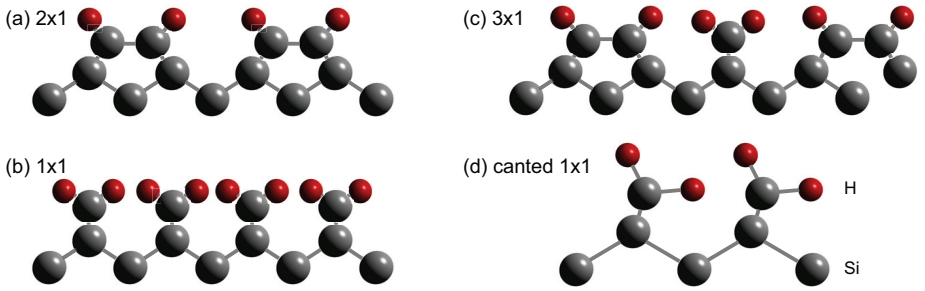

Figure 5.16.: Si (001) surface reconstructions. Clean Si (001) reconstructs as (2×1) dimers (*a*) and would have the least dense H-termination. The bulk (1×1) surface has the most dense H-termination (*b*). However, mixed variants like (3×1) are energetically favorable (*c*), and in reality, a canted (1×1) H-Si surface is usually observed (*d*). After Northrup (1991).[206]

Dangling bonds of the Si (001) bulk (1×1) surface will either form a reconstructed (2×1) surface under clean UHV conditions, or react with air or organic adsorbates to form a bulk-like yet contaminated surface layer. Here, we discuss the *in situ* hydrogen passivation of the Si (001) dangling bonds. Predicted reconstructions of the Si (001) surface with H-termination are compiled in Fig. 5.16. Experimentally, this is achieved *in situ* by a special atomic hydrogen supply as introduced in the experimental chapter (Ch. 3.3).

Routinely, the Si wafer pieces of prime quality are treated with an *in situ* flashing procedure at a background pressure better than 5×10^{-10} mbar, this yields a superior clean and atomically smooth Si (001) surface, as controlled by Auger electron spectroscopy and LEED.

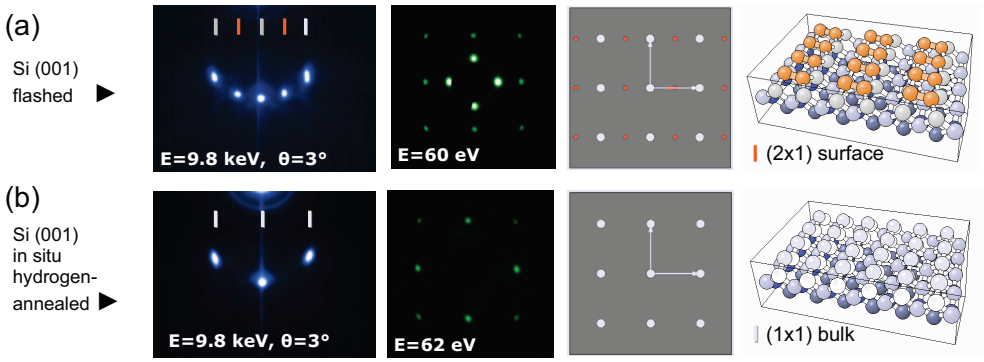

Figure 5.17.: Hydrogen termination of the clean Si (001) surface as observed by RHEED (blue), LEED (green), and simulated by LeedPat[224] and SSD[226]. The flashed Si (001) surface (*a*) shows diffraction pattern of the bulk and the (2x1) surface reconstruction dimers as indicated orange.

These cleaned Si substrates show a (2×1) reconstruction dimers aligned along the [100] as well as [010] axes of the Si (001) single-crystal, as observed in Fig. 5.17a. After applying the *in situ* hydrogen passivation procedure, the surface reconstruction completely vanishes and only the (1×1) bulk structure of Si is observed by electron diffraction (Fig. 5.17b). Remarkably, the RHEED and LEED spots of the passivated H-Si (001) surface are equally sharp as for the freshly flashed Si surface, and no polycrystalline fraction is emergent. The latter would be indicated by diffuse circular intensities in LEED.* A chemical characterization by Auger electron spectroscopy of the H-Si surface in comparison with other surface treatments can be found in the appendix (Ch. A.2).

Structural optimization of EuO and the EuO/Si interface

With a chemically clean and structurally crystalline H-passivated Si (001) surface at hand, we proceed to the synthesis of EuO on top of H-Si and as a reference on clean Si (001). We recorded electron diffraction pattern during EuO deposition (RHEED) and after EuO growth has finished (LEED), as compiled in Fig. 5.18. For bare Si (001), the clean and single-crystalline surface allows for an initial heteroepitaxial growth of EuO, as indicated by streaks in the RHEED pattern (Fig. 5.18a). The EuO diffraction pattern, however, develops vertically aligned spots and a diffuse background from non-crystalline scattering already after 2 nm growth. Finally, after 7 nm EuO synthesis, the crystalline pattern are largely replaced by circular intensities as expected for a polycrystalline film. No LEED is observed after EuO growth. High-resolution transmission electron microscopy (HR-TEM) provides a cross-sectional view of the EuO/Si heterostructure in the nanometer regime. In Fig. 5.18b, the Si substrate shows a perfect diamond structure, but in the 10 nm-thick EuO slab, a polycrystalline EuO layer of 3 nm thickness is identified in contact with the Si surface. Above this intermediate layer, crystalline EuO is observed. However, bulges of lateral dimension

*However, we remark that such a clean hydrogen passivation needs weeks of bake out of the H_2 supply lines and a cryo trap system for residual vapors such as oxygen or organics. The H_2 cracker itself must be properly cleaned and degased, too.

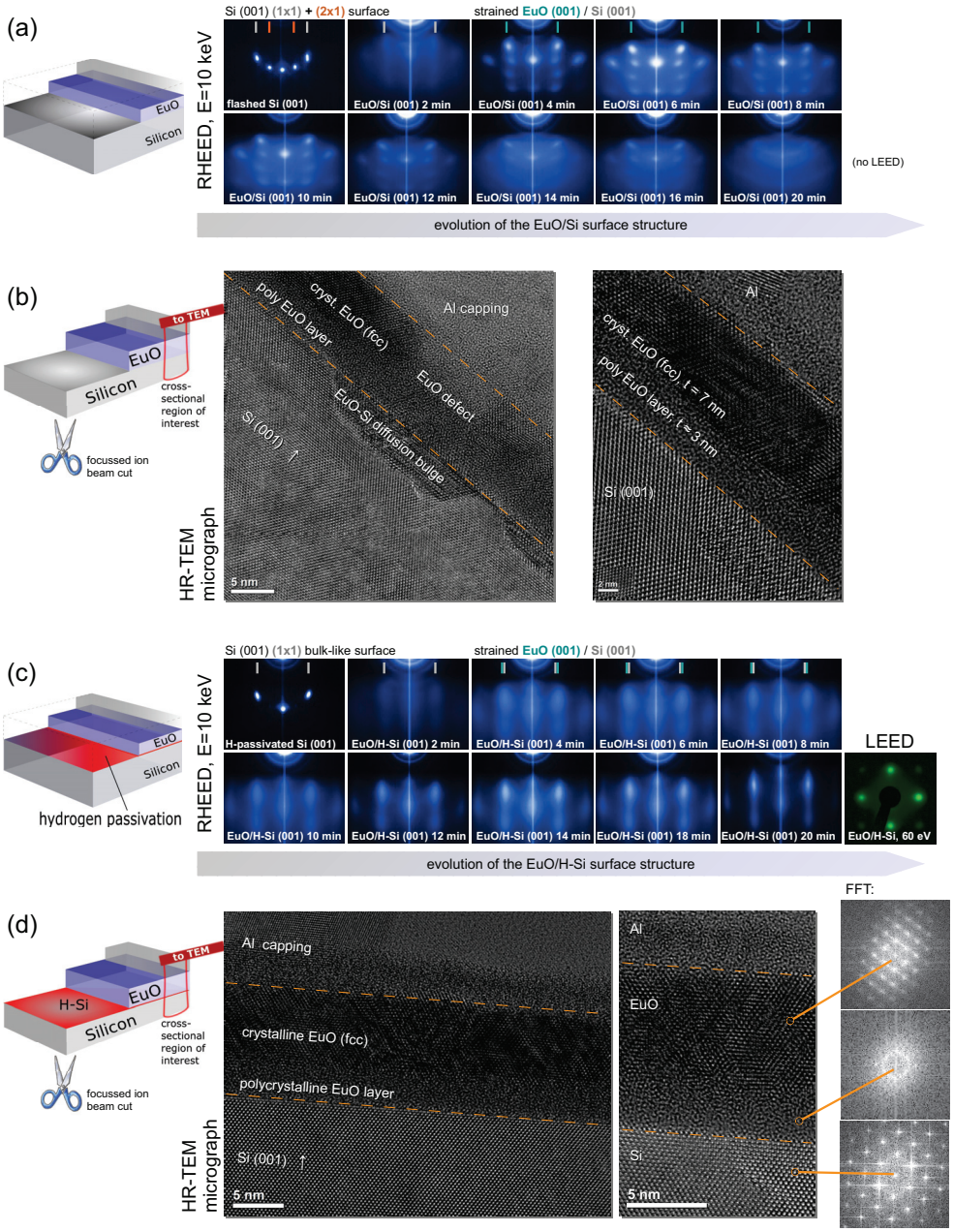

Figure 5.18.: Surface and interface structure development of EuO on Si (001) and on H-passivated Si (001). RHEED photographs elucidate the EuO surface structure when grown on clean Si (001) (*a*), the cross-section is depicted by HR-TEM in (*b*). EuO growth on hydrogen-passivated Si (001) is documented by RHEED and LEED in (*c*), and the cross-section in real space and selected images of the reciprocal space are depicted in (*d*).

10–20 nm in the Si substrate occur frequently, and one is shown as an example in the TEM micrograph (Fig. 5.18b). We interpret these bulges as Eu diffusion regions, containing probably Eu silicides. The EuO/Si diffusion regions not only alter the Si and Eu chemistry readily towards metallic silicides, but also dramatically change the crystal structure affecting the EuO/Si interface (bulge), the lower EuO layer (polycrystalline layer), and also the upper EuO layer (instability with the EuO/Al interface).

If, however, a complete hydrogen-passivation is applied to the Si (001) surface, the successive EuO growth steps are depicted in Fig. 5.18c. From the initial bulk-like Si (001) (1×1) pattern, first diffraction streaks of EuO are already observable at 1 nm EuO synthesis. Unlike the EuO growth on bare Si, here with H-passivated Si the EuO surface structure develops towards good crystallinity, as indicated by streaks in the RHEED photographs representing the EuO reciprocal lattice. After 10 nm EuO synthesis on H-Si (001), we observe the crystal structure of EuO (by RHEED and LEED) to be of a crystal quality comparable with EuO on cubic substrates under biaxial tensile strain (as discussed in Ch. 4.2). A cross-sectional HR-TEM study of the EuO/H-Si interface in Fig. 5.18d proves the successful prevention of diffusion effects, which were, in contrast, observed for EuO on bare Si (001). A 3 nm polycrystalline EuO layer forms in contact with Si, as indicated by the circular intensity of the Fourier transform picture. On top of this polycrystalline EuO, a single-crystalline EuO phase constitutes the residual EuO slab. However, the crystal structure of this EuO phase coincides best with Eu_2O_3 which is deduced to be formed during sample transfer through ambient air. Without doubt, during MBE synthesis we observed divalent epitaxial EuO by its *fcc* rocksalt lattice, and this allows one to interpret the Eu_2O_3 in the HR-TEM micrograph to represent the initial divalent EuO morphology.

Thus, a complete hydrogen-passivation of Si (001) allows for persistent heteroepitaxial growth of EuO/H-Si structures with no indication of large diffusion areas in Si or the EuO slab. Only a polycrystalline EuO layer of about 3 nm remains in direct contact with Si. EuO layers above this poly-EuO layer are deduced to grow largely single-crystalline.

Chemical optimization of the EuO/Si interface

In order to achieve a minimization of the interfacial $EuSi_2$ in EuO/H-Si (001) heterostructures, we investigate the impact of two parameters: (*i*) the *in-situ* hydrogen passivation of the clean Si (001) surface "H-Si", and (*ii*) the temperature of synthesis "T_S" as the general thermodynamic driving force. We vary the temperature between T_S = 350 °C and T_S = 450 °C, and we use the silicon (001) substrate either *in situ* hydrogen-passivated or with a clean (flashed) surface. These two parameters permit four variants of combinations, which we investigate in the following.

For a correlation of passivation steps with the surface crystallinity, we first analyze the RHEED pattern: Figure 5.19b depicts the RHEED pattern after growth of the ultrathin EuO films (d = 2 nm) at an electron energy of 10 keV and the beam along the [100] direction. We observe RHEED patterns of the EuO *fcc* lattice at T_S = 350 °C only in the absence of hydrogen termination. The higher substrate temperature (T_S = 450 °C) allows one to observe sharper RHEED patterns than for the lower synthesis temperature. Here, the impact of H-passivation is a roughening of the surface as indicated by dot-like intensities inside the RHEED streaks. Thus, we conclude that excess Eu from an incomplete Eu distillation at lower T_S hinders

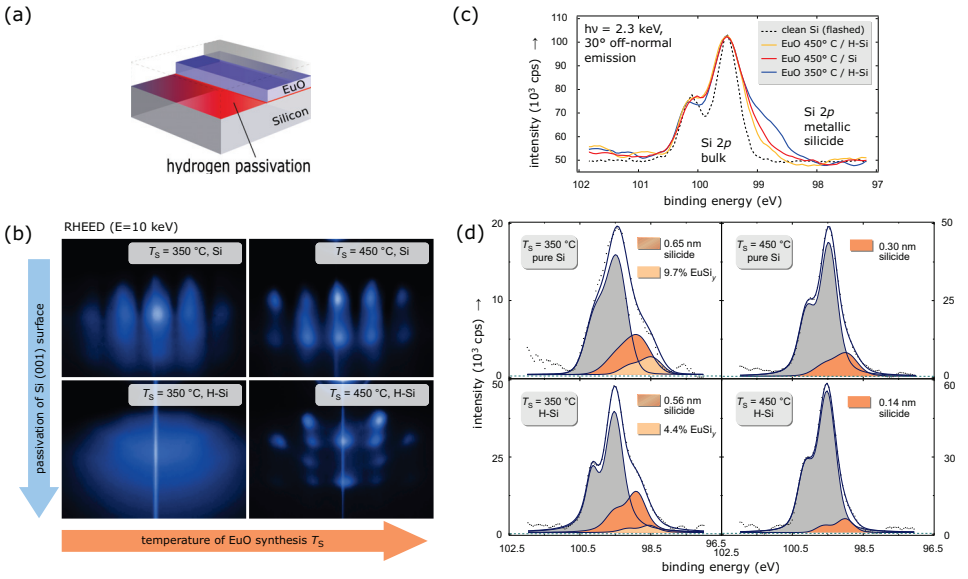

Figure 5.19.: The EuO/H-Si interface analyzed by least-squares peak fitting of the Si 2*p* core-levels.

the epitaxial growth mode of thin EuO films on Si, while at higher T_S heteroepitaxy of EuO directly on Si (001) is generally possible.

A chemical insight into the buried EuO/Si (001) heterointerface is obtained by a HAXPES analysis of the Si orbitals from the interface. We select an interface-sensitive geometry by tuning the excitation energy to a minimum of 2.3 keV together with off-normal emission. The recorded Si 2*p* peaks are shown in Fig. 5.19c–d for the different interface treatments. With a chemical shift of −0.6 eV, the silicide component can be clearly identified on the low binding energy side of the bulk Si doublet peak. The silicide fraction shows a clear development: an increase of substrate temperature as well as the hydrogen passivation of Si reduce the silicide thickness.

In order to quantify the silicide reaction at the EuO/Si interface for every set of passivation parameters, we conduct a peak fitting analysis based on the least squares method. The resulting thicknesses of the buried interfacial silicide layer are summarized in Fig. 5.20. Comparing the diminishments of the interfacial silicide, the impact of synthesis temperature from 350 °C to an optimum of 450 °C on the EuO/Si interface reaction is larger (−38% silicide) than the application of hydrogen termination (−14% silicide) to the clean Si surface. The advantage of a higher synthesis temperature can be understood from a thermodynamic analysis of $EuSi_2$ (Ch. 5.2): this silicide favors a disappearance reaction during EuO distillation growth (Fig. 5.10) yielding EuO and Eu. Any excess Eu, however, is readily re-evaporated at higher T_S, thus minimizing the available constituents for silicide formation. The advantage of a hydrogen passivation, although smaller than for the temperature variation, is explained by its larger thermodynamic stability compared to the silicide (Fig. 5.8). In conclusion, the parameters for a minimized interfacial silicide formation ($d_{min}(EuSi_2) = 0.14$ nm) are the ap-

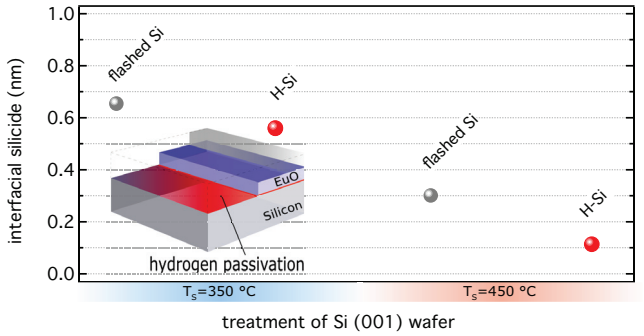

Figure 5.20.: Quantitative results of the EuO/H-Si silicide analysis by HAXPES.

plication of a higher synthesis temperature (450 °C) and a complete hydrogen passivation of Si (001).

The thin film magnetic properties were investigated by SQUID magnetometry. Three magnetization curves are depicted in Fig. 5.21a, which originate from polycrystalline bulk-like EuO on Si (001) with a native oxide SiO_2 layer at the interface, and two ultrathin EuO layers (~2 nm) on *in situ* hydrogen-passivated Si (001), which exhibited epitaxial growth. Coinciding with the HAXPES results, the dominating effect of the temperature of synthesis on the silicide formation is observed in the ferromagnetic properties of the EuO/Si heterostruc-

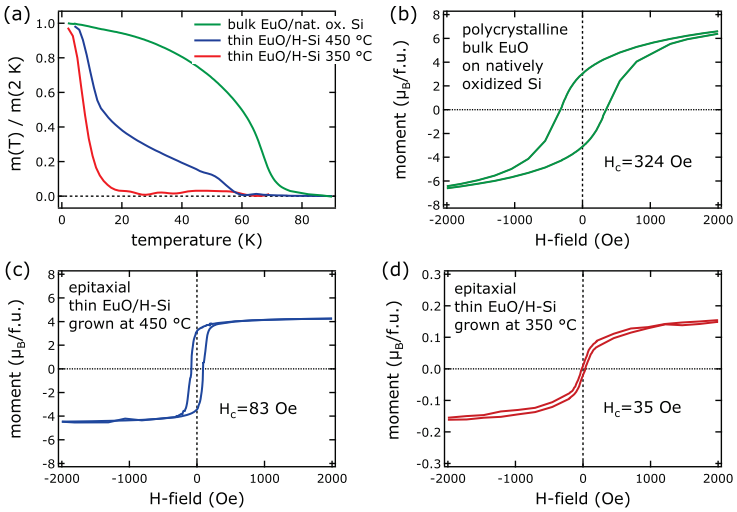

Figure 5.21.: Magnetic properties of EuO on Si, dependent on synthesis temperature and H-passivation.

tures: (*i*) we clearly observe a Brillouin-shaped magnetization curve for the bulk EuO film with the native silicon oxide as diffusion barrier (green curve). The blue and red lines represent the $M(T)$ curves of ultrathin EuO on H-passivated Si (001) with the only difference being the temperature of synthesis: a low temperature of 350 °C vs. a high temperature of 450 °C are chosen in order to provide consistency with the EuO/Si heterostructures investigated by HAXPES. Both curves of ultrathin EuO exhibit a reduced Curie temperature of $T_C = 58$ K for the high T_S heterostructure (blue curve) and $T_C \approx 10$ K for the low T_S structure (red curve). The T_C of the high temperature EuO ($T_S = 450$ °C) agrees well with the magnetic results obtained for 2 nm-thin EuO films on Si from a previous work;[48] therefore, we ascribe the reduction of the magnetic ordering temperature to the reduced nearest-neighbor (NN) interaction in ultrathin EuO films. The high magnetic moment at $T \to 0$ K may be partly induced by residual $EuSi_2$ which is predicted to be paramagnetic.[191] Moreover, the specific magnetic moment per EuO formula unit (f.u.) shows a moderate reduction to about $4.4\,\mu_B$/f.u. for the high T_S sample, whereas the low temperature EuO ($T_S = 350$ °C) shows a clearly reduced magnetic moment, saturating at only $0.15\,\mu_B$/f.u. This is in agreement with the HAXPES quantification of interfacial silicides (Fig. 5.19) and conveys the crucial influence of the interfacial silicide on the magnetic properties of ultrathin EuO on H-Si (001).

In conclusion, an optimized magnetic EuO/Si (001) heterostructure should be treated with a complete *in situ* hydrogen passivation and a high temperature of synthesis (450 °C) at which the Eu distillation condition is perfectly maintained.

5.4. Interface engineering II: Eu monolayer passivation of the EuO/Si interface

In this section, we aim to minimize the interfacial SiO_x which – from all reaction products considered in this thesis – is chemically most stable on the Si surface. From its thermodynamic stability,* a hydrogen-passivated Si (001) surface is not stable enough to prevent SiO_2 formation. Thus, the only remaining approach is to shift the chemical regime at the beginning of EuO synthesis away from any oxidation regime, in order to render an SiO_x formation least probable. In the Gibbs triangle (Fig. 5.8), consequently this means a shift towards Eu-rich EuO growth regimes II or III in the initial stage. In practice, we apply one up to three monolayers (ML) of metallic Europium to the Si surface immediately before EuO synthesis.

In order to analyze, whether an Eu monolayer coverage of the Si (001) surface is energetically favorable at all, we carry out a simulation of Eu monolayers on the Si (001) surface after the solid-on-solid model including surface diffusion. The two-dimensional hopping ratio per time is referred to as surface diffusivity and defined as

$$\nu = \nu_0 \cdot e^{-\frac{E_{\text{barrier}}}{k_B T}}. \tag{5.4}$$

In Fig. 5.22, the images for 0.5 up to three monolayers Eu coverage of the Si (001) surface are depicted. We present calculated meshes of 50×50 cells, in which one cell corresponds to the area of one atomic site of the Si (001) surface. The ratio of Eu surface diffusivity over arrival of new Eu atoms is $\nu/F = 1250$. Larger values of ν which may be apparent in Eu–Eu will in-

*as depicted in Fig. 5.7 on p. 96.

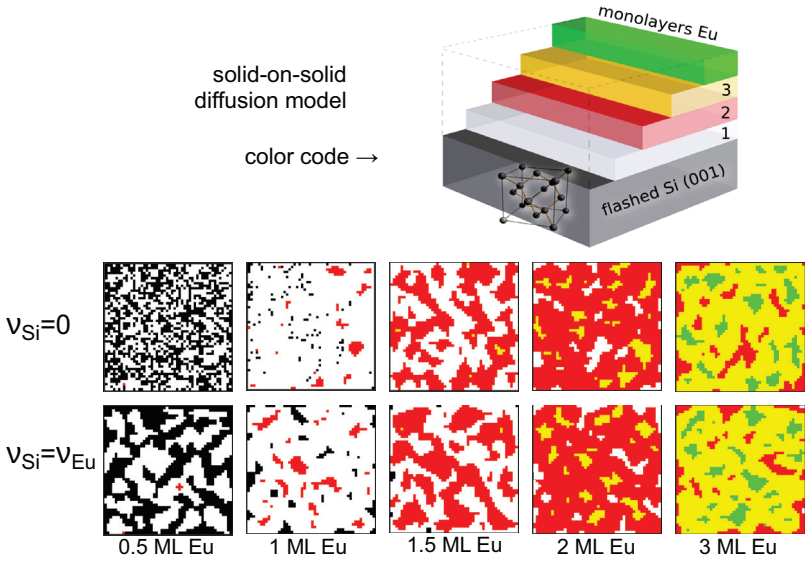

Figure 5.22.: Eu monolayers on top of the Si (001) surface under surface diffusion. The simulation is carried out for vanishing Eu–Si surface diffusion (*top row*), and for Eu–Si surface diffusion assumed to be equal with Eu–Eu self diffusion (*bottom row*). Programmed in HT-Basic by Ibach (2013).[207]

crease island sizes but their large scale distribution does not change.* As Eu is highly mobile near its sublimation point during the Eu distillation condition (T_S = 450 °C), a distinction between Eu–Eu diffusivity (ν large) and Eu–Si (ν small) is realistic. Therefore, in the upper row of Fig. 5.22 we assume the very first Eu layer in contact with the Si surface to show no surface diffusion. For comparison, in the second row the Eu–Si surface diffusivity is the same as for Eu–Eu.
For vanishing Eu–Si surface diffusion (*top row*), a characteristic difference for 0.5 an one monolayer Eu is that Eu atoms on Si (001) form many single nucleation sites which are randomly distributed and will form islands upon ongoing coverage. The difference between the two initial values for surface diffusivity vanishes already after 1.5 monolayers Eu. Remarkably, no islands of height two are identified. In the pictures of the second Eu layer, no larger islands form, but the Eu atoms are rather diffusing and settling in sites with larger coordination number (holes, sites with only one ML Eu).
From two monolayers Eu on, a closed coverage of the Si (001) surface is confirmed and the difference in island height is mostly not exceeding one monolayer. We consider Eu this coverage as a promising basis for an oxygen-protective passivation of the Si (001) surface.

In Fig. 5.23b, we analyze the the surface crystal structure of 2 nm EuO/Eu-Si (001) heterostructures (Fig. 5.23a) by RHEED (E = 10 keV) pattern recorded immediately after EuO growth. As a reference, the clean (flashed) Si (001) surface exhibits a clear pattern of (1 × 1)

*No diffusion barrier at island edges (Ehrlich-Schwoebel barrier) is included in the calculation, this is a reasonable assumption for the highly mobile Eu ions.

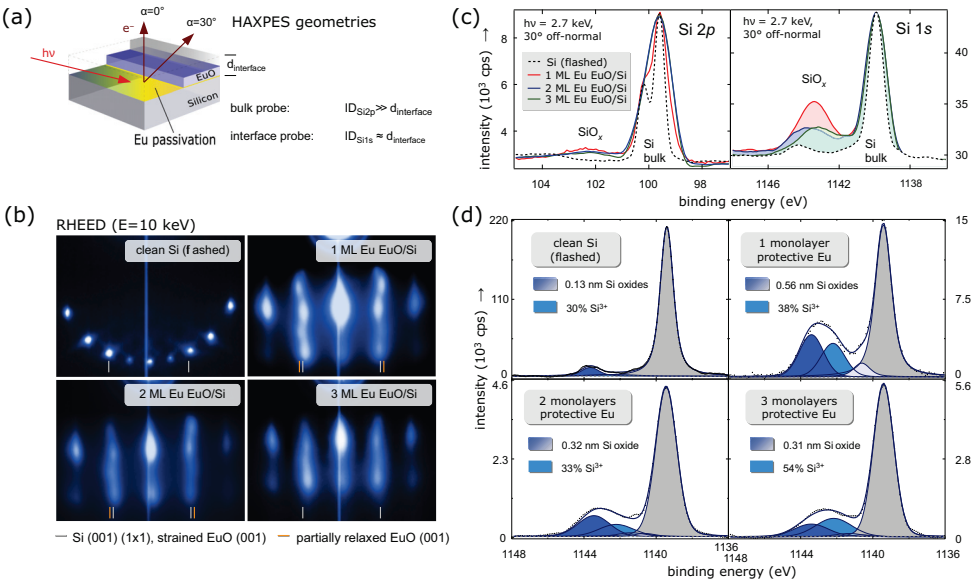

Figure 5.23.: The EuO/Eu-Si interface analyzed RHEED and by peak fitting of the Si 2*p* and 1*s* core-levels measured by HAXPES.

bulk diamond structure as well as an interstitial pattern of the Si (001) (2×1) surface reconstruction.
The EuO/Si heterostructure with 1 ML protective Eu shows a streaky pattern of the EuO *fcc* lattice, whereas the rods have a larger distance in the upper region ($\theta = 2°$ "grazing") of the pattern than in the lower region ($\theta = 6°$). From the lower end of the diffraction rods to the upper end the information depth of diffraction is altered from a few lattice parameters to the topmost layer. The diffraction features from the surface agree nearly with the EuO reciprocal lattice parameter, while the diffraction from deeper layers agrees with the lattice of Si (001). This is an example of strained growth (6% difference) of EuO on Si (001) maintaining epitaxy, where with the fourth ML of EuO (i. e. 20 Å EuO) the EuO lateral lattice parameter relaxes.
The RHEED pattern for samples with 2 ML protective Eu at the EuO/Si interface also displays streaky rods of EuO. Here, EuO mainly adapts the Si (001) lattice parameter and shows only small relaxation. The EuO lattice parameter from the surface layer is determined as 5.3 Å which indicates the EuO lattice is only partially relaxed to the literature value of 5.144 Å.
For the EuO/Si heterostructure with 3 ML protective Eu, the RHEED pattern of EuO consists of smooth rods and EuO is homogeneously strained in the lateral dimension adapting the Si (001) cubic lattice parameter. From these electron diffraction results we conclude that epitaxial growth of smooth EuO on clean Si (001) is feasible, where EuO mainly adapts the Si cubic lattice parameter.

A detailed picture of the interfacial electronic structure is obtained from HAXPES core-level spectra of the EuO/Eu-Si (001) interface. In order to tune the information depth to selectively probe the EuO/Si interface layer, the low excitation energy of $h\nu = 2.7$ keV and off-normal

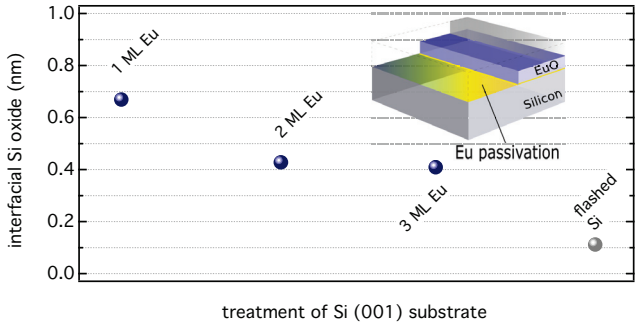

Figure 5.24.: Quantitative results of the SiO_x analysis in EuO/Eu-Si.

emission are used (Fig. 5.23a). By increasing the off-normal emission angle further than to $\alpha = 30°$, the information depth underruns the minimum for an acquisition of Si 1*s* spectra; this indicates thus the threshold of probing exclusively the Si interface layer. Two core-level photoemission spectra of Si, Si 2*p* and 1*s*, are inspected as depicted in the two panels of Fig. 5.23c. A quantitative analysis, however, that demands for a smooth and well-resolved curve of the SiO_x components is only feasible with the Si 1*s* deep core-level, as compiled in Fig. 5.23d.

The chemical shifts of the silicon oxide are reduced due to final state effects, in agreement with a comprehensive SiO_x/Si PES study [139] for ultrathin SiO_x films in the 2 nm range. Evaluating the chemical shifts of the SiO_x in detail reveals the shift to be not compatible with solely Si^{4+} (SiO_2), but rather a mixture of oxidation states of Si. If one or two ML Eu were applied, the fraction of Si^{3+} ranges from 33% to 38%, whereas this fraction is increased up to 54% on the cost of Si^{4+} if three ML protective Eu were applied. The redistribution of the silicon oxide to the valency Si^{3+} – different to the native oxide which is always Si^{4+} – points out a characteristic low oxidation of the silicon wafer, which takes place during the oxygen-limited (1.5×10^{-9} Torr) synthesis of EuO.

In order to quantify the interfacial SiO_x formation, we apply a least-squares peak fitting analysis after Levenberg-Marquardt for the three EuO/Si heterostructures with one up to three ML of protective Eu at the EuO/Si interface. The minimization of interfacial SiO_x in the EuO/Si heterointerface with Eu passivation monolayers (ML) results in 0.67 nm SiO_x for one ML Eu, 0.43 nm SiO_x for two ML Eu, and a minimum of 0.42 nm SiO_x if 3 ML Eu were provided onto Si (001) just before EuO synthesis (summarized in Fig. 5.24). The residual silicon oxide from a flashed clean silicon wafer was determined to be only 0.11 nm and is included in all heterostructures.

In conclusion, two ML of protective Eu the silicon (001) surface has been passivated with are sufficient to limit the total thickness of interfacial Si oxidation to 0.43 nm. Moreover, the dominant oxidation state of the Si interface changes from Si^{4+} to the Si^{3+} valence state, and a EuO/Si (001) heteroepitaxy with adaption of the Si lattice parameter can be maintained.

Combination of Eu- and H-passivation of Si (001) to maintain a minimum of interfacial contamination

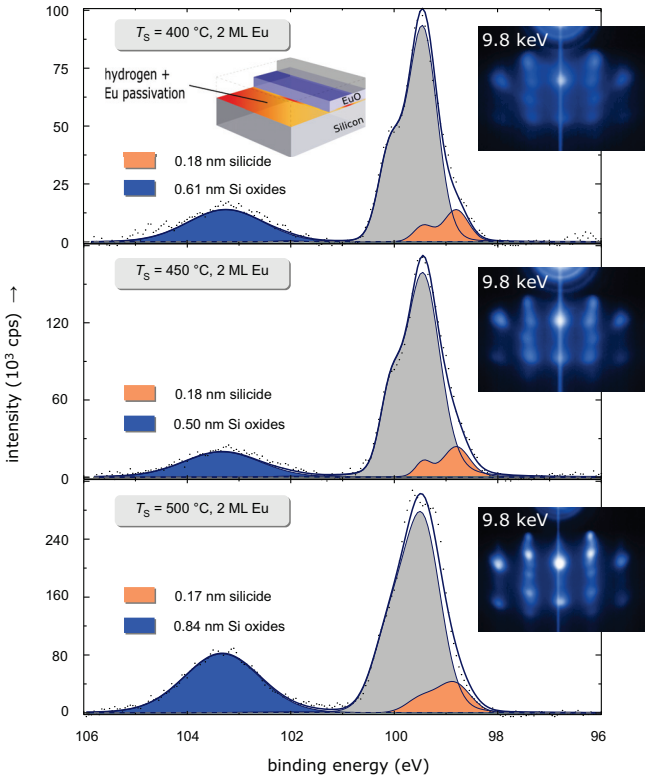

Figure 5.25.: The EuO/Si interface with a combined optimization against silicides and SiO_x. Both H-passivation of the Si (001) are applied and oxygen protective Eu monolayers. As a free parameter, the temperature of synthesis T_S is varied. After EuO growth, RHEED pattern are recorded (*inset*).

In this section, we optimize the EuO/Si interface by means of two complementary methods: (*i*) the hydrogen-passivated Si (001) surface is capable to avoid silicides but has shown to allow for a certain Si oxidation, and (*ii*) the Eu monolayer-passivated Si interface shows a minimized SiO_x contamination but establishes an environment for silicide formation. Thus, combining these two passivation techniques from the previous sections promises a simultaneous minimization of silicides as well as SiO_x at the EuO/Si (001) interface.

Taking the optimum set of interface passivation parameters for the silicide and the silicon oxide minimization from sections 5.3 and 5.4 into account, we point out the optimum parameters to be two monolayers of oxygen-protective Eu combined with a complete *in-situ* hydrogen passivation of Si (001). As a free parameter, we choose the temperature of synthesis T_S, which constitutes the thermodynamic driving force for the exchange of heat and entropy, while the volume and system pressure are constant. Thus, a temperature increase pushes the possible interface reactions towards their thermodynamically expected results (as discussed in Ch. 5.2), but also promotes kinetics such as interdiffusion of Eu or Si atoms. The temperature of EuO synthesis T_S is kept in a range in which the Eu distillation condition is still valid. We chose T_S to vary around T_S = 450 °C, at which an optimum structural quality

of EuO was observed in EuO on cubic oxide studies (Ch. 4). In this way, we prepare three EuO/H-Si heterostructures with two monolayers oxygen-protective Eu at temperatures

$$T_S = 400\,^\circ\text{C}, \quad 450\,^\circ\text{C}, \quad \text{or } 500\,^\circ\text{C}.$$

After synthesis of the EuO/Si (001) heterostructures, we analyze the surface structure of the EuO magnetic oxide layer by RHEED. The pattern of an *fcc* rocksalt lattice of EuO (001) is clearly observed after 2 nm EuO growth, with a lattice constant matching the silicon cubic lattice parameter. In the EuO reciprocal rods, the vertical intensities are distributed dot-like, which indicates an epitaxial growth with three-dimensional structures on the passivated Si (001).

A quantitative analysis of the chemistry at the EuO/Si heterointerface with combined passivations is obtained from Si 2*p* spectra by HAXPES, in a geometry adjusted to probe precisely down to the Si interface. This is achieved by using the minimum excitation energy of $h\nu = 2.3$ keV of the HAXPES beamline (KMC1, see Ch. 3.4.3) and an off-normal emission angle of 30°. The Si 2*p* doublet provides the advantage that both the silicides and oxides can be well distinguished from bulk Si and quantitatively analyzed in one core-level (Fig. 5.25). For the silicides, the temperature variation does not affect the interfacial thickness of $EuSi_2$, which we determined as $d_{EuSi_2} = 0.2$ nm for all three heterostructures, in good agreement with the optimum value of the silicide optimization series (Ch. 5.3). The oxidation of the Si interface exhibits a minimum value of $d_{SiO_x} = 0.69$ nm for the heterostructure synthesized at $T_S = 450\,^\circ$C, while a maximum oxidation of the Si interface is observed for the EuO/Si interface exposed to the highest temperature of EuO synthesis, $T_S = 500\,^\circ$C. Interfacial silicide and SiO_x thicknesses are summarized in Fig. 5.26.

We identify a general shift to slightly higher values of interfacial SiO_x in this study of combined Si passivation when compared to the explicit optimization regarding SiO_x by protective Eu monolayers in Ch. 5.4. This can be explained by the additional hydrogen termination procedure of Si (001), which systematically introduces a fraction of at least 10^{-6} oxygen in the hydrogen gas during the *in-situ* H-annealing process. The largest oxidation of the EuO/Si interface at $T_S = 500\,^\circ$C can be understood by an increased diffusion of Si surface atoms in the high temperature regime, changing the interface morphology and thus providing more reactive faces in contact with the EuO synthesis.

In conclusion, we carried out three comprehensive HAXPES studies in order to investigate and optimize the chemical properties of the passivated EuO/Si interface by a quantitative analysis of silicon core-level spectra. The HAXPES results for the EuO/Si interface are compiled in Fig. 5.26. In a first step, the interfacial silicide was minimized by an increase of synthesis temperature from 350 °C to 450 °C (black spheres in Fig. 5.26), while the application of H-passivation to the Si (001) surface yields only a smaller reduction of the silicide content (red spheres in Fig. 5.26), resulting in a minimum of 0.14 nm silicide at the EuO/Si interface. In a second step, the SiO_x contamination at the EuO/Si interface is diminished by oxygen-protective Eu monolayers, resulting in a minimum of 0.42 nm interfacial oxide (golden spheres). Finally, a combination of the advantageous passivation parameters from the silicide and the SiO_x optimization studies reveal an optimum set (blue spheres in Fig. 5.26)

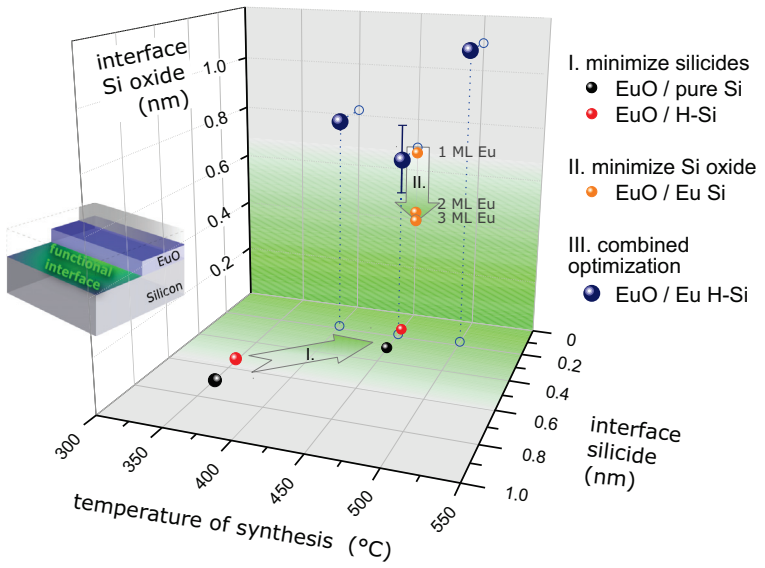

Figure 5.26.: Summary of EuO/Si interface optimization including silicides, SiO_x, and the combination of them. The aim of the optimization is to reduce interface contaminants into the green-shaded slot of silicide and SiO_x thicknesses.
(*I*) Silicide minimization is accomplished by the tuning of the synthesis temperature and the surface hydrogen termination of Si (001). (*II*) Silicon oxides are diminished by protective monolayers of Eu on Si (001). (*III*) Finally, optimum parameters including H-Si and a protective Eu monolayer are checked against synthesis temperature to yield a combined optimization accounting for both the silicides and SiO_x.

for the synthesis of EuO on passivated Si (001) heterostructures:

H-passivated Si (001),	2 ML protective Eu,	a medium $T_S = 450\,°C$.

During all three studies, EuO on Si (001) could be observed to grow heteroepitaxially on Si (001) by RHEED. The sharpest EuO diffraction pattern are observed in the combined passivation series – this is due to the net contamination ($EuSi_2$ + SiO_x) being smallest only in this combined interface optimization series.

5.5. Interface engineering III: SiO_x passivation of the EuO/Si interface

The challenge to prevent metallic contaminations at the EuO/Si interface involves two major aspects: the avoidance of (*i*) silicides due to Eu–Si reactions, and (*ii*) excess Eu from a seed layer for EuO synthesis in order to initialize the Eu distillation growth. We address these issues by an alternative passivation method, the *in situ* application of ultrathin SiO_x in

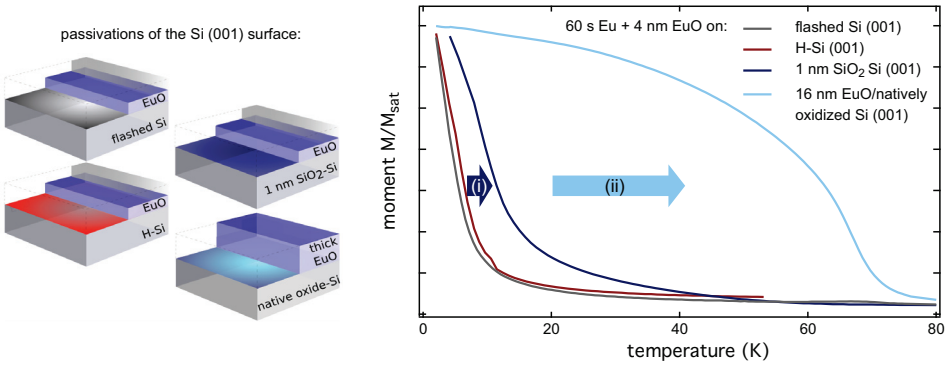

Figure 5.27.: Magnetization behavior of 4 nm EuO on passivated Si (001) with interfacial silicide. Si (001) is passivated with hydrogen, SiO_2, or left clean after flashing. In (*i*), the change of magnetization from hydrogen passivation to ultrathin SiO_2 is highlighted, and in (*ii*) from ultrathin SiO_2 to the thick native SiO_x.

the sub-nanometer regime to the clean Su surface. This approach shifts the thermodynamic environment at the EuO/Si interface towards the oxygen-rich regime.*

We characterize the SiO_x passivation by presenting magnetic properties of four different EuO/Si heterostructures, as compiled in Fig. 5.27. By excess Eu and an elevated EuO synthesis temperature, we pursue a significant formation of interfacial silicide which is paramagnetic[191] at $T \to 0$ K. As a result, we find a gradual optimization of the Si passivation methods with respect to their chemical stability as against silicide formation: while EuO/H-Si preserves a T_C of the magnetization curve only 2 K higher than for EuO/flashed Si, we observe a significant increase of T_C for the EuO on 1 nm SiO_x-Si hybrid structure – from ~12 K to ~40 K. A Brillouin-shaped magnetization curve without any paramagnetic contamination is observed only for EuO on natively oxidized Si ($d_{SiO_x} \geqslant 2$ nm). This preservation of ferromagnetism motivates the study of this section, which combines chemical (by HAXPES), structural (by RHEED) and magnetic (by SQUID) optimization of EuO/Si hybrid structures using ultrathin *in situ* SiO_x passivation of the Si (001) surface.

HAXPES analysis of the SiO_x-passivated EuO/Si interface

First, we clean Si (001) by thermal flashing ($T_{Si} \geqslant 1100$ °C), followed by the *in situ* surface passivation with either molecular oxygen ($p \sim 10^{-7}$ mbar, $T_{Si} = 700$ °C) or atomic hydrogen ($p \sim 10^{-2}$ mbar, T_{Si} = RT). We confirmed the chemical cleanliness after the Si passivation step using Auger electron spectroscopy. The crystalline structure of the passivated Si surface is checked by LEED which reveals exclusively a (1×1) Si (001) bulk diamond structure, in contrast, a flashed Si (001) surface would show the (2×1) surface reconstruction.
Second, 4 nm EuO thin films are grown directly on the Si (001) substrates. In order to stabilize stoichiometric EuO, a low oxygen partial pressure ($p_{O_2} \sim 1.5 \times 10^{-9}$ Torr) and the Europium distillation condition[32,45] are applied, in agreement with the optimum EuO synthesis yielding stoichiometric EuO in Ch. 4. During EuO synthesis, the surface crystal structure is mon-

*referred to as thermodynamic region "I" in the Gibbs triangle (see Fig. 5.8 on p. 97).

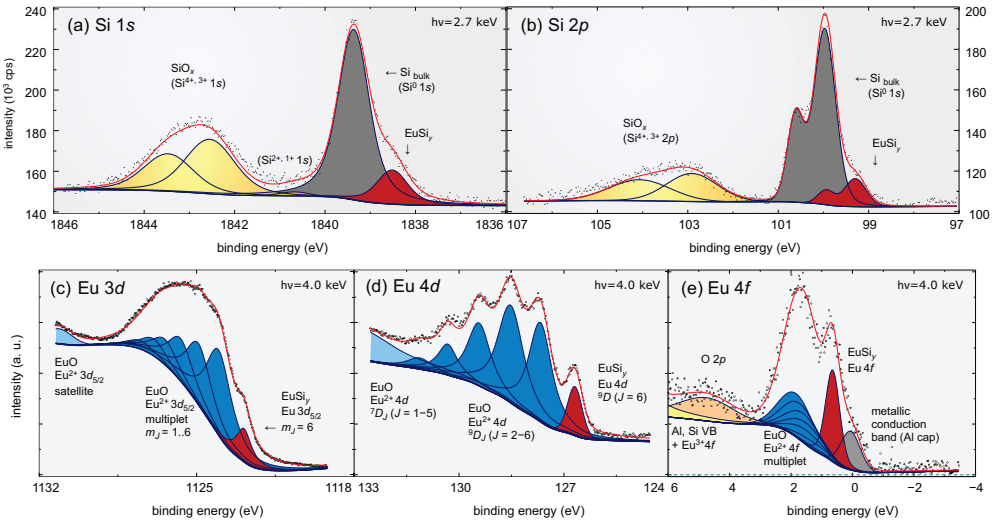

Figure 5.28.: Consistent peak fit analysis of the SiO_x-passivated EuO/Si (001) interface using Si and Eu core-levels of the HAXPES experiments.

itored by RHEED. Finally, the EuO/Si heterostructures are capped with 5 nm air-protective Al. In order to investigate the electronic structure at the EuO/Si interface, we conducted HAXPES studies of the EuO/Si hybrid structures at the undulator beamline P09 at PETRA III (DESY, Hamburg),[97] and at the KMC-1 dipole beamline at BESSY II (Berlin) with the HIKE endstation.[98] The Fermi edge of Au foil on the sample serves as calibration for the binding energy. Tougaard-type backgrounds are used to account for inelastic photoelectron scattering.

Interface-sensitive HAXPES spectra of the EuO/Si heterostructures are depicted in Fig. 5.28a, b. Stable silicon oxide is observed at chemical shifts of 3.2 and 4.1 eV in the Si 1*s* spectrum, which identify Si^{3+} (Si_2O_3) and Si^{4+} (SiO_2), in good agreement with recent PES studies of ultrathin SiO_2/Si (001).[139,208] Another component at the EuO/Si interface with a chemical shift to lower BE is observed in the Si spectra as well as in the Eu3*d*, 4*d*, and 4*f* spectra, which is identified as a metallic Eu silicide ($EuSi_y$). Due to the small chemical shift of $EuSi_y$ (−0.65 eV for Si 2*p*), only the Si spectra and the narrow Eu 4*f* multiplet allow for a quantitative deconvolution of the entire silicide fraction silicide components. In case of the complex Eu 3*d* and 4*d* multiplets, we can separate only the silicide component of one *J* final state at the lower binding energy side. A quantitative thickness determination of the SiO_x passivation at the Si (001) interface and of the resulting silicide reaction layer is accomplished by consistent least squares peak fitting after Levenberg-Marquard of the HAXPES spectra. The thickness *c* of the interfacial passivation (SiO_x) and $EuSi_y$ reaction layers are determined from their relative spectral weight, as derived in equations (3.16) and (3.19) (in Ch. 3.4.4 on p. 51). The results are compiled in Fig. 5.29. Regarding the chemical reactivity of the EuO/Si interface we found interfacial silicides to exceed 10 Å thickness for flashed Si (001), however by applying an ultrathin SiO_x interface passivation (d_{SiO_x} = 10–13 Å) silicide formation is suppressed

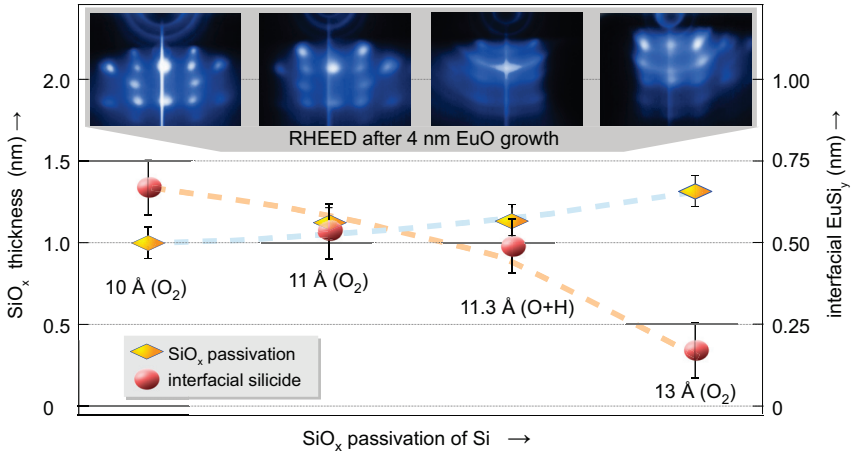

Figure 5.29.: Quantification of the SiO_x passivation and silicides at the EuO/SiO_x-Si interface.

to $d_{EuSi_2} \leqslant 7.5$ Å. The effect of additional hydrogen passivation shows a small reduction of $EuSi_y$ of about 9%, whereas the SiO_x passivation (increased from 11 Å to 13 Å) reduces the silicide formation by ~68%. The optimum value for the quasi-contamination free EuO/Si interface is achieved with 13 Å passivation with SiO_x: the silicide is diminished down to 1.8 Å, well below one monolayer of interface coverage.

In a further step, we use RHEED to investigate the crystalline structure of the EuO thin films grown on passivated Si (001) (Fig. 5.29 inset), revealing a clear dependence on d_{SiO_x}: for a thin SiO_x passivation ($d_{SiO_x} = 10$ Å), a sharp EuO (001) *fcc* pattern is observed, with separations of the reciprocal rods indicating an island-like (3D) growth mode. For thicker SiO_x passivation ($d_{SiO_x} = 13$ Å), a RHEED pattern of the EuO (001) *fcc* lattice is still observable, however, circular intensities indicate a polycrystalline fraction of EuO. In the case of an additional hydrogen passivation of the Si, an increased disorder of the H-passivated Si (001) surface[206] leads to the growth of mainly polycrystalline EuO.

Magnetic properties of the SiO_x-passivated EuO/Si heterostructures

Finally, we investigate how the magnetic properties of the EuO/Si heterostructures depend on the SiO_x interface passivation. Figure 5.30 summarizes the in-plane magnetic properties $M(T)$ and $M(H)$ of 4 nm EuO/Si (001) samples with varying SiO_x passivation thicknesses. First, EuO thin films grown on flashed Si (001) without any SiO_x passivation show a strongly reduced magnetic moment and Curie temperature of 10 K (bulk EuO: $T_C = 69$ K). As we deduce from the HAXPES results, the formation of a $EuSi_y$ reaction layer largely alters the EuO ferromagnetic behavior towards paramagnetic.[191] Remarkably, such a contamination would significantly reduce the spin filter functionality of magnetic oxide EuO/Si tunnel junctions.[7] Second, applying an SiO_x interface passivation clearly improves the magnetic properties of the EuO thin film. The most effective interface passivation of 13 Å SiO_x yields an M_s of ~5μ_B/EuO and a T_C of 68 K, close to the EuO bulk values 7μ_B/EuO and $T_C = 69.3$ K. Finally,

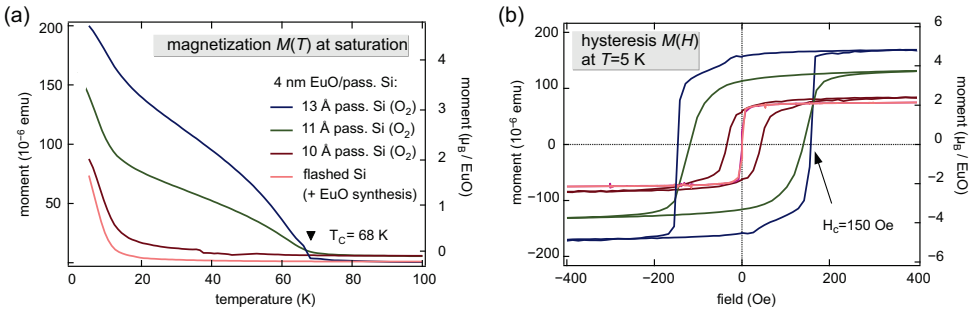

Figure 5.30.: Magnetic properties of epitaxial EuO/Si hybrids with SiO_x passivation.

with increasing SiO_x passivation thickness, the polycrystalline nature of Si oxide and surface defects cause an increase of the EuO coercive field up to 180 Oe.

In conclusion, we combined the chemical and structural optimization of the functional EuO/Si (001) interface by applying the robust *in situ* passivation with monolayer-thin SiO_x on clean Si (001) surfaces. The SiO_x passivation layer is quantified by interface-sensitive HAXPES, which reveals SiO_x thicknesses in the lattice constant regime. In particular, an only 13 Å-thick SiO_x passivation layer reduces the interfacial silicide contamination down to 1.8 Å, and a heteroepitaxial growth of EuO (001) is observed, with bulk-near EuO magnetic saturation M_S and T_C. The results of this section are published in Caspers et al. (2013).[6]

Towards EuO tunneling...

The desired tunnel functionality of EuO has recently been demonstrated in a $EuO/SiO_2/Si$ tunnel contact (not shown) by Flade (2013).[128] While the thick native oxide of Si in this particular tunnel junction permits one to observe the spin-selective tunneling, the crystal structure of the EuO/Si interface and EuO tunnel barrier is completely polycrystalline (not shown). A complementary study of EuO tunnel contacts on flashed Si and on H-Si shows heteroepitaxy, but no tunnel behavior due to ohmic conduction, most likely caused by metallic silicide contaminations. Between these two extremes, our current research is proceeding with the fine tuning of SiO_x passivations of the Si (001) surface – aiming towards both a quenched interface diffusion keeping it chemically clean and a EuO-on-Si (001) heteroepitaxy for possible coherent tunnel functionality (also band engineering[7]).

5.6. Summary

We discussed EuO integrated directly on Si (001) with the aim of understanding and optimizing the spin-functional EuO/Si (001) heterointerface. First, we established a synthesis of bulk-like polycrystalline EuO directly on HF-cleaned Si (001) by Oxide-MBE using two different oxidation parameters. This yielded two complementary EuO valency phases: either mainly divalent EuO, or oxygen-rich Eu_1O_{1+x} as characterized by 66% Eu^{3+} ions by a HAXPES study. For divalent EuO/HF-Si, which is necessary for magnetic EuO tunnel contacts, bulk-like magnetic properties could be confirmed by SQUID.

Going one step further, for spin-functional interfaces allowing for an advanced tunnel approach ("coherent tunneling") from EuO directly into silicon, we aim towards the the *epitaxial integration* of ultrathin EuO directly with Si (001). Thus, we focus on interface engineering of the chemically challenging EuO/Si (001) heterointerface. In response to the extremely high reactivity and surface kinetics of Eu, EuO, and Si during EuO synthesis at elevated temperatures, we conducted a thermodynamic analysis of the EuO/Si interface. Thereby, we selected three *in situ* passivation procedures for the Si (001) surface in order to prevent metallic and oxide contaminations at the EuO/Si interface, both being the main antagonists for spin-functional tunneling.
As a first step, we engineer the functional EuO/Si interface with an *in situ* hydrogen passivation of clean Si (001), which is thermodynamically suited to prevent metallic silicides. We optimized interface-passivated EuO/H-Si (001) heterostructures under a variation of the synthesis temperature and hydrogen passivation procedure. By interface-sensitive HAXPES, we controlled the minimization of interfacial silicides: at higher temperature of EuO synthesis (T_S = 450 °C) and for a complete H-passivation of the Si (001) surface, the minimum thickness of interfacial silicides is determined from Si 2*p* core-levels to equal $d_{opt}(EuSi_2)$ = 0.16 nm – clearly below now monolayer coverage of this metallic contamination. The second interface contamination, SiO_2, is treated by the consequent application of the Eu-rich growth regime. For this, we chose a Eu seed layer in the thickness regime 1–3 monolayers, in order to passivate the Si surface against oxidation. Those EuO/Si (001) heterostructures were fabricated by Oxide-MBE and quantitatively analyzed by HAXPES. Using Si 1*s* core-level spectra, we determined a minimization of interfacial Si oxide down to $d_{opt}(SiO_x)$ = 0.42 nm. The silicide $EuSi_2$ and silicon oxides are contaminations originating from complementary growth regimes, either Eu-rich or oxygen-rich. Hence, these contaminants cannot simultaneously be diminished by a shift towards one of these chemical regimes. In order to optimize both contaminants, we combined the beneficial parameters of H-passivation, higher synthesis temperature, and Eu passivation in the monolayer regime. Using HAXPES, we evaluated Si 2*p* spectra and found an optimum of $d_{opt}(SiO_x)$ = 0.69 nm simultaneously with $d_{opt}(EuSi_2)$ = 0.20 nm, both of which clearly in the subnanometer regime.
An alternative route to a chemical passivation of the EuO/Si interface is the application of ultrathin SiO_x in the Ångström regime. This approach benefits from the high chemical and structural stability of SiO_2 and its electrical insulation, thus principally concordant with the intended tunnel functionality. We applied an *in situ* SiO_x passivation to the clean Si (001) surface, and investigated the passivation and resulting contaminants at the EuO/Si heterointerface by HAXPES. The thickness of the SiO_x passivation to ranges from 10–13 Å. In this passivation regime, we observed a clear reduction of interfacial silicides down to $d_{opt}(EuSi_2)$ = 0.18 nm. With increasing SiO_x passivation, the magnetic properties of EuO/SiO_x-Si (001) heterostructures developed stepwise towards the EuO bulk magnetization with a maximum specific magnetic moment of 5 μ_B/EuO for 13 Å SiO_x passivation.

For all EuO/Si (001) heterostructures with optimized interface passivation in our studies, the EuO and Si reciprocal patterns could be observed by RHEED and indicate heteroepitaxial, yet partly three-dimensional growth with an adaption the Si (001) lateral lattice parameter. This is the first time, that a direct integration of EuO on silicon was experimentally realized – without additionally deposited oxide buffer layers. Such chemically and structurally optimized EuO/Si (001) heterostructures may be effectively utilized as spin-functional tunnel contacts for silicon spintronics devices such as a spin-FET in the near future.

6. Conclusion and Outlook

In the thesis at hand, we explore ultrathin films of the magnetic oxide europium oxide (EuO) with two complementary goals. First, we investigate fundamental structural and magnetic properties of EuO as a model Heisenberg ferromagnet. We tune the lateral lattice parameter of EuO, which allows us to elucidate the response of the ferromagnetic coupling of the localized $4f$ magnetism by biaxial strain.

Our second goal is to establish ultrathin EuO layers for spin-functional tunnel contacts on silicon. Until today, a challenging bulk and interface chemistry of the highly reactive materials EuO and Si has hampered a seamless integration into silicon heterostructures. Therefore, we develop the integration of ultrathin EuO directly with silicon focusing on the structural and chemical control of the spin-functional EuO/Si interface.

In the first part of this thesis, we discuss the synthesis and throughout characterization of high-quality ultrathin EuO films on cubic oxides for our fundamental studies. We established the growth of epitaxial EuO thin films on cubic oxides by Oxide-MBE from bulk-like thicknesses down to one nanometer. By a precise control of synthesis parameters, we achieved a sustained layer-by-layer growth of EuO on conductive YSZ (001). During MBE growth, we verified the single-crystalline quality and epitaxy of the ultrathin films by electron diffraction techniques, and confirmed a bulk-like magnetization down to 2 nm thickness. We determined a nearly perfect stoichiometry of the metastable EuO thin films by HAXPES for various EuO thicknesses down to 1 nm. Thus, we could establish EuO ultrathin films as a magnetic oxide with reference quality. This is an important prerequisite for our further studies on fundamental electronic and magnetic properties.

In order to further investigate the nature of the ferromagnetic coupling in EuO, we experimentally realized to apply tensile and compressive biaxial strain in epitaxial EuO/$LaAlO_3$ (100) and EuO/MgO (001) heterostructures, respectively. We compare their magnetic properties obtained by the SQUID technique – yielding an averaged macroscopic moment – with the local and element-sensitive magnetic circular dichroism (MCD) in photoemission; this technique gives insight into the intra-atomic exchange coupling of EuO. Tensile biaxial strain causes a larger reduction of the core-level MCD asymmetry than of the averaged magnetic moment of the ultrathin strained EuO film as observed by SQUID. Thus, by strain-engineering we could tune the magnetic exchange in ultrathin epitaxial EuO, and quantify this effect by MCD in hard X-ray core-level photoemission, which is significantly different from the averaged macroscopic magnetization.

In the second part of this thesis, we investigate heterostructures of ultrathin EuO grown directly on silicon. EuO is the only binary magnetic oxide thermodynamically stable in direct contact with silicon, and it also permits up to 100% spin filter efficiency due to its exchange-split conduction bands. Thus, we are aiming towards a controlled integration of ultrathin EuO tunnel barriers directly with Si (001) without additional buffer layers. In particular,

we focus on the characterization and careful optimization of the spin-functional EuO/Si heterointerface.

First, we explore how to stabilize metastable EuO on Si using Oxide-MBE. We adapt a common strategy from silicon technology, the surface etching with hydrofluoric acid (HF), in order to remove native SiO_2 and chemically passivate the Si surface (H-Si). On such passivated Si substrates, we synthesized polycrystalline EuO using different growth parameters. By means of HAXPES, we clearly distinguished two EuO valency phases: stoichiometric EuO and over-oxidized Eu_1O_{1+x}. For the stoichiometric EuO heterostructures, we confirmed a bulk-like ferromagnetism – this is an important prerequisite for magnetic EuO tunnel contacts. This result paves the way for a following interface study of ultrathin EuO tunnel barriers directly on Si (001).

In the next step of our integration of ultrathin EuO directly with silicon, we focus on experimentally realizing a high structural and chemical quality of the EuO/Si heterointerface. Such atomically sharp interfaces of high crystalline quality may lead to coherent tunneling. Thus, we carefully studied how to chemically control the highly reactive EuO/Si heterointerface in order to permit an epitaxial integration of EuO on Si (001). Our thermodynamic analysis of the EuO/Si interface – taking into account the high chemical reactivity of Eu, EuO, and Si during EuO synthesis at elevated temperatures – gives us a guideline of probable reaction paths. In this way, we decided to compare three complementary *in situ* passivation procedures of the Si (001) surface: (*i*) hydrogen passivation, (*ii*) Eu passivation in the monolayer regime, and (*iii*) SiO_x formation in the Ångström regime. We apply these passivations selectively against interfacial silicon oxides and silicide formation – both being major antagonists to efficient spin filter tunneling.

In order to quantify the impact of different chemical passivations of the Si (001) surface on the EuO/Si interface properties, we conducted optimization studies comprising the control of surface crystalline structure and chemical interface properties by electron diffraction techniques and HAXPES, respectively. We conclude, that the respective Si surface passivations have minimized silicon oxides to below 1 nm and interfacial silicides to 2 Ångströms, which is clearly in the sub-nanometer regime. In particular, for an optimum passivation using the SiO_x method, the ultrathin EuO layer showed a magnetic saturation moment of $5\,\mu_B$/EuO, comparable to that of bulk EuO. Thus, our work demonstrates how to successfully apply chemical passivations to the Si (001) surface and – at the same time – maintain a mainly heteroepitaxial integration of EuO with the Si (001) wafer. This is an important result for possible spin-dependent coherent tunneling in EuO/Si contacts. Such optimized EuO/Si heterointerfaces may be used as spin-functional EuO tunnel contacts for silicon spintronic devices in the near future.

Outlook and perspectives

In the course of ongoing research in our group, polycrystalline EuO tunnel contacts with a native SiO_2 diffusion barrier on silicon have recently shown spin filter tunneling in electrical DC transport. In view of silicon spintronics, this result is a proof of principle for the spin filter effect in EuO tunnel barriers on silicon. This motivates a further improvement of the interface chemical properties which enables a simultaneous heteroepitaxial integration of EuO directly with Si (001). With regard to the thermal sensitivity of the passivated Si surface and pronounced surface kinetics of Si and Eu atoms, we propose a reduction of the synthesis temperature. Due to our thermodynamic analysis, a reduced temperature is suitable to maintain the hydrogen passivation of the Si surface in order to avoid interfacial silicides – the main antagonist to any tunnel functionality. Indeed, by a synthesis temperature of EuO as low as 200 °C, very recently crystalline EuO could be stabilized.[209] We consider this approach as the most promising route towards a further improvement of the chemical quality of the EuO/Si heterointerface.

Moreover, coherent tunneling may be feasible in epitaxial tunnel contacts of EuO on Si (001). In order to compare experimental findings of epitaxial EuO/Si (001) tunnel junctions – which are experimentally feasible, as concluded by the thesis at hand – with predictions for the spin filter efficiency, an appropriate modeling is needed. This motivates to launch spin-dependent density functional theory calculations for coherent tunneling through epitaxial EuO/Si (001) tunnel contacts.

The magnetic oxide EuO is a model system to propel fundamental research on localized $4f$ ferromagnetism. One approach is strain engineering, which modifies the magnetic coupling of EuO by lateral tension or compression, as shown in this thesis. This renders ultrathin epitaxial EuO films interesting for further investigations using the MCD effect in hard X-ray photoemission spectroscopy, since this technique yields element-specific information on intra-atomic exchange coupling in EuO, and in addition permits a depth-selective profiling. Using the MCD in hard X-ray photoemission, one can selectively investigate properties of buried interfaces, the bulk EuO layer, or identify possible magnetic dead layers – thus providing access to a complete set of the chemical and local magnetic properties of a layered magnetic heterostructure.

Furthermore, recent calculations predict that epitaxial EuO becomes ferroelectric under biaxial strain (tensile $\geqslant 4\%$, or compressive $\leqslant 3\%$).[21] Very recently, indeed a magnetization modulation in EuO by ferroelectric polarization pinning is reported for strained ferromagnetic–ferroelectric EuO/$BaTiO_3$ heterostructures.[20] This motivates further studies on epitaxial EuO under sufficient biaxial strain by suited substrates. Thereby, EuO may even provide a route to a multiferroic functionality, that combines ferromagnetic and ferroelectric order. For this, high-quality EuO thin films need to be epitaxially integrated with cubic substrates providing an appropriate biaxial strain, as has been successfully initiated in this thesis.

In that, future research on magnetic oxides like EuO offers exciting perspectives both for fundamental physics and silicon spintronics applications.

A. Appendix

A.1. Properties of EuO-related phases and cubic oxide substrates

EuO is metastable and easily reacts to thermodynamically competing compounds. In Tab. A.1, we provide an overview of the most common Eu reaction products which are possibly related to EuO during synthesis.

One objective of this thesis is the investigation of single-crystalline EuO epitaxially integrated on different cubic substrates providing biaxial strain, $m = \frac{a_S - a_F}{a_F}$. In order to allow for a gradation of available substrates, in Tab. A.2, we compile lattice parameters and strain with respect to single-crystalline EuO for different temperatures: at liquid helium, liquid nitrogen, room temperature, and during MBE synthesis of EuO. For the substrates used in this thesis, Fig. A.1 illustrates the cubic cells of EuO relative to underlying oxide substrates with an indication of biaxial strain, m, and interface reactivity.

For *lattice-matched* EuO growth, one may consider SrO (a = 5.161 Å, m = +0.4%) as well as $Sr_xBa_{1-x}O$, in which the cubic lattice parameter a is tunable by composition x (Lettieri et al. (2003)),[24,217] but these two are not commercially available due to their high reactivity in air and with humidity. The cubic ITO substrate allows for coherent EuO growth, yet tends to reduce its lattice constant for lower doping (e. g. 6% Sn). In this case, ITO would provide a small compressive strain with respect to EuO, if integrated epitaxially on cubic planes. Also the ITO crystals or films need to be synthesized on-site.

For *moderate tensile strain*, comparable to Si (001), CeO_2 (a = 5.412 Å, m = +5.2%) would be an option.

Among the commercially available substrates, cubic CaO (a = 4.815 Å, m = −6.3%) would be suited for a *moderate compressive strain* provided to EuO (001). CaO is chemically reactive with water and also carbon, which destroys the surface crystal structure immediately. Thus, we estimate its thermodynamic stability: CaO has a Gibbs free energy of formation of −636 kJ/mol which is larger than for EuO ($\Delta_f G(\mathrm{EuO}) \approx -500$ kJ/mol). This predicts the thermodynamic stability of CaO in contact with EuO synthesis. However, during oxygen-limited EuO synthesis at elevated temperatures, the reaction $\mathrm{CaO} + 3\mathrm{EuO} \longrightarrow \mathrm{Eu_3O_4} + \mathrm{Ca}$ results in a Gibbs free energy balance near zero. Thus, EuO may reduce CaO to propel its own oxidation, however the energy gain for that reaction is small which renders the reaction in the reversible regime (see Fig. 2.2). In conclusion, CaO is promising by means of its compressive strain, but chemically challenging due to its air-sensitivity and comparable thermodynamic stability with EuO.

Table A.1.: Eu compounds chemically adjacent to EuO and their properties at a glance. Sorted descendent by chemical stability. Applications in brackets are under development or suggestions by the author.

formula	magnetism	color	application
Eu_2O_3	PM [147,210]	redish	fluorescence color in displays
Eu_3O_4	AF [148,149], $T_N = 5.4$ K	white	white fluorescence bulb
$Eu(OH)_3$		transparent	
EuC_2	FM [211], $T_C = 15$ K	yellow	
EuC_6	spin frustration [212], $T_N = 42$ K		
EuO	FM [18,213], $T_C = 69$ K	blue	fluorescence color in displays (spintronics)
EuS	FM [18,189], $T_C = 16$ K	black	spintronics
$EuSi_y$	PM [191] / AF [214]		(metallic electrodes)
Eu	AF [215], $T_N = 90$ K / spin spiral [191]	grey	neutron absorber, (hydrogen storage [216])

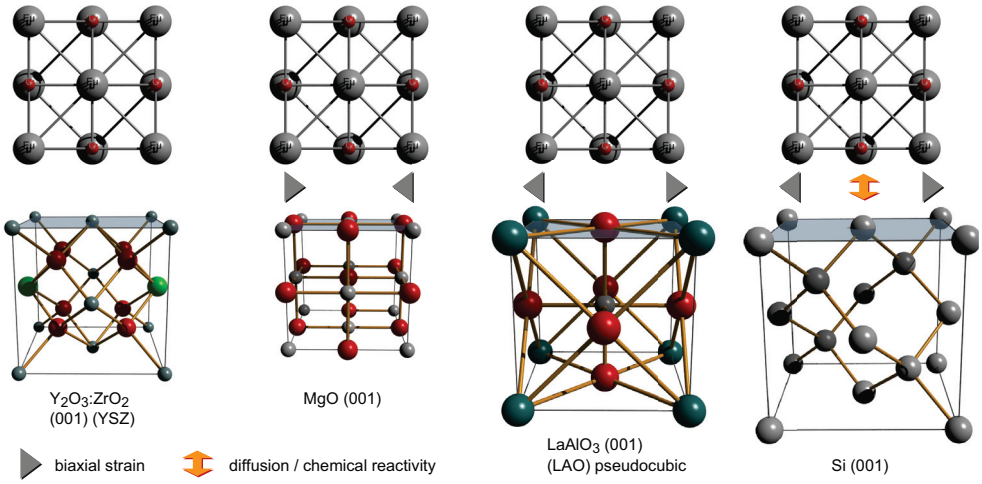

Figure A.1.: EuO in relation to the substrates YSZ (001), MgO (001), LAO (100), and Si (001). Biaxial strain acting on EuO is indicated by arrows. Interface reactivity may occur for the Si substrate.

Table A.2.: Cubic oxides as substrate: lattice parameters and strain with EuO. Negative strain is compressive for EuO, while positive strain is tensile. For $LaAlO_3$, the hexagonal lattice parameter is used; and for $YAlO_3$, the pseudocubic cell is used. EuO and substrates used in this work are shaded. The substrates are sorted by increasing lateral strain.

oxide orientation	EuO (001)	$SrTiO_3$ STO(001)	MgO (001)	CaO (001)	12%Sn:In_2O_3 ITO(001)	9%Y:ZrO_2 YSZ(001)	$YAlO_3$ (110)*	$LaAlO_3$ LAO(100)	Si (001)	CaF_2 (001)	$SrTiO_3$ STO(110)
linear lattice expansion, $a_T + \Delta a = a_{T_0}(1 + \alpha \Delta T)$											
α ($10^{-6}\,K^{-1}$) in plane, RT	13	9	14	28	10.2	9.2	8.1	10	2.6	18.7	9
cubic lattice parameter $a = a_T$											
$a_{750\,K}$ (nm) "MBE growth"	0.5172	0.3917	0.4239	0.4872	1.0178	0.514	0.7458 in $[1\bar{1}0]$ 0.7398 in [001]	0.5381	0.5436	0.5517	0.5545 × 0.3917
$a_{300\,K}$ (nm) "RT"	0.5142	0.3901	0.4212	0.4811	1.0131	0.512	0.7431 in $[1\bar{1}0]$ 0.7371 in [001]	0.5357	0.5431	0.5471	0.5523 × 0.3901
$a_{77\,K}$ (nm) "LN_2"	0.5127	0.3893	0.4199	0.4781	1.0108	0.511	0.7418 in $[1\bar{1}0]$ 0.7358 in [001]	0.5345	0.5428	0.5448	0.5512 × 0.3893
$a_{2\,K}$ (nm) "LHe"	0.5122	0.3890	0.4194	0.4771	1.0100	0.510	0.7413 in $[1\bar{1}0]$ 0.7358 in [001]	0.5341	0.5426	0.5440	0.5508 × 0.3890
strain $m = \frac{a_S - a_F}{a_F}$											
$m_{750\,K}$ "MBE growth"	—	−24.27%	−18.04%	−5.80%	−1.60%	−0.62%	+1.96% in $[1\bar{1}0]$ +1.14% in [001]	+4.04%	+5.10%	+6.67%	+7.21% × −24.27%
$m_{300\,K}$ "RT"	—	−24.13%	−18.08%	−6.43%	−1.49%	−0.43%	+2.19% in $[1\bar{1}0]$ +1.36% in [001]	+4.18%	+5.62%	+6.40%	+7.40% × −24.13%
$m_{77\,K}$ "LN_2"	—	−24.07%	−18.10%	−6.75%	−1.42%	−0.33%	+2.32% in $[1\bar{1}0]$ +1.48% in [001]	+4.25%	+5.87%	+6.26%	+7.51% × −24.07%
$m_{2\,K}$ "LHe"	—	−24.05%	−18.12%	−6.85%	−1.40%	−0.43%	+2.34% in $[1\bar{1}0]$ +1.51% in [001]	+4.28%	+5.94%	+6.21%	+7.54% × −24.05%

*) the epitaxial relation between EuO (001) and $YAlO_3$ (110) is 45° rotated in plane, as illustrated nicely in Ulbricht et al. (2008)[25,186].

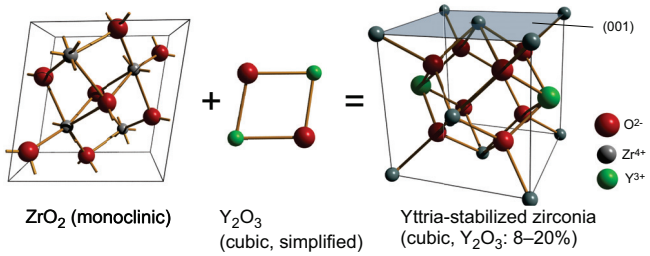

Figure A.2.: Structure and (001) plane of yttria-stabilized zirconia (YSZ).

In the following, we describe the crystal structure of substrates used in this thesis. Yttria-stabilized zirconia (YSZ) is used as a seed for coherent EuO growth of reference quality. Pure zirconium dioxide (ZrO_2) undergoes a phase transformation from monoclinic (stable at the room temperature) to tetragonal (at about 1000 °C) and then to cubic (at about 2370 °C). A stabilization of the desired cubic phase of zirconia can be accomplished by substitution of some of the Zr^{4+} ions (ionic radius of 0.82 Å, too small for ideal cubic lattice) in the crystal lattice with slightly larger ions, e. g. those of Y^{3+} (ionic radius of 0.96 Å). The result is cubic yttria-stabilized zirconia (YSZ). Doping with Y^{3+} ions produces oxygen vacancies, as three O^{2-} ions are bound to Y^{3+} rather than four O^{2-} ions in case of Zr^{4+}. This permits YSZ to conduct O^{2-} ions (and thus conduct an electrical current), provided there is a sufficient vacancy site mobility, a property that increases with temperature.[227]

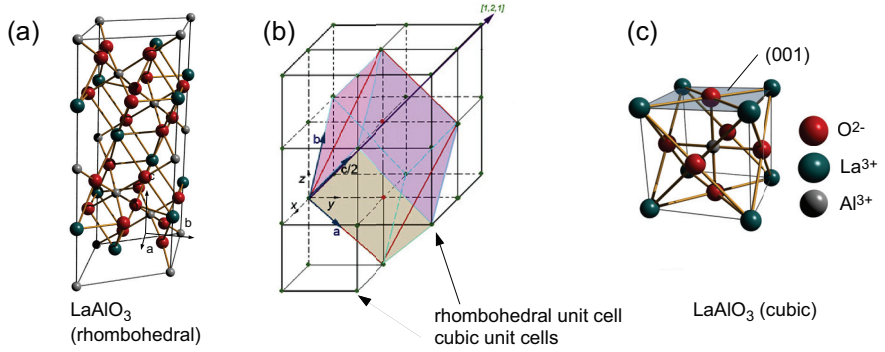

Figure A.3.: Rhombohedral structure, conversion, and pseudocubic structure with (001) plane of $LaAlO_3$ (LAO).

Pseudocubic $LaAlO_2$ (LAO) is used for epitaxial EuO/LAO (100) heterostructures with tensile biaxial strain. The transformation between rhombohedral and cubic structure for LAO is illustrated in Fig. A.3b.[218] The LAO $(100)_{cubic}$ plane is parallel to the $(0\bar{1}2)_{rhomb}$ plane, and $[01\bar{1}]_{cubic} \parallel [100]_{rhomb}$ and $[011]_{cubic} \parallel [121]_{rhomb}$. The LAO substrates are cut along $(100)_{cubic}$ planes. We will use the cubic indexing for LAO in this work. LAO is rhombohedral (pseudocubic) at room temperature, and undergoes a structural displacement transition at ~540 °C.[164]

The MgO and Si cubic unit cells rely on the well-known rock-salt and diamond lattice, respectively, and are not further discussed.

A.2. *In situ* analysis of the Si (001) surface after different treatments, conducted by Auger electron spectroscopy

In order to control the chemical quality of Si (001) surfaces in our studies, we conduct Auger electron spectroscopy (AES) routinely on clean (i. e. after a flashing procedure) and *in situ* surface-passivated Si substrates. The results of AES are summarized in Fig. A.4. Untreated Si ("as introduced") shows a large fraction of oxidized silicon (a). Here, the Si peak is hardly observable, according to a closed native SiO_2 surface layer. DHF-etched Si has a reduced oxide signal (b), however, this procedure introduces C contaminations. Flashed Si (c) is observed to be chemically clean and serves as a reference. The same is true for Si after an *in situ* hydrogen passivation (d, e), whereas an oxygen contribution near the detection limit can be observed.

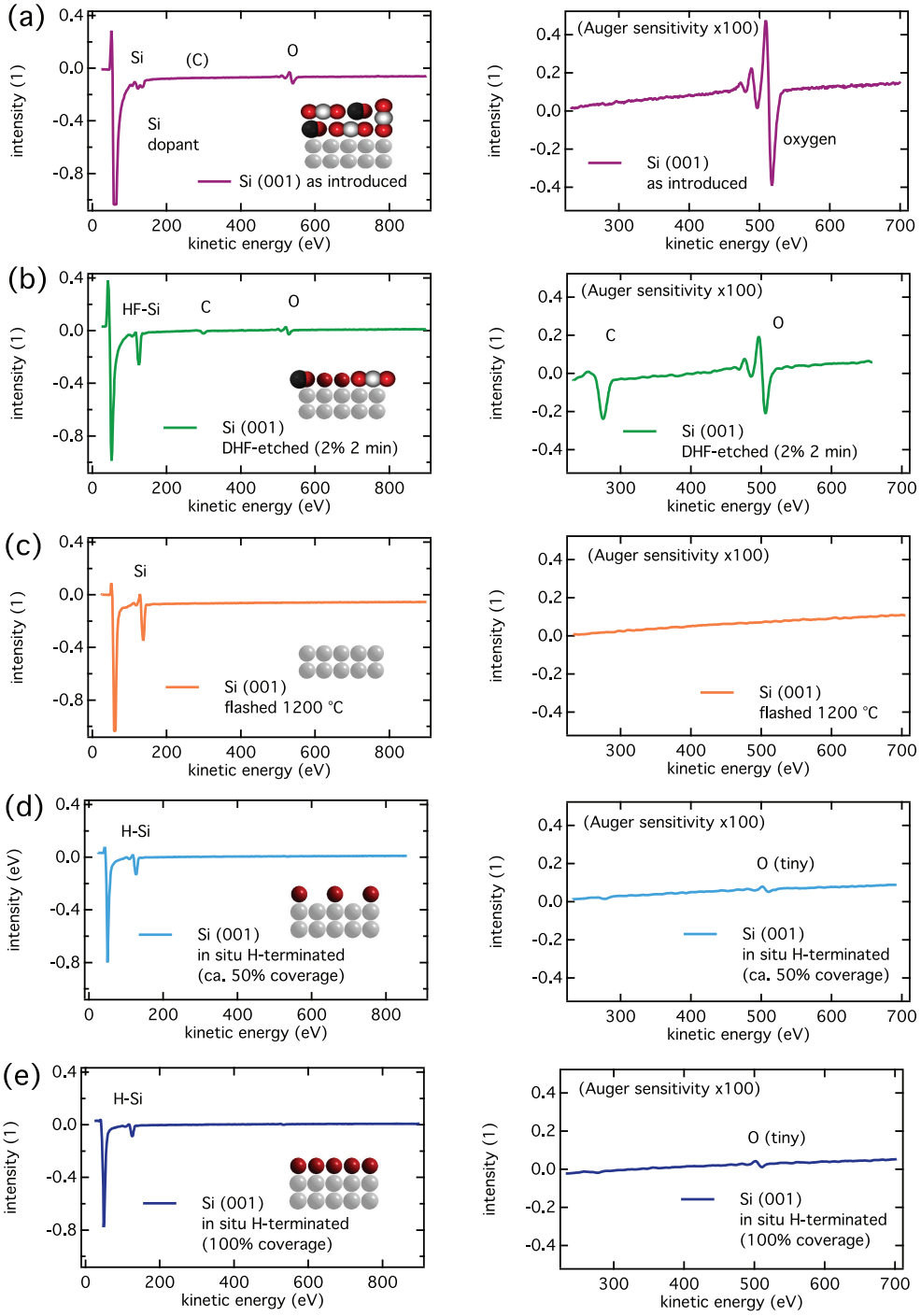

Figure A.4.: *In situ* analysis of the Si (001) surface with different types of hydrogen passivation, conducted by Auger electron spectroscopy in the Oxide-MBE system.

Bibliography

[1] G. Binasch, P. Grünberg, F. Saurenbach, and W. Zinn. Enhanced magnetoresistance in layered magnetic structures with antiferromagnetic interlayer exchange. *Phys. Rev. B*, 39:4828–4830, Mar 1989. doi: 10.1103/PhysRevB.39.4828. → pp. 1 and 43

[2] J. Sinova and I. Žutić. New moves of the spintronics tango. *Nat. Mater.*, 11(5):368–371, 2012. doi: 10.1038/nmat3304. → p. 1

[3] E. I. Rashba. Theory of electrical spin injection: Tunnel contacts as a solution of the conductivity mismatch problem. *Phys. Rev. B*, 62:R16267–R16270, 2000. doi: 10.1103/PhysRevB.62.R16267. → p. 1

[4] R. C. Sousa and I. L. Prejbeanu. Non-volatile magnetic random access memories (MRAM). *Compt. Rend. Physique*, 6(9):1013–1021, 2005. doi: 10.1016/j.crhy.2005.10.007. → p. 1

[5] S. Datta and B. Das. Electronic analog of the electro-optic modulator. *Appl. Phys. Lett.*, 56(7):665–667, 1990. doi: 10.1063/1.102730. → p. 1

[6] I. Žutić, J. Fabian, and S. C. Erwin. Spin injection and detection in silicon. *Phys. Rev. Lett.*, 97(2):026602, 2006. doi: 10.1103/PhysRevLett.97.026602. → p. 1

[7] R. Jansen, S. P. Dash, S. Sharma, and B. C. Min. Silicon spintronics with ferromagnetic tunnel devices. *Semicond. Sci. Tech.*, 27(8):083001, 2012. doi: 10.1088/0268-1242/27/8/083001. → pp. 1, 17, 85, 96, 105, 120, and 121

[8] M. Bibes and A. Barthélemy. Oxide Spintronics. *IEEE Electron. Devices*, 54(5):1003–1023, 2007. doi: 10.1109/TED.2007.894366. → p. 1

[9] F. Pulizzi. Oxidized spintronics. *Nat. Mater.*, 11:564, 2012. doi: 10.1038/nmat3375. → p. 1

[10] J. S. Moodera, T. S. Santos, and T. Nagahama. The phenomena of spin-filter tunnelling. *J. Phys-Condens. Mat.*, 19(16):165202, 2007. doi: 10.1088/0953-8984/19/16/165202. → pp. 1, 5, and 16

[11] G. Schmidt, D. Ferrand, L. W. Molenkamp, A. T. Filip, and B. J. van Wees. Fundamental obstacle for electrical spin injection from a ferromagnetic metal into a diffusive semiconductor. *Phys. Rev. B*, 62(8):R4790–R4793, Aug 2000. doi: 10.1103/PhysRevB.62.R4790. → pp. 1 and 17

[12] S. Yuasa, T. Nagahama, A. Fukushima, Y. Suzuki, and K. Ando. Giant room-temperature magnetoresistance in single-crystal Fe/MgO/Fe magnetic tunnel junctions. *Nat. Mat.*, 3 (12):868–871, 2004. doi: 10.1038/nmat1257. → pp. 2 and 17

[13] S. S. P. Parkin, C. Kaiser, A. Panchula, P. M. Rice, B. Hughes, M. Samant, and S.-H. Yang. Giant tunnelling magnetoresistance at room temperature with MgO (100) tunnel barriers. *Nat. Mat.*, 3(12):862–867, 2004. doi: 10.1038/nmat1256. → pp. 2 and 17

[14] K. J. Hubbard and D. G. Schlom. Thermodynamic stability of binary oxides in contact with silicon. *J. Mater. Res.*, 11(11):2757–2776, Nov 1996. doi: 10.1557/JMR.1996.0350. → pp. 2, 17, 85, 86, 95, 96, and 101

[15] S. G. Altendorf, A. Efimenko, V. Oliana, H. Kierspel, A. D. Rata, and L. H. Tjeng. Oxygen off-stoichiometry and phase separation in EuO thin films. *Phys. Rev. B*, 84:155442, 2011. doi: 10.1103/PhysRevB.84.155442. → pp. 2, 6, 11, 14, 60, 86, and 96

[16] R. Sutarto. *EuO and Gd-doped EuO thin films: Epitaxial growth and properties*. PhD thesis, Universität zu Köln, Jul. 2009. → pp. 2 and 68

[17] X. Wang, P Liu, K.A. Fox, J. Tang, J. A. Colon Santana, K. Belashchenko, P. A. Dowben, and Y. Sui. Effects of Gd Doping and Oxygen Vacancies on the Properties of EuO Films Prepared via Pulsed Laser Deposition. *IEEE Trans. Magn.*, 46(6):1879–1882, 2010. doi: 10.1109/TMAG.2010.2046314. → p. 2

[18] A. Mauger and C. Godart. The Magnetic, Optical, and Transport Properties of Representatives of a Class of Magnetic Semiconductors: the Europium Chalcogenides. *Phys. Rep.*, 141(2 & 3):51–176, 1986. doi: 10.1016/0370-1573(86)90139-0. → pp. 2, 9, 13, 14, 87, and 127

[19] P. A. Grünberg. Nobel Lecture: From spin waves to giant magnetoresistance and beyond. *Rev. Mod. Phys.*, 80:1531–1540, 2008. doi: 10.1103/RevModPhys.80.1531. → p. 2

[20] S. Cao, P. Liu, J. Tang, C. W. Bark, S. Ryu, C. B. Eom, P. Dowben, and A. Gruverman. Magnetoelectric coupling at the EuO/$BaTiO_3$ interface. In *Bulletin of the American Physical Society*, volume 58 (Baltimore, MD, USA), Mar 22nd 2013. APS March Meeting, presentation: J17.00013. → pp. 2 and 125

[21] E. Bousquet, N. A. Spaldin, and P. Ghosez. Strain-Induced Ferroelectricity in Simple Rocksalt Binary Oxides. *Phys. Rev. Lett.*, 104:037601, 2010. doi: 10.1103/PhysRevLett.104.037601. → pp. 2 and 125

[22] P. G. Steeneken. *New Light on EuO Thin Films*. PhD thesis, Rijksuniversiteit Groningen, Oct 2002. Preparation, transport, magnetism and spectroscopy of a ferromagnetic semiconductor. → pp. 2, 6, and 12

[23] C. Caspers. *Magnetic and light-induced properties of doped EuO thin films*. Diploma thesis, Universität zu Köln, Feb. 2010. → pp. 2, 6, 11, 14, 15, 58, and 60

[24] J. Lettieri, V. Vaithyanathan, S. K. Eah, J. Stephens, V. Sih, D. D. Awschalom, J. Levy, and D. G. Schlom. Epitaxial growth and magnetic properties of EuO on (001) Si by molecular-beam epitaxy. *Appl. Phys. Lett.*, 83(5):975–977, 2003. doi: 10.1063/1.1593832. → pp. 4 and 126

[25] A. Schmehl, V. Vaithyanathan, A. Herrnberger, S. Thiel, C. Richter, M. Liberati, T. Heeg, M. Röckerath, L. F. Kourkoutis, S. Mühlbauer, P. Böni, D. A. Muller, Y. Barash, J. Schubert, Y. Idzerda, J. Mannhart, and D. G. Schlom. Epitaxial integration of the highly spin-polarized ferromagnetic semiconductor EuO with silicon and GaN. *Nat. Mater.*, 6 (11):882–887, 2007. doi: 10.1038/nmat2012. → pp. 6, 18, 59, 85, 96, and 128

[26] A. G. Swartz, J. Ciraldo, J. J. I. Wong, Yan Li, Wei Han, Tao Lin, S. Mack, J. Shi, D. D. Awschalom, and R. K. Kawakami. Epitaxial EuO thin films on GaAs. *Appl. Phys. Lett.*, 97(11):112509, 2010. doi: 10.1063/1.3490649.

[27] A. G. Swartz, J. J. I. Wong, I. V. Pinchuk, and R. K. Kawakami. TiO_2 as an electrostatic template for epitaxial growth of EuO on MgO (001) by reactive molecular beam epitaxy. *J. Appl. Phys.*, 111(8):083912, 2012. doi: 10.1063/1.4704685. → pp. 4, 6, 18, 74, 80, 81, and 85

[28] P.-O. Löwdin. *Nobel Lectures Physics: 1971–1980*, chapter "The Nobel Prize in Physics 1977" – Award Ceremony Speech. River Edge, NJ, 1992. ISBN: 9789810207267, Speech at Nobelprize.org. → p. 5

[29] P. Wachter. *Europium chalcogenides: EuO, EuS, EuSe, and EuTe*, volume 2 of *Handbook on the Physics and Chemistry of Rare Earths*. Elsevier, New York, 2011. ISBN: 9780080932583. → pp. 5 and 10

[30] L. R. Morss and G. Meyer. *Synthesis of Lanthanide and Actinide Compounds*, volume 2 of *Topics in F-Element Chemistry*. Kluwer Academic Publ., 1991. ISBN: 9780792310181. → pp. 6 and 96

[31] F. Lévy. Effets magnétostrictifs spontanés de quelques composés des terres rares. *Physik kondens. Materie*, 10:71–84, 1969. doi: 10.1007/BF02422420. → p. 5

[32] R. Sutarto, S. G. Altendorf, B. Coloru, M. Moretti Sala, T. Haupricht, C. F. Chang, Z. Hu, C. Schüßler-Langeheine, N. Hollmann, H. Kierspel, H. H. Hsieh, H.-J. Lin, C. T. Chen, and L. H. Tjeng. Epitaxial and layer-by-layer growth of EuO thin films on yttria-stabilized cubic zirconia (001) using MBE distillation. *Phys. Rev. B*, 79(20):205318, May 2009. doi: 10.1103/PhysRevB.79.205318. → pp. 6, 18, 58, 59, 79, 80, 86, 96, and 118

[33] A. Melville, T. Mairoser, A. Schmehl, T. Birol, T. Heeg, B. Hollander, J. Schubert, C. J. Fennie, and D. G. Schlom. Effect of film thickness and biaxial strain on the curie temperature of euo. *Appl. Phys. Lett.*, 102(6):062404, 2013. doi: 10.1063/1.4789972. → pp. 6 and 74

[34] K. A. Gschneidner, Jr. *Physical Properties of the Rare Earth Metals*, chapter 4 "Properties of the Elements and Inorganic Compounds", page 130f. CRC Handbook of Chemistry and Physics. CRC Press, 90 edition, 2010. ISBN: 9780849304859. → pp. 7 and 96

[35] Scientific Group Thermodata Europe (SGTE). *The Landolt-Börnstein Database: Thermodynamic Properties of Inorganic Materials*, volume 19, subvolume A of *new series (editor: W. Martienssen)*, chapter Physical Chemistry (Group IV). Springer Materials, 2000. doi: 10.1007/b68802. → pp. 7, 92, and 96

[36] R. E. Dickerson. *Molecular thermodynamics*. Physical chemistry monograph series. Benjamin-Cummings Publishing Co., Subs. of Addison Wesley Longman, 1969. LCCN: 70794801. → pp. 7 and 97

[37] G. F. Dionne. *Magnetic Oxides*. Springer-Verlag, 2009. ISBN: 9781441900548. → pp. 9 and 12

[38] T. Kasuya. Exchange Mechanisms in Europium Chalcogenides. *IBM J. Res. Dev.*, 14(3): 214–223, 1970. doi: 10.1147/rd.143.0214. → p. 9

[39] R. Schiller and W. Nolting. Temperature-dependent band structure of bulk EuO. *Solid State Commun.*, 118(4):173–178, 2001. doi: 10.1016/S0038-1098(01)00073-4. → p. 9

[40] R. Schiller, O. Myrasov, A. J. Freeman, and W. Nolting. Temperature-dependent electronic structure of EuO films. *J. Mag. Magn. Mat.*, volumes 226–230 (part 1)(0):388–390, 2001. doi: 10.1016/S0304-8853(00)01186-0. → p. 34

[41] D. B. Ghosh, M. De, and S. K. De. Electronic structure and magneto-optical properties of magnetic semiconductors: Europium monochalcogenides. *Phys. Rev. B*, 70(11):115211, 2004. doi: 10.1103/PhysRevB.70.115211. → pp. 10 and 87

[42] T. Kasuya. Exchange interactions in rare earth compounds. *Journal of Alloys and Compounds*, 192(1–2):11–16, 1993. doi: 10.1016/0925-8388(93)90171-I. → pp. 9, 13, and 14

[43] G. Busch, P. Junod, and P. Wachter. Optical absorption of ferro- and antiferromagnetic europium chalcogenides. *Phys. Lett.*, 12(1):11–12, 1964. doi: 10.1016/0031-9163(64)91155-2. → p. 10

[44] W. Nolting, W. Borgiel, and G. Borstel. Dynamical corrections to density-functional theory for quasiparticles in ferromagnetic $4f$ systems. II. Finite-temperature results for EuO. *Phys. Rev. B*, 35:7025–7037, 1987. doi: 10.1103/PhysRevB.35.7025. → pp. 10 and 11

[45] P. G. Steeneken, L. H. Tjeng, I. Elfimov, G. A. Sawatzky, G. Ghiringhelli, N. B. Brookes, and D.-J. Huang. Exchange Splitting and Charge Carrier Spin Polarization in EuO. *Phys. Rev. Lett.*, 88(4):047201, 2002. doi: 10.1103/PhysRevLett.88.047201. → pp. 10, 59, 80, 86, 96, and 118

[46] M. R. Oliver, J. O. Dimmock, and T. B. Reed. Temperature and Magnetic Field Dependence of the Conductivity of EuO. *IBM J. Res. Develop.*, 14(276), 1970. → p. 11

[47] Storchak, V. G. and Eshchenko, D. G. and Morenzoni, E. and Ingle, N. and Heiss, W. and Schwarzl, T. and Springholz, G. and Kallaher, R. L. and von Molnár, S. Magnetic polarons in Eu-based films of magnetic semiconductors. *Phys. Rev. B*, 81(15):153201, 2010. doi: 10.1103/PhysRevB.81.153201.

[48] M. Müller, G.-X. Miao, and J. S. Moodera. Thickness dependence of ferromagnetic- and metal-insulator transition in thin EuO films. *J. Appl. Phys.*, 105(7):07C917, 2009. doi: 10.1063/1.3063673. → pp. 15, 66, and 111

[49] M. Arnold and J. Kroha. Simultaneous Ferromagnetic Metal-Semiconductor Transition in Electron-Doped EuO. *Phys. Rev. Lett.*, 100(4):046404, 2008. doi: 10.1103/PhysRevLett.100.046404.

[50] P. Sinjukow and W. Nolting. Metal-Insulator Transition in EuO. *Phys. Rev. B*, 68(12): 125107, 2003. doi: 10.1103/PhysRevB.68.125107.

[51] A. Mauger and C. Godart. Metal-insulator transition in Eu-rich EuO. *Solid State Commun.*, 35(10):785–788, 1980. doi: 10.1016/0038-1098(80)91074-1.

[52] A. Mauger. Magnetic Polaron: Theory and Experiment. *Phys. Rev. B*, 27(4):2308–2324, 1983. doi: 10.1103/PhysRevB.27.2308. → p. 11

[53] D. A. Atwood. *The Rare Earth Elements: Fundamentals and Applications*. Wiley, 2013. ISBN: 9781118632635. → p. 11

[54] J. Stöhr and H. C. Siegmann. *Magnetism: From Fundamentals to Nanoscale Dynamics*. Springer Series in Solid-state Sciences, vol. 152. Springer London, 2006. ISBN: 9783540302834. → pp. 12 and 63

[55] C.-C. Huang and J. T. Ho. Faraday rotation near the Curie point of EuO. *Phys. Rev. B*, 12:5255–5260, 1975. doi: 10.1103/PhysRevB.12.5255. → pp. 12 and 13

[56] P. M. Chaikin and T. C. Lubensky. *Principles of Condensed Matter Physics*, page of table 5.4.2. Cambridge University Press, 2000. ISBN: 9780521794503. → p. 13

[57] N. Menyuk, K. Dwight, and T. B. Reed. Critical Magnetic Properties and Exchange Interactions in EuO. *Phys. Rev. B*, 3(5):1689–1698, 1971. doi: 10.1103/PhysRevB.3.1689. → p. 13

[58] M. I. Darby. Tables of the Brillouin function and of the related function for the spontaneous magnetization. *Brit. J. Appl. Phys.*, 18(10):1415, 1967. doi: 10.1088/0508-3443/18/10/307. → p. 13

[59] H. A. Mook. Temperature Dependence of the Spin Dynamics of EuO. *Phys. Rev. Lett.*, 46:508–511, 1981. doi: 10.1103/PhysRevLett.46.508. → p. 13

[60] P. Liu and J. Tang. Antiferromagnetic coupling in EuO_{1-x}. *Phys. Rev. B*, 85:224417, 2012. doi: 10.1103/PhysRevB.85.224417. → pp. 13 and 14

[61] P. Liu, J. A. C. Santana, Q. Dai, X. Wang, P. A. Dowben, and J. Tang. Sign of the superexchange coupling between next-nearest neighbors in EuO. *Phys. Rev. B*, 86:224408, 2012. doi: 10.1103/PhysRevB.86.224408. → p. 74

[62] V. Lee and L. Liu. Exchange Mechanism in Europium Compounds. *Phys. Rev. B*, 30(4): 2026–2035, 1984. doi: 10.1103/PhysRevB.30.2026. → p. 13

[63] A. Kornblit and G. Ahlers. Heat capacity of EuO near the Curie temperature. *Phys. Rev. B*, 11:2678–2688, 1975. doi: 10.1103/PhysRevB.11.2678. → p. 14

[64] N. J. C. Ingle and I. S. Elfimov. Influence of epitaxial strain on the ferromagnetic semiconductor EuO: First-principles calculations. *Phys. Rev. B*, 77(12):121202, 2008. doi: 10.1103/PhysRevB.77.121202. → pp. 14 and 74

[65] R. Sutarto, S. G. Altendorf, B. Coloru, M. Moretti Sala, T. Haupricht, C. F. Chang, Z. Hu, C. Schüßler-Langeheine, N. Hollmann, H. Kierspel, J. A. Mydosh, H. H. Hsieh, H.-J. Lin, C. T. Chen, and L. H. Tjeng. Epitaxy, stoichiometry, and magnetic properties of Gd-doped EuO films on YSZ (001). *Phys. Rev. B*, 80(8):085308, Aug 2009. doi: 10.1103/PhysRevB.80.085308. → p. 14

[66] H. Miyazaki, H. J. Im, K. Terashima, S. Yagi, M. Kato, K. Soda, T. Ito, and S. Kimura. La-doped EuO: A rare earth ferromagnetic semiconductor with the highest Curie temperature. *Appl. Phys. Lett.*, 96(23):232503, 2010. doi: 10.1063/1.3416911. → p. 14

[67] A. Melville, T. Mairoser, A. Schmehl, D. E. Shai, E. J. Monkman, J. W. Harter, T. Heeg, B. Hollander, J. Schubert, K. M. Shen, J. Mannhart, and D. G. Schlom. Lutetium-doped EuO films grown by molecular-beam epitaxy. *Appl. Phys. Lett.*, 100(22):222101, 2012. doi: 10.1063/1.4723570. → p. 14

[68] M. Barbagallo, N. D. M. Hine, J. F. K. Cooper, N.-J. Steinke, A. Ionescu, C. H. W. Barnes, C. J. Kinane, R. M. Dalgliesh, T. R. Charlton, and S. Langridge. Experimental and theoretical analysis of magnetic moment enhancement in oxygen-deficient EuO. *Phys. Rev. B*, 81:235216, 2010. doi: 10.1103/PhysRevB.81.235216. → p. 14

[69] N. M. Souza-Neto, D. Haskel, Y.-C. Tseng, and G. Lapertot. Pressure-Induced Electronic Mixing and Enhancement of Ferromagnetic Ordering in EuX (X = Te, Se, S, O) Magnetic Semiconductors. *Phys. Rev. Lett.*, 102:057206, 2009. doi: 10.1103/PhysRevLett.102.057206. → p. 15

[70] R. Schiller and W. Nolting. Prediction of a Surface State and a Related Surface Insulator-Metal Transition for the (100) Surface of Stochiometric EuO. *Phys. Rev. Lett.*, 86:3847–3850, 2001. doi: 10.1103/PhysRevLett.86.3847. → pp. 15 and 63

[71] J. S. Moodera, X. Hao, G. A. Gibson, and R. Meservey. Electron-Spin Polarization in Tunnel Junctions in Zero Applied Field with Ferromagnetic EuS Barriers. *Phys. Rev. Lett.*, 61(5):637–640, Aug 1988. doi: 10.1103/PhysRevLett.61.637. → p. 17

[72] T. S. Santos and J. S. Moodera. Observation of Spin Filtering with a Ferromagnetic EuO Tunnel Barrier. *Phys. Rev. B*, 69(24):241203, Jun 2004. doi: 10.1103/PhysRevB.69.241203. → p. 17

[73] Guo-Xing Miao and Jagadeesh S. Moodera. Magnetic tunnel junctions with MgO-EuO composite tunnel barriers. *Phys. Rev. B*, 85:144424, Apr 2012. doi: 10.1103/PhysRevB.85.144424. → p. 17

[74] R. Jansen. Silicon spintronics. *Nat. Mater.*, 11(5):400–408, 2012. doi: 10.1038/nmat3293. → pp. 17 and 96

[75] V. Lukashev, A. L. Wysocki, J. P. Velev, M. van Schilfgaarde, Sitaram S. Jaswal, K. D. Belashchenko, and E. Y. Tsymbal. Spin filtering with EuO: Insight from the complex band structure. *Phys. Rev. B*, 85:224414, 2012. doi: 10.1103/PhysRevB.85.224414. → pp. 17 and 18

[76] N. Jutong, I. Rungger, C. Schuster, U. Eckern, S. Sanvito, and U. Schwingenschlögl. Electronic transport through EuO spin-filter tunnel junctions. *Phys. Rev. B*, 86:205310, Nov 2012. doi: 10.1103/PhysRevB.86.205310. → pp. 17 and 18

[77] H. Hertz. Über den Einfluß des ultravioletten Lichtes auf die electrische Entladung. *Ann. Phys.-Berlin*, 267(8):983–1000, 1887. doi: 10.1002/andp.18872670827. → p. 18

[78] A. Einstein. Über einen die Erzeugung und Verwandlung des Lichtes betreffenden heuristischen Gesichtspunkt. *Ann. Phys.-Berlin*, 322(6):132–148, 1905. doi: 10.1002/andp.19053220607. → p. 19

[79] H. Lüth. *Solid Surfaces, Interfaces and Thin Films*. Springer-Verlag, 5th edition, 2010. ISBN: 9783540423317. → pp. 19, 36, 40, 41, and 42

[80] S. Hüfner. *Photoelectron Spectroscopy: Principles and Applications*. Advanced Texts in Physics. Springer, 3rd edition, Apr. 2010. ISBN: 9783642075209. → pp. 19, 22, 24, 25, 26, and 28

[81] C. N. Berglund and W. E. Spicer. Photoemission Studies of Copper and Silver: Experiment. *Phys. Rev.*, 136:A1044–A1064, Nov 1964. doi: 10.1103/PhysRev.136.A1044. → p. 19

[82] Surfaces and Interfaces: Photoemission spectroscopy I. Institut für Physik, Universität Augsburg, 2008. Lecture of Experimentalphysik. → p. 19

[83] S. Tanuma, C. J. Powell, and D. R. Penn. Calculations of electron inelastic mean free paths. V. Data for 14 organic compounds over the 50–2000 eV range. *Surf. Interf. Anal.*, 21(3):165–176, 1994. doi: 10.1002/sia.740210302. → p. 21

[84] S. Tanuma, C. J. Powell, and D. R. Penn. Calculations of electron inelastic mean free paths. IX. Data for 41 elemental solids over the 50 eV to 30 keV range. *Surf. Interf. Analysis*, 43(3):689–713, 2011. doi: 10.1002/sia.3522. → pp. 21, 28, 48, 51, 53, and 88

[85] C. S. Fadley. X-ray photoelectron spectroscopy: Progress and perspectives. *J. Electron Spectrosc.*, 178(Sp. Iss. SI):2–32, 2010. doi: 10.1016/j.elspec.2010.01.006. → pp. 22, 25, 26, 28, 48, and 52

[86] A. X. Gray. *Depth-resolved electronic structure of spintronic nanostructures and complex materials with soft and hard x-ray photoemission*. PhD thesis, University of California Davis, Dec. 2011. → pp. 22, 26, and 28

[87] J. Henk, A. M. N. Niklasson, and B. Johansson. Multiple-scattering theoretical approach to magnetic dichroism and spin polarization in angle-resolved core-level photoemission. *Phys. Rev. B*, 59:13986–14000, 1999. doi: 10.1103/PhysRevB.59.13986. → pp. 22 and 32

[88] J. Henk. *Theory of Low-energy Electron Diffraction and Photoelectron Spectroscopy from Ultra-thin Films*, volume 2 "Characterization and Spectroscopy" of *Handbook of Thin Film Materials*, chapter 10. Academic Press, 2001. ISBN: 9780125129084. → p. 22

[89] J. E. Inglesfield. Plasmon satellites in core-level photoemission. *J. Phys. C*, 16(2):403, 1983. doi: 10.1088/0022-3719/16/2/023. → p. 24

[90] H.-J. Hinz and H. Raether. Line shape of the volume plasmons of silicon and germanium. *Thin Solid Films*, 58(2):281–284, 1979. doi: 10.1016/0040-6090(79)90249-9. → pp. 24 and 69

[91] P. Braun, M. Arias, H. Störi, and F. P. Viehböck. Plasmon excitation in Al-Mg surfaces. *Surf. Sci.*, 126(1–3):714–718, 1983. doi: 10.1016/0039-6028(83)90779-3. → p. 24

[92] C. S. Fadley, S. B. M. Hagström, J. M. Hollander, M. P. Klein, and D. A. Shirley. Chemical bonding information from photoelectron spectroscopy. *Science*, 157(3796):1571–1573, 1967. doi: 10.1126/science.157.3796.1571. → p. 24

[93] J. H. Van Vleck. The Dirac Vector Model in Complex Spectra. *Phys. Rev.*, 45:405–419, Mar 1934. doi: 10.1103/PhysRev.45.405. → p. 25

[94] E. D. Tober, F. J. Palomares, R. X. Ynzunza, R. Denecke, J. Morais, J. Liesegang, Z. Hussain, A. B. Shick, W. E. Pickett, and C. S. Fadley. Observation of dynamical spin-dependent electron interactions and screening in magnetic transitions via core-level multiplet-energy separations. *J. Electron Spectrosc.*, in press:–, 2013. doi: 10.1016/j.elspec.2012.12.009. → pp. 25 and 93

[95] F. R. McFeely, S. P. Kowalczyk, L. Ley, and D. A. Shirley. Multiplet splittings of the 4*s* and 5*s* core levels in the rare earth metals. *Phys. Lett. A*, 49(4):301–302, 1974. doi: 10.1016/0375-9601(74)90821-4. → p. 25

[96] C. Nordling, E. Sokolowski, and K. Siegbahn. Precision Method for Obtaining Absolute Values of Atomic Binding Energies. *Phys. Rev.*, 105:1676–1677, 1957. doi: 10.1103/PhysRev.105.1676. → p. 25

[97] A. Gloskovskii, G. Stryganyuk, G. H. Fecher, C. Felser, S. Thiess, H. Schulz-Ritter, W. Drube, G. Berner, M. Sing, R. Claessen, and M. Yamamoto. Magnetometry of buried layers—Linear magnetic dichroism and spin detection in angular resolved hard X-ray photoelectron spectroscopy. *J. Electron Spectrosc.*, 185(1-2):47–52, 2012. doi: 10.1016/j.elspec.2011.11.005. → pp. 25, 50, and 119

[98] M. Gorgoi, S. Svensson, F. Schäfers, G. Öhrwall, M. Mertin, P. Bressler, O. Karis, H. Siegbahn, A. Sandell, H. Rensmo, W. Doherty, C. Jung, W. Braun, and W. Eberhardt. The high kinetic energy photoelectron spectroscopy facility at BESSY progress and first results. *Nuclear Instr. Meth.*, 601(1–2):48–53, 2009. doi: 10.1016/j.nima.2008.12.244. → pp. 25, 49, and 119

[99] W. Drube. HAXPES spectra of metallic Al. Results from P09 at PETRAIII (DESY, Hamburg), 2012. personal communication. → pp. 25 and 90

[100] C. S. Fadley. X-ray photoelectron spectroscopy and diffraction in the hard X-ray regime: Fundamental considerations and future possibilities. *Nucl. Instr. Methods A*, 547(1):24–41, 2005. doi: 10.1016/j.nima.2005.05.009. → p. 26

[101] J. J. Yeh. *Atomic Calculation of Photoionization Cross-Sections and Asymmetry Parameters*. Gordon & Breach Science, 1993. ISBN: 9782881245855. → p. 26

[102] K. A. Thompson and C. S. Fadley. X-ray photoelectron diffraction from adsorbate core levels in the energy range 500–10000 eV and with polarized radiation: a theoretical study. *J. Electron Spectrosc.*, 33(1):29–50, 1984. doi: 10.1016/0368-2048(84)80004-3. → pp. 26 and 27

[103] L. Plucinski, J. Minár, B. C. Sell, J. Braun, H. Ebert, C. M. Schneider, and C. S. Fadley. Band mapping in higher-energy x-ray photoemission: Phonon effects and comparison to one-step theory. *Phys. Rev. B*, 78:035108, Jul 2008. doi: 10.1103/PhysRevB.78.035108. → p. 27

[104] B. T. Thole and G. van der Laan. Spin polarization and magnetic dichroism in photoemission from core and valence states in localized magnetic systems. *Phys. Rev. B*, 44: 12424–12439, Dec 1991. doi: 10.1103/PhysRevB.44.12424. → p. 29

[105] K. Starke. *Magnetic Dichroism in Core-Level Photoemission*, volume 159 of *Springer Tracts in Modern Physics*. Springer-Verlag, 2000. ISBN: 9783540662686. → pp. 29, 31, and 55

[106] K. Starke. *Magnetic Dichroism in Core-Level Photoemission*, chapter 2. Habilitation thesis, 1999. → pp. 29, 30, and 31

[107] J. G. Menchero. Spin polarization and many-body effects in Ni 3*p* core-level photoemission. *Phys. Rev. B*, 57:1001–1006, Jan 1998. doi: 10.1103/PhysRevB.57.1001. → p. 31

[108] L. Baumgarten, C. M. Schneider, H. Petersen, F. Schäfers, and J. Kirschner. Magnetic x-ray dichroism in core-level photoemission from ferromagnets. *Phys. Rev. Lett.*, 65: 492–495, Jul 1990. doi: 10.1103/PhysRevLett.65.492. → p. 30

[109] R. D. Cowan. *The Theory of Atomic Structure and Spectra*, volume 3 of *Los Alamos Series in Basic and Applied Sciences*. University of California Press, 1981. ISBN: 9780520906150. → p. 32

[110] E.-J. Cho, S.-J. Oh, S. Imada, S. Suga, T. Suzuki, and T. Kasuya. Origin of the high-binding-energy structure in the 3*d* core-level spectra of divalent Eu compounds. *Phys. Rev. B*, 51(15):10146–10149, 1995. doi: 10.1103/PhysRevB.51.10146. → pp. 33, 69, 71, 89, 90, 91, 92, and 93

[111] E.-J. Cho and S.-J. Oh. Surface valence transition in trivalent Eu insulating compounds observed by photoelectron spectroscopy. *Phys. Rev. B*, 59(24):R15613–R15616, 1999. doi: 10.1103/PhysRevB.59.R15613. → pp. 33, 69, 89, 90, 91, 92, and 93

[112] R. Denecke, J. Morais, R. X. Ynzunza, G. H. Fecher, J. G. Menchero, J. Liesegang, J. Kortright, Z. Hussain, and C. S. Fadley. Angular and temperature dependence of the magnetic circular dichroism in 4*d* core-level photoemission from Gd(0001). *Phys. Rev. B*, 65: 245421, 2002. doi: 10.1103/PhysRevB.65.245421. → pp. 33, 70, and 94

[113] A. Sankari, R. Sankari, S. Heinäsmäki, M. Huttula, S. Aksela, and H. Aksela. 4*d* photoionization and subsequent Auger decay in atomic Eu. *Phys. Rev. A*, 77:052703, 2008. doi: 10.1103/PhysRevA.77.052703.

[114] Ch. Gerth, K. Godehusen, M. Richter, P. Zimmermann, J. Schulz, Ph. Wernet, B. Sonntag, A. G. Kochur, and I. D. Petrov. Multiplet and lifetime effects in the 4*d* photoelectron spectrum of Eu. *Phys. Rev. A*, 61(2):022713, Jan 2000. doi: 10.1103/PhysRevA.61.022713. → pp. 69, 70, 71, and 94

[115] H. Ogasawara, A. Kotani, and B. T. Thole. Lifetime effect on the multiplet structure of 4*d* x-ray-photoemission spectra in heavy rare-earth elements. *Phys. Rev. B*, 50(17): 12332–12341, Nov 1994. doi: 10.1103/PhysRevB.50.12332. → pp. 33, 69, 70, 71, and 94

[116] S. Hüfner. *Photoelectron Spectroscopy: Principles and Applications*, chapter 2.3 "Core Polarization", pages 83–92. Advanced Texts in Physics. Springer, 3rd edition, 2010. ISBN: 9783642075209. → p. 33

[117] F. Gerken. Calculated photoemission spectra of the $4f$ states in the rare-earth metals. *J. Phys F*, 13(3):703, 1983. doi: 10.1088/0305-4608/13/3/021. → p. 34

[118] O. Gunnarsson and K. Schönhammer. Double occupancy of the f orbital in the Anderson model for Ce compounds. *Phys. Rev. B*, 31:4815–4834, 1985. doi: 10.1103/PhysRevB.31.4815. → p. 34

[119] R. Schiller. *Correlation Effects and Temperature Dependencies in Thin Ferromagnetic Films: Magnetism and Electronic Structure*. PhD thesis, Humboldt-Universität zu Berlin, 2000. → p. 34

[120] R. Schiller and W. Nolting. Temperature-dependent Band Structure of a Ferromagnetic Semiconductor Film. *Phys. Rev. B*, 60(1):462–471, 1999. doi: 10.1088/0953-8984/11/48/316. → p. 34

[121] E. Bauer. Phänomenologische Theorie der Kristallabscheidung an Oberflächen. *Z. Krist.*, 110(1–6):372–394, Jan 1958. doi: 10.1524/zkri.1958.110.1-6.372. → p. 36

[122] D. Sander and H. Ibach. *Surface free energy and surface stress*, volume 42 section A2 of *The Landolt-Börnstein database*, chapter 4.4.7, pages 19–44. SpringerMaterials, 4-2012 edition, 2002. doi: 10.1007/b79071. → p. 37

[123] F. J. Himpsel, J. E. Ortega, G. J. Mankey, and R. F. Willis. Magnetic nanostructures. *Adv. Phys.*, 47(4):511–597, 1998. doi: 10.1080/000187398243519. → p. 37

[124] A. Tsoga and P. Nikolopoulos. Surface and grain-boundary energies in yttria-stabilized zirconia (YSZ 8 mol%). *J. Mat. Science*, 31:5409–5413, 1996. doi: 10.1007/BF01159310. → p. 37

[125] E. A. Paisley, M. D. Losego, B. E. Gaddy, J. S. Tweedie, R. Collazo, Z. Sitar, D. L. Irving, and J.-P. Maria. Surfactant-enabled epitaxy through control of growth mode with chemical boundary conditions. *Nat. Commun.*, 2:461, 2011. doi: 10.1038/ncomms1470. → p. 37

[126] B. E. Deal and A. S. Grove. General Relationship for the Thermal Oxidation of Silicon. *J. Appl. Phys.*, 36(12):3770–3778, 1965. doi: 10.1063/1.1713945. → p. 37

[127] C. Krzeminski, G. Larrieu, J. Penaud, E. Lampin, and E. Dubois. Silicon dry oxidation kinetics at low temperature in the nanometric range: Modeling and experiment. *J. Appl. Phys.*, 101(6):064908, 2007. doi: 10.1063/1.2711764. → pp. 37 and 38

[128] S. D. Flade. *Spin-Filter Tunneln in magnetischen Oxid-Silizium-Kontakten*. Master's thesis, Universität Duisburg-Essen, Jan 2013. → pp. 38 and 121

[129] A. Tempel and B. Schumann. Determination of lattice parameters at thin epitaxial layers by RHEED. *Kristall und Technik*, 14(5):571–574, 1979. doi: 10.1002/crat.19790140510. → p. 39

[130] W. Braun. *Applied RHEED: Reflection High-Energy Electron Diffraction During Crystal Growth*, pages 14–17, 25, 75. Tracts in Modern Physics Series, No. 154. Springer Berlin, 1999. ISBN: 9783540651994. → p. 40

[131] F. Jona, J. A. Strozier, Jr., and W. S. Yang. Low-energy electron diffraction for surface structure analysis. *Rep. Prog. Physics*, 45(5):527, 1982. doi: 10.1088/0034-4885/45/5/002. → p. 40

[132] J. T. Yates, Jr. *Experimental Innovations in Surface Science: A Guide to Practical Laboratory Methods and Instruments*. Springer-Verlag, 1998. → p. 44

[133] C. Westphal. Practical advice for the construction of Si flashing stages, 2011. personal communication. → p. 44

[134] J. N. Smith, Jr. and W. L. Fite. Reflection and Dissociation of H_2 on Tungsten. *J. Chem. Phys.*, 37(4):898–904, 1962. doi: 10.1063/1.1733181. → p. 44

[135] L. Spieß, G. Teichert, R. Schwarzer, H. Behnken, and C. Genzel. *Moderne Röntgenbeugung*. Teubner Lehrbuch Physik. Vieweg + Teubner, 2. edition, 2009. ISBN: 9783519005223. → pp. 46 and 47

[136] L. G. Parratt. Surface Studies of Solids by Total Reflection of X-Rays. *Phys. Rev.*, 95(2): 359–369, Jul 1954. doi: 10.1103/PhysRev.95.359. → p. 46

[137] J. Rubio-Zuazo and G. R. Castro. Non-destructive compositional depth profile analysis by hard x-ray photoelectron spectroscopy. *J. Phys. Conf.*, 100(1):012042, 2008. doi: 10.1088/1742-6596/100/1/012042. → p. 52

[138] C. J. Powell and A. Jablonski. Electron effective attenuation lengths for applications in Auger electron spectroscopy and X-ray photoelectron spectroscopy. *Surf. Interf. Anal.*, 33(3):211–229, 2002. ISSN 1096-9918. doi: 10.1002/sia.1204. → p. 52

[139] Th. Eickhoff, V. Medicherla, and W. Drube. Final state contribution to the Si 2*p* binding energy shift in SiO_2/Si(100). *J. Electron Spectrosc.*, 137–140:85–88, 2004. doi: 10.1016/j.elspec.2004.02.026. → pp. 52, 95, 114, and 119

[140] S. Tougaard. Quantitative analysis of the inelastic background in surface electron spectroscopy. *Surf. Interf. Anal.*, 11(9):453–472, 1988. doi: 10.1002/sia.740110902. → p. 55

[141] A. Schnellbügel and R. Anton. On background subtraction for quantitative analysis of X-ray photoelectron spectra of rare earth fluorides. *Surf. Sci.*, 492(3):305–314, 2001. doi: 10.1016/S0039-6028(01)01422-4. → p. 55

[142] S. Tougaard. Universality Classes of Inelastic Electron Scattering Cross-sections. *Surf. Interf. Anal.*, 25(3):137–154, 1997. doi: 10.1002/(SICI)1096-9918(199703)25:3<137::AID-SIA230>3.0.CO;2-L.

[143] R. Hesse and R. Denecke. Improved Tougaard background calculation by introduction of fittable parameters for the inelastic electron scattering cross-section in the peak fit of photoelectron spectra with UNIFIT 2011. *Surf. Interf. Anal*, 43(12):1514–1526, 2011. doi: 10.1002/sia.3746. → p. 55

[144] R. Feder and J. Henk. *Spin-Orbit Influenced Spectroscopies of Magnetic Solids*, volume 466 of *Lecture Notes in Physics*, chapter "Magnetic dichroism and spin polarization in valence band photoemission", pages 85–104. Springer-Verlag, 1996. ISBN: 9783540608431. → p. 55

[145] W. Kuch, M.-T. Lin, W. Steinhögl, C. M. Schneider, D. Venus, and J. Kirschner. Angle-resolved study of magnetic dichroism in photoemission using linearly polarized light. *Phys. Rev. B*, 51:609–612, Jan 1995. doi: 10.1103/PhysRevB.51.609. → p. 56

[146] J. Chakhalian, A. Millis, and J. Rondinelli. Whither the oxide interface. *Nat. Mater.*, 11: 92, 2012. doi: 10.1038/nmat3225. → pp. 57 and 85

[147] N. L. Huang and J. H. Van Vleck. Effect of the Anisotropic Exchange and the Crystalline Field on the Magnetic Susceptibility of Eu_2O_3. *J. Appl. Phys.*, 40(3):1144–1146, 1969. doi: 10.1063/1.1657569. → pp. 60 and 127

[148] L. Holmes and M. Schieber. Magnetic Ordering in Eu_3O_4 and $EuGd_2O_4$. *J. Appl. Phys.*, 37(3):968–969, 1966. doi: 10.1063/1.1708542. → p. 127

[149] K. Ahn, V. K. Pecharsky, and K. A. Gschneidner, Jr. The magnetothermal behavior of mixed-valence Eu_3O_4. *J. Appl. Phys.*, 106(4):043918, 2009. doi: 10.1063/1.3204662. → pp. 60 and 127

[150] A. S. Borukhovich and V. G. Bamburov. Magnetism and magnetic heterogeneity of EuO films. *J. Magn. Magn. Mater.*, 53(1–2):80–82, 1985. doi: 10.1016/0304-8853(85)90132-5. → p. 63

[151] K. Y. Ahn and M. W. Shafer. Switching Properties of Europium Oxide. *J. Appl. Phys.*, 38(3):1197–1198, 1967. doi: 10.1063/1.1709536. → p. 63

[152] E. Arenholz, A. Schmehl, D. G. Schlom, and G. van der Laan. Contribution of Eu $4f$ states to the magnetic anisotropy of EuO. *J. Appl. Phys.*, 105(7):07E101, 2009. doi: 10.1063/1.3054364. → p. 64

[153] G. Suran, H. Ouahmane, and J. Sztern. Coercive field of amorphous soft ferromagnetic films: dependence upon thickness. *J. Magn. Magn. Mater.*, 140–144, Part 1(0):691–692, 1995. doi: 10.1016/0304-8853(94)00901-5. → p. 65

[154] P. J. Jensen, H. Dreyssé, and K. H. Bennemann. Calculation of the Film-Thickness-Dependence of the Curie Temperature in Thin Transition Metal Films. *Europhysics Lett.*, 18(5):463, 1992. → p. 66

[155] R. Schiller and W. Nolting. Thickness dependent Curie temperatures of ferromagnetic Heisenberg films. *Solid State Commun.*, 110(2):121–125, 1999. ISSN 0038–1098. doi: 10.1016/S0038-1098(98)00593-6. → p. 66

[156] B. C. H. Steele and A. Heinzel. Materials for fuel-cell technologies. *Nature*, 414:345–352, 2001. doi: 10.1038/35104620. → p. 66

[157] X. Guo, Y.-Q. Sun, and K. Cui. Darkening of zirconia: a problem arising from oxygen sensors in practice. *Sensors and Actuators B*, 31(3):139–145, 1996. doi: 10.1016/0925-4005(96)80058-X. → p. 66

[158] K. Kobayashi, S. Yamaguchi, T. Higuchi, S. Shin, and Y. Iguchi. Electronic transport properties and electronic structure of TiO_2-doped YSZ. *Solid State Ionics*, 135(1–4):643–651, 2000. doi: 10.1016/S0167-2738(00)00426-4. → p. 66

[159] B. A. Orlowski, S. Mickievicius, V. Osinniy, A. J. Nadolny, B. Taliashvili, P. Dziawa, T. Story, R. Medicherla, and W. Drube. High-energy X-ray photoelectron spectroscopy study of MBE grown (Eu, Gd) Te layers. *Nuclear Instr. Meth.*, 238(1–4):346–352, 2005. doi: 10.1016/j.nimb.2005.06.074. → pp. 69, 88, and 91

[160] E.-J. Cho, S.-J. Oh, S. Suga, T. Suzuki, and T. Kasuya. Electronic structure study of Eu intermetallic compounds by photoelectron spectroscopy. *J. Electron Spectrosc.*, 77(2): 173–181, 1996. doi: 10.1016/0368-2048(95)02495-6. → pp. 69 and 88

[161] K. Starke, E. Navas, E. Arenholz, and G. Kaindl. Magnetic Circular Dichroism in Photoemission from Lanthanide Materials. In *Spin–Orbit-Influenced Spectroscopies of Magnetic Solids*, pages 65–74. Springer-Verlag, 1995. → p. 70

[162] J. Szade, M. Neumann, I. Karla, B. Schneider, F. Fangmeyer, and M. Matteucci. Photon energy dependence of the Gd 4*d* photoemission. *Solid State Commun.*, 113(12):709–712, 2000. doi: 10.1016/S0038-1098(99)00563-3. → p. 70

[163] J. P. Velev, P. A. Dowben, E. Y. Tsymbal, S. J. Jenkins, and A. N. Caruso. Interface effects in spin-polarized metal/insulator layered structures. *Surf. Sci. Rep.*, 63(9):400–425, 2008. doi: 10.1016/j.surfrep.2008.06.002. → p. 74

[164] H. Lehnert, Hans Boysen, J. Schneider, Friedrich Frey, D. Hohlwein, P. Radaelli, and H. Ehrenberg. A powder diffraction study of the phase transition in $LaAlO_3$. *Z. Kristallographie–Crystalline Materials*, 215:536, 2000. doi: 10.1524/zkri.2000.215.9.536. → pp. 74 and 129

[165] R. Liu and M. Canonico. Applications of UV-Raman spectroscopy and high-resolution X-ray diffraction to microelectronic materials and devices. *Microelectron. Eng.*, 75(3): 243–251, 2004. doi: 10.1016/j.mee.2004.06.004. → p. 76

[166] N. Iwata, G. Pindoria, T. Morishita, and K. Kohn. Preparation and Magnetic Properties of EuO Thin Films Epitaxially Grown on MgO and $SrTiO_3$ Substrates. *J. Phys. Soc. Jpn*, 69(1):230–236, 2000. doi: 10.1143/JPSJ.69.230. → p. 79

[167] R. D. Shannon. Revised effective ionic radii and systematic studies of interatomic distances in halides and chalcogenides. *Acta Cryst. A*, 32(5):751–767, 1976. doi: 10.1107/S0567739476001551. → p. 81

[168] R. A. McKee, F. J. Walker, E. D. Specht, G. E. Jellison, L. A. Boatner, and J. H. Harding. Interface stability and the growth of optical quality perovskites on MgO. *Phys. Rev. Lett.*, 72:2741–2744, 1994. doi: 10.1103/PhysRevLett.72.2741. → p. 81

[169] H. Y. Hwang and J. Chakhalian. The interface is still the device. *Nat. Mater.*, 11:91, 2012. doi: 10.1038/nmat3244. editorial page. → p. 85

[170] H. Y. Hwang. Emergent phenomena at oxide interfaces. *Nat. Mater.*, 11:103, 2012. doi: 10.1038/nmat3223. → p. 85

[171] H. Miyazaki, T. Ito, H. J. Im, S. Yagi, M. Kato, K. Soda, and S. Kimura. Direct observation of momentum-dependent exchange interaction in a heisenberg ferromagnet. *Phys. Rev. Lett.*, 102(22):227203, 2009. doi: 10.1103/PhysRevLett.102.227203. → p. 87

[172] J. K. Lang, Y. Baer, and P. A. Cox. Study of the 4*f* and valence band density of states in rare-earth metals. II. Experiment and results. *J. Phys. F*, 11(1):121, 1981. doi: 10.1088/0305-4608/11/1/015. → pp. 88, 89, 90, and 93

[173] W.-D. Schneider, C. Laubschat, I. Nowik, and G. Kaindl. Shake-up excitations and core-hole screening in Eu systems. *Phys. Rev. B*, 24(9):5422–5425, 1981. doi: 10.1103/PhysRevB.24.5422. → pp. 88 and 91

[174] Y. Ohno and T. Urata. Photoelectron spectra and surface valence fluctuation of Eu in the misfit-layer compound $\{(EuS)_{1.15}\}_{1.5}NbS_2$. *J. Electron Spectrosc.*, 125(3):171–180, 2002. doi: 10.1016/S0368-2048(02)00163-9. → pp. 88, 89, 90, and 93

[175] K. H. J. Buschow, M. Campagna, and G. K. Wertheim. Intermediate valence in $YbAl_3$ and $EuCu_2Si_2$ by X-ray Photoemission (XPS). *Solid State Commun.*, 24(3):253–256, 1977. doi: 10.1016/0038-1098(77)91208-X. → pp. 88, 89, 90, and 93

[176] B. A. Orlowski, S. Mickevicius, M. Chernyshova, I. Demchenko, A. Y. Sipatov, T. Story, V. Medicherla, and W. Drube. Photoemission study of EuS layers buried in PbS. *J. Electron Spectrosc.*, 137–140:763–767, 2004. doi: 10.1016/j.elspec.2004.02.096. → pp. 88, 91, and 92

[177] Seiichi Miyazaki. Photoemission study of energy-band alignments and gap-state density distributions for high-*k* gate dielectrics. *J. Vac. Sci. B*, 19(6):2212–2216, 2001. doi: 10.1116/1.1418405. → p. 90

[178] L. Ley, S. Kowalczyk, R. Pollak, and D. A. Shirley. X-Ray Photoemission Spectra of Crystalline and Amorphous Si and Ge Valence Bands. *Phys. Rev. Lett.*, 29(16):1088–1092, 1972. doi: 10.1103/PhysRevLett.29.1088. → p. 90

[179] C. J. Powell, A. Jablonski, I. S. Tilinin, S. Tanuma, and D. R. Penn. Surface sensitivity of Auger-electron spectroscopy and X-ray photoelectron spectroscopy. *J. Electron Spectrosc.*, 98–99:1–15, 1999. ISSN 0368-2048. doi: 10.1016/S0368-2048(98)00271-0. → p. 88

[180] F. Mercier, C. Alliot, L. Bion, N. Thromat, and P. Toulhoat. XPS study of Eu(III) coordination compounds: Core levels binding energies in solid mixed-oxo-compounds $Eu_mX_xO_y$. *J. Electron Spectrosc.*, 150(1):21–26, 2006. ISSN 0368-2048. doi: 10.1016/j.elspec.2005.08.003. → pp. 91 and 92

[181] R. Vercaemst, D. Poelman, L. Fiermans, R. L. Van Meirhaeghe, W. H. Laflère, and F. Cardon. A detailed XPS study of the rare earth compounds EuS and EuF_3. *J. Electron Spectrosc.*, 74(1):45–56, 1995. doi: 10.1016/0368-2048(95)02349-6. → p. 91

[182] A. Kotani and H. Ogasawara. Theory of core-level spectroscopy of rare-earth oxides. *J. Electron Spectrosc.*, 60(4):257–299, 1992. doi: 10.1016/0368-2048(92)80024-3. → p. 92

[183] J. A. Rard. Chemistry and thermodynamics of europium and some of its simpler inorganic compounds and aqueous species. *Chemical Reviews*, 85(6):555–582, 1985. doi: 10.1021/cr00070a003. → pp. 92 and 96

[184] B. Sinković, D. J. Friedman, and C. S. Fadley. Theory of spin polarized photoelectron diffraction. *J. Mag. Mag. Mat.*, 92(3):301–343, 1991. doi: 10.1016/0304-8853(91)90846-3. for rare earth systems, read p. 303. → p. 93

[185] G.-X. Miao, M. Münzenberg, and J. S. Moodera. Tunneling path toward spintronics. *Rep. Progr. Physics*, 74(3):036501, 2011. → p. 96

[186] R. W. Ulbricht, A. Schmehl, T. Heeg, J. Schubert, and D. G. Schlom. Adsorption-controlled growth of EuO by molecular-beam epitaxy. *Appl. Phys. Lett.*, 93(10):102105, 2008. doi: 10.1063/1.2973180. → pp. 96 and 128

[187] Chris G. Van de Walle. Energies of various configurations of hydrogen in silicon. *Phys. Rev. B*, 49:4579–4585, Feb 1994. doi: 10.1103/PhysRevB.49.4579. → p. 96

[188] U. Hansen and P. Vogl. Hydrogen passivation of silicon surfaces: A classical molecular-dynamics study. *Phys. Rev. B*, 57(20):13295–13304, 1998. doi: 10.1103/PhysRevB.57.13295.

[189] O. D. McMasters, K. A. Gschneidner, E. Kaldis, and G. Sampietro. High-temperature enthalpies and standard Gibbs free energies of formation of the europium chalcogenides: EuO, EuS, EuSe, and EuTe. *J. Chem. Thermodyn.*, 6(9):845–857, 1974. ISSN 0021-9614. doi: 10.1016/0021-9614(74)90229-8. → pp. 96 and 127

[190] S. Hara, S. Izumi, T. Kumagai, and S. Sakai. Surface energy, stress and structure of well-relaxed amorphous silicon: A combination approach of ab initio and classical molecular dynamics. *Surf. Sci.*, 585(1-2):17 – 24, 2005. doi: 10.1016/j.susc.2005.03.061. → p. 98

[191] M. Ležaić. Heat of formation at $T = 0$ for paramagnetic and antiferromagnetic $EuSi_2$. Results from density-functional perturbation theory, 2011. personal communication. → pp. 98, 99, 111, 118, 120, and 127

[192] K. Rushchanskii. Enthalpy and entropy of $EuSi_2$. Results from density-functional perturbation theory using Quantum espresso code, 2012. personal communication. → p. 99

[193] S. Baroni, S. de Gironcoli, A. Dal Corso, and P. Giannozzi. Phonons and related crystal properties from density-functional perturbation theory. *Rev. Mod. Phys.*, 73:515–562, Jul 2001. doi: 10.1103/RevModPhys.73.515. → p. 99

[194] J. P. Perdew and Alex Zunger. Self-interaction correction to density-functional approximations for many-electron systems. *Phys. Rev. B*, 23:5048–5079, May 1981. doi: 10.1103/PhysRevB.23.5048. → p. 99

[195] A. Neumann and D. Walter. The thermal transformation from lanthanum hydroxide to lanthanum hydroxide oxide. *Thermochimica Acta*, 445(2):200–204, 2006. doi: 10.1016/j.tca.2005.06.013. → p. 102

[196] C. Besson. Verification of chemical equations, 2013. personal communication. → pp. 102 and 103

[197] J. Qi, T. Matsumoto, M. Tanaka, and Y. Masumoto. Europium silicate thin films on Si substrates fabricated by a radio frequency sputtering method. *J. Phys. D*, 33(16):2074, 2000. doi: 10.1088/0022-3727/33/16/321. → p. 103

[198] E. Kaldis, P. Streit, S. Vaccani, and P. Wachter. Synthesis, magneto-optics and fluorescence of the ferromagnetic semiconductor $Eu_3^{(II)}SiO_5$. *J. Phys. Chem. Solids*, 35(2): 231–240, 1974. doi: 10.1016/0022-3697(74)90039-0. → p. 103

[199] G. Zhao, J. Sun, Y. Gu, and Y. Wang. Density-functional study of structural, electronic, and magnetic properties of the $EuSi_n$ (n = 1–13) clusters. *J. Chem. Phys.*, 131(11):114312, 2009. doi: 10.1063/1.3232009. → p. 103

[200] W. A. Henle, M. G. Ramsey, F. P. Netzer, and K. Horn. Formation of divalent Eu silicides at the Eu–Si(111) interface. *Surf. Sci.*, 254(1–3):182–190, 1991. doi: 10.1016/0039-6028(91)90650-H. → p. 103

[201] F. Weitzer, Y. Prots, W. Schnelle, K. Hiebl, and Y. Grin. The novel silicide Eu_3Si_4: structure, chemical bonding, magnetic behavior and electrical resistivity. *J. Solid State Chem.*, 177(6):2115–2121, 2004. doi: 10.1016/j.jssc.2004.02.013. → p. 103

[202] J. D. Weeks and G. H. Gilmer. *Dynamics of Crystal Growth*, pages 157–228. John Wiley & Sons, Inc., 1979. doi: 10.1002/9780470142592.ch4. → p. 103

[203] J. A. Venables. *Thin Films: Heteroepitaxial Systems*, volume 15 of *Series on Directions in Condensed Matter Physics*, chapter 1–2. World Scientific Publishing, Singapore, 1999. ISBN: 9789810233907. → p. 103

[204] J. A. Venables. Atomic processes in crystal growth. *Surf. Sci.*, 299–300(0):798–817, 1994. doi: 10.1016/0039-6028(94)90698-X. → p. 104

[205] M. Biehl, W. Kinzel, and S. Schinzer. A simple model of epitaxial growth. *Europhys. Lett.*, 41(4):443–448, 1998. doi: 10.1209/epl/i1998-00171-0. → p. 105

[206] J. E. Northrup. Structure of Si(100)H: Dependence on the H chemical potential. *Phys. Rev. B*, 44:1419–1422, 1991. doi: 10.1103/PhysRevB.44.1419. → pp. 105 and 120

[207] H. Ibach. HT-Basic simulation of solid-on-solid surface diffusion, 2013. personal communication. → p. 112

[208] K. Hirose, M. Kihara, H. Okamoto, H. Nohira, E. Ikenaga, Y. Takata, K. Kobayashi, and T. Hattori. Valence charges for ultrathin sio_2 films formed on si(100). *J. Phys. IV France*, 132:83–86, 2006. doi: 10.1051/jp4:2006132016. → p. 119

[209] I. Moder, G. Garcia, J. Santiso, J. S. Moodera, G. X. Miao, A. F. Lopeandía, and J. Rodríguez-Viejo. Reduction of the deposition temperature of high quality EuO films on Yttria Stabilized Zirconia by incorporating an MgO buffer layer. *Thin Solid Films*, 531 (0):466–470, 2013. doi: 10.1016/j.tsf.2012.12.030. → p. 125

[210] W. Nolting and A. Ramakanth. *Quantum theory of magnetism*. Springer-Verlag, viii edition, 2010. ISBN: 9783540854166. → p. 127

[211] D. Wandner, P. Link, O. Heyer, J. Mydosh, M. A. Ahmida, M. M. Abd-Elmeguid, M. Speldrich, H. Lueken, and U. Ruschewitz. Structural Phase Transitions in EuC_2. *Inorganic Chem.*, 49(1):312–318, 2010. doi: 10.1021/ic901979v. → p. 127

[212] G. Lamura, T. Shiroka, S. Cahen, H. Rida, N. Emery, J.-F. Marêché, P. Lagrange, and C. Hérold. The zero-field magnetic ground state of EuC_6 investigated by muon spectroscopy. *Carbon*, 50(11):3995–4001, 2012. doi: 10.1016/j.carbon.2012.04.028. → p. 127

[213] B. T. Matthias, R. M. Bozorth, and J. H. Van Vleck. Ferromagnetic Interaction in EuO. *Phys. Rev. Lett.*, 7(5):160–161, 1961. doi: 10.1103/PhysRevLett.7.160. → p. 127

[214] J. Evers, G. Oehlinger, A. Weiss, and F. Hulliger. Strukturelle und magnetische Daten von $EuSi_2$. *J. Less Comm. Met*, 90(2):L19–L23, 1983. doi: 10.1016/0022-5088(83)90080-2. → p. 127

[215] R. M. Bozorth and J. H. Van Vleck. Magnetic susceptibility of metallic europium. *Phys. Rev.*, 118(6):1493–1498, 1960. ISSN 0031-899X. → p. 127

[216] V. I. Mikheeva and M. E. Kost. The Hydrides of the Rare-Earth Metals. *Russ. Chem. Rev.*, 29(1):28, 1960. doi: 10.1070/RC1960v029n01ABEH001216. → p. 127

[217] J. Lettieri, J. H. Haeni, and D. G. Schlom. Critical issues in the heteroepitaxial growth of alkaline-earth oxides on silicon. *J. Vac. Sci. Technol. A*, 20(4):1332–1340, 2002. doi: 10.1116/1.1482710. → p. 126

[218] Z. Zhai, Q. Xie, T. Lin, J. Xu, and X. Wu. Variation in structure and photoluminescence in $SrTiO_3$ film buffered by $SrRuO_3$. *J. Crystal Growth*, 327(1):267–271, 2011. doi: 10.1016/j.jcrysgro.2011.06.009. → p. 129

Software and Internet Resources

[219] The Nobel Prize in Physics 2007. Illustrated Information. Nobelprize.org (website), 2012. URL http://www.nobelprize.org/nobel_prizes/physics/laureates/2007/illpres/illpres.html.

[220] Haiyong Li. Ellingham Diagram Web Project. San José Sate University – College of Engineering (interactive website), 2013. URL http://www.engr.sjsu.edu/ellingham/.

[221] Saiht. Photoemission Spectroscopy. Wikipedia (website), 2009. URL http://en.wikipedia.org/wiki/Photoemission_spectroscopy.

[222] (author unknown). Thermische Oxidation von Silizium. Wikipedia (website), 2012. URL http://de.wikipedia.org/wiki/Thermische_Oxidation_von_Silizium.

[223] Lippmaa laboratory. Reflection High-Energy Electron Diffraction. University of Tokyo (website), 2012. URL http://lippmaa.issp.u-_tokyo.ac.jp/rheed/.

[224] K. Hermann and M. A. Van Hove. LEEDpat3 (LEED pattern analyzer). FHI Berlin (website), 2012. URL http://www.fhi-_berlin.mpg.de/KHsoftware/LEEDpat/index.html.

[225] P. Giannozzi, S. Baroni, N. Bonini, M. Calandra, R. Car, C. Cavazzoni, D. Ceresoli, G. L. Chiarotti, M. Cococcioni, I. Dabo, A. Dal Corso, S. de Gironcoli, S. Fabris, G. Fratesi, R. Gebauer, U. Gerstmann, C. Gougoussis, A. Kokalj, M. Lazzeri, L. Martin-Samos, N. Marzari, F. Mauri, R. Mazzarello, S. Paolini, A. Pasquarello, L. Paulatto, C. Sbraccia, S. Scandolo, G. Sclauzero, A. P. Seitsonen, A. Smogunov, P. Umari, and R. M. Wentzcovitch. QUANTUM ESPRESSO: a modular and open-source software project for quantum simulations of materials. *J. Phys. Condensed Matter*, 21(39):395502, 2009. doi: 10.1088/0953-8984/21/39/395502.

[226] P. R. Watson, M. A. Van Hove, and K. Hermann. Surface Structure Database. NIST Standard Reference Database 42, 2012. URL http://www.chem.qmul.ac.uk/surfaces/scc/scat1_6a.htm.

[227] University of Cambridge. Fuel Cells. DoITPoMS Teaching and Learning Packages, 2012. URL http://www.doitpoms.ac.uk/tlplib/fuel-_cells/printall.php.

[228] M. Müller. Oxide Spintronics Laboratory. Helmholtz Young Investigators Group (website), 2013. URL http://www.fz-_juelich.de/pgi/pgi-_6/DE/Forschung/NachwuchsgruppeMueller/Home/artikel.html.

List of own publications

[1] **Caspers, C.**, M. Müller, A. X. Gray, A. M. Kaiser, A. Gloskovskii, C. S. Fadley, W. Drube, and C. M. Schneider. Chemical stability of the magnetic oxide EuO directly on silicon observed by hard X-ray photoemission spectroscopy. *Phys. Rev. B*, 84:205217, 2011. doi: 10.1103/PhysRevB.84.205217.

[2] **C. Caspers**, A. Gloskovskii, W. Drube, C. M. Schneider, and M. Müller. Towards combined spin- and symmetry filtering: Oxide heteroepitaxy and ferromagnetism of ultrathin EuO/MgO(001). *submitted to a peer-reviewed journal*, 2013.

[3] **Caspers, C.**, M. Müller, A. X. Gray, A. M. Kaiser, A. Gloskovskii, C. S. Fadley, W. Drube, and C. M. Schneider. Electronic structure of EuO spin filter tunnel contacts directly on silicon. *Phys. Status Solidi (RRL)*, 5(12):441–443, 2011. doi: 10.1002/pssr.201105403.

[4] **Caspers, C.**, M. Müller, A. X. Gray, A. M. Kaiser, A. Gloskovskii, C. S. Fadley, W. Drube, and C. M. Schneider. Cover Picture: Electronic structure of EuO spin filter tunnel contacts directly on silicon. *Phys. Status Solidi (RRL)*, 5, 2011. doi: 10.1002/pssr.201190027. Cover picture of this PSS volume.

[5] **Caspers, C.**, M. Müller, A. X. Gray, A. M. Kaiser, A. Gloskovskii, C. S. Fadley, W. Drube, and C. M. Schneider. Electronic structure of EuO spin filter tunnel contacts directly on silicon. *Best of pss 2011*, Jan 2012. The PSS (RRL) 5, 441 publication has been selected together with 11 other papers from 2011 to be presented in the Best of PSS 2011 special issue.

[6] **C. Caspers**, S. D. Flade, M. Gorgoi, A. Gloskovskii, W. Drube, C. M. Schneider, and M. Müller. Ultrathin magnetic oxide EuO films on Si (001) using SiO_x passivation—controlled by hard X-ray photoemission spectroscopy. *J. Appl. Phys.*, 113(17):17C505, 2013. doi: 10.1063/1.4795010.

[7] M. Müller, **C. Caspers**, A. Gloskovskii, W. Drube, and C. M. Schneider. Biaxial Lattice Strain on the Magnetic Oxide EuO – Effect on the Magnetic Circular Dichroism Observed in Hard X-ray Core-level Photoemission. In *DESY Annual Report 2012*. Deutsches Elektronen-Synchrotron, 2013.

[8] M. Müller, **C. Caspers**, M. Gorgoi, A. Gloskovskii, W. Drube, and C. M. Schneider. Engineering the spin-functional interface EuO/Si (001). In *DESY Annual Report 2012*. Deutsches Elektronen-Synchrotron, 2013.

[9] S. G. Altendorf, N. Hollmann, R. Sutarto, **C. Caspers**, R. C. Wicks, Y.-Y. Chin, Z. Hu, H. Kierspel, I. S. Elfimov, H. H. Hsieh, H.-J. Lin, C. T. Chen, and L. H. Tjeng. Spectroscopic observation of strain-assisted T_C enhancement in EuO upon Gd doping. *Phys. Rev. B (R)*, 85:081201, 2012. doi: 10.1103/PhysRevB.85.081201.

[10] R. Wicks, S. G. Altendorf, **C. Caspers**, H. Kierspel, R. Sutarto, L. H. Tjeng, and A. Damascelli. NO-assisted molecular-beam epitaxial growth of nitrogen substituted EuO. *Appl. Phys. Lett.*, 100(16):162405, 2012. doi: 10.1063/1.3701589.

List of conference contributions

[11] **C. Caspers**, B. Zijlstra, S. D. Flade, M. Gorgoi, A. Gloskovskii, W. Drube, C. M. Schneider, and M. Müller. EuO on Cubic Oxides and Directly on Silicon. In *Joint European Magnetic Symposia (JEMS)*, Rhodes (Greece), 2013. Poster.

[12] **C. Caspers**, S. F. Flade, M. Gorgoi, A. Gloskovskii, W. Drube, C. M. Schneider, and M. Müller. Designing magnetic functionality in spin filter oxides on silicon. In *DPG Spring meeting – Section Condensed Matter*, Regensburg (Germany), 2013. DPG e.V. Short talk.

[13] **C. Caspers**, S. D. Flade, A. Gloskovskii, W. Drube, M. Gorgoi, C. M. Schneider, and M Müller. EuO for Silicon Spintronics. In *DESY Photon Science Users' meeting*, Hamburg (Germany), 2013. DESY Photon Science. Poster.

[14] **C. Caspers**, A. Gloskovskii, M. Gorgoi, W. Drube, C. S. Fadley, C. M. Schneider, and M. Müller. Ultrathin magnetic oxide EuO films on Si using SiO_x passivation—controlled by HAXPES. In *12th Joint MMM/Intermag conference*, Chicago (USA), 2013. AIP and the IEEE Magnetics Society. Poster.

[15] **C. Caspers**, M. Müller, M. Gorgoi, and C. M. Schneider. The Magnetic Oxide EuO on Si for Spintronics: Bulk and Interface Optimization controlled by HAXPES. In *4th Joint BER II and BESSY II User's Meeting*, Berlin (Germany), 2012. Helmholtz-Zentrum für Materialien und Energie. Poster.
This Poster presentation has been awarded with the *HZB User Commitee Best Poster Award* of the Helmholtz-Zentrum Berlin.

[16] **C. Caspers**, M. Müller, A. Gloskovskii, M. Gorgoi, W. Drube, C. S. Fadley, and C. M. Schneider. Functionalization of the EuO/Si interface for spintronics. In *Joint European Magnetic Symposia (JEMS)*, Parma (Italy), 2012. Short talk.

[17] **C. Caspers**, M. Müller, A. Gloskovskii, M. Gorgoi, W. Drube, C. S. Fadley, and C. M. Schneider. Functionalization of the EuO/Si interface. In *DPG Spring meeting – Section Condensed Matter*, Berlin (Germany), 2012. DPG e.V. Short talk.

[18] **C. Caspers**, M. Müller, A. Gloskovskii, M. Gorgoi, W. Drube, C. S. Fadley, and C. M. Schneider. EuO on Si for Spintronics: Electronic structure of the bulk and the interface investigated by HAXPES. In *3rd Joint BER II and BESSY II User's Meeting*, Berlin (Germany), 2011. Helmholtz-Zentrum Berlin für Materialien und Energie. Poster.

[19] **C. Caspers**, M. Müller, A. X. Gray, A. M. Kaiser, A. Gloskovskii, W. Drube, C. S. Fadley, and C. M. Schneider. The Magnetic Oxide EuO on Silicon for Spinfilters. In *JARA-FIT Science Days*, Schleiden (Germany), 2011. Jülich-Aachen Research Alliance – Future Information Technology. Poster.

[20] **C. Caspers**, M. Müller, A. X. Gray, A. M. Kaiser, A. Gloskovskii, W. Drube, C. S. Fadley, and C. M. Schneider. The Magnetic Oxide EuO on Silicon for Spinfilters. In *HAXPES 2011*, Hamburg (Germany), 2011. DESY Photon Science. Poster.

[21] **C. Caspers**, M. Müller, A. Gray, C. S. Fadley, S. Döring, C. Westphal, R. Dittmann, and C. M. Schneider. Bulk and Interface Properties of Magnetic Oxides for Spin Filters. In *PhD seminar*, Köln (Germany), 2011. II. Physikalisches Insitut der Universität zu Köln. Talk.

[22] **C. Caspers**, M. Müller, A. Gray, C. S. Fadley, S. Döring, C. Westphal, R. Dittmann, and C. M. Schneider. The Magnetic Oxide Europium Oxide as Spin Filter Material. In *DPG Spring meeting – Section Condensed Matter*, Dresden (Germany), 2011. DPG e.V. Short talk.

[23] **C. Caspers**, M. Müller, A. Gray, C. S. Fadley, S. Döring, C. Westphal, R. Dittmann, and C. M. Schneider. Magnetic Properties and Electronic Structure of EuO and $NiFe_2O_4$. In *471. Wilhelm und Else Heraeus Seminar – Functional Magnetoelectric Oxide Heterostructures*, Bad Honnef (Germany), 2011. DPG e.V. Short talk.

[24] **C. Caspers**, M. Müller, A. Gray, C. Fadley, S. Döring, C. Westphal, R. Dittmann, and C. M. Schneider. Growth and Characterization of Ferromagnetic Insulators for Tunnel Magnetoresistance (TMR) Applications. In *JARA-FIT nanoelectronics days*, Aachen (Germany), 2010. Jülich-Aachen Research Alliance – Future Information Technology. Poster.

Acknowledgement

> ...These days, it is truism to say that education is vital, but it is important to remind ourselves of the larger purpose of education. After all, what good is the accumulation of knowledge if it does not lead to a happier life?
>
> *(the Dalai Lama, 2009)*

This scientific work was created under valuable support of many individuals. The author expresses his deep gratitude to

- My doctoral advisor Prof. Dr. Claus M. Schneider, who provided the opportunity for pursuing this doctoral thesis in his group and shared his treasure trove of experience with us, which helped to render our experiments fruitful.
- The co-corrector of my thesis Prof. Dr. Carsten Westphal and the committee members Prof. Dr. Dieter Mergel and Prof. Dr. Klaus Hornberger.
- Dr. Martina Müller, for her sedulous and professional guidance through the doctoral studies. Being a part of the fresh and open-minded Young Investigators Group "Oxide Spintronics Laboratory" was an invaluable experience.[228]
- Dr. Andrei Gloskovskij, Dr. Mihaela Gorgoi, Dr. Wolfgang Drube, Dr. Sven Döring, Dr. Alexander X. Gray, Dr. Slavomir Nemsac, Dr. Alexander M. Kaiser, and Prof. Dr. Charles S. Fadley for enduring and fruitful support during several HAXPES beamtimes.
- JuProf. Dr. Marjana Ležaić and Dr. Konstantin Rushchanskii for the calculation of thermodynamic properties of silicides.
- Dr. Martina Luysberg, Doris Meertens, Dr. Claire Besson, Dr. Lutz Baumgarten, Prof. Dr. Harald Ibach, PD Dr. Daniel Bürgler for experimental support and helpful discussions.
- The mechanical and electronic workshops, under direction of Kurt Hirtz and Heinz Pfeifer, respectively. In particular, indispensable technical support was provided by Thomas Jansen, Franz-Josef Köhne, Bernd Küpper, and Norbert Schnitzler.
- My colleagues Bernardus Zijlstra, Sebastian D. Flade, Michael Hoppe, Stephan Kramer-Sinzinger, Hatice Doğanay, Xiangzhong Zhou, and Rajeswari Jayaraman for experimental support, correcting my writing, and a pleasant atmosphere.

ராஜ்ஜி, பெகௌஸெ ஒஂப் யொஉர் ஷ்ய்னெஸ்ஸ் யொஉ ஸைட் னொ டொ ம்ய் ஃபிர்ஸ்ட் கிஸ்ஸ் ஒன் யொஉர் லிப்ஸ். ஈ ஸ்டில்ல் ஹவெ இட் ஸஃபெ அஸ் ஒஉர் லொவெஸ் ஃபிர்ஸ்ட் ஹொல்ய் ஸிக்ன்.

Ich danke meinen Eltern für ihre liebevolle Unterstützung.

Band / Volume 55
Aufbau einer Vierspitzen-Rastertunnelmikroskop/Rasterelektronenmikroskop-Kombination und Leitfähigkeitsmessungen an Silizid Nanodrähten
E. Zubkov (2013), 150 pp
ISBN: 978-3-89336-848-8

Band / Volume 56
Interplay between magnetic and dielectric phenomena at transition metal oxide interfaces
D. Schumacher (2013), IV, 128 pp
ISBN: 978-3-89336-855-6

Band / Volume 57
Single $NdPc_2$ Molecules on Surfaces: Adsorption, Interaction, and Molecular Magnetism
S. Fahrendorf (2013), viii, 100 pp
ISBN: 978-3-89336-856-3

Band / Volume 58
Heyd-Scuseria-Ernzerhof Screened-Exchange Hybrid Functional for Complex Materials: All-Electron Implementation and Application
M. Schlipf (2013), XV, 170 pp
ISBN: 978-3-89336-857-0

Band / Volume 59
Orbital-dependent exchange-correlation functionals in density-functional theory realized by the FLAPW method
M. Betzinger (2013), vi, 173 pp
ISBN: 978-3-89336-858-7

Band / Volume 60
Structural influences on electrical transport in nanostructures
R. D. Frielinghaus (2013), viii, 190 pp
ISBN: 978-3-89336-867-9

Band / Volume 61
Study of intermolecular interactions in hetero-organic thin films
B. Stadtmüller (2013), viii, 198 pp
ISBN: 978-3-89336-871-6

Band / Volume 62
Structure, magnetism and excitations in some Mn-based magnetocaloric effect compounds
M. Gottschlich (2013), 175 pp
ISBN: 978-3-89336-874-7

Band / Volume 63
Neutron Scattering
Lectures of the JCNS Laboratory Course held at Forschungszentrum Jülich and the research reactor FRM II of TU Munich
edited by Th. Brückel, G. Heger, D. Richter, G. Roth and R. Zorn (2013),
ca 350 pages
ISBN: 978-3-89336-880-8

Band / Volume 64
Neutron Scattering
Experiment Manuals of the JCNS Laborator Course held at Forschungszentrum Jülich and the research reactorFRM II of TU Munich
edited by Th. Brückel, G. Heger, D. Richter, G. Roth and R. Zorn (2013),
ca. 150 pages
ISBN: 978-3-89336-881-5

Band / Volume 65
Solutions of Exercises in "An Introduction to Dynamics of Colloids"
J. K. G. Dhont, K. Kang (2013), 143 pp
ISBN: 978-3-89336-882-2

Band / Volume 66
Strukturelle und chemische Charakterisierung von selbst-assemblierten Monolagen organischer Moleküle auf Oberflächen
M. Müller (2013), 168 pp
ISBN: 978-3-89336-883-9

Band / Volume 67
Adsorption of (hetero-)organic Phthalocyanine and PTCDA thin films on Ag(111)
C. Kleimann (2013), iv, 149 pp
ISBN: 978-3-89336-888-4

Band / Volume 68
High-energy high-momentum surface spin waves of ultrathin epitaxial 3d transition metal films
R. Jayaraman (2013), ix, 135 pp
ISBN: 978-3-89336-890-7

Band / Volume 69
Magnetic Oxide Heterostructures: EuO on Cubic Oxides and on Silicon
C. Caspers (2013), xiii, 153 pp
ISBN: 978-3-89336-891-4

Schlüsseltechnologien / Key Technologies
Band / Volume 69
ISBN 978-3-89336-891-4

JÜLICH
FORSCHUNGSZENTRUM